České vysoké učení technické v Praze

Fakulta elektrotechnická

Katedra mikroelektroniky

Řízení experimentálních aparatur pro ultrazvukovou diagnostiku materiálů

Disertační práce

Ing. Martin Ševčík

Praha, *srpen, 2019*

Doktorský studijní program: P2612 - Elektrotechnika a informatika

Studijní obor: 2612V015 - Elektronika (doktorský)

Školitel: *prof. Ing. Miroslav Husák, CSs.*

Prohlášení

Prohlašuji, že jsem svoji disertační práci vypracoval samostatně pod odborným vedením vedoucího práce pana prof. Ing. Miroslava Husáka, CSc. a použil jsem pouze podklady (literaturu, projekty, software, atd.) uvedené v této práci. Nemám závažný důvod proti užití tohoto díla ve smyslu §60 Zákona č.121/2000 Sb. (a jeho novel č. 81/2005 Sb. a 216/2006 Sb.) o právu autorském.

V Praze dne .....

.....

Martin Ševčík

Poděkování

Na tomto místě bych chtěl poděkovat vedoucímu disertační práce, panu prof. Ing. Miroslavu Husákovi, CSc., za odborné vedení, slova povzbuzení, cenné připomínky a podněty a za čas, který mé práci věnoval.

Dále bych chtěl poděkovat všem kolegům z oddělení Ultrazvukových metod Ústavu termomechaniky AV ČR a zejména zesnulému Ing. Michalu Landovi, CSc. za jeho neutuchající entuziasmus nejen pro vědu, ale i za možnost, že jsem se mohl podílet na zajímavém vědeckém tématu. Doufám, že by na mne byl hrdý a chtěl bych pokračovat v cestě, kterou mi pomohl nalézt.

Chtěl bych poděkovat kolegům Ing. Martině Thomasové a Ing. Tomáši Grabcovi za jejich pomoc a připomínky k teoretickému rozboru. Také bych chtěl poděkovat rodině za jejich slova povzbuzení a podporu, kterou mi poskytli.

Martin Ševčík

Abstrakt:

Předmětem této práce je vývoj měřicích aparatur založených na laserově-ultrazvukových metodách. Tyto systémy představují unikátní možnosti v měření vývoje elastických konstant materiálů během různých procesů (strukturní změny v důsledku změn teploty, mechanického zatížení, atd.). Cílem práce je popsat tyto aparatury a jejich softwarové řízení a představit možnosti jejich využití v základním výzkumu v oblasti fyziky materiálů. Práce se zaměřuje především na řešení problémů kompatibility a možností komunikace mezi jednotlivými komponentami zařízení, dále pak na řízení a zpracování měřicích protokolů a vývoj rozhraní pro ovládání aparatury. Pro každou aparaturu jsou uvedeny příklady využití pro konkrétní materiálové problémy, včetně diskuze dosažených výsledků. Vývoj těchto měřicích systémů má velký přínos pro materiálový výzkum, neboť v mnoha případech neexistuje jiná možnost, jak experimentálně zjišťovat vývoj elastických konstant během výše uvedených procesů.

Klíčová slova: Elastické vlastnosti, NiTi, FePd, napěťově indukovaná reorientace, rezonanční ultrazvuková spektroskopie.

Abstract:

The subject of this thesis is the development of measuring devices based on laser-ultrasonic methods. These systems represent unique possibilities in measuring the development of elastic constants of materials during various processes (structural changes due to changes in temperature, mechanical load, etc.). The aim of this work is to describe these apparatuses and their software management and to present possibilities of their use in basic research in the field of material physics. The work focuses mainly on solving compatibility problems and possibilities of communication between individual components of the device, then on control and processing of measurement protocols and development of interface for controlling the apparatus. For each apparatus there are examples of usage for specific material problems, including discussion of the achieved results. The development of these measuring systems has great benefits for material research, since in many cases there is no other way of experimentally detecting the development of elastic constants during the above processes.

Key words: Elastic properties, NiTi, FePd, Stress-induced Reorientation, Resonant ultrasound spectroscopy.

Obsah

Seznam použitých symbolů

Obecné značení

a	skalární veličina
$\boldsymbol{a}$	vektorová veličina
$\boldsymbol{a}^T$	transpozice vektoru $\boldsymbol{a}$
a_i, a_x	složka vektoru
$\boldsymbol{A}$	matice vektorů $\boldsymbol{a}$
a_{ij}, a_{ijkl}	prvek matice nebo tenzoru
$grad_a$	gradient v souřadnicích $\boldsymbol{a}$
δa	relativní odchylka a od tabelované nebo průměrné hodnoty (v procentech)
i, j, k, l, m, n	index
a^{exp}	experimentální hodnota veličiny a
a^{calc}	vypočtená hodnota veličiny a
$\boldsymbol{\Gamma}$	matice
ψ_{abc}	systém ortogonálních funkcí
$u_{i,j}$	parciální derivace podle x_j
n_j	složky normálového vektoru
$\boldsymbol{K}$	matice tuhosti
$\boldsymbol{M}$	matice hmotnosti
$\boldsymbol{\alpha}$	vlastní vektor
Θ_V	Teplota odpařování
Θ_i	Počáteční teplota
C	Tepelná kapacita
Δ	Doba trvání pulsu
v	Poasonův poměr
F	Budící síla

Fyzikální veličiny

f	[MHz]	frekvence
v	$[\mathrm{m{\cdot}ms^{-1}}]$	rychlost
ρ	$[\frac{\mathrm{g}}{\mathrm{cm}^3}]$	hustota
C_{ijkl}	[GPa]	tenzor elastických koeficientů
c_{ij}	[GPa]	matice elastických koeficientů
T	[°C]	teplota
ω	$[\mathrm{s}^{-1}]$	úhlová frekvence
d_i	[mm]	rozměry substrátu
h	[mm]	výška vrstvy
t	[s]	čas
Λ	[J]	časově vystředovaná Lagrangeova energie
L	[J]	Lagrangeova energie
E_p	[J]	potenciální energie
E_k	[J]	kinetická energie
G	[GPa]	modul pružnosti ve smyku
E	[GPa]	modul pružnosti v tahu (Youngův modul)
K	[GPa]	modul objemové pružnosti
V	$[\mathrm{mm}^3]$	objem vzorku
$\boldsymbol{u}$	$[\mathrm{mm}, \mathrm{s}]$	pole posuvů $\boldsymbol{u} = \boldsymbol{u}(\boldsymbol{x}; t)$
R_s	[°C]	R–fáze v martenzitické transformaci
M_s	[°C]	počáteční teplota přechodu z austenitu do martenzitu
M_f	[°C]	konečná teplota přechodu z austenitu do martenzitu
A_s	[°C]	počáteční teplota přechodu z martenzitu do austenitu
A_f	[°C]	konečná teplota přechodu z martenzitu do austenitu
U	$[\frac{\mathrm{J}}{\mathrm{kg}}]$	hustota vnitřní energie
S	$[\frac{\mathrm{J}}{\mathrm{Km}^3}]$	hustota entropie
v_φ	$[\frac{\mathrm{m}}{\mathrm{s}}]$	fázová rychlost elastické vlny

$\mathcal{F}$	hustota Helmholtzovy volné energie
$\mathcal{G}$	hustota Gibbsovy volné energie
σ_{ij}	tenzor napětí
ε_{ij}	tenzor deformace
Γ	Christoffelova matice
$\boldsymbol{k}$	vlnový vektor

Matematické symboly

$P_n(x)$	Legendrovy polynomy n-tého stupně
π	Ludolfovo číslo

Seznam zkratek

RUS	Resonanční ultazvuková spektroskopie
DSC	Diferenční skenovancí kalolimetr
SRAS	Prostorově řešená akustická spektroskopie
TGS	Transmisní mřížková spektroskopie
BD	Laseová refrakce
SKED	Přesný bodový detektor
FPGA	Programovatelné hradolové pole
PID	Proporcionální, integrační a derivační regulační konstanta
FFT	Rychlá furierova transformace
DBT	Přechod do křehkého stavu
BDT	Reverzní teplota ve slitině
GBS	Pokluz po hranici zrna
SPD	Plasitcká deformace
ECAP	Metoda bezkontrakčního protlačování
EBSD	Difrakce zpětně odražených elektronů
PT	Pokojová teplota
G	Smykový modul
Q^{-1}	Vnitřní tření
E	Youngův modul
LVDT	Magnetický snímač pro kontaktní detekci vzdálenosti
SAW	Povrchová akustická vlna
SMA	Kov s tvarovou pamětí

1 Úvod

V rámci této práce se budeme zabývat jednou z velmi důležitých součástí materiálového výzkumu, a to charakterizačními metodami. Ve světě existuje celá řada komerčně dostupných charakterizačních metod (např. difrakční metody, mikroskopie, DSC...), ovšem tato práce se bude věnovat málo rozšířeným metodám, a to metodě laserově-ultrazvukové. Laserově-ultrazvuková metoda poskytuje velmi cenné a jinak nezískatelné informace o materiálech. Její velký přínos je v bezkontaktním měřením, a proto se může za určitých podmínek používat v různých konfiguracích.

Aparatury, které jsou založeny na principu laserově-ultrazvukových metod, nejsou komerčně dostupné, a proto je nutné tyto systémy vyvíjet. Při vývoji je nutné brát ohled na potřebu ruční kontroly a automatického řízení s automatickým ukládáním dat. Tato data je nutné ukládat v otevřených formátech, aby byla zajištěna snadná přenositelnost mezi různými systémy a vyhodnocovacími programy.

Měřené elastické konstanty jsou silně teplotně závislé, proto je velmi nutná stabilní teplotní regulace. Řada velmi zajímavých procesů v materiálech probíhá s teplotou či mechanickým napětím, proto je potřeba v těchto aparaturách možnost definované změny teploty či mechanického napětí.

Cílem práce je tedy vývoj řízení aparatur, založených na laserově-ultrazvuvokých metodách. Tyto systémy jsou umístěny v laboratořích Ultrazvukových metod na Ústavu Termomechanika AV ČR v Praze. V této práci budou popsány různé aparatury, jejich možnosti, ovládání a automatické řízení pro sledování vývoje procesů s teplotou (mechanickým napětí) v čase.

Řízení těchto systémů musí být dostatečně variabilní, aby je bylo možné používat pro různé specifické materiálové problémy. Pro řízení je velmi důležitá i robustnost systému. Musí být zajištěny ochrannými algoritmy a externími systémy, aby nedošlo k poškození měřeného vzorku materiálu. Tyto vzorky jsou velmi často dostupné jen v omezeném množství a v některých případech se jedná o unikátní materiály.

Aparatury, uvedené v této práci, jsou světově unikátní. Z toho důvodu jsou tyto aparatury využívány v rámci řady mezinárodních spoluprací, jak je v této práci ilustrováno na příkladech jejich použití.

1.1 Cíle disertační práce

1. Hlavní cíle

   (a) Návrh a realizace měřícího systému založeného na laserově-ultrazvukové metodě

   (b) Rozšíření měřícího systému na možnost sledování vývoje elastyckých konstatnt merariálů s teplotní změnou

   (c) Rozšíření systémů o možnost měření anizotropie materiálů

   (d) Návrh a realizace měřícího systému měření vývoje elastických konstatn materiálů během mechanického zatěžování

   (e) Měřící systémy plně zautomatizovat z důvodu dlouhodobých měření (cca 14 dní)

2. Vedlejší cíle

   (a) Změření a vyhodnocení vnitřního tření ultrajemnozrnné slitiny hořčíku AZ31

   (b) Definování vývoje elastických konstant ve slitině s tvarovou pamětí Fe-Pd pod zatížením

   (c) Charakterizace elasticity a fázové transformovace slitiny NiTi s tvarovou pamětí

   (d) Ultrazvuková detekce fázových přechodů v hliníkových slitinách

2 Metody

Díky vývoji v laserovém průmyslu, který přináší menší, stabilnější a také cenově dostupnější lasery, se začal zvyšovat zájem o využití těchto laserů v ultrazvukových metodách. Ty kombinují známé vlastnosti a výhody ultrazvuku při testování a vyhodnocování vlastností materiálů, s doplněním o bezkontaktní charakter přivedený lasery. Aby však bylo dosaženo plně bezkontaktního nastavení, musí být zajištěno použití laserového buzení a detekce. Hlavní charakteristiky těchto funkcí jsou popsány v této kapitole.

2.1 Rezonanční ultrazvuková spektroskopie

Díky spojení šíření ultrazvukových vln s termodynamickými vlastnostmi a mikrostrukturou zkoumaných materiálů má měření pomocí ultrazvuku v experimentální oblasti velký význam. Vedle tradiční pulzně odrazové metody (tzv. Pulse-Echo) se rozvíjejí metody rezonanční, které běžně mají přesnosti až v řádech 10^{-6}. Tyto metody umožňují testovat i velmi malé vzorky a analyzovat i obecně anizotropní materiály [1, 2].

2.1.1 Princip rezonanční ultrazvukové spektroskopie

Rezonanční ultrazvuková spektroskopie (RUS) využívá skutečnosti, že rezonanční frekvence závisí na hustotě, tvaru, orientaci krystalografických os a elastických konstantách vzorku. Díky těmto skutečnostem je možné z rezonančních frekvencí určit blíže tyto vlastnosti. Schéma na obr. 2.1 zobrazuje různé stupně ze kterých se RUS skládá.

Měření frekvenčních spekter V experimentální části metody RUS jsou měřeny amplitudy volného harmonického kmitání vzorku jako odezvy na široko-spektrální buzení. Na obr. 2.2 jsou zobrazeny první vlastní módy rovnoběžnostěnu s nejnižšími frekvencemi.. Povrch kmitajícího vzorku je snímám laserovým vibrometrem. Snímání je nutné provést na více místech povrchu vzorku. Z těchto dat je možné získat frekvenční spektra i průměty vlastních tvarů [3].

Vyhodnocení frekvenčních spekter V naměřených frekvenčních spektrech jsou hledány lokální maxima amplitudy a skokové změny fáze. Tím jsou získány rezonanční frekvence vzorku.

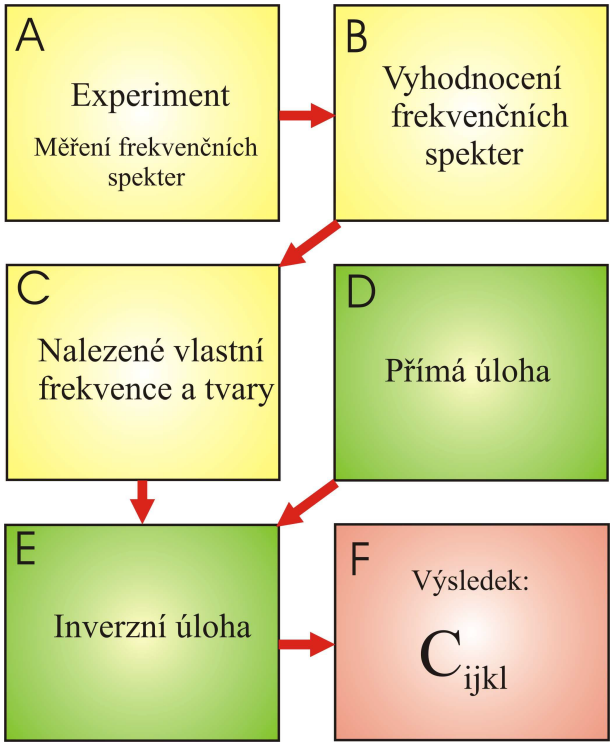

Obrázek 2.1: Schéma metody RUS [3]

.

Nalezení vlastních frekvencí a tvarů jsou získána data obsahující vlastní frekvence a jim příslušející vlastní tvary kmitání vzorku na obr. 2.3 [3].

Přímá úloha je výpočet předpokládaných vlastních frekvencí vzorku o daných rozměrech a pro daný odhad elastických konstant. Vypočítané vlastní frekvence jsou později porovnávány s naměřenými hodnotami. O tomto výpočtu více 2.1.2 [3].

Inverzní úloha využívá získaná data "Přímé úlohy"a "Vlastních frekvencí a tvarů". Jde o minimalizaci odchylek vypočtených a naměřených rezonančních frekvencí. Opakovaným výpočtem dochází ke zpřesnění vstupního odhadu elastických koeficientů v přímé úloze, tím je dosažena minimální odchylka výpočtu a výsledkem jsou přesné elastické koeficienty materiálu. O této metodě výpočtu v kapitole 2.1.3 [3].

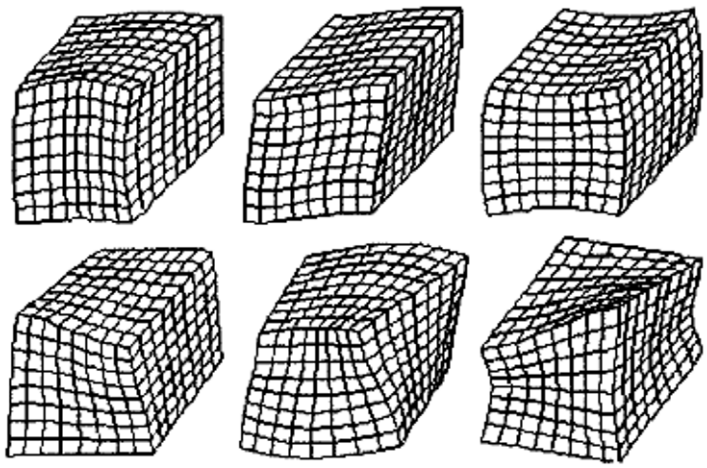

Obrázek 2.2: První vlastní módy s nejnižšími frekvencemi [3]

.

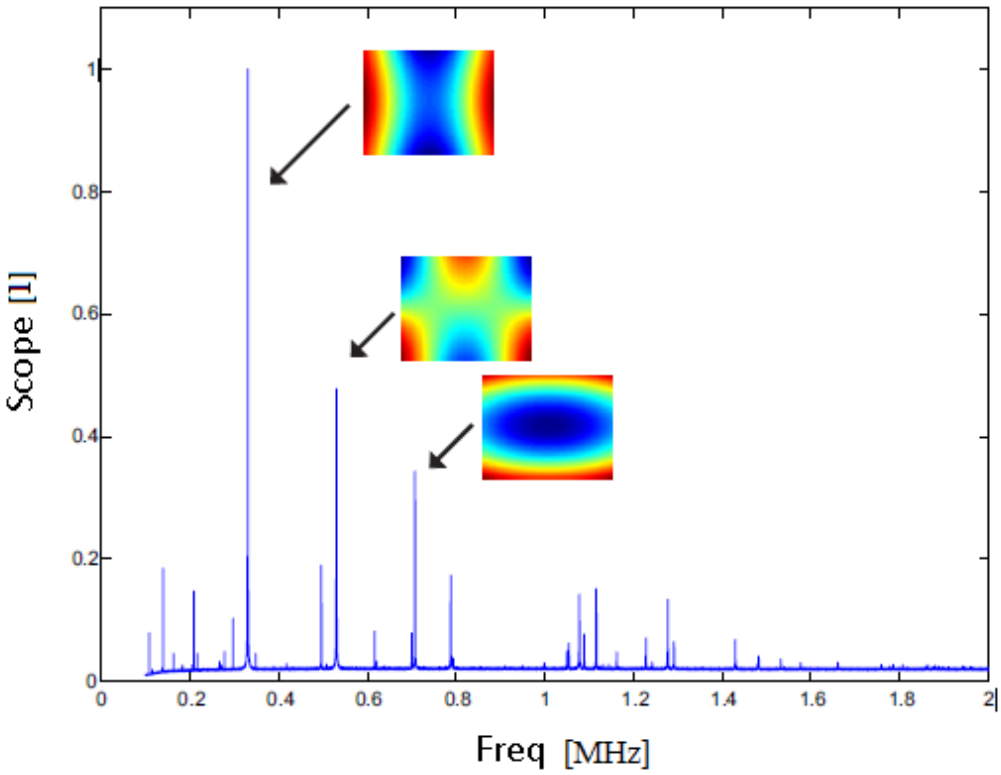

Obrázek 2.3: Ukázka identifikace rezonančních píků pomocí tvarů vlastních módů [3]

.

2.1.2 Přímá úloha

Ze znalosti elastických koeficientů C_{ijkl} a vlastností vzorku (rozměry, hustota, úhly stran a krystalografická orientace) můžeme pomocí přímé metody určit vlastní frekvence kmitání vzorku. Výpočet je možné provést metodou konečných prvků, nebo lépe pomocí Ritzovy metody [4, 5, 6, 1, 7, 8, 9].

Pole posuvů označíme $\boldsymbol{u} = \boldsymbol{u}(\boldsymbol{x}, t)$, jeho časovou derivaci $\dot{\boldsymbol{u}}$, objem vzorku V a jeho hustotu ρ. Potenciální energie E_P je potom rovna

$$E_P = \frac{1}{2} \int_V C_{ijkl} \frac{\partial u_i}{\partial x_j}(x,t) \frac{\partial u_k}{\partial x_l}(x,t) \mathrm{d}V \tag{2.1}$$

a kinetická energie E_K je

$$E_K = \frac{1}{2} \int_V \rho \dot{u}_i(x,t) \dot{u}_i(x,t) \mathrm{d}V \,. \tag{2.2}$$

Pro hledání tvarů vlastních módů kmitání, zapíšeme pole posuvů s vlastní úhlovou frekvenci ω ve tvaru

$$\boldsymbol{u}(\boldsymbol{x}, t) = \boldsymbol{u}(\boldsymbol{x}) \cos(\omega t) \,. \tag{2.3}$$

Lagrangián je pak roven

$$L = E_K - E_P = \frac{1}{2} \int_V \left(\rho \omega^2 u_i^2(x) \sin^2(\omega t) - C_{ijkl} \cos^2(\omega t) \frac{\partial u_i}{\partial x_j}(x) \frac{\partial u_k}{\partial x_l}(x) \right) \mathrm{d}V \,. \tag{2.4}$$

Podle Hamiltonova principu nejmenší akce pro libovolné pevně dané časy t_1 a t_2, kde $t_1 < t_2$, platí

$$\delta \int_{t_1}^{t_2} L \mathrm{d}t = 0 \,. \tag{2.5}$$

Pokud zvolíme časy t_1 a t_2 tak, aby

$$t_1 = t_2 + k \frac{2\pi}{\omega}, \;\; k \in \mathbb{N} \,, \tag{2.6}$$

a využijeme rovnost integrálů

$$\int_0^{\frac{2\pi}{\omega}} \cos^2(\omega t)\mathrm{d}t = \int_0^{\frac{2\pi}{\omega}} \sin^2(\omega t)\mathrm{d}t\,, \tag{2.7}$$

čímž získáme rovnici 2.5 ve tvaru

$$\delta\Lambda\left(\boldsymbol{u}(\boldsymbol{x})\right) = \delta\frac{1}{2}\int_V \lambda\left(\boldsymbol{u}(\boldsymbol{x})\right)\mathrm{d}V = \delta\frac{1}{2}\int_V \left(\rho\omega^2 u_i^2(x) - C_{ijkl}\frac{\partial u_i}{\partial x_j}(x)\frac{\partial u_k}{\partial x_l}(x)\right)\mathrm{d}V = 0\,, \tag{2.8}$$

kde Λ značí střední Lagrangeovu energii a λ její hustotu.

V objemu V pak podle základních vět variačního počtu plyne z rovnice (2.8) rovnice stojaté vlny

$$\rho\omega^2 u_i(x) + C_{ijkl}\frac{\partial^2 u_k}{\partial x_j \partial x_l}(x) = 0 \tag{2.9}$$

a podmínka volného okraje vzorku, kde n_j značí složky normálového vektoru kolmého k povrchu vzorku

$$n_j C_{ijkl}\frac{\partial u_k}{\partial x_l}(x) = 0\,. \tag{2.10}$$

Z důvodu zjednodušení výpočtu dále předpokládejme, že vzorek je tvaru kvádru. Souřadný systém x je umístěn tak, aby počátek ležel ve středu vzorku a byl souhlasně orientovaný s hranami vzorku. Rozměry vzorku značíme d_1, d_2, a d_3.

Lagrangián pak může být zapsán ve tvaru:

$$\Lambda = \frac{1}{2}\int_{-\frac{d_1}{2}}^{\frac{d_1}{2}}\int_{-\frac{d_2}{2}}^{\frac{d_2}{2}}\int_{-\frac{d_3}{2}}^{\frac{d_3}{2}} \left(\rho\omega^2 u_i^2(x) - C_{ijkl}\frac{\partial u_i}{\partial x_j}(x)\frac{\partial u_k}{\partial x_l}(x)\right)\mathrm{d}x_1\mathrm{d}x_2\mathrm{d}x_3 \tag{2.11}$$

Tuto úlohu řešíme dále pomocí Ritzovy metody. Pro tuto metodu je třeba pole posuvů $(\boldsymbol{u}(\boldsymbol{x}))$ vyjádřit rozvojem

$$u_i(x) = \sum_{a,b,c=1}^{N} \alpha_{abc,i}\psi_{abc}(x) = \sum_{a,b,c=1}^{N} \alpha_{abc,i} P_a\left(\frac{2x_1}{d_1}\right) P_b\left(\frac{2x_2}{d_2}\right) P_c\left(\frac{2x_3}{d_3}\right), \tag{2.12}$$

kde $\psi_{abc}(x)$ značí systém ortogonálních funkcí. Vhodnou volbou této báze jsou normalizované Legendreovy polynomy $P_{n=a,b,c}$:

$$P_n(x) = \sqrt{\frac{2n+1}{2}} \frac{1}{2^n n!} \frac{\mathrm{d}^n}{\mathrm{d}x^n}(x^2-1)^n \tag{2.13}$$

$$a, b, c = 0, 1, 2, \ldots \qquad a + b + c \leq N\,. \tag{2.14}$$

Rovnice 2.8 je splněna, platí-li

$$\frac{\partial \Lambda}{\partial \alpha_{abc,i}} = 0\,. \tag{2.15}$$

Po dosazení 2.12 do 2.11 dostaneme tvar:

$$\Lambda(\boldsymbol{\alpha}) = \frac{1}{2}\omega^2 \boldsymbol{\alpha}^T \boldsymbol{M} \boldsymbol{\alpha} - \frac{1}{2}\boldsymbol{\alpha}^T \boldsymbol{K} \boldsymbol{\alpha}\,, \tag{2.16}$$

kde jsou ve vektoru $\boldsymbol{\alpha}$ zahrnuty všechny koeficienty $\alpha_{abc,i}$, matice $\boldsymbol{M}$ je maticí hmotnosti a matice $\boldsymbol{K}$ maticí tuhosti. Platí pro ně vztahy:

$$M_{[abc,p][def,q]} = \frac{d_1 d_2 d_3}{8} \rho \delta_{ad} \delta_{be} \delta_{cf} \delta_{pq} \tag{2.17}$$

$$K_{[abc,p][def,q]} = \frac{d_1 d_2 d_3}{2} \frac{C_{pjql}}{d_j d_l} \int_{-1}^{1}\int_{-1}^{1}\int_{-1}^{1} \frac{\partial \psi_{abc}}{\partial y_j} \frac{\partial \psi_{def}}{\partial y_l} \mathrm{d}y_1 \mathrm{d}y_2 \mathrm{d}y_3\,. \tag{2.18}$$

Díky ortogonalitě Legendrových polynomů je matice $\boldsymbol{M}$ diagonální. Matice $\boldsymbol{K}$ je ze symetrie tenzoru C_{ijkl} symetrická a pozitivně definitní. Pro stacionární body potom vyplývají podmínky

$$0 = \nabla_\alpha \Lambda_(\boldsymbol{\alpha}) = (\omega^2 \boldsymbol{M} - \boldsymbol{K})\boldsymbol{\alpha}\,, \tag{2.19}$$

tím získáváme úlohu na řešení vlastních čísel a odpovídají přímo frekvencím odpovídajících vlastním kmitům. Tvary vlastních kmitů jsou dány vlastními vektory α, jako koeficienty pole posuvů podle (2.12).

2.1.3 Inverzní úloha

Inverzní úloha se používá pro určení konstant ze zkoumaného materiálu pomocí rezonančního spektra. Jejich přesné určení spočívá v minimalizaci odchylek naměřených a vypočítaných frekvencí. Je důležitě, aby jednotlivé módy vlastních vypočítaných frekvencí co nejlépe seděli k módům naměřeným [4]. Správně určit k sobě náležející módy je možné především z průmětu průmětu vlastního tvaru do naměřené strany. Určení jinou metodou, například pomocí číselné hodnoty frekvence, je více náchylné k chybám [3].

Informace o elastických konstantách je v rezonančním spektru rozložena tak, že nejnižší rezonanční frekvence nesou informaci o nižších elastických konstantách, zejména smykových. Tyto módy jsou označované jako měkké. S rostoucí frekvencí se objevují módy tvrdé, které jsou z většiny svázané s módy měkkými [7].

Naměřené rezonanční frekvence označíme $f^{exp.}_{1,2\ldots,n} = \omega^{exp.}_{1,2\ldots,n}/2\pi$, k nim příslušející vlastní vektory označíme $\alpha_{1,2\ldots,n}$ a nezávislé elastické konstanty označíme $C_{k=1,2\ldots,m}$. Pro derivaci frekvence $f^{exp.}_p$ podle elastického koeficientu C_k lze psát [4, 9]:

$$\frac{\partial f^{exp.}_p}{\partial C_k} = \frac{\alpha_p^T \frac{\partial \Gamma}{\partial C_k} \alpha_p}{8\pi^2 f^{exp.}_p} \,. \tag{2.20}$$

Díky vztahu 2.20 je možné stanovit míru citlivosti S_k rezonančního spektra vůči k-tému elastickému koeficientu a to tak, že bude vypočtena suma čtverců těchto derivací přes celé spektrum [4]:

$$S_k^2 = \sum_{p=1,\ldots,n} \left(\frac{\partial f^{exp.}_p}{\partial C_k} \right)^2 = \sum_{p=1,\ldots,n} \left(\frac{\alpha_p^T \frac{\partial \Gamma}{\partial C_k} \alpha_p}{8\pi^2 f^{exp.}_p} \right)^2 \,. \tag{2.21}$$

Elastické koeficienty je možné z rezonančních frekvencí určit nejlépe inverzní metodou a to pomocí vlastních tvarů naměřených módu [7]. Z tohoto důvodu je vhodné pro výpočet použít lineární kombinace C_l^*, jež je možno získat z rovnice 2.22

$$C_k = \phi_{kl} C_l^* \,, \tag{2.22}$$

kde C_k označují původní elastické koeficienty a ϕ tvarovou funkci [7]. Pro vyhodnocení citlivosti těchto kombinací je nutno transformovat rovnici do tvaru

$$S_k^{*2} = \sum_{p=1,\dots,n} \left(\frac{\partial f_p^{exp.}}{\partial C_l^*} \right)^2 = \sum_{p=1,\dots,n} \left(\phi_{kl} \frac{\alpha_p^T \frac{\partial \Gamma}{\partial C_l^*} \alpha_p}{8\pi^2 f_p^{exp.}} \right)^2 = \phi_{.l} \mathbf{G}^T \mathbf{G} \phi_{.l}^T \,. \tag{2.23}$$

Zde má tvarová funkce tvar $\phi_{.l} = (\phi_{1l}, \phi_{2l}, ...\phi_{nl})$ a matice $\mathbf{G}$ je maticí derivací

$$\mathbf{G} = \begin{pmatrix} \frac{\partial f_1^{exp.}}{\partial C_1} & \cdots & \frac{\partial f_1^{exp.}}{\partial C_m} \\ \vdots & \ddots & \vdots \\ \frac{\partial f_n^{exp.}}{\partial C_1} & \cdots & \frac{\partial f_n^{exp.}}{\partial C_m} \end{pmatrix} . \tag{2.24}$$

Výsledná matice $\mathbf{G}^T\mathbf{G}$ je symetrická a pozitivně definitní, což znamená, že vlastní vektory mohou být vhodně zvoleny ve formě ortogonálního systému. Seřazením vlastních čísel v sestupném pořadí a výběrem $\phi_{.l}$ l-tého vlastního vektoru je získána lineární kombinace C_l^*, kde pořadí závisí na vypočtené citlivosti [4].

Následně je v inverzní úloze minimalizována rovnice typu

$$\Delta(c_{ij}) = \sum_{p=1}^{n} w_p (f_p^{exp.} - f_p^{calc.}(c_{ij}))^2 \,. \tag{2.25}$$

Váhy přiřazené jednotlivým rezonančním frekvencím jsou značené w_p. Nyní je možné z této úlohy získat informaci o rozložení hledaného elastického koeficientu v rezonančním spektru. Pro zvýšení spolehlivosti určení elastických koeficientů a jejich kombinací je vhodné měření doplnit měřením pomocí pulzně odrazové metody. Doplněním informací o fázových rychlostech se zlepší stabilita výpočtu inverzní úlohy [4, 10, 7].

Minimalizovaná funkce pak získává tvar

$$\begin{aligned} \Delta(c_{ij}, \lambda_x, \lambda_y, \lambda_z) = \sum_{p=1}^{n} \left(f_p^{exp.} - f_p^{calc.}(c_{ij}) \right)^2 + \lambda_x \left(v_x^{qL,exp.} - v_x^{qL,calc.}(c_{ij}) \right)^2 + \\ + \lambda_y \left(v_y^{qL,exp.} - v_y^{qL,calc.}(c_{ij}) \right)^2 + \lambda_z \left(v_z^{qL,exp.} - v_z^{qL,calc.}(c_{ij}) \right)^2 \,, \end{aligned} \tag{2.26}$$

kde c_{ij} jsou hledané elastické koeficienty, $v_x^{qL}, v_y^{qL}, v_z^{qL}$ značí podélné fázové rychlosti ve směrech kolmých ke stěnám vzorku a Lagrangeovy multiplikátory λ_x, λ_y a λ_z reprezentující omezení [5]. Asociace vypočtených rezonančních frekvencí s experimentálními daty odpovídají první sumě rovnice 2.26, přiřazení se provádí na základě tvarů jednotlivých módů vibrací, které jsou zaznamenány pomocí laserové Dopplerovské interferometrie. Pro výpočet jsou použity pouze spolehlivě identifikovatelné módy [5].

Podmínky $v_{x,y,z}^{qL,calc.}\left(C_k\right) = v_{x,y,z}^{qL,exp.}$ pro vyjádření odhadu chyby výpočtu elastických koeficientů mohou být ve vzájemné blízkosti linearizované, tedy existují takové koeficienty $B_{x,y,z}^{k}$ a $B_{x,y,z}^{0}$, pro které platí [5, 7]:

$$v_{x,y,z}^{qL,calc.}\left(C_k\right) = \sum_{k=1}^{K} B_k^x C_k + B_x^0 \ldots \text{atd.}\,. \tag{2.27}$$

Díky této linearizaci a s využitím ortogonality β_{ij} je možné napsat systém lineárních rovnic

$$\begin{pmatrix} \beta_{11} & \cdots & \beta_{K1} \\ \vdots & \ddots & \vdots \\ \beta_{1K} & \cdots & \beta_{KK} \\ B_x^1 & \cdots & B_x^K \\ B_y^1 & \cdots & B_y^K \\ B_z^1 & \cdots & B_z^K \end{pmatrix} \begin{pmatrix} C_1 \\ \vdots \\ C_K \end{pmatrix} = \begin{pmatrix} C_1^* \\ \vdots \\ C_K^* \\ v_x^{qL,exp.} - B_x^0 \\ v_y^{qL,exp.} - B_y^0 \\ v_z^{qL,exp.} - B_z^0 \end{pmatrix}, \tag{2.28}$$

kde je experimentální přesnost pravé strany rovnic známa [4]. Následně je možné zapsat přesnost jednotlivých koeficientů, jejichž chyba je minimalizována vázanou optimalizací 2.26.

$$\Delta C_l^* = \sqrt{\frac{\sum_p^{k=1} \left(\omega_k^{calc.} - \omega_k^{exp.}\right)^2}{\lambda_l}} \tag{2.29}$$

Přesnost jednotlivých hodnot $\Delta v_{x,y,z}^{qL,exp.}$ je dána experimentem. Následujícím krokem je vydělení každého sloupce matice 2.28 odpovídající experimentální chybou, čímž bude získán podobný systém, avšak přesnost pravé strany bude rovna 1. Jelikož je tento systém dobře určený, je možné hledat inverzní lineární vztahy pouze metodou nejmenších čtverců. Pro tyto výpočty je používána rutina Moorse-Penroseova pseudo-inverze. Jelikož se přesnosti pravé strany rovnic rovnají jedné, lze vyjádřit přesnost jednotlivých koeficientů ΔC_k přímo z Euklidovských norem příslušných sloupců pseudo-inverzní matice [5, 7].

Symetrie a třída anizotropie vzorku výrazně ovlivňují náročnost určení elastických konstant. Čím komplikovanější tyto materiálové vlastnosti jsou, tím je nutné pro výpočet použít více rezonančních frekvencí [1].

Konstanty nejsou určeny se stejnou přesností, protože k některým je metoda RUS citlivá, ale k jiným mnohem méně. Obecně je metoda RUS nejcitlivější pro určování měkkých

smykových parametrů a nejméně citlivá pro objemový modul pružnosti, odpovídající hydrostatické deformaci materiálu [9].

2.2 Metoda povrchových vln

2.2.1 Buzení laserovým pulsem

Prvním důležitým aspektem laserových ultrazvukových metod je způsob excitace elastických vln pomocí laserů. To je zajištěno fenoménem nazývaným fototermální nebo fotoakustické buzení. Jak tyto buzení probíhají je znázorněno na obr. 2.4.
Mezi hlavní výhody rozšíření ultrazvukových metod o laserovou generaci vln patří bezkontaktnost excitace a variabilita zdroje ve smyslu jeho pozice, tvaru a energie pulzu.

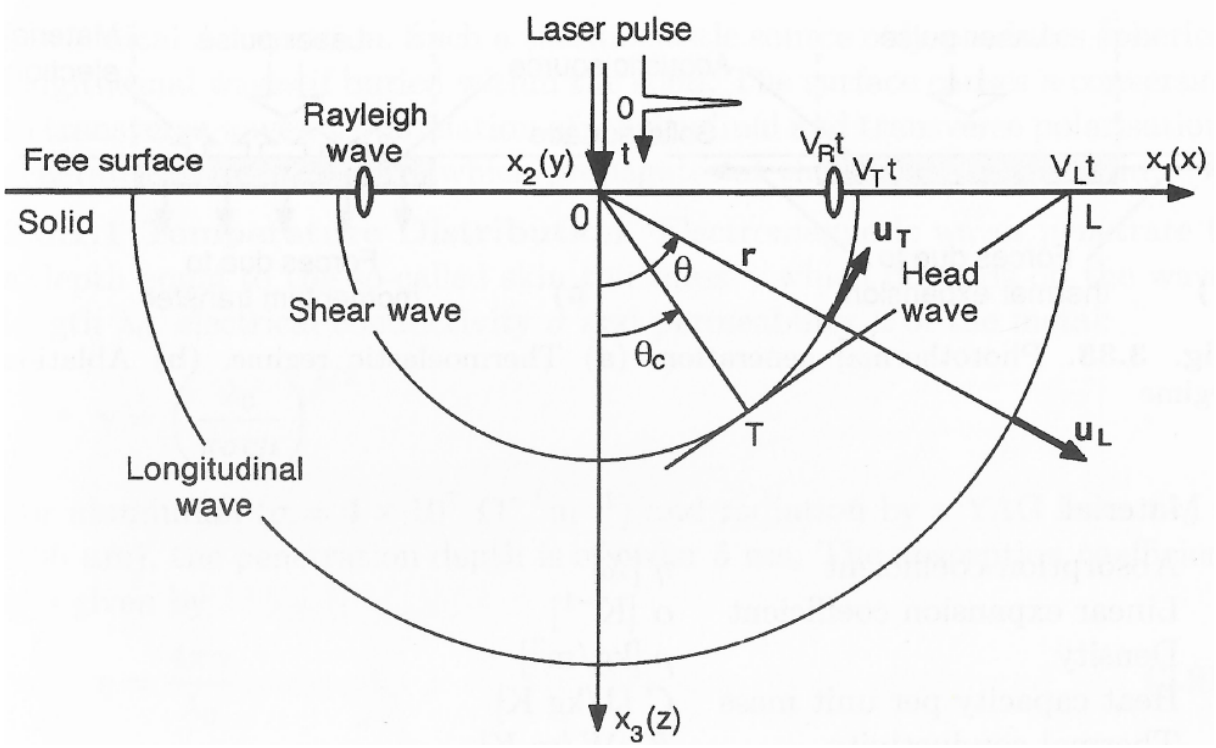

Obrázek 2.4: Schematické znázornění buzení elastické vlny, generované bodově zaostřeným laserovým pulsem v izotopní pevné látce [11]

.

Výkonové režimy

V závislosti na výkonu laserového paprsku, resp. přesněji na energii laserového paprsku

absorbovaného materiálem dochází k excitaci elastických vln různými mechanismy. Existují dva extrémní případy: režim ablace, ve kterém dochází po dopadu k odpaření hmoty vzorku, a režim termoelastický, kdy nedochází k žádnému poškození vzorku. Tyto režimy vedou na odlišné elastické síly, viz. 2.5. Reálně se často setkáváme s případem mezi těmito režimy, kdy dochází k lokálnímu natavení materiálu v místě dopadu laserového svazku, avšak nedochází k jeho odpařování.

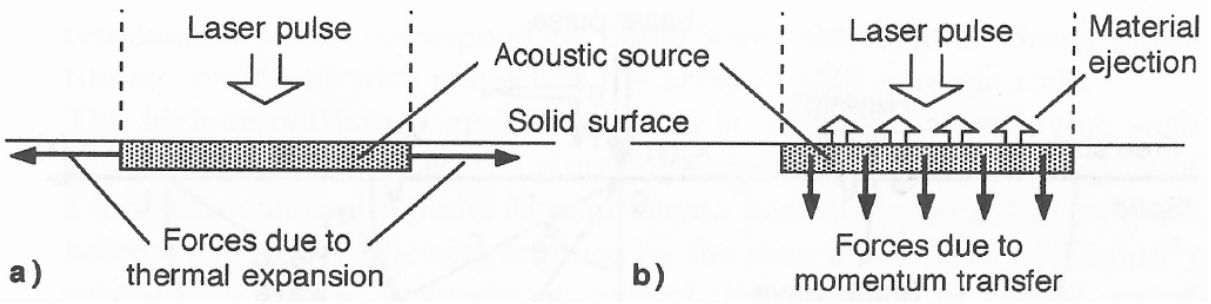

Obrázek 2.5: Elastické síly excitované přes a) termoelastické a b) ablační mechanismy buzení [11]

.

Termoelastický režim Když je intenzita dopadajícího záření na kovový povrch dostatečně nízká, část energie je absorbována a přeměněna na teplo Jouleovým efektem, zatímco zbytek se odráží. Laserový puls pak hraje roli tepelného zdroje energie a vytváří mechanickou deformaci. Tepelná vlna neproniká hluboko do materiálu, a proto je termoelastický zdroj lokalizován pod povrchem ve velmi tenkém prostoru ve srovnání s akustickými vlnovými délkami. Očekávaný signál povrchového posunu způsobeného termoelastickým bodovým zdrojem je znázorněn na obr. 2.7. Výpočty podle Roseho [13] týkající se aproximace vzdáleného pole ukázaly vzorce směrovosti intenzity excitovaných vln v různých směrech s ohledem na volný povrch. Vzory závisí na vlastnostech materiálu. Například u duralu je maximální emise podélných vln v 65° a příčných vlnách v 45° (viz obr. 2.6a, b). V této aproximaci neexistuje žádné záření podélných vln podél normály k povrchu. Příčné vlny jsou generovány efektivněji než podélné - příčný posun je více než řádově větší než posun podélný.

Ablační režim Když absorbovaná hustota výkonu způsobí tavení a odpařování malého množství hmoty, přenos momentu způsobený vypuzováním částic vytváří sílu kol-

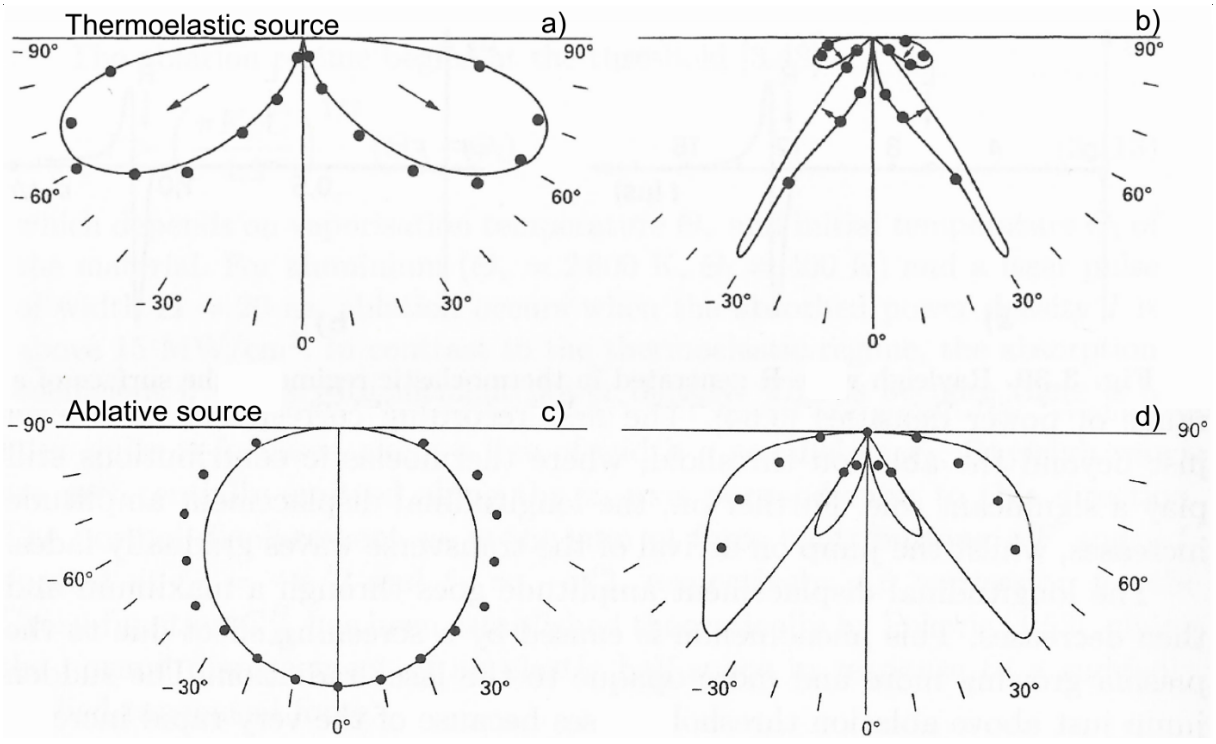

Obrázek 2.6: Vzory směrovosti a), c) podélných a b), d) příčných vln pro bodový termoelastický a ablační zdroj. Body označují experimentální hodnoty převzaté z [12]. [11]

.

mou k povrchu (viz obr. 2.5). Prahová hodnota absorbované hustoty výkonu závisí na vlastnostech materiálu a vlastnostech laserového pulsu [14]:

$$I > \left(\frac{\pi K \rho C}{4\Delta}\right)^{\frac{1}{2}} (\Theta_V - \Theta_i) \tag{2.30}$$

kde Θ_V a Θ_i jsou teplota odpařování a počáteční teplota, C je tepelná kapacita, K tepelná vodivost a Δ doba trvání impulsu. Prahová hustota výkonu je typicky v desítkách megawattů na centimetr čtvereční.

Jak je znázorněno na obr. 2.6 (c, d), je v tomto případě směrovost odlišná. Emise podélné vlny je všesměrová (ale ne izotropní). Amplitudy generovaných vln jsou obecně vyšší než v případě termoelastických vln.

Charakter očekávaného signálu zůstane stejný, avšak s převráceným píkem Rayleigho vlny (zrcadlově symetrickým přes rovinu umístěnou kolmo na osu a procházejícím

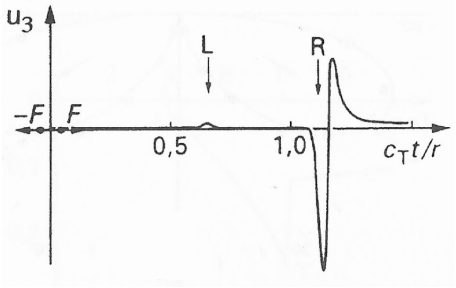

Obrázek 2.7: Dislokace $u3$ (normála k povrchu) způsobená bodovým termoelastickým zdrojem v materiálu s Poissonovým poměrem $v = 0 : 25$. F označuje budící sílu, vrcholy L a R povrchovou podélnou a Rayleigho vlnu. Jednotky jsou normalizovány na rychlost příčných vln c_T, čas t a vzdálenost od zdroje r. [11]

.

středem pulzu). To lze vysvětlit odlišným pohybem povrchu vzorku, jelikož při ablačním režimu se nejdříve pohybuje směrem dovnitř vzorku (oproti termoelastickému režimu, kdy pohyb začíná směrem ven ze vzorku kvůli tepelnému rozpínání).

Prostorová modulace

Hustota výkonu budícího paprsku je ovlivněna prostorovou částí. Podle požadované situace lze použít několik různých přístupů. Hlavní rozdělení je mezi širokopásmovou a úzkopásmovou excitací: zatímco širokopásmové metody excitují vlny celého spektra frekvencí s maximem daným velikostí excitačního bodu na vzorku, úzkopásmové metody excitují pouze zvolenou vlnovou délku, obvykle danou excitačním vzorem.

Širokopásmové buzení Bodový zdroj je nejjednodušší variantou (pulzní laser je jednoduše zaměřen na bod požadovaného průměru). Vybuzené vlny jsou v takovém případě radiální, a spektrum takto vybuzených vln je širokopásmové, s nejvyšší frekvencí danou průměrem bodu.

Pokud pošleme laserový paprsek skrz válcovou čočku, dostaneme tzv. čárový zdroj. V takovém případě jsou dominantně vybuzeny vlny s k vektorem kolmým k excitační čáře, a nejvyšší frekvence buzeného spektra je dána šířkou excitační čáry. Tyto metody jsou obvykle kombinovány s měřením doby příchodu vln v různých bodech,

tj. v různé relativní vzdálenosti mezi excitací a detekcí. Tak lze získat informaci o rychlosti fázového čela vlny.

Úzkopásmové buzení Úzkopásmové buzení povrchových vln se obvykle dostane ve formě mřížky. Dominantní vlnová délka je dána rozestupem mezi čárovými zdroji v důsledku destruktivního a konstruktivního rušení vln buzených každým jednotlivým čárovým zdrojem (viz obr. 2.8). Výsledný budící vzor může být dosažen buď vysláním paprsku přes amplitudovou masku (jednoduše blokující určité části paprsku) nebo interferencí dvou paprsků na vzorku. První z nich se používá například v metodě "Spatially Resolved Acoustic Spectroscopy"(SRAS) [15], zatímco druhá se používá v metodách běžně nazývaných "Transient Grating Spectroscopy"(TGS) [16] a [17]. Kromě úzkopásmové povahy takového zdroje spočívá výhoda také v prostorovém rozložení laserové energie. Proto je hustota výkonu obvykle dostatečně nízká, aby zůstala v termoelastickém režimu, což umožňuje opakování experimentu na stejném místě pro velký počet měření. Tyto metody jsou obvykle kombinovány s výpočtem dominantní frekvence signálu. Rychlost povrchových vln je pak získána pomocí základního vztahu $c_R = f\lambda$, kde λ je dána vzorem buzení a f je měřená frekvence. Rozdílným způsobem získání úzkopásmové excitace je kmitočtová modulace laseru s kontinuální vlnou. V takovém nastavení je výkon laseru modulován tak, že výsledná intenzita na místě vybudí požadovanou frekvenci kontinuálních vln.

2.2.2 Optické měření povrchových vln

Pro návrh plně bezkontaktní metody materiálové charakterizace založené na šíření elastické vlny musí být vyvinuta také metoda detekce elastických vln pomocí laseru. Pro spolupráci s laserovým buzením popsaným v předchozí části musí být metoda citlivá na výchylku kolmou k povrchu (tzv. out-of-plane) posunutí v řádech nanometrů a kmitočtů v pásmu MHz a GHz. Existují dvě hlavní skupiny metod detekce: Metody průhybu a difrakce, které jsou citlivé na zvlnění povrchu; a interferometrické metody, které mohou detekovat jakýkoliv typ posunu mimo rovinu.

2.2.2.1 Metody průhybu a difrakce

Tyto metody jsou citlivé na povrchové vlnění a specializují se na povrchové vlny, jako

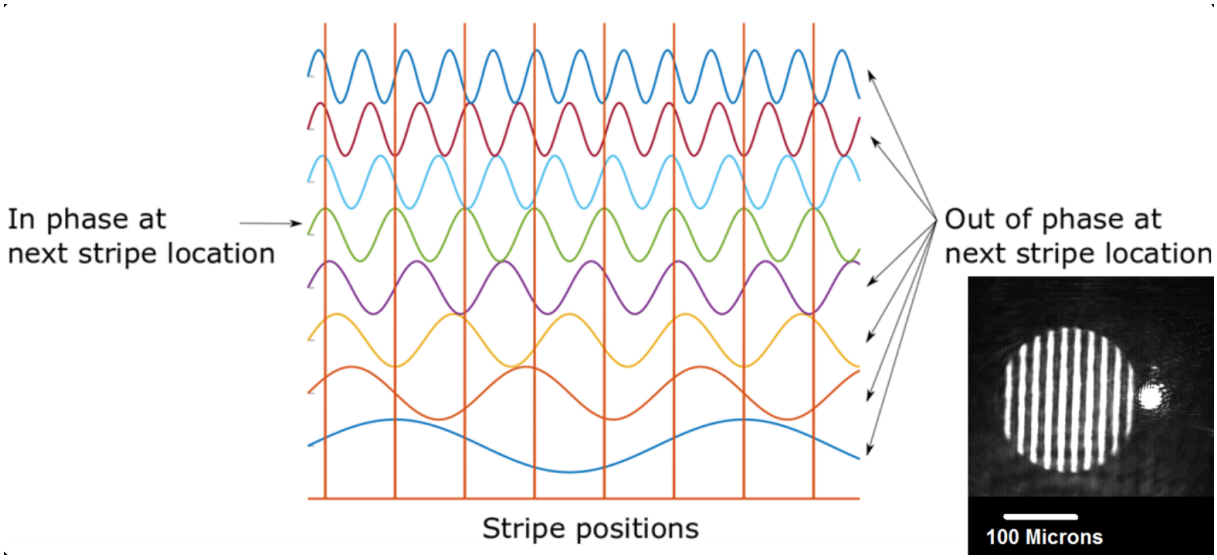

Obrázek 2.8: Princip úzkopásmového buzení využívající rastrový vzor: každý jednotlivý proužek působí jako jediný čárový zdroj buzení (širokopásmový), ale budí se pouze vlnová délka ve fázi. Na pravé straně je obraz pořízený z kamery. [18]

je Rayleighova vlna. Rozdíl mezi nimi spočívá ve srovnání velikostí detekčního bodu d a elastické vlnové délky Λ: V případě, že $d \ll \Lambda$ mluvíme o metodě průhybu a pro $d \gg \Lambda$ metodu difrakce.

Metoda průhybu Běžné metody založené na vychýlení paprsku (BD - beam deflection) zahrnují detektor s "knife-edge", dělenou fotodiodu a nastavení pomocí diferenciálního fotodetektoru. Ve všech případech se dopadající laserový paprsek zaměřuje na vzorek a úhel odrazu se mění úměrně se změnou sklonu povrchu způsobeného šířící se povrchovou vlnou. V případě detektoru "knife-edge"(obr. 2.9a) je polovina odraženého paprsku na své cestě do fotodetektoru blokována. Když tedy SAW prochází detekčním bodem, intenzita přijímaná jednou diodou se mění v důsledku úhlové odchylky odraženého paprsku. Pro optimální citlivost by bodová velikost měla být polovina elastické vlnové délky. Knife-edge metoda je jednoduchá a nenákladná, ale detekční plochy musí být opticky ploché a reflexní. Uspořádání s rozdělenými fotodiodami nebo zrcadlovými paprsky a diferenciálním fotodetektorem dosahují vyšší citlivosti, protože neztrácejí polovinu intenzity signálu blokováním, ale ome-

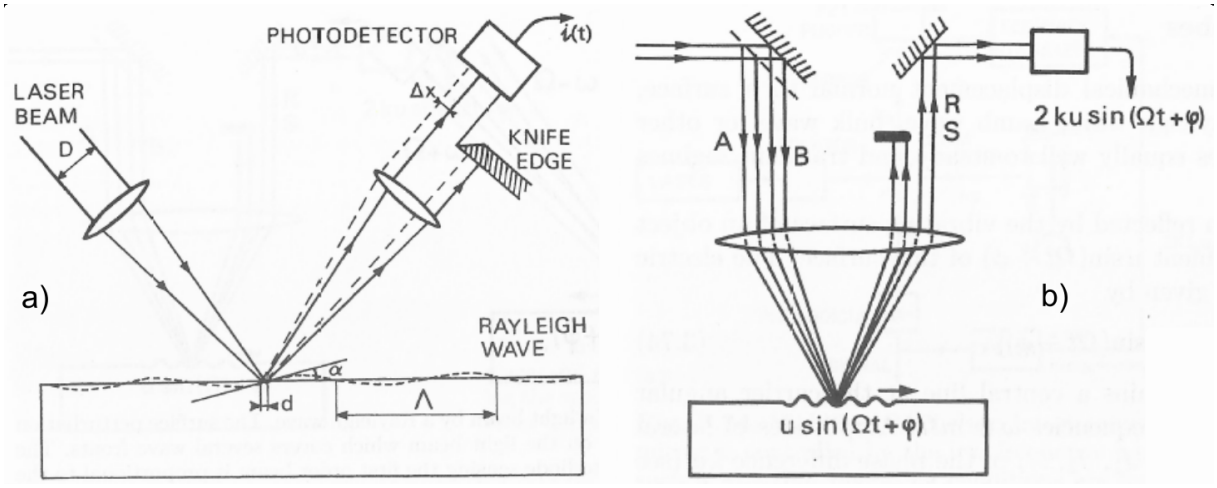

Obrázek 2.9: Schéma metod průhybu a) a difrakce b). [11]

.

zení na povrchu zůstávají. V poslední době byl vyvinut "Speckle knife-edge detector"(SKED) [19], který zvyšuje použitelnost na drsných površích.

Metoda difrakce Když bodový průměr pokrývá několik vlnových délek povrchové vlny, má účinek fázového pole. Světelný paprsek je rozptýlen do paprsků kmitočtů daných $\omega \pm m\Omega (m = 0, 1, 2, ...)$, kde ω je centrální frekvence světelného paprsku a Ω je frekvence elastické vlny. Pro $ku \ll 1$ (k je vlnový vektor a u mechanický posun) je intenzita svazku prvního řádu dána čtvercem posunutí u. Měření je tedy založeno na změně relativní intenzity paprsku centrálního a prvního řádu. Svazky musí být oddělené, aby se umožnilo jejich porovnání; proto jsou typické frekvence elastických vln pro difrakční metody vyšší než 100 MHz. Také jsou nutné velké posuny. Vzhledem k tomu, že fáze elastické vlny je obsažena ve fázi difrakčních paprsků, může být získána interferencí difrakčního paprsku prvního řádu se zrcadlově odraženým paprskem [20]. To vede k nastavení, které se blíží jedné běžně používané sondě zvané Heterodyne, popsané dále v této kapitole.

2.2.2.2 Interferometrické metody

Interferometrické metody mohou být použity v ustálených i přechodových režimech pro měření jakéhokoliv mechanického posunu mimo rovinu. Když se povrch pohybuje, paprsek odraženého světla se mění ve fázi. Poté se smísí s referenčním paprskem přicházejícím ze stejného zdroje a výsledná intenzita na fotodetektoru je dána rozdílem ve frekvenci a fázi.

Rozdíl ve fázi je výsledkem různých optických drah paprsků. Pro snížení vlivu kolísání optických drah pocházejících z jiných zdrojů, než je povrchový posun, může být použito několik různých metod, jako je například stabilizované nebo heterodynové schéma.

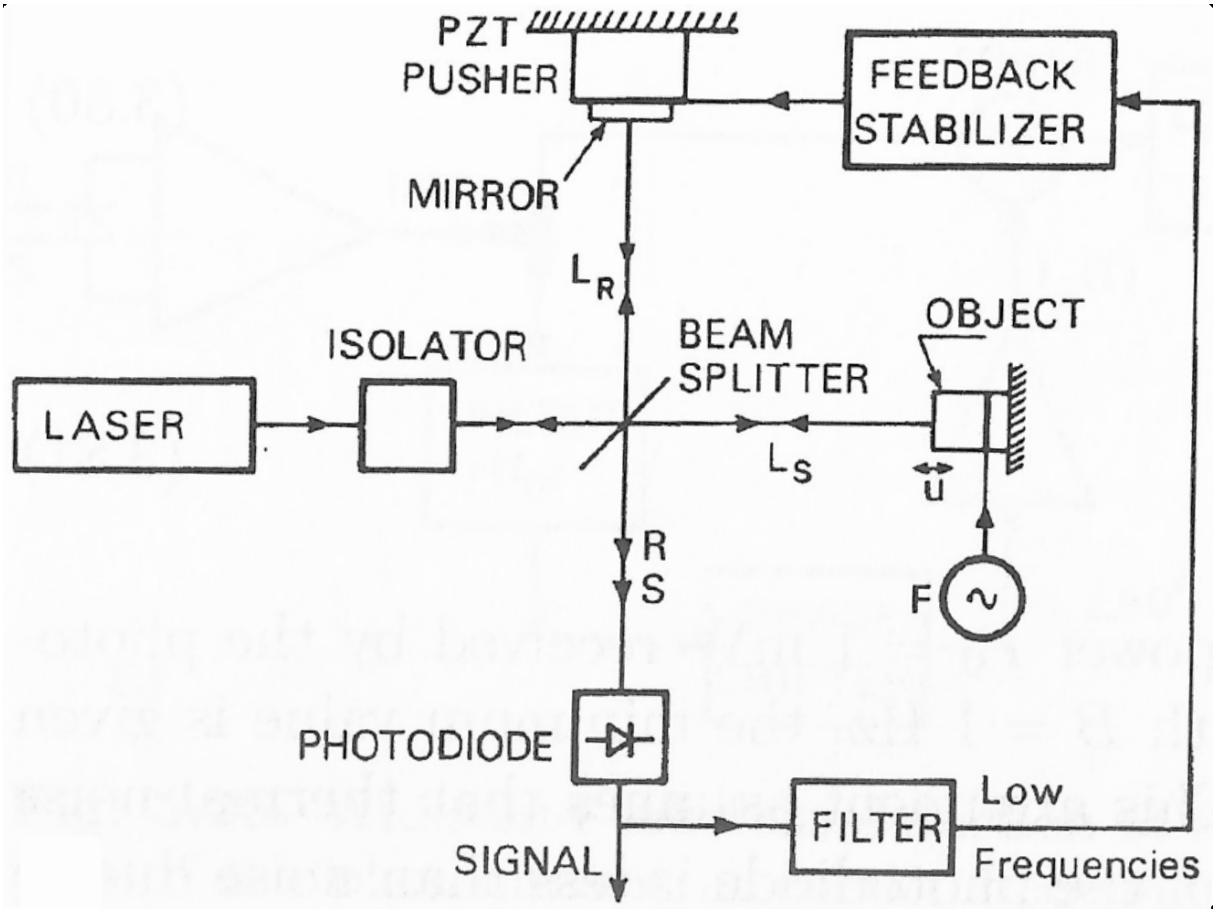

Obrázek 2.10: Schematické znázornění stabilizovaného Michelsonova interferometru s polohou referenčního zrcátka řízeného nízkofrekvenční částí výstupního signálu fotodiody takovým způsobem, že provozní podmínky jsou pevně stanoveny navzdory optickým výkyvům dráhy. [11]

.

Stabilizovaný Michelsonův interferometr Michelsonův interferometr, na obr. 2.10, je klasické schéma používané v různých oblastech měření posunu. Laserový paprsek je rozdělen do detekčního a referenčního paprsku, oba se pohybují po optické dráze stejné délky a jsou pak smíseny na fotodiodu. Intenzita fotoproudu je funkcí rozdílu dráhy. Výsledná informace obsahuje jak fázi, tak amplitudu vlny, tj. posunutí povrchu. Pro filtrování nízkofrekvenčních vibrací je délka referenční optické dráhy

řízena ve smyčce zpětné vazby v režimu nejvyšší citlivosti. Toto je obvykle děláno piezoelektrickým členem spojeným se zrcadlem v cestě [21].

Heterodyne Heterodynová detekce může být použita pro měření ustálených povrchových vibrací, které v případě difrakčních měření vytvářejí vlny. V zásadě je svazek sondy rozdělen do dvou paprsků, např. pomocí difrakční masky, a tyto dva paprsky jsou pak přeneseny zpět do jednoho bodu ve stejném úhlu. Oba dopadající paprsky difraktují na povrchové mřížce způsobené excitací, a při dodržení tzv. Littrowovy konfigurace má difraktovaný paprsek nulového řádu (tj. zrcadlově odražený) jednoho dopadajícího paprsku shodný směr s difraktovaným paprskem prvního řádu od druhého dopadajícího paprsku, a naopak. Od vzorku tedy odchází dva páry paprsků, vždy jeden odražený a druhý difraktovaný. Odražený paprsek se považuje za referenční; difrakce nese informaci o frekvenci vibrací povrchu. Je dostačující přivést jeden z těchto párů do detektoru, ale poměr signálu k šumu může být zlepšen, když jsou oba páry vedeny do diferenciálního detektoru. Možné nastavení, jak navrhuje [16] je znázorněno na obr. 2.11.

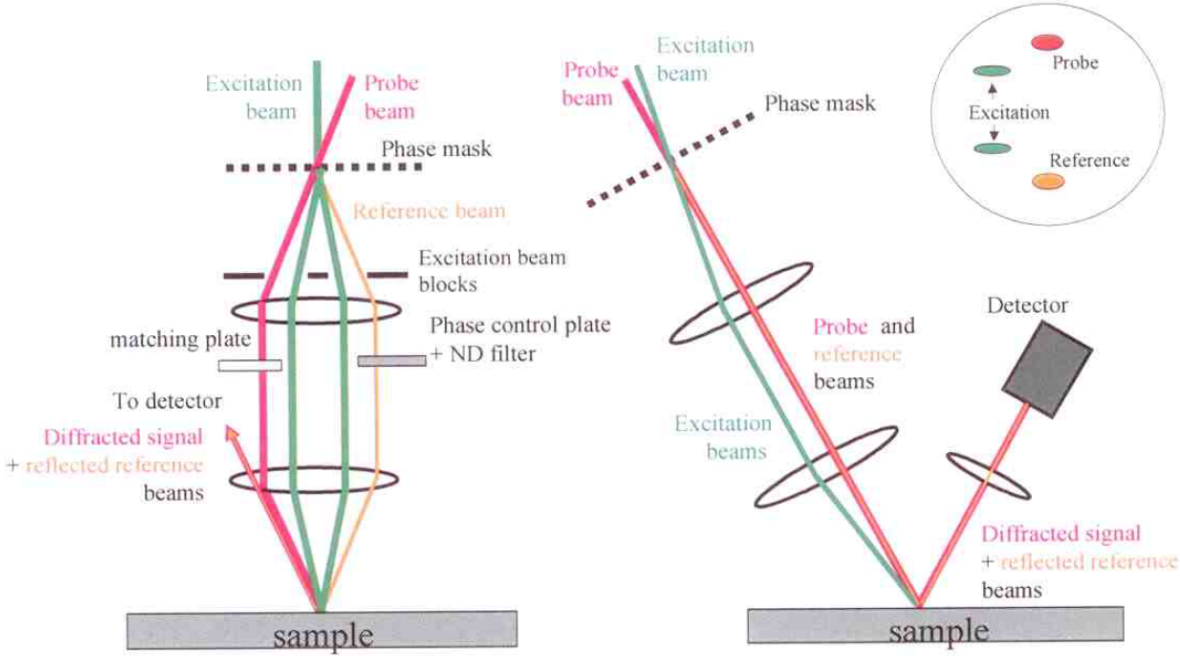

Obrázek 2.11: Hlavní schéma nastavení heterodynu. Vlevo: Pohled zepředu. Vpravo: Boční pohled. Vpravo nahoře vpravo: Průřez průchodem paprsku za první čočkou, ukazující umístění všech čtyř paprsků. [16]

.

3 Aparatury

3.1 Resonanční ultrazvuková spektroskopie

3.1.1 Peltierova komora

Popis aparatury

Jedná se základní měřicí aparaturu, která byla vyvinuta pro měření pomocí rezonanční ultrazukové spektroskopie. Tato měřicí aparatura se sestává z vakuové peltierové komory, která je schopná teplotního rozsahu mezi 220 K až 400 K. Blokové schéma tohoto měřicího systému je na obr. 3.1.

Teplotní regulaci zajišťují tři samostatné peltierovy články. Mezi každým peltierovým článkem je umístěn termočlánek a tento termočlánek slouží k samostatné regulaci jednotlivých peltierový článků. Každý z peltierových článků má rozdílné parametry. Tím jsme schopni dostávat takto velký teplotní rozsah s přiměřeně rychlou rampou a stabilizací teploty. K napájení a řízení těchto peltierových článků nám společnost Space Research Instruments s.r.o. vyrobila speciální řízené zdroje. Deska plošného spoje jednoho tohoto řízeného zdroje je uvedena v příloze na obr. A.1.

K řízení a regulaci těchto zdrojů se využívá regulační karta společnosti National Instruments *NI PXI-7830R*. Jedná se o programovatelné hradlové pole (FPGA). Na tomto poli jsou vytvořeny jednotlivé regulační smyčky tak, aby byla regulace schopná rychlých změn s dostatečnou teplotní přesností. Díky tomuto spojení vlastních zdrojů a FPGA pole jsme schopni nastavit i velmi rychlé rampy s teplotní tolerancí pod 0.01 K.

Tato komora obsahuje tři termočlánky typu T. Dva termočlánky jsou umístěny vždy ve spojení dvou peltierových členů. Poslední termočlánek je umístěn blízko měděné prohlubně, kam se umisťuje měřený vzorek. Měření teploty na těchto termočláncích zajišťuje měřicí karta od National Instruments *NI USB-9211* (4-kanál, 14 S/s).

Teplotní stabilizaci peltierových článků a zároveň chlazení této komory je zajištno vodním chlazením společnosti JULABO (FP-50). V tomto měřicím systému je dále pulsní infračervený laser od společnosti Quantel (120 mj, 1064 nm, 20 Hz). Tento laser se využívá k lokálnímu ohřevu měřeného vzorku a tím vybuzení vlastních rezonancí tohoto vzorku.

K měření těchto rezonancí se využívá skenovací interferometr společnosti Polytec

MSA-500. Tento interferometr je samostatná měřicí jednotka, ve které probíhá nastavení a měření matice bodů na vzorku. Hlavní výhodou použití tohoto řešení je velmi rychlé skenování pomocí vnitřních zrcátek. Další výhodou je možnost použití diferenciálního a stroboskopického měření, měření v bílém světle, z-sken a mnoho dalšího. Jak už bylo zmíněno, jedná se o základní měřicí systém a to právě z důvodu možnosti naskenování celého povrchu vzorku. Po změření vlastních kmitů při stabilní pokojové teploty je možné tento vzorek měřit dalšími dostupnými systémy, popsanými v dalších kapitolách. K synchronizaci měření je použita multifunkční měřicí karta společnosti National Instruments *NI USB-6009*.

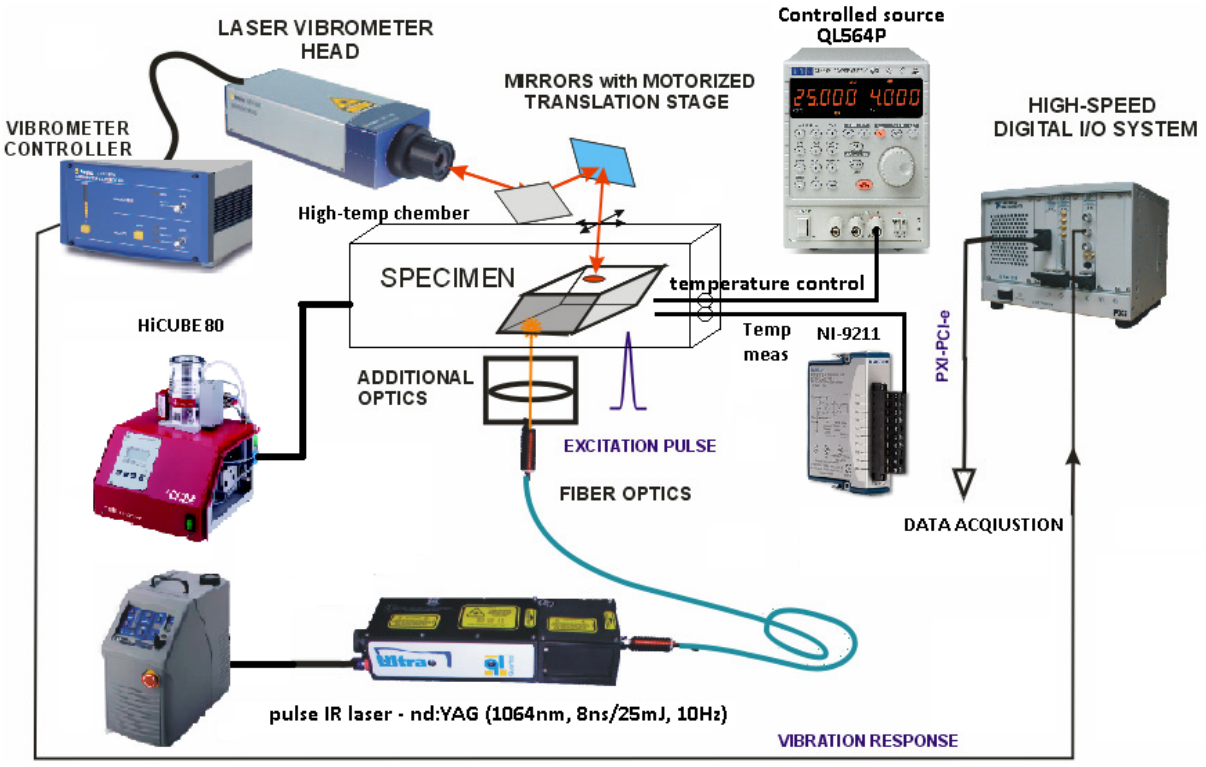

Obrázek 3.1: Blokové schéma měřicího systému RUS s peltierovou vakuovou komorou

V současné době se tento systém modernizuje výkonější teplotní komorou a novým skenovacím systémem společnosti Polytec *MSA-600*. V tomto novém systému budeme vlastní rezonance měřit externími digitalizačními kartami společnosti National Instruments. Díky tomuto vlastnímu měření budeme moci ukládat časový signál měřený v jednotlivých bodech, což přinese rozšířené možnosti využití tohoto systému.

Popis ovládání

Pro vývoj ovládacího programu bylo zvoleno vývojové prostředí *LabView* společnosti National Instruments. Obr. 3.2 ukazuje původní ovládací program, který je v současnosti již modernizován, nicméně stále ve fázi vývoje.

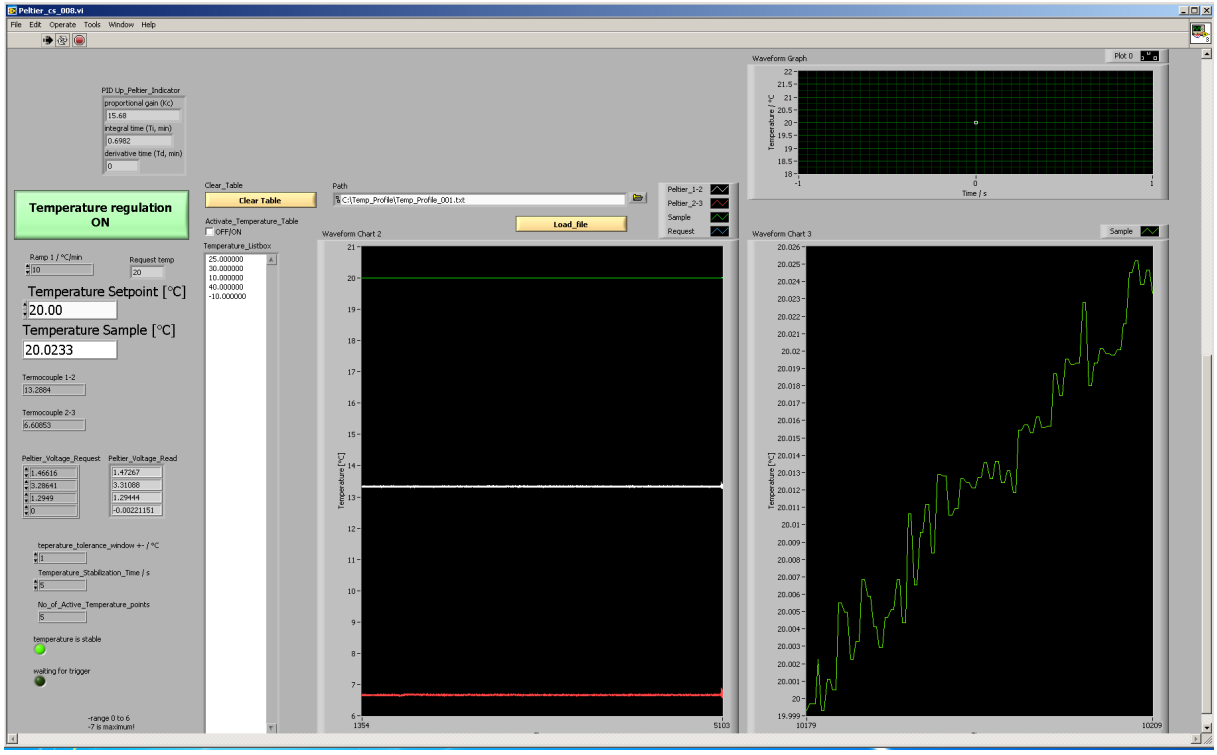

Obrázek 3.2: Ovládací program měřicího systému RUS s peltierovou vakuovou komorou

Na ovládacím panelu najdeme možnost načtení tabulky teplot, nastavení požadované rampy a možnost ručního nastavení teploty. Dále máme možnost nastavení teplotní tolerance a doby stabilizace teploty. V levé spodní části jsou uvedeny dva indikátory (`temperature is stable` a `waiting for trigger`). Tyto indikátory jsou fyzickým zobrazením jednoduché komunikace mezi řízením teplotní komory a ovládacím programem skenovacího interferometru *MSA-500*. Při spuštění automatického měření je operátor nucen stejnou tabulku teplot nastavit pomocí námi vytvořeného makra B i v ovládacím programu interferometru. A právě díky této synchronizaci je celé měření možno provádět automaticky.

Indikátor *temperature is stable* dá interferometru informaci o stabilní teplotě a tím tedy impuls ke spuštění vlastního měření všech bodů, které v rámi měření chceme měřit. Indikátor `waiting for trigger` naopak regulační program pozastaví na aktuálně nastavené a regulované teplotě, dokud neproběhne celé nastavené měření a uložení všech

spekter.

Na ovládacím panelu obr. 3.2 je dále možné vidět několik grafických zobrazení teplotní regulace. Graf `waveform graph` slouží k zobrazení nastavení rampy a časovému odhadu do nastavení požadované teploty. Ostatní dva grafy zobrazují aktuální teplotu na jednotlivých termočláncích.

Výpis makra, používaného pro měření a vzájemnou komunikaci s regulačním počítačem, je v příloze B. V tomto makru se importuje tabulka teplot (musí být stejná, jako tabulka, která se použije pro nastavování daných teplot) a nastavení cesty pro ukládání jednotlivých měřených signálů.

3.1.2 Vysokoteplotní komora

Popis aparatury

Tato sestava byla navrhnuta, neboť bylo zapotřebí měřit fázové přechody, které se projevují až při vyšších teplotách. V současné době tato konfigurace nabízí rozsah teplot od 320K do 1000K. Tato komora, stejně jako předchozí, je navrhnuta a zkonstruována na míru podle našich specifikací. Jedná se tedy o vakuovou komoru, ve které se nachází teplotní člen (tento člen umí pouze topit, je tedy obtížnější řízení a regulace, neboť při stabilizaci teploty je použit efekt vlastního teplotního spádu), tepelný radiační štít (díky tomuto radiačnímu štítu jsme schopni dosáhnout vyšších teplot a zároveň se tolik nezahřívá plášť komory), teplotní senzor (v tomto případě termočlánek typu K), dvě optické průchodky (zdola je obsazena fokusační čočkou pro buzení vlastních kmitů, shora pro paprsek interferometru).

Plášť této komory je chlazen vodním chlazením společnosti JULABO *FP-50*. Tato sestava dále obsahuje senzor tlaku (regulace a kontrola vnitřního prostoru) společnosti Pfeiffer *D-35614* s kontrolerem, taktéž společnosti Pfeiffer DCU 100. Pro vakuolizaci je použita vývěva rovněž společnosti Pfeiffer *Hi-Cube 80* a pro regulaci vnitřního tlaku v komoře, je použit elektromagnetický vakuový ventil, který se ovládá vstupním napětím. Pro měření rezonančního spektra je použit interferometr *OFV-505* a kontroler *OFV-2570* společnosti Polytec.

Regulaci teploty zajišťuje řízený napěťový zdroj společnosti TTI *QL564TP*. Měření teplot (teplota pláště a vnitřního prostoru) a digitalizace měřeného signálu byly svěřeny

společnosti National Instruments. Pro měření teplot je použito měřicí zařízení *NI USB-9211* (4-kanál, 14 S/s). Jako digitalizační karta byla vybrána *NI PXI-5142* (100 Mhz, 100 Ms/s, 14 bit), pro zesílení tohoto signálu byl vybrán zesilovač Krohn-Hite, model *3945*. O ovládání elektromagnetického vakuového ventilu se stará *NI USB-6008*. Tato karta zároveň měří sílu odraženého detekčního svazku. Pro vybuzení vlastních rezonancí byl zvolen pulzní laser společnosti CryLaS *DSS 1064-3000*.

Všechna tato zařízení byla vybrána i z důvodu jejich připojení k PC a možnému vzdálenému ovládání. Pro ovládání všech komponent byl zvolen, jako v jiných případech, program *LabView* společnosti National Instruments.

Popis ovládání

Ovládací program tohoto měřicího systému byl vyvíjen v prostředí *LabView*. Obr. 3.3 ukazuje screen shot nastavení přístrojů pro měření. V sekci `Devices identification` jsou uvedeny všechny přístroje a jejich komunikační rozhraní, se kterými tento program pracuje. V sekci `Scope parametrs` je možné měnit nastavení digitalizační karty, dle potřeby. `Source parametrs` jsou zde pro nastavení PID regulační smyčky, která se stará o regulaci teploty. `Security parametrs` nastavujeme pro případ, že by došlo ke ztrátě vakua v komoře, případně vypadl chladící systém pláště. V této sekci můžeme dle potřeby nechat regulovat vnitřní tlak komory. V poslední sekci tohoto nastavení je možno si všimnout ručního ovládání laseru, včetně nastavení energie buzení.

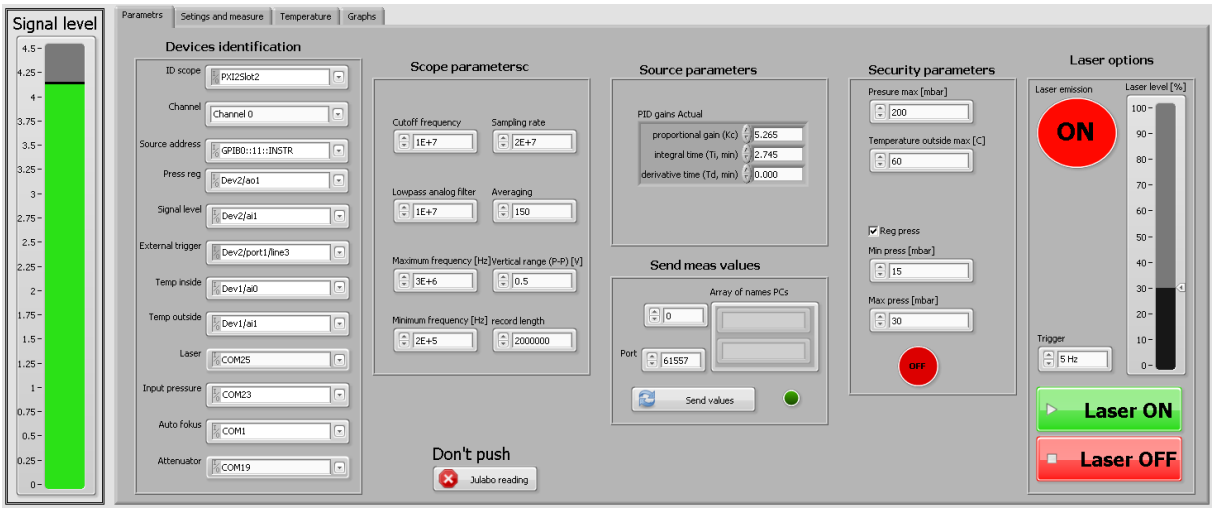

Obrázek 3.3: Vysokoteplotní RUS, ovládací program (nastavení přístrojů)

Sekce na obr. 3.4 slouží k nastavení a základnímu ovládání programu. Podsekce `Load table` slouží k načtení dat z EXCELU (vektor teplot, rampy a čas stability). Vektor teplot udává požadované teploty, při kterých bude měření probíhat. Parametr rapma je rychlost s jakou se na danou teplotu chceme dostat (např. 7 °C×min^{-1}) a čas stability znamená, jak dlouho se na dané těplotě (včetně nastavených tolerancí) musí počkat, než měření proběhne. Je možné tento systém používat pro ruční měření v dané teplotě nebo systém pustit na automatické měření. V automatickém módu bude teploty nastavovat a regulovat podle požadavku v tabulce. Automaticky ukládá každý časový signál do binárního souboru. V sekci `Temperature meas and ind` jsou vidět indikace teplot v komoře, na plášti, chlazení, času měření a podobně.

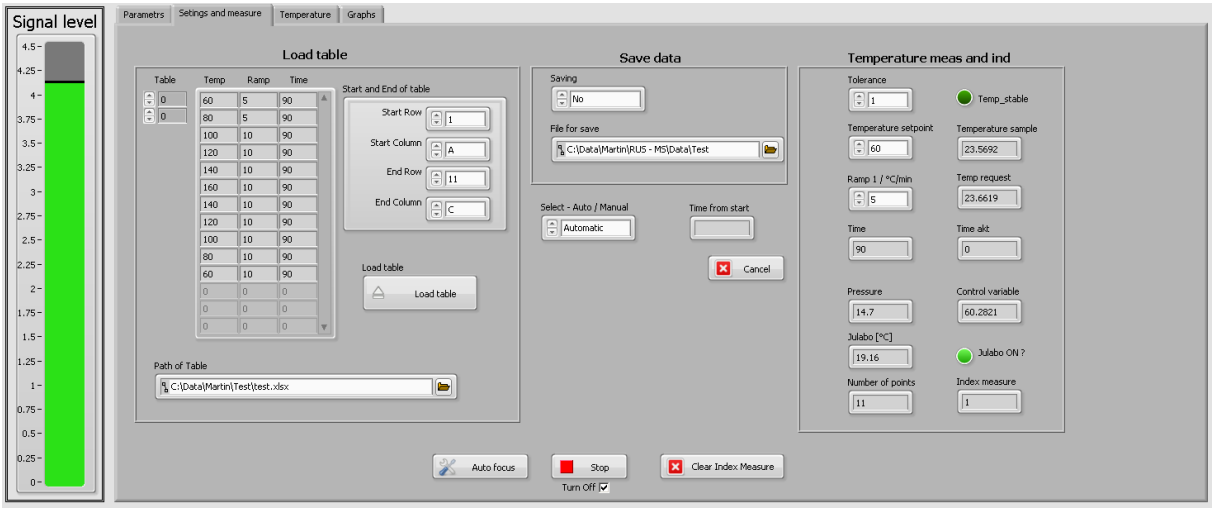

Obrázek 3.4: Vysokoteplotní RUS, ovládací program (nastavení měření)

Obr. 3.5 slouží ke grafickému zobrazení teplot a rampy. Všechny tyto teploty se ukládají s určitým časovým intervalem do databáze. Stejně jako odkazy na měřená data. Z této databáze může kdokoliv daná data vyvolat, včetně měřených dat a dále s nimi podle potřeby pracovat.

Stejně jako na všech předešlých obr.(3.3, 3.4 a 3.5), tak i tento obr. 3.6 zobrazuje v levé části sílu odraženého interferometrického paprsku. Dále na tomto obr. 3.6 vidíme měřený časový signál a jeho furierovu transformaci. Právě ta slouží, jako u ostatních metod, k vyhodnocení vývoje elastických konstant.

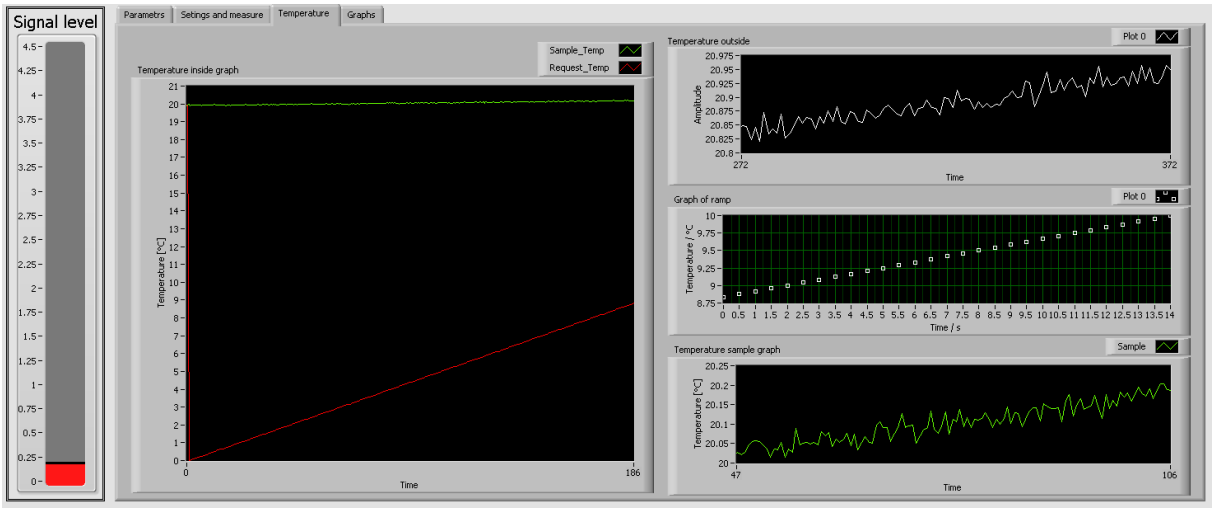

Obrázek 3.5: Vysokoteplotní RUS, ovládací program (vývoj teplot)

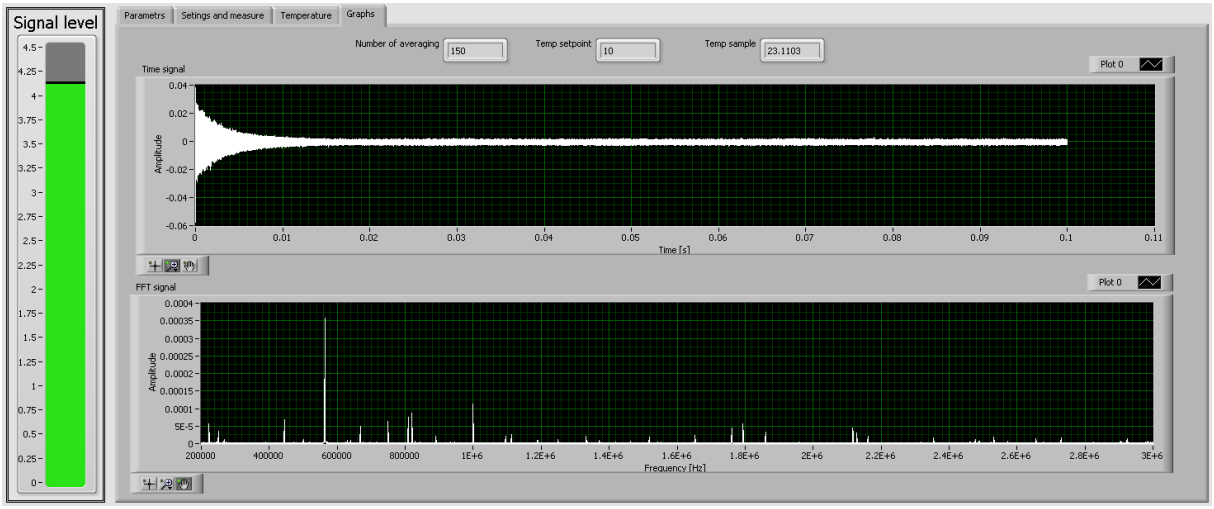

Obrázek 3.6: Vysokoteplotní RUS, ovládací program (časový signál a jeho FFT)

3.1.3 Kryostatická komora

Popis aparatury

Systém s kryostatem byl sestaven s podobným požadavkem, jako RUS s vysokoteplotní komorou. Bylo zapotřebí měřit změnu fázových rychlostí a transformace materiálů s teplotami výrazně nižšími pod bod mrazu. Rozsah teplot v tomto případě je tedy $85 - 310K$. Součástí této aparatury je dusíkový kryostat společnosti Oxford Instuments *Optistat CF* s použitím kontroleru stejné společnosti *Mercury iTC*. Pro regulaci průtoku dusíku byl společností dodán ruční jehlový ventil.

Jako při konstrukci výše popsaného systému, byl použit stejný interferometr společnosti

Polytec *OFV-505* s kontrolerem *OFV-2570*. Vzhledem k tomu, že se jedná se dusíkový kryostat, je potřeba mít jako součást tohoto systému i tlakovou dusíkovou *Dewarovu nádobu*. V tomto případě byla zvolena Dewarova nádoba s objemem 50 l. Aby kryostat správně pracoval, je nutné udržovat (regulovat) tlak uvnitř Dewarovy nádoby. O regulaci tohoto tlaku se stará řízený napěťový zdroj *QL564TP*, společnosti TTi. V nádobě je umístěno topné těleso, které zajišťuje přeměnu tekutého dusíku v plynný. Tím se v této nádobě zvyšuje tlak. Je tam také umístěn tlakový senzor, který se využívá k regulaci. Samozřejmostí je i několik bezpečnostních prvků (přetlakové ventily). Kromě přetlaku se pro zajištění průtoku dusíku kryostatem používá čerpadlová pumpa.

Vzhledem k faktu, že tato dusíková nádoba je pod stálým tlakem, tedy uzavřená, není možné kontrolovat množství kapalného dusíku. Tato kontrola je nutná, aby se nedocházelo k případu, že tekutý dusík v průběhu měření dojde. Proto byla pod tuto nádobu umístěna váha, kter8 odesílá aktuální zatížení. Před vlastním měřením, po umístění vzorku do kryostatu, je nutné ve vnitřní komoře tohoto kryostatu vyměnit vzduch (při vkládání vzorku) za helium.

K tomuto slouží turbomolekulární stanice *T-Station 85* společnosti Edwards. Tato vývěva je po vyčerpání vzduchu z vnitřní komory použita pro vakuolizaci vnitřního pláště, aby nedocházelo k námraze vnějšího pláště a rosení optických průchodek. Jako budící laser byl zvolen pulsní laser *STA-01-8-1053* od společnosti Standa (v budoucnu tento laser bude nahrazen pulsním laserem od společnosti CryLaS). Pro budící laser je nutné mít externí hodinový signál, který určuje rychlost buzení. Pro tento účel je zde generátor funkcí *DG1022Z* společnosti Rigol.

Měření časového signálu, který měří interferometr a zesiluje zesilovač Krohn-Hite model *3945*, zajišťuje digitalizační karta *NI PXI-5142* (100 Mhz, 100 Ms/s, 14 bit). Intenzitu odraženého detekčního svazku a vnitřní tlak v dusíkové nádobě měří *USB-6008*. Obě tato měřicí zařízení jsou od společnosti National Instruments. Program pro řízení, regulaci, měření, ovládaní a ukládání dat byl programován v prostředí *LabView* společnosti National Instruments.

Popis ovládání

Ovládání a regulace tohoto systému není plně automatizovaná. Důvodem je ruční ovládání

jehlového ventilu (v budoucnu bude vyměněn za programovatelný). Kromě tohoto je systém programově ovladatelný. Obr. 3.7 ukazuje nejdůležitější část ovládacího programu. Je zde vidět několik částí. Část nazývaná `Komunikace` nastavuje komunikační kanály a protokoly, které se používají ke komunikaci s jednotlivými částmi aparatury. Vidíme tedy, které části je možné ovládat, případně použít k měření. Sekce `Scope` slouží pro nastavení digitalizační karty, a tedy měřeného časového signálu. Pod touto sekcí je možné sestavit počet průměrů, abychom se zbavili nežádoucích parazitních signálů, typu šum a podobně.

V sekci `Tekutý dusík` je graf hmotnosti nádoby na dusík. V tomto případě víme, že plná nádoba má cca 60 kg a prázdná 22 kg. Ze zkušenosti také víme, kolik kilogramů tekutého dusíku je na jedno celé měření nutné. Proto jsme schopni odhadnout, zda bude dostupný tekutý dusík k měření stačit. V této sekci je také graf vnitřního tlaku v Dewarově nádobě. Tento tlak je možné v této sekci i regulovat.

Sekce `Nastavení tabulky teplot` slouží k importu dat z EXCELu. Na základě těchto údajů program automaticky nastavuje a měří v požadovaných teplotách. V poslední sekci `Ovládání` je k dispozici základní nutné ovládání tohoto programu. Je zde možnost ručního nastavení požadované teploty (v Kelvinech), ruční měření a uložení signálu, nastavení tolerance teplot a takzvaný `Watchdog`. To slouží k vypnutí a zapnutí pumpy pro průtok dusíku. Po levé straně je opět viděna intenzita odraženého detekčního svazku. Čím vyšší, tím lepší signál dostaneme.

Velmi důležitá je pro špatně rezonující vzorky. Graf na obr. 3.8 slouží ke grafickému zobrazení teplot (požadovaná a dvě teploty uvnitř kryostatu, regulovaná a teplota na vzorku). Teplota regulovaná a na vzorku se může v řádech jednotek kelvina lišit. Pro vyhodnocení je tato hodnota ovšem důležitá. Zobrazení časového signálu a jeho fourierovou transformaci, je možné vidět na obr. 3.9.

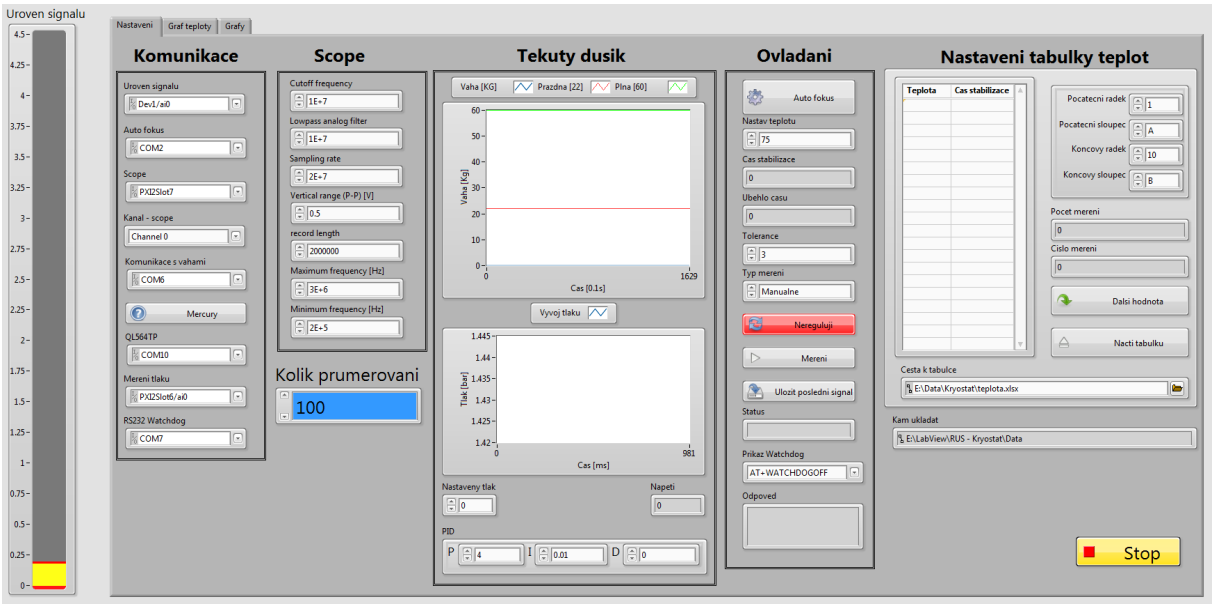

Obrázek 3.7: RUS-Kryostat, ovládací program (nastavení)

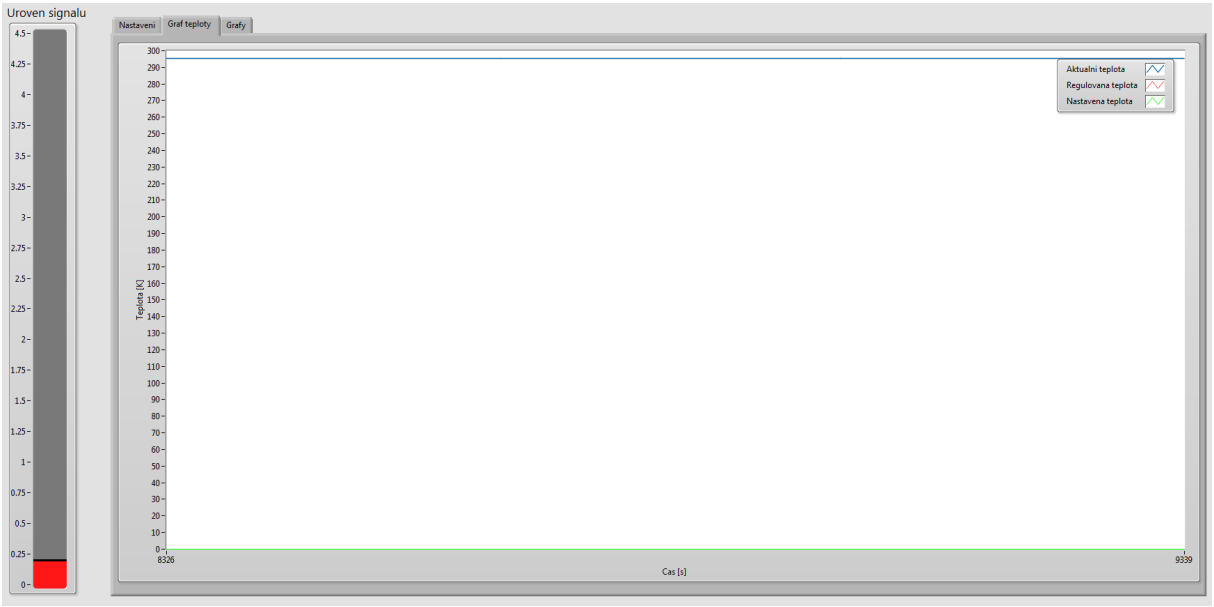

Obrázek 3.8: Rus-Kryostat, ovládací program (vývoj teplot)

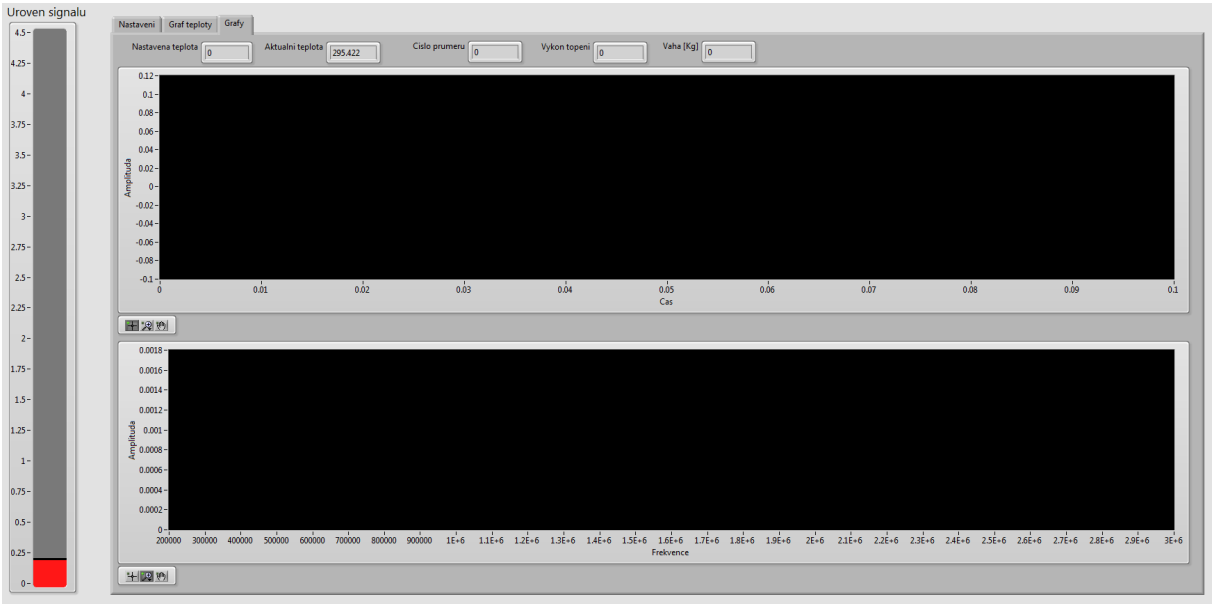

Obrázek 3.9: RUS-Kryostat, ovládací program (měřený signál a jeho FFT)

3.2 Měření povrchových vln

Vývoj těchto aparatur je motivován požadavkem na měření, které nelze provést pomocí metody RUS 3.1. Jde například o vzorky vykazující silný útlum (kdy rezonanční spektrum obsahuje velmi málo rezonancí, nebo v extrémních případech ani nelze řádně vybudit), měření vzorků pod mechanickým napětím (které nelze měřit rezonanční metodou už z principu měření volných kmitů), měření tenkých vrstev (které je pomocí metody RUS poměrně časově náročné, neboť je nutné měřit jak vzorek s tenkou vrstvou, tak poté samostatný substrát), atd.

3.2.1 TGS s rotačním podstavcem

Popis aparatury

Na tomto sestavení se běžně měří anizotropie daného materiálu. Tato sestava se dá rozdělit na dvě části: optická cesta a měřicí s regulační cestou. Tyto dvě části budou popsány zvlášť.

Optická cesta je dána primárně optickými prvky, doplněnými lasery a detektorem. Schéma této optické cesty je zobrazeno na obr. 3.10[1] a její princip je popsán v sekci 2.2. Optická cesta tedy začíná dvěma lasery. Pulsní infračervený laser je použit pro vybuzení povrchových akustických vln a zelený kontinuální laser slouží pro jejich detekci. Jak je vidět na obrázku, oba tyto lasery mají totožnou cestu. Tedy na začátku cesty se pomocí polopropustného zrcátka spojí a poté projdou válcovou čočkou. Z válcové čočky projdou tyto svazky fázovou mřížkou, na které se difraktují a získáváme tak dva svazky. Ty pokračují soustavou sférických čoček následovanou polarizačním optickým rozbočovačem, který na zpáteční cestě oddělí zelený detekční svazek. Z rozbočovače dopadají svazky skrz čtvrt-vlnu na měřený vzorek. Na vzorku se vybudí akustická vlna a zelený detekční svazek se přes rozbočovač oddělí a pomocí dvojice zrcátek dopadne na PIN diody detektoru.

Měřicí a regulační cesta se skládá z detektoru, osciloskopu a rotačního posuvníku. Detektor obsahuje dvojici PIN diod, které jsou zapojeny diferenciálně. Signál z těchto diferenciálně zapojených diod pokračuje do zesilovače *HSA-1-40* (1 GHz, 40 dB)

[1] autor P. Stoklasová, Akademie Věd ČR, Ústav Termomechaniky, Laboratoř ultrazvukových metod

společnosti FEMTO. Z tohoto zesilovače se berou dva signály. Jeden signál je stejnosměrná složka, která slouží k seřízení zrcátek pro co nejlepší dopad detekčního svazku na PIN diody. Druhý signál již zmiňovaný měřený. Oba tyto signály se měří pomocí osciloskopu LeCroy *725Zi* (2.5 GHz, 20 GS/s, 8 bit). Rotační motorizovaný krokový posuvník je připojen do kontroleru společnosti STANDA *8SMC1*. Kontroler i osciloskop jsou připojeny do ovládacího počítače, ve kterém se používá pro automatické měření program, který byl vyvinut v prostředí LabView.

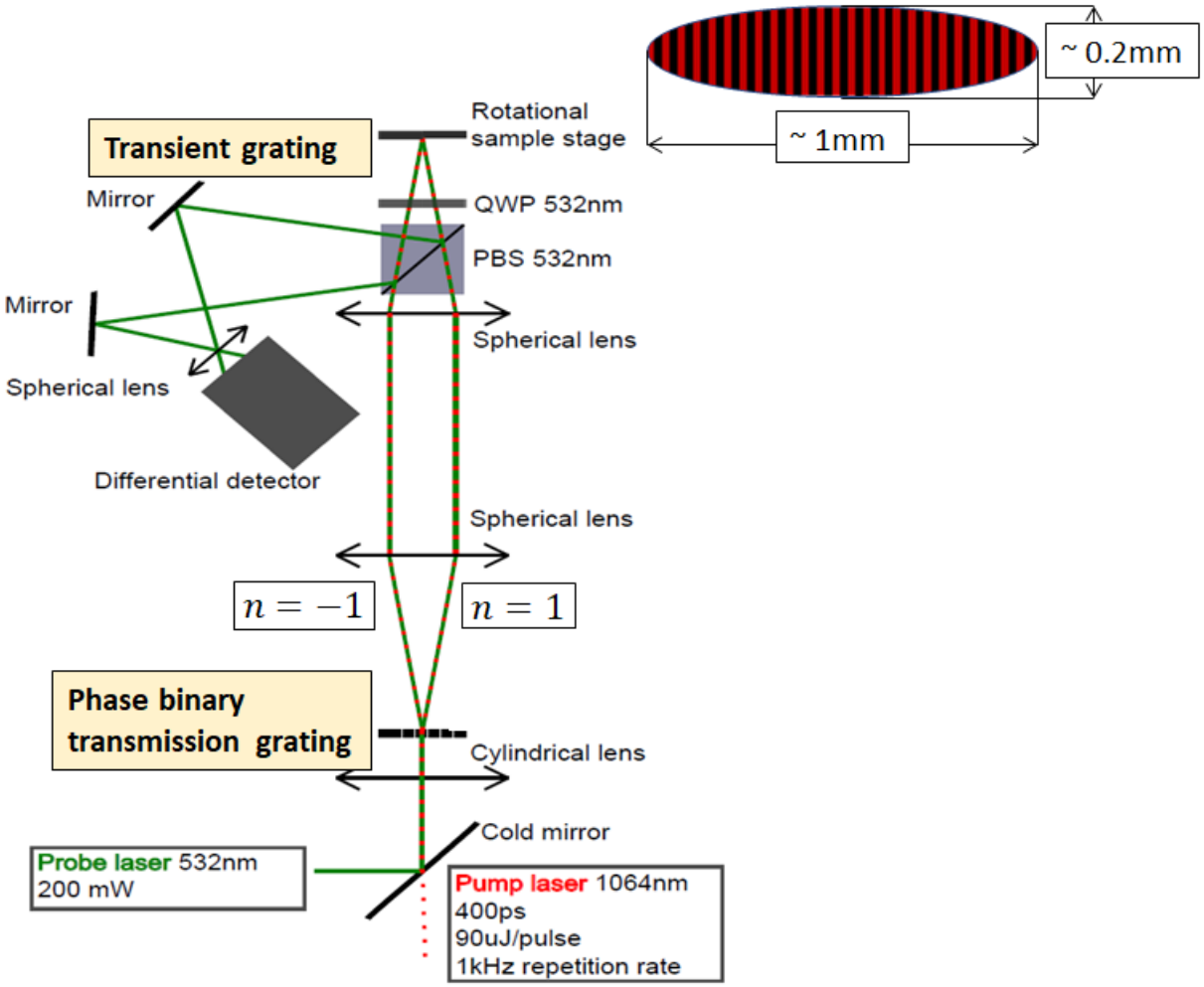

Obrázek 3.10: Blokové schéma optické cesty TGS-rotace

Popis ovládání

Na obr. 3.11 je ovládání této sestavy zobrazeno. Je rozděleno do několika částí. V první části, nazvané `Komunikace`, se nastavuje komunikace s přístroji, které se měření účastní.

V tomto případě pouze osciloskop a kontroler rotačního posuvníku. V sekci `Načtení tabulek` se jako v jiných případech načte sekvence měření. V tomto případě úhly, ve kterých má dané měření probíhat. Sekce `Ovládání` slouží pro nastavení rychlosti rotace a jaký signál se z osciloskopu má uložit. Vlastní nastavení signálu se určuje ručně na daném osciloskopu. Data jsou ukládána automaticky do databáze MS SQL. Z této databáze se tato data dají vyhodnocovat, případně exportovat pro další potřebu.

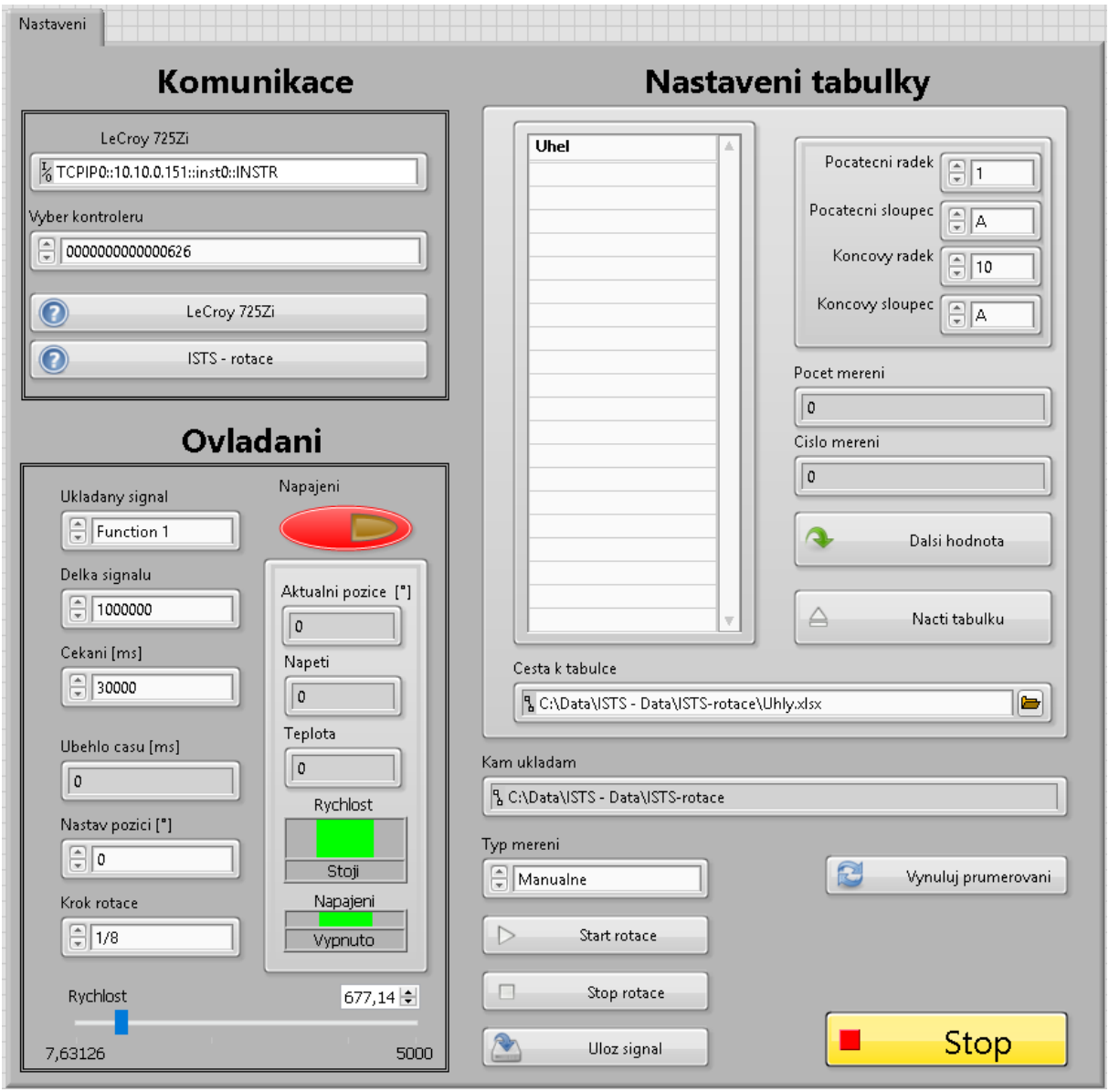

Obrázek 3.11: TGS-rotace, Ovládací program

3.2.2 TGS s teplotní komorou

Popis aparatury

Tato sestava se opět skládá ze dvou částí. Optická cesta je stejná, jako v kapitole 3.2.1. Proto se v této kapitole zaměříme pouze na cestu měřící a regulační. V první řadě se jedná o komerční teplotní komoru společnosti Instec, která má teplotní rozsah 80-850 K. Tato komora je vakuová, proto je k této komoře připojena vývěva *Hi Cube 80* společnosti Pfeiffer. I když je komora vakuovatelná, je nutné mít plášť této komory teplotně stabilní. O tuto teplotní stabilizaci se stará vodní chlazení Oasis *160*. Do této komory byl umístěn teplotní senzor v podobě PT100. Měření teploty na tomto senzoru obstarává *NI-9219* (100 S/s, 24 bit) společnosti National Instruments. Detektor, stejně jako v případě 3.2.1, je konstruován ze dvou PIN diod, které jsou zapojeny diferenciálně a výsledný signál zesílen zesilovačem *HSA-1-60* (1 GHz, 60 dB) společnosti FEMTO. Zesílený signál se měří na osciloskopu LaCroy *640Zi* (4 Ghz, 20 GS/s, 8 bit). Všechny tyto části jsou propojeny s řídícím počítačem, na kterém je ovládací program. Tento program byl vyvinut v prostředí *LabView*.

Popis ovládání

Ovládání této soustavy je zobrazeno na obr. 3.12. V sekci `Komunikace` se vybírají komunikační kanály a protokoly, které se používají ke komunikaci s jednotlivými částmi této sestavy. V nastavení `Oasis 160` se může měnit teplta vnějšího pláště komory Instec. Tato funkce je důležitá, neboť může zabraňovat namrzání optických průchodů. Sekce `Načtení tabulky teplot` je, stejně jako v jiných případech, pro načtění soustavy měřících bodů. V tomto případě teploty a potřebného času stability na dané teplotě, než začne vlastní měření. Data jsou opět ukládána do databáze MS SQL. Pomocí sekce `Ovládání` je možno ručně nastavovat teploty a na těchto teplotách měřit. Případně spustit automatické měření, které nastaví požadovanou teplotu uvedenou v tabulce a na této teplotě provede automatické měření. V této sekci se vybírá kanál osciloskopu, na kterém se daný signál měří. Grafy teploty a výkonu komory jsou na obr. 3.13. Díky těmto údajům jsme schopni zjistit, jak dlouho trvalo dostat se na jednotlivé teploty.

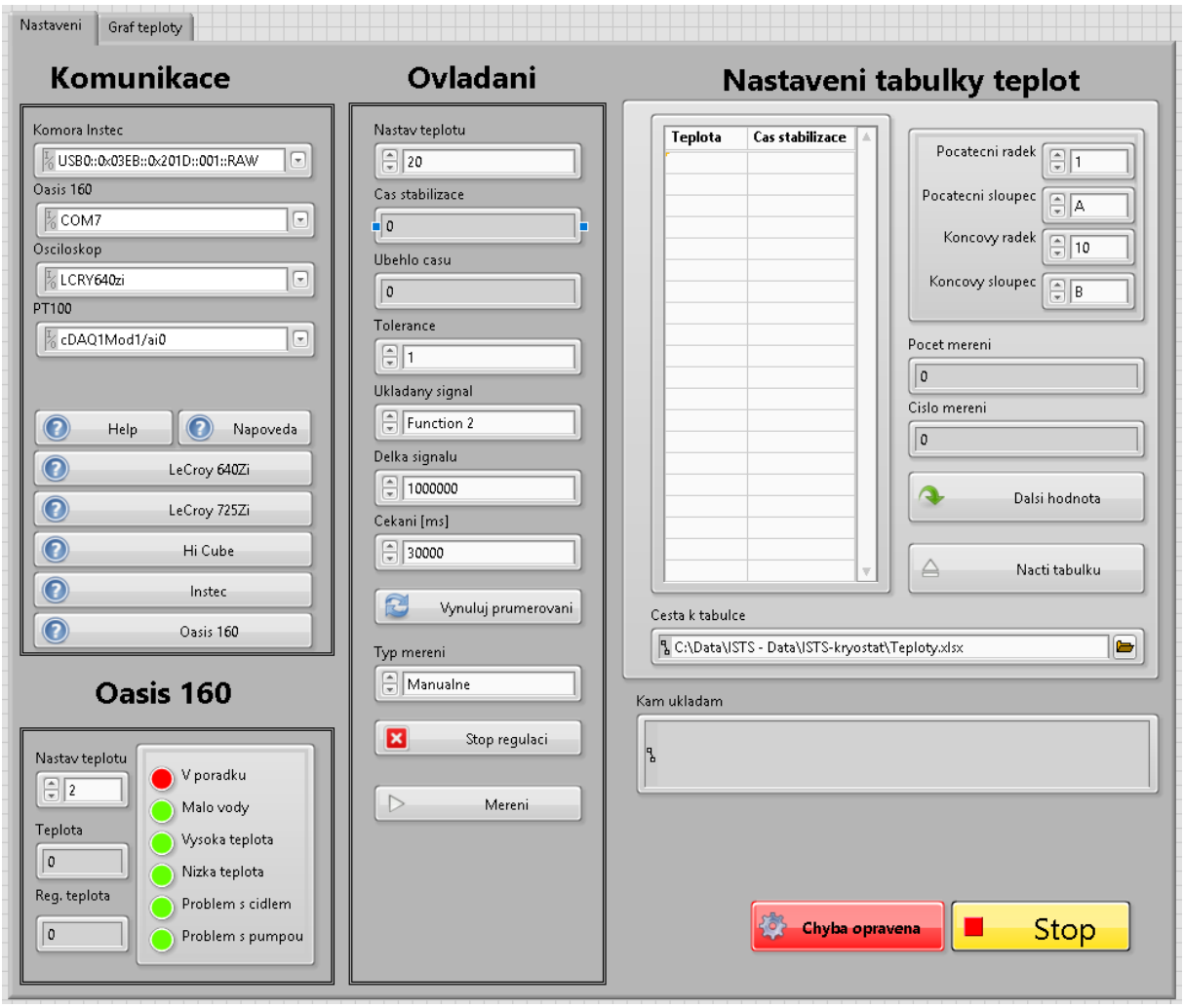

Obrázek 3.12: TGS-teplotni komora, ovladací program (nastaveni)

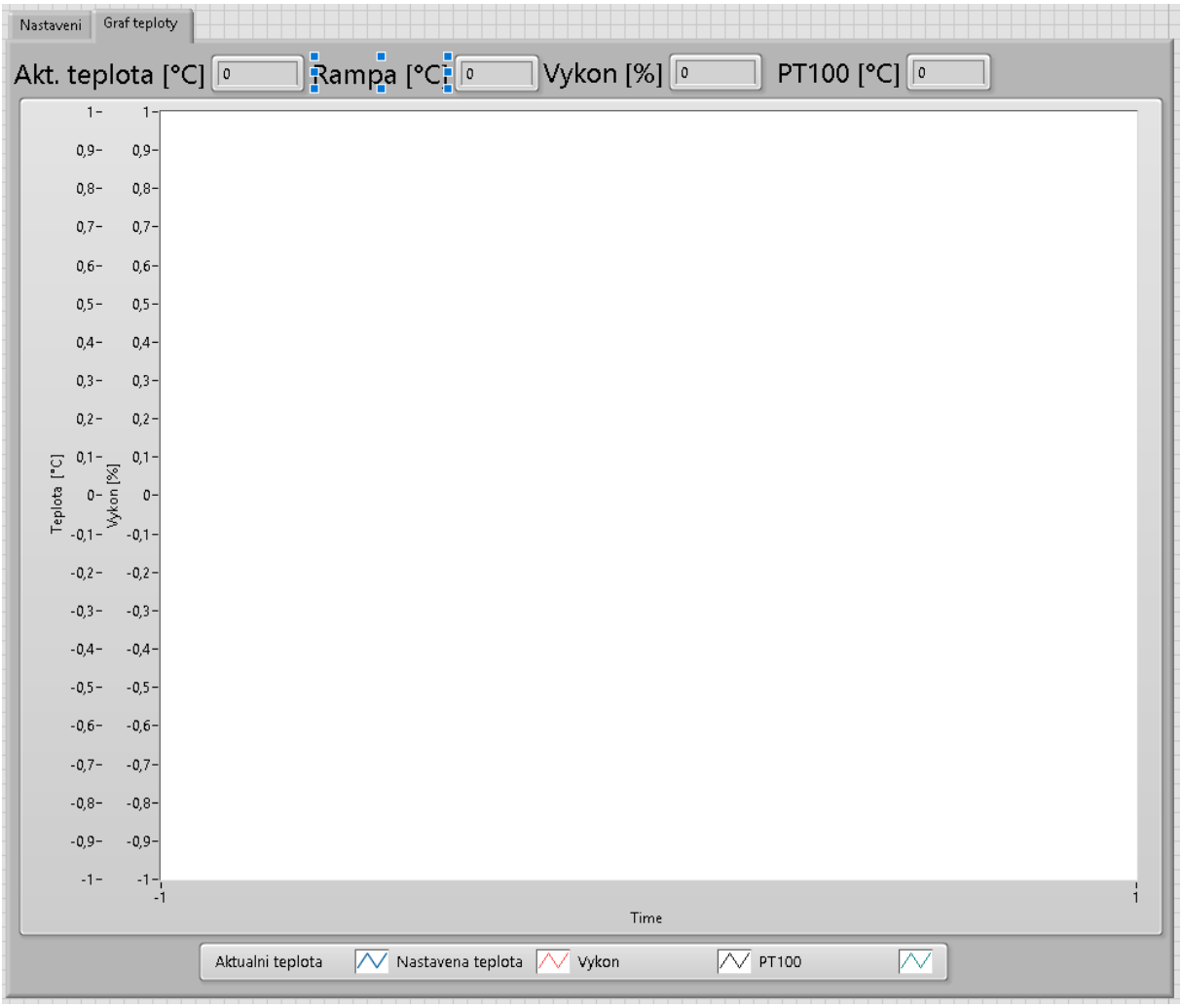

Obrázek 3.13: TGS-teplotni komora, ovladací program (vývoj teploty)

3.2.3 Širokopásmová aparatura se zatěžovacím zařízením

Popis aparatury

Tato aparatura vznikla za účelem měření elastických vlastností materiálu pod mechanickým napětím. Výše popsané motody 3.1 jsou pro tento účel nevhodné, neboť jsou založeny na vlastním kmitání. Což při mechanickém zatížení není možné. Deformační zařízení bylo vyvinuto Ing. J. Zídkem[2] a řízení s ovládáním tohoto deformačního zařízení je popsáno dále v této práci. Zařízení pro deformaci se skládá z několika částí. V první části je pohyblivá čelist, která řídí deformaci a zatížení, a pevná čelist, která dané zatížení měří pomocí tenzometrů. Další částí je pohon pohyblivé čelisti, kterým je krokový motorek. Tento motorek je připojen k pohyblivé čelisti přes převodovku 100:1. Poslední částí tohoto deformačního zařízení je indukční snímač polohy použitý pro měření deformace daného vzorku.

Deformační zařízení je umístěno na soustavě posuvníků jimiž se v případě potřeby posouvá střed rotace. Rotaci zde zajišťuje motorizovaný posuvník a jeho přítomnost zde je pro měření úhlové disperze rychlosti šíření povrchových vln, ze které je možné určit anizotropii měřeného vzorku. Pro vybuzení povrchových vln se používá infračervený pulsní laser `STA-01-7` společnosti STANDA. Laserový svazek je pomocí atenuátoru odkloněn do synchronizační PIN diody. Dále je přes soustavu zlatých zrcátek veden skrz cylindrickou čočku (z bodového svazku tato čočka udělá svazek čárový) na vzorek. Detekci v tomto případě zajišťuje interferometr `Femto` společnosti Bossa Nova Tech (dnes Sound & Bright). Apertura tohoto zeleného interferometru je cca $5cm$.

Detekční svazek je pomocí dvou stříbrných zrcátek veden skrz objektiv na vzorek. Stříbrná zrcátka, stejně jako objektiv, jsou připevněna k motorizovaným posuvníkům společnosti Physical Instruments. Pomocí těchto motorizovaných posuvníků je možné jemné a přesné X-Y skenování povrchu daného vzorku. Rozlišení těchto posuvníků je 50nm. Pro digitalizaci měřeného signálu je použita digitalizační karta společnosti National Instruments `PXIe-5162` (1.5 GHZ, 5 GS/s, 10 bit) a pro měření ostatních veličin (deformace, síly, teploty a úrovně signálu) `NI-9219` (100 S/s, 24 bit). Pro ovládání motorku sloužícího k posuvu volné čelisti je použit kontrolér `SMCI33` společnosti Nanotec. U ostatních posuvníků je použit kontrolér `Appolo` Physical Instruments. Všechna tato měřicí

[2]Akademie Věd ČR, Ústav Termomechaniky, Ultrazvukové metody

a ovládací zařízení jsou přes různé sběrnice připojena k ovládacímu počítači, a pomocí programu, programovanému v prostředí `LabView`, ovládána a regulována [22].

Popis ovládání

V této kapitole se budeme zabývat vlastním ovládáním této měřicí aparatury. Na obr. 3.14 je zobrazena část programu, určenou pro konfiguraci sestavy. V této konfiguraci se nastavují komunikační protokoly a kanály pro jednostlivé segmenty této meřicí aparatury. Definuje se tu komunikace s jednotlivými kontrolery motorizovaných posuvníků, měřicí kanály pro teplotu, sílu, deformaci, úroveň signálu a digitalizační kartou. V části nadepsané jako `Nastavení` je možné definovat maximální zatížení daného materiálu.

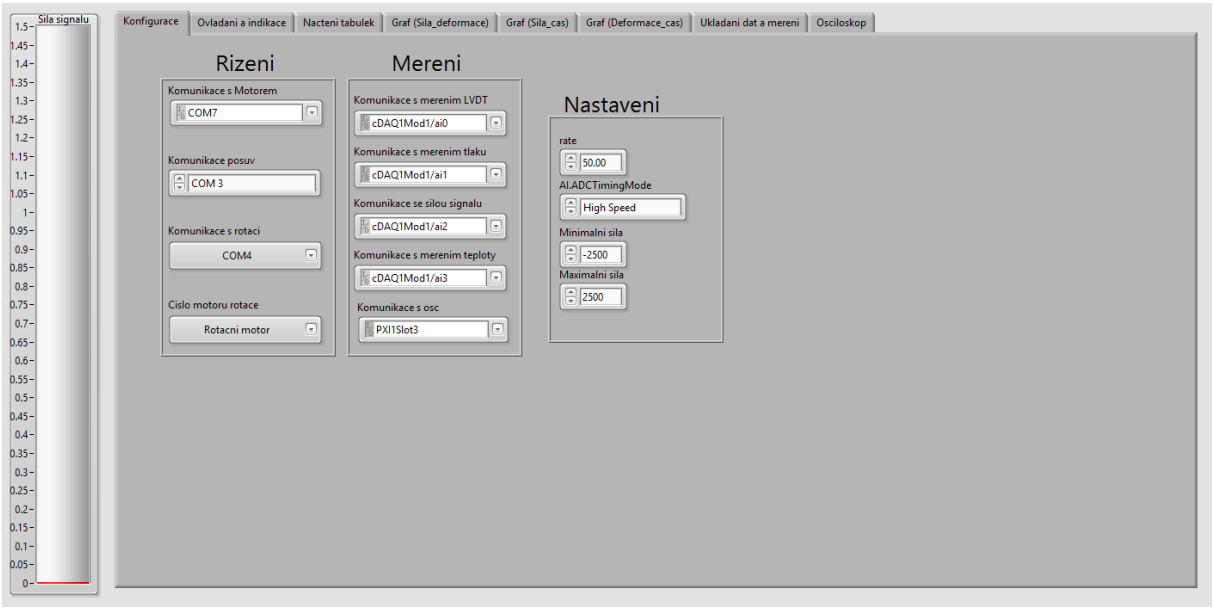

Obrázek 3.14: SAW-Trha4ka, ovládací program (konfigurace)

Ovládání na obr. 3.15 ovládá veškeré motorizované posuvníky, které jsou této aparatury součástí. Můžeme tu ručně ovládat motorek pro zatížení, tzn. ručně nastavit sílu, případně deformaci. Ručně se zde také ovládá rotace deformačního zařízení. Tím získáme jistotu, že budící a detekční svazek nikdy neopustí oblast měřeného materiálu. Pomocí X-Y posuvu se hledají měřicí body. Vzhledem k tomu, že měření veličin (síla a deformace) je diferenciální, je nutné před začátkem měření nastavit výchozí úroveň těchto měřených veličin.

Pomocí `Načtení tabulek` na obr. 3.16 zvolíme měřicí body na vzorku (Osa X a Osa

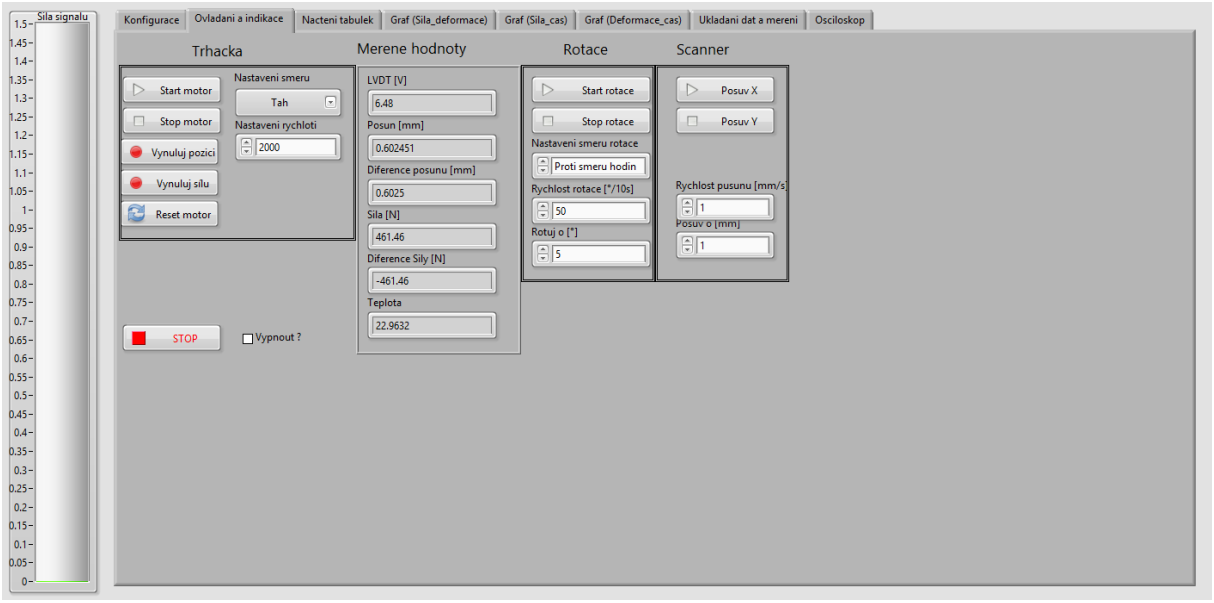

Obrázek 3.15: SAW-Trha4ka, ovládací program (ovládání)

Y) a také definujeme při jakém zatížení, případně deformaci, má automatické měření probíhat. Pokud chceme při měření měřit i anizotropii daného materiálu, použijeme i tabulku pro načtení rotace. Měření probíhá následovně (s měřením anizotropie):

A Nastavení požadované síly (deformace)

B Změření sítě bodů na vzorku

C Nastavení rotace

Nastaví se bod A. Po nastavení bodu A, nastane bod B. Jakmile se doměří celá požadovaná síť, použije se bod C. Po nastavení v bodu C, probíhá opět bod B. Tímto způsobem se změří při bodu A, pro všechny body C, bod B. Po skončení měření všech požadovaných hodnot bodu C, případně bodu B, se nastaví další hodnota v bodě A a měření pokračuje dokud se nezměří všechny body A, jejich podbody C a B. Grafy na obr. 3.17, 3.18 a 3.19 zobrazují aktuální stav zatížení a deformaci.

Nastavení ukládání, obr. 3.20, slouží pro výběr regulační veličiny. Tedy buď se reguluje na sílu nebo deformaci. Záleží na požadavcích. Poslední karta, zobrazena na obr. 3.21, je ovládání digitalizační karty. Na tomto grafu je zobrazen, a následně ukládán, měřený signál interferometru. Na všech obrázcích této kapitoly 3.2.3 je také zobrazen po levé straně ukazatel úrovně odraženého detekčního svazku od vzorku.

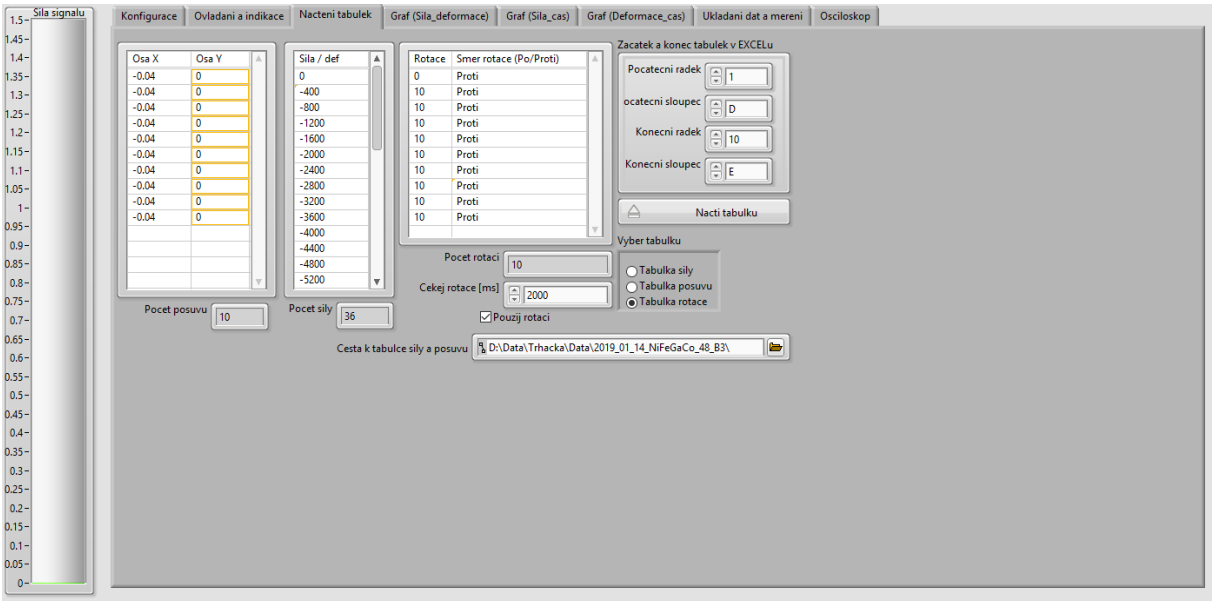

Obrázek 3.16: SAW-Trhačka, ovládací program (načtení dat pro měření)

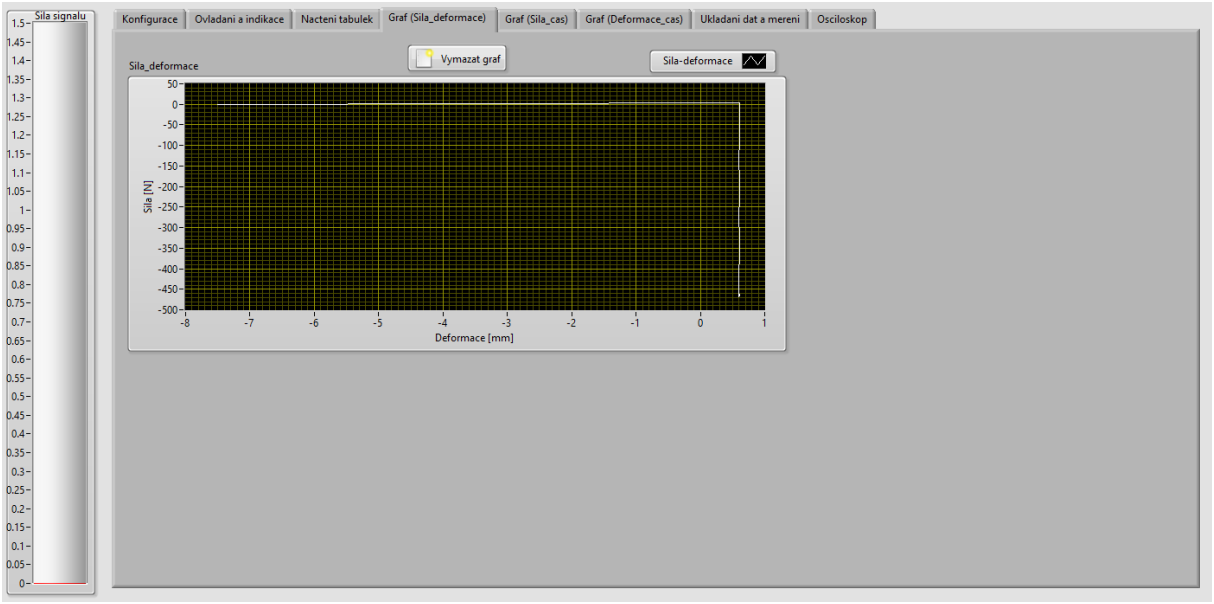

Obrázek 3.17: SAW-Trhačka, ovládací program (graf sila-deformace)

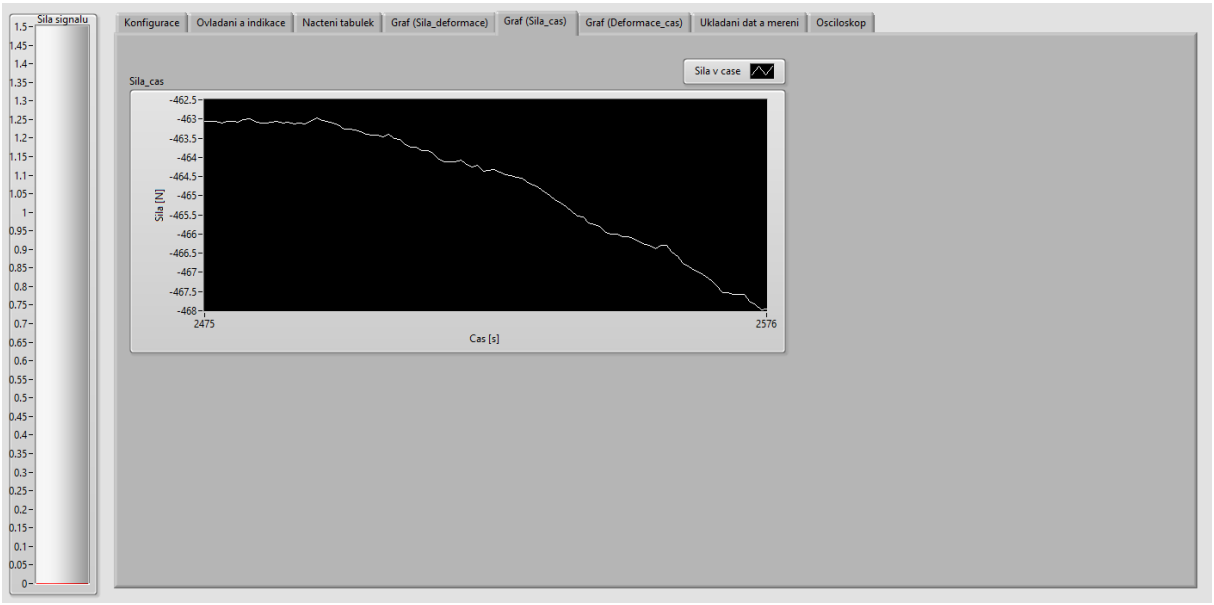

Obrázek 3.18: SAW-Trhačka, ovládací program (graf sila-cas)

Obrázek 3.19: SAW-Trhačka, ovládací program (graf deformace-cas)

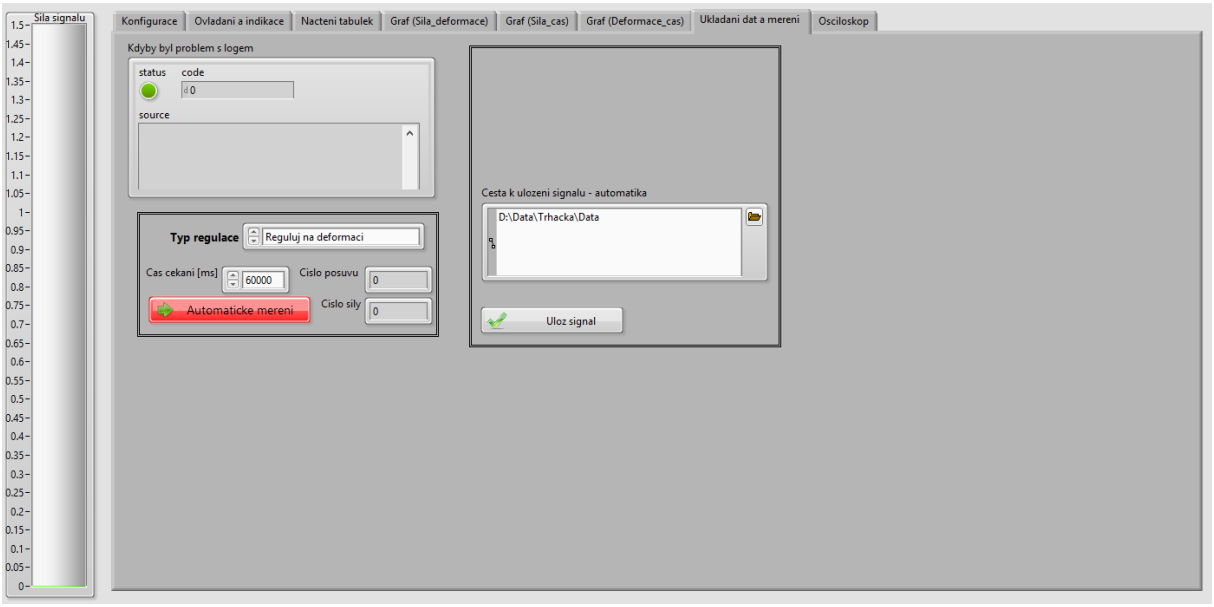

Obrázek 3.20: SAW-Trhačka, ovládací program (nastavení ukládání dat)

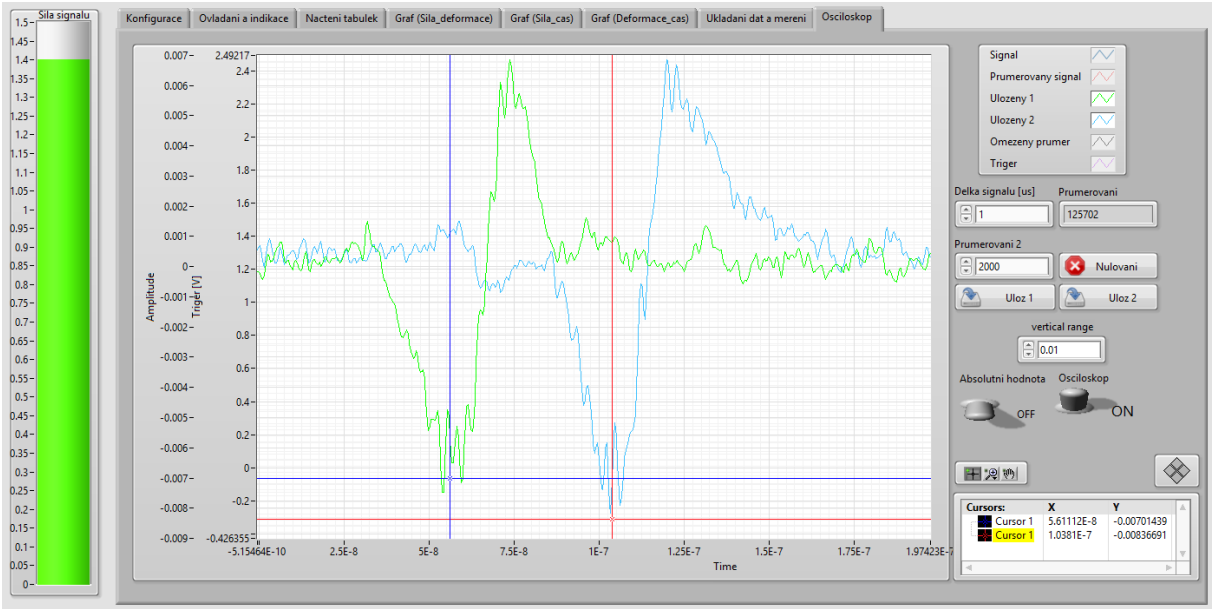

Obrázek 3.21: SAW-Trhacka, ovládací program (digitalizační karta)

3.3 Zjednodušený vývojový diagram

3.3.1 Sdílený vývojový diagram

Na obr. 3.22 je znázorněn zjednodušený vývojový diagram. Tento diagram se týká aparatur 3.1.3, 3.1.2, 3.1.1, 3.2.2 a s lehkou změnou i 3.2.1. Tato změna se týká pouze toho, že místo teploty se nastavuje úhel rotace.

Všechny systémy, kterých se to týká, se řídí tímto algoritmem. Je samozřejmostí, že každý systém má své vlastní komunikační protokoly a ochranné nastavení, pro případ kolize.

Na začátku každého spuštění příslušného programu je nutné načíst tabulku s hodnotami (teplota, rotace), při kterých bude měření probíhat. Tyto hodnoty se používají pro vstup do regulačních smyček. Zároveň tyto tabulky mohou obsahovat rampu a dobu stabilizace. Rampa v tomto kontextu znamené rychlost regulační smyčky. Doba stabilizace je čas, po kterou musí daná veličina splňovat kritéria, než je započato vlastní měření. Například, pokud se jedná o teplotní stabilizaci, je v programu k dispozici nastavení tolerance, ve které se má daná taplota před a během měření pohybovat.

Tato tolerance a další parametry (např. počet průměrování, délka měřeného signálu...) se nastaví podle potřeby měřeného vzorku. Každý měřený vzorek materiálu je jedinečný a potřebuje tedy i jedinečný přístup. Pokud operátor nastaví všechny parametry a zkontroluje i nastavení bezpečnostních prvků (např. vypadnutí externího chlazení pláště), může dané měření spustit.

Program se v tuto chvíli chová zcela autonomně. Hlavní výhoda tohoto autonomního provozu je, že některá měření mohou trvat i několik týdnů. Během této doby je dohled operátora pouze minimální.

Po spuštění se načtou hodnoty z tabulky a regulační smyčka se snaží daných parametrů dosáhnout. Během tohoto snažení se daná veličina porovnává s hysterezí danou nastavenou tolerancí. Ve chvíli, kdy se daná veličina ustabilizuje v daném tolerančním pásu, dochází ke spuštění časovače. Hodnota časovače je opět brána ze vstupní tabulky hodnot. Po uplynutí dané doby (pokud stabilizovaná veličina nepřekročí toleranční pás) se zapne pulsní laser.

Zapnutí a vypnutí pulsního laseru je nezbytnou součástí těchto programů. Jak už bylo

proklamováno, některá měření mohou trvat i několik týdnů. A pokud by během této doby byl pulsní laser stále sepnut, mohlo by dojít k jeho degradaci. Většina výrobců udává předpokládaný počet pulsů, které daný laser může během funkční doby vystřelit.

Po zapnutí laseru se spustí i měřící karty, které daný signál digitalizují. Toto měření probíhá tak dlouho, dokud není splněna podmínka pro nastavený počet průměrů. V těchto algoritmech se používají pouze správně měřené signály. Občas může dojít k nepředpokládanému incidentu a jeden (nebo více) signálů (během fáze průměrování) by nebylo úspěšně změřeno. To by samozřejmě mohlo vyústit v konečném důsledku v chybný záznam dat. Po změření všech signálů (průměrování) se laser opět vypne a daný zprůměrovaný signál se uloží.

Po úpěšném uložení signálu a přiřazení informací o tomto signálu do databáze, se algoritmus podívá do vstupních dat a podle toho vyhodnotí další krok. Pokud je v tabulce potřeba měření na další hodnotě, algoritmus provede nastavení potřebných veličin a cyklus se opakuje. Pokud byla změřena poslední hodnota, algoritmus většinu zařízení uvede do výchozího stavu a je připraven pro další použití.

Všechny programy jsou opatřeny ovládáním pro ruční přerušení algoritmu. Samozřejmostí jsou i možnosti drobných změn jako změna počtu průměrovaných signálů, změna tolerančního pásu, délky měřeného signálu a podobně.

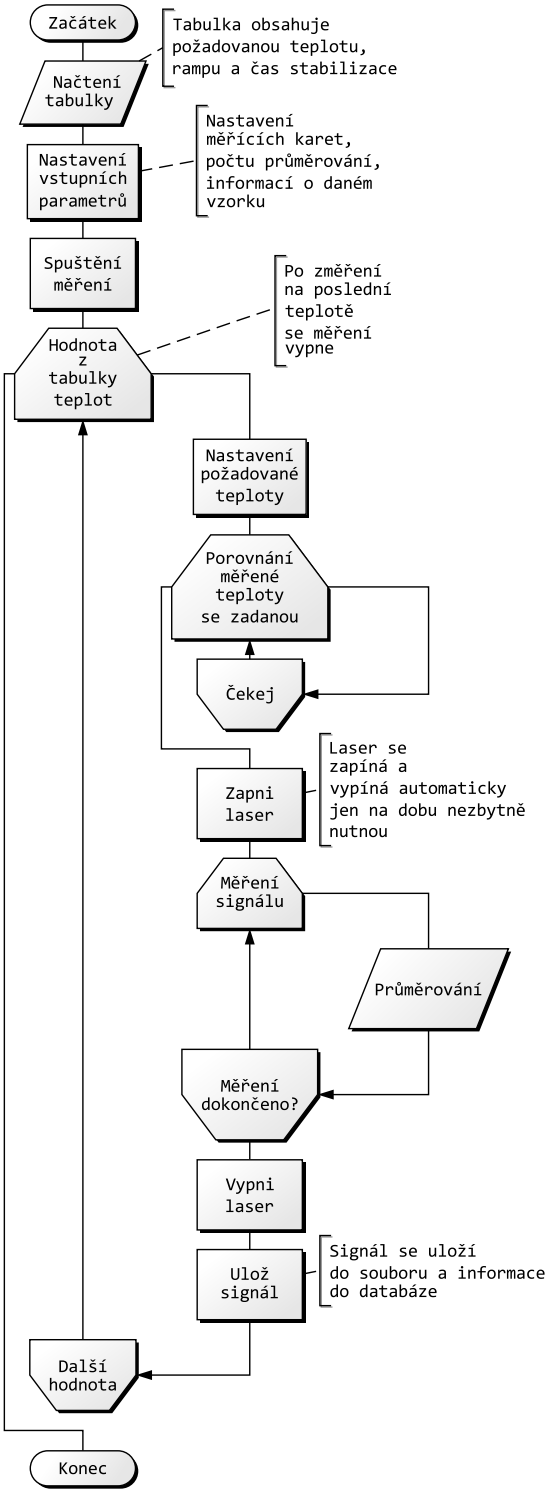

Obrázek 3.22: Zjednodušený vývojový diagram pro výše popsané systémy

3.3.2 Vývojový diagram pro 3.2.3

Tento algoritmus je složitější a obsahuje možnou modifikaci, kterou operátor může využít. Na obr. 3.23 je znázorněn zjednodušený popis algoritmu, který využívá sestava 3.2.3. Začátek tohoto algoritmu je velmi podobný jako algoritmus předchozí. Na začátku se ovšem musí operátor rozhodnout, zda při měření využije i možnost rotace vzorku. Po tomto rozhodnutí je nucen načíst příslušný počet tabulek (dvě nebo tři). První dvě tabulky je nucen operátor načíst v každém případě. Jedná se o tabulku posuvů a zatížení.

Tabulka posuvů zajišťuje matici bodů, ve kterých měření bude probíhat. Tabulka zatížení obsahuje vektor síly nebo deformace. Operátor je nucen se v této úrovni rozhodnout, zda bude deformační zařízení regulováno podle deformace, nebo podle síly (tj. v tak zvaném tvrdém nebo měkkém zatěžování). Je výhodné mít možnost obou těchto možností, neboť každé přináší jiné vlastnosti. Výběr se tak provede na základě požadavku na měřený vzorek a požadované získané informace. Pokud se očekává, že vzorek je anizotropní, má operátor možnost načíst také tabulku rotací, tj. relativních úhlů zatěžování vůči měřenému směru šíření vln.

Po zvolení výše uvedených možností a načtení příslušných tabulek je také nutné nastavit bezpečnostní meze, nastavit výchozí pozice síly a deformace, nastavit digitalizační kartu a uvést základní informace u měřeného materiálu. Po splnění všech těchto náležitostí je možné dané měření spustit. Algoritmus napřed načte první hodnotu z tabulky síly/deformace a na tuto hodnotu deformační zařízení nastaví a reguluje. Po dosažení této hodnoty jsou dvě možnosti (zde bude popsána možnost s rotací). Program nastaví deformační zařízení na požadovaný úhel, který je uveden v příslušné tabulce. Jakmile se deformační zařízení nastaví do požadované polohy, začíná skenování povrchu vzorku.

Díky nastavení os X a Y je tedy možné nastavit detekci do libovolné pozice vůči čárovému zdroji buzení povrchových vln. Toto skenování povrchu se tedy děje v cyklu. Během skenování se každý jednotlivý signál několikrát zprůměruje a tento průměrovaný signál se uloží. K tomuto signálu se samozřejmě uloží i potřebné informace o pozici. Po skončení tohoto skenu, je nastaven další úhel a tato matice je změřena znovu. Toto se děje pro každý jednotlivý úhel.

Po změření posledního úhlu a skenovací matice, se deformační zařízení vrátí do výchozí

pozice a program začne regulovat na další hodnotu v tabulce síla/deformace. Takto probíhá celé automatické měření, dokud se nezměří poslední požadovaná síla/deformace, poslední úhel rotace a skenování podle definované matice bodů. Z výše uvedeného je tedy na první pohled patrná časová zátěž celého měření. Měření na této sestavě může reálně trvat i několik dní.

V programu se dají nastavit mezní síly, přes který by se daný vzorek neměl dostat. Toto nastavení je primárně důležité při regulaci na deformaci vzorku, případně na manuální nastavení. Při překročení těchto mezních sil se deformační zařízení zastaví a vypne se daný algoritmus. Zároveň kontroler tohoto motorku pulsně kontroluje, zda algoritmus odpovídá. Ve chvíli, kdy testovací paket není přijmut, kontroler automaticky krokový motorek zastaví a odepne. Tím je zabráněno poškození vzorku či zařízení, pokud by došlo v ovládacím počítači ke kolizi.

Výše bylo uvedeno, že jsou dvě možnosti měření. Pokud není nutné měřit anizotropii, je možné nastavit programové přeskočení nastavení rotace deformačního zařízení.

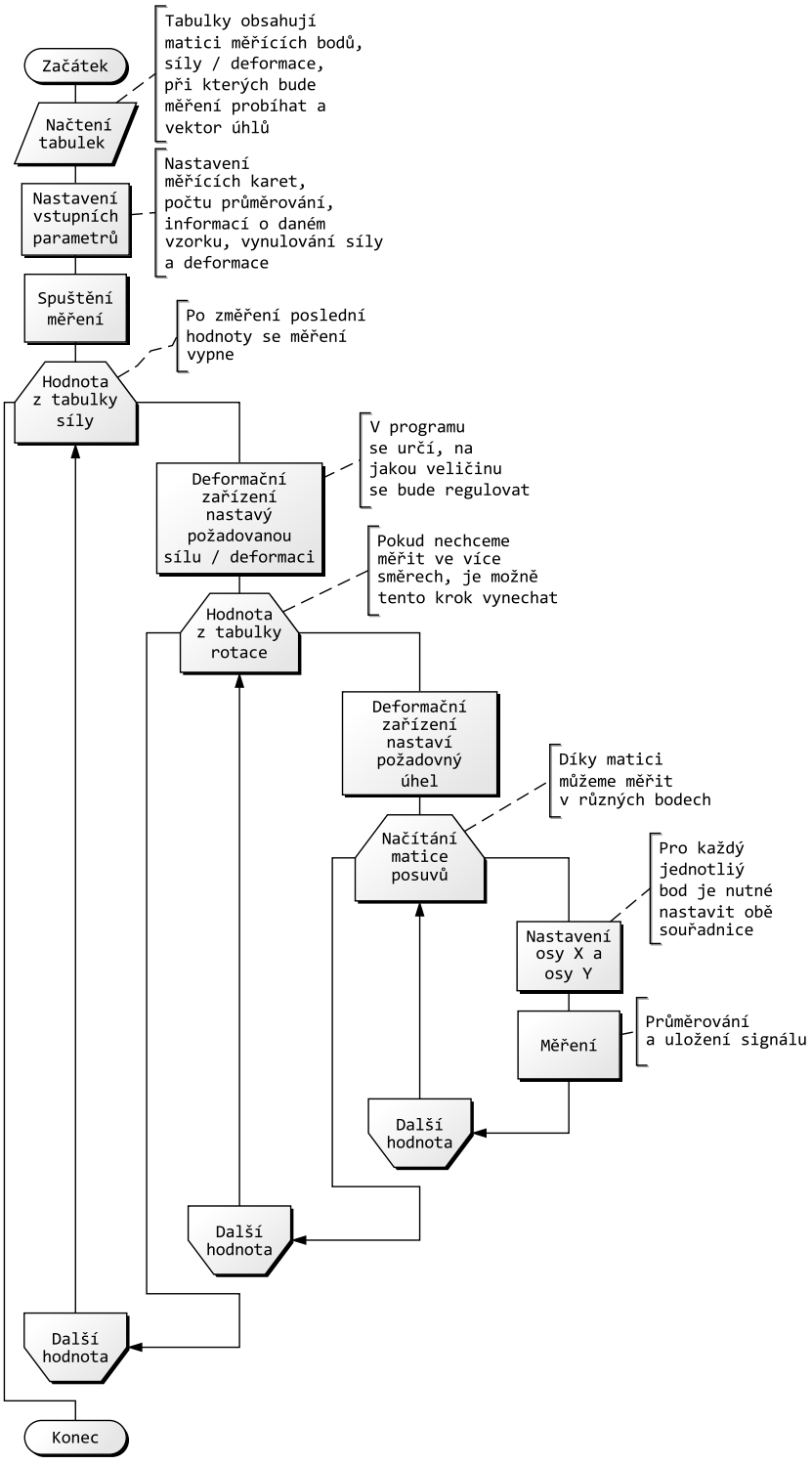

Obrázek 3.23: Zjednodušený vývojový diagram pro 3.2.3

4 Příklady aplikací aparatur v materiálových vědách

4.1 Ultrazvuková detekce fázových přechodů v hliníkových slitinách

Tato kapitola bude věnována použití rezonanční ultrazvukové spektroskopie (RUS) k detekci fázových přechodů v hliníkové slitině AA6262 při tepelném cyklování. Bude zde ukázáno, že metoda RUS je dostatečně citlivá, aby spolehlivě detekovala teploty tání a tuhnutí mikročástic Mg_4Bi_2-Bi, které jsou odpovědné za tyto fázové přechody, ačkoli objemový podíl částic je velmi malý (1%) a dokonce klesá s proběhnutými teplotními cykly. [23]

Fázové přechody mikro a nano částic v pevných látkách vykazují několik rozdílů ve srovnání s objemovými přechody stejných materiálů [24, 25, 26]. Například rozsáhlé studie akustické a magnetické rezonance tání a tuhnutí různých materiálů v porézních sklech [27, 28, 29, 30, 31] ukázaly, že teploty přechodu těchto částic se snižují a vždy existuje také pozorovatelná hystereze mezi táním a tuhnutím částic.

Mezi systémy s kovovou matricí / kovovými částicemi je z hlediska aplikace zjevně zajímavá hliníková slitina AA6262 [32]. Tato slitina má nominálně podobné složení jako slitina AA6082 (nebo AA6061) AlMgSi, ale její obrobitelnost je zvýšena přidáním malých množství Pb a Bi, které při správném teplotním zpracování vytvářejí mikročástice dispergované podél zrna hranice. Tyto částice mají poměrně složitou, vícesložkovou strukturu [33], včetně také určitého množství Mg_3Bi_2-Bi. Při teplotě tání se částice částečně roztaví a slitina prochází přechodem do křehkého stavu (DBT). Zkřehnutí nastává v důsledku přítomnosti taveniny.

To je výhodné pro obrábění, protože tavení materiálu Mg_2Bi_2-Bi v blízkosti řezného nástroje snižuje pevnost materiálu a vede k tvorbě krátkých a lámatelných třísek. Znalost teploty DBT je tedy nezbytná pro návrh procesu obrábění. Podobný význam má také znalost možného vývoje této teploty přechodu během tepelného cyklování (tj. opakované tavení a tuhnutí v důsledku teplotních oscilací), protože odráží změny vlastností materiálu během obrábění.

DBT v AA6262 a podobných slitinách ([34, 35]) mají zcela odlišnou povahu než v konvenčních strukturálních materiálech, jako jsou nízkouhlíkové oceli, kde ke křehnutí dochází v důsledku redukce dislokačního skluzu, a kde jsou tedy možnosti ultrazvukové

nedestruktivní detekce teplot DBT omezené [36, 37, 38]. V případě AA6262 může být teplota DBT detekována nepřímo z detekce bodů tání a tuhnutí částic, například diferenční skenovací kalorimetrií. Avšak vzhledem k malému objemovému podílu částic Pb + Bi (1%) mohou být odpovídající exo- a endotermické píky DSC malé, srovnatelné s hladinou šumu zařízení DSC a nesrovnatelně menší než píky různých procesů v matrici.

Vhodnou alternativou k měření DSC v takovém případě může být detekce fázových přechodů z malých změn elastických modulů slitiny. Tyto změny mohou být detekovány buď měřením rychlostí akustických vln pulzním ozvěnou v materiálu [26, 28], nebo rezonanční ultrazvukovou spektroskopií 2.1. Jak bude dále ukázáno, tato metoda je pro systematické studium DBT a reverzních (BDT) teplot v této slitině, vhodná. A díky 3.1.2 bylo možné provádět několik teplotních cyklů bez přestávky za sebou. [23]

Zkoumaným materiálem byla komerční slitina AA6262 (Constellium Extrustions, Děčín, Česká Republika) vyrobená formou extruze (průměr $18,8$ mm). Materiál byl zahřát na teplotu T8 (tyče byly za studena zpracovány na průměr $18,1$ mm (redukce $7,3\%$), žíhání bylo prováděno při 160 °C po dobu 10 hodin.) Výsledná mikrostruktura slitiny je na obr. 4.1: sestává z vláknitých zrn prodloužených podél směru vytlačování.

Částice obsahující Pb a Bi jsou rozptýleny a jsou také protaženy podél směru vytlačování. DBT teplota v této slitině byla stanovena pomocí Charpyho testu ([33]); teplota přechodu byla indikována prudkým poklesem lomové houževnatosti při přibližně 250 °C. Pro samotné měření RUS (3.1.2) byl připraven pravoúhlý obdélníkový průřez $2,61 \times 3,21 \times 1,94 mm^3$ (přesnost $\pm 0,01$ mm) s hranami orientovanými podél směrů zpracování.

Před tepelnými cykly byly změřeny a stanoveny elastické konstanty za pokojové teploty výše popsaného vzorku AA6262 kombinací měření RUS 3.1.1 a konvenční technikou pulzního echa. Cílem tohoto předběžného měření bylo zjistit, zda vláknitá struktura indukuje jakoukoli měřitelnou elastickou anizotropii v materiálů. Taková anizotropie by mohla následně ovlivnit interpretaci RUS spekter měřených při vyšších teplotách.

Po změření při pokojové teplotě byl vzorek podroben tepelnému cyklování. Vzorek zkoumané slitiny AA6262 byl podroben pěti tepelným cyklům s příslušnými teplotními rozsahy uvedenými v tabulce 4.1 Maximální teploty byly pro všechny cykly nad očekávanou teplotou DBT pro slitinu AA626 (250 °C). Pro 2. a 4. cyklus je maximální teplota zvolená nad bodem tání Pb ($T_{Pb} = 325$ °C), aby se zjistilo, zda má tání a tuhnutí

Pb uvnitř částic Pb + Bi nějaký dopad na DBT a BDT teploty.

Tabulka 4.1: Rozsahy tepelných cyklů zkoumané slitiny AA6262; PT označuje pokojovou teplotu

Cyklus	Teploty
1	PT → 290 °C → PT
2	PT → 350 °C → PT
3	PT → 290 °C → PT
4	PT → 350 °C → PT
5	PT → 290 °C → PT

Během každého teplotního cyklu byl měřen vývoj rezonančního spektra volných elastických vibrací vzorku v teplotní oblasti, kde se očekávaly DBT a BDT, tj. přibližně mezi 150 °C a 300 °C. Teplotní kroky mezi jednotlivými měřeními byly zvoleny mezi 10 °C (daleko od očekávaných přechodových teplot) a 2 °C (blízko očekávaných přechodných teplot). Rychlost zahřívání a chlazení byla pomalé (1 °C×min^{-1}) s dalšími 2 minutami stabilizační doby při každé měřené teplotě před samotným měřením RUS(3.1.2). Tento přístup byl zvolen tak, aby byla zajištěna teplotní homogenita v celém objemu vzorku a po celou dobu záznamu spektra.

Na obr. 4.2 je zobrazen příklad teplotního vývoje zvoleného píku slitiny AA6262 během zahřívacího cyklu. Kvalita píku rychle klesá v důsledku nárůstu tlumení. Je patrné, že pík s téměř konstantním sklonem klesá se zvyšující se teplotou na nižší frekvence, což ukazuje na významné změkčení AlMgSi v důsledku zahřívání.

Výsledky (vývoj δG s teplotou) získané pro vzorek AA6262 jsou znázorněny na obr. 4.3 (zahřívání) a obr. 4.4 (chladnutí). Pro první zahřívací cyklus Mg_2Si indukuje určité ztvrdnutí při teplotě nad 180 °C, což je však přerušeno při 253 °C prudkým poklesem označujícím tání částic. Toto rapidní snížení $\delta G_{\mathrm{DBT}} = 1.65 \times 10^{-3}$ se dokončí při teplotě 262 °C. Maximální sklon $\mathrm{d}(\delta G)/\mathrm{d}T$ se objevuje přibližně při $T_{\mathrm{DBT}} = 257$ °C.

Podobně ostré poklesy δG lze pozorovat také pro všechny ostatní zahřívací cykly. Teplota přechodu pro druhý cyklus se mírně posunula dolů ($T_{\mathrm{DBT}} = 254$ °C). Pro třetí a další cykly zůstává tato teplota přibližně stejná, stejně jako šířka přechodových intervalů

(~ 10 °C). Naopak velikost skoku spojeného s přechodem (δG_{DBT}) se v důsledku cyklování významně mění. Maximum se objeví ve druhém cyklu ($\delta G_{\mathrm{DBT}} = 2.9 \times 10^{-3}$ po odečtení celkového konkávního trendu křivky), což však může být ovlivněno skutečností, že v prvním cyklu změkčení z DBT stále superponuje s vyztužením způsobeným precipitací Mg_2Si. Dále se hodnota δG_{DBT} postupně snižuje z 1.5×10^{-3} (třetí cyklus) na 0.6×10^{-3} (pátý cyklus). Zdá se, že vývoj teplot DBT ani šířek přechodného intervalu a δG_{DBT} není nijak ovlivněn přehřátím nad T_{Pb} ve druhém a čtvrtém cyklu.

Pro chladnutí je výrazně odlišný obrázek (obr. 4.4). V prvním cyklu se objevuje v širokém teplotním intervalu (240 °C až 220 °C) s velikostí $\delta G_{\mathrm{BDT}} = 2.7 \times 10^{-3}$. Maximální změna sklonu indikující teplotu BDT se objevuje přibližně při $T_{\mathrm{BDT}} = 235$ °C. Podobné šířky intervalů BDT (~ 20 °C, tj. dvakrát širší než pro DBT) lze pozorovat také pro třetí a pátý tepelný cyklus, tj. pro ty cykly, u nichž maximální teplota nepřekročila T_{Pb}. Teplota BDT pro tyto cykly se systematicky zvyšuje až na $T_{\mathrm{BDT}} = 250$ °C pro pátý cyklus.

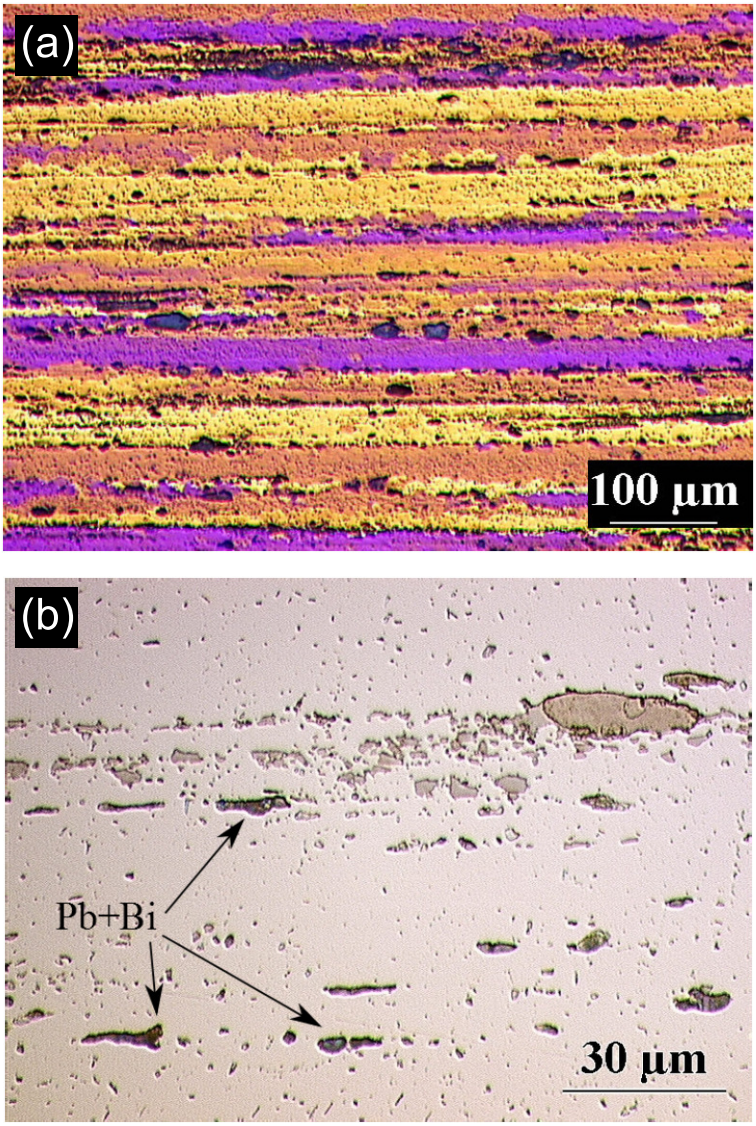

Obrázek 4.1: Mikrostruktura studované slitiny AA6262: (a) struktura vláknitých zrn zvýrazněná anodizací Barkerovým činidlem; (b) detail částic obsahujících olovo a bizmut. [23]

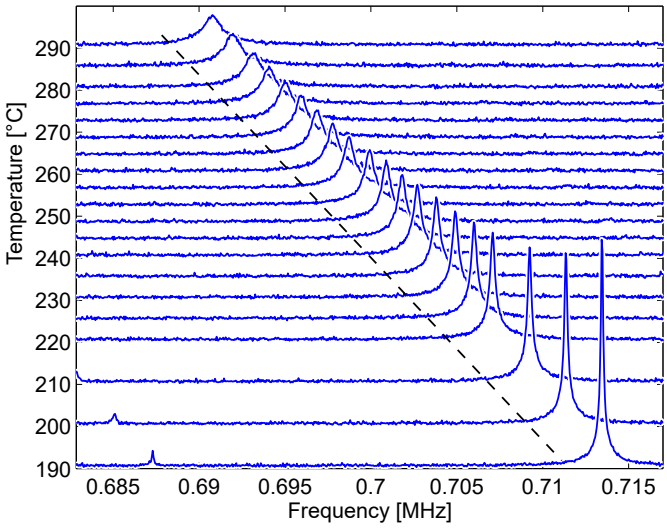

Obrázek 4.2: Příklad vývoje jednoho rezonančního píku s teplotou během zahřívání vzorku AA6262. Přerušovaná čára představuje globální lineární trend (G'_0). [23]

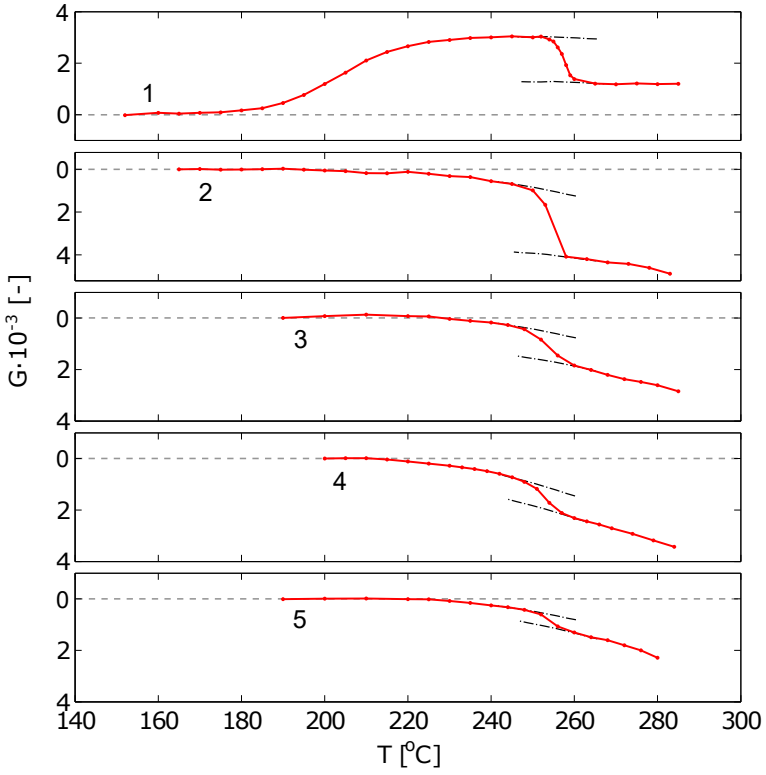

Obrázek 4.3: Vývoj δG s teplotou během ohřevu probíhá po dobu pěti následných tepelných cyklů. Čísla 1 a 5 označují čísla cyklů, přerušované čáry indikují přibližné oblasti přechodů BDT. [23]

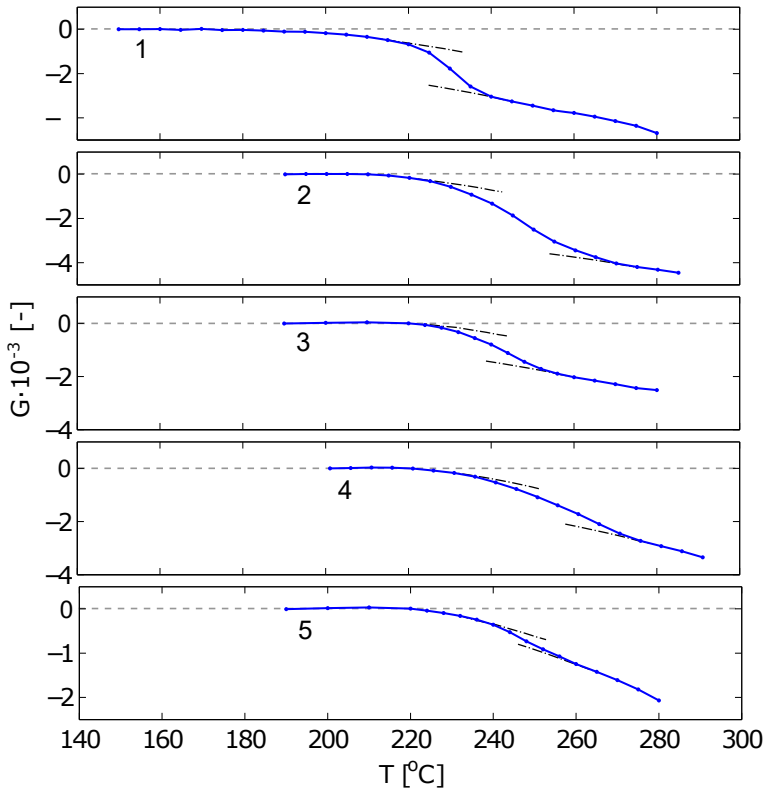

Obrázek 4.4: Vývoj δG s teplotou během chladnutí probíhá po dobu pěti následných tepelných cyklů. Čísla 1 a 5 označují čísla cyklů, přerušované čáry indikují přibližné oblasti přechodů BDT. [23]

4.2 Studie vnitřního tření ultrajemnozrnné slitiny hořčíku AZ31

Vnitřní tření v slitině hořčíku AZ31 bylo zkoumáno pomocí rezonanční ultrazvukové spektroskopie 2.1. Bude ukázáno, že vnitřní tření se výrazně zvyšuje při vyšších teplotách ($\geq$ 100 °C) a že toto zvýšení lze připsat pokluzu po hranicích zrn (GBS). Vývoj tohoto jevu s různou velikostí zrna je studován porovnáním výsledků získaných pro extrudovaný materiál a pro materiály po dalším jednom, dvou a čtyřech průchodech. Bylo pozorováno, že aktivační energie pro difúzní GBS se s klesající velikostí zrn významně snižuje, a tím také klesá prahová teplota, nad kterou je tento vnitřní třecí mechanismus dominantní. Výsledky ukazují, že ultrajemnozrnné slitiny AZ31 vykazují difúzní GBS při teplotách blízkých teplotě okolí, což je zajímavé zjištění s ohledem na možné aplikace těchto slitin v superplastických formovacích technologiích. [39]

Tažnost slitin hořčíku může být významně zlepšena zjemněním zrna, a to zejména zpracováním s výraznou plastickou deformací (SPD) [40, 41, 42, 43]. Tento účinek je částečně způsoben randomizací orientací zrna v důsledku SPD, což naruší jinak silnou krystalografickou texturu tvářených slitin hořčíku, která má za následek plastickou anizotropii. Kromě toho zjemnění zrna a odpovídající zvýšení objemové frakce hranic zrn, umožňují snadnější plasticitu pomocí pokluzu po hranicích zrn (GBS) [44, 45, 46, 47, 48], a také pomocí dislokačního skluzu [49, 50]. Jak GBS, tak skluz mohou významně přispět ke zvýšené zpracovatelnosti jemnozrnných slitin hořčíku.

Měření vnitřního tření byla mnohokrát ukázána jako citlivý a spolehlivý nástroj pro detekci GBS [51, 52, 53, 54], jakož i aktivity dislokací [55, 56, 57, 58], a mohla by tedy být schopna detekovat vývoj obou těchto účinků v důsledku ECAP [44]. Protože je však relaxační síla pro GBS mnohem vyšší než u dislokačního skluzu [59], a protože bazální systémy skluzu v slitinách jsou relativně rigidní, je pravděpodobné, že vnitřní tření v jemnozrnném AZ31 je dominantně dáno GBS. Ileva a kol. [60] pozorovali rychlý nárůst vnitřního tření ECAPovaného AZ31 po zahřátí nad pokojovou teplotu a ukázali, že toto zvýšení lze skutečně připsat GBS.

Podobné výsledky byly získány Watanabe a kol. [51], kteří kromě toho pozorovali závislost tohoto nárůstu na velikosti zrn porovnáním výsledků vnitřního tření pro dva různé válcované plechy a pro odlitý materiál. Fan a kol. [61, 62] pozorovali velmi podobný nárůst vnitřního tření pro čistý jemnozrnný hořčík, což ukazuje, že toto zvýšení

lze opět připsat GBS. Zatímco při nižších teplotách byl pozorován výrazně menší pík vnitřního tření související s dislokačním skluzem. V této kapitole přinášíme srovnání tohoto nárůstu vnitřního tření pro extrudované vzorky AZ31 a AZ31, které byly kromě extruze zpracovány 1, 2 a 4 průchody ECAP. Hlavním cílem této práce je ukázat, že vnitřní tření (zejména v ultrazvukovém kmitočtovém rozsahu) je schopno citlivě sledovat mikrostrukturální procesy v ultrajemnozrnném AZ31 a přispět k porozumění vývoje těchto procesů.

Zkoumaným materiálem byla komerční slitina AZ31 (nominální složení Mg – 3% Al – 1% Zn). Tento materiál, původně ve stavu odlitku, byl nejprve extrudován při 350 °C s vytlačovaným poměrem 22. Následně byl zpracován ECAP prováděným při 180 °C (další podrobnosti viz [63]) po cestě B_C (otáčení vzorku o 90 ° mezi jednotlivými průchody).

Připraveny byly čtyři vzorky materiálu. Základní (0P) a po jednom (1P), dvou (2P) a čtyřech (4P) průchodech přes ECAP. Podrobné informace o vlastnostech a mikrostrukturální charakterizaci těchto materiálů lze nalézt [63, 64, 65, 66], zde je pouze stručné shrnutí. Výchozí extrudovaný materiál (0P) vykazoval bimodální distribuci velikosti zrn, současně velká zrna (průměr 50 μm) a malá zrna (průměru několika mikrometrů). Následné průchody ECAP vedly k homogenizaci mikrostruktury a celkovému zjemnění zrna. Na obr. 4.5 jsou porovnány EBSD obrazy mikrostruktur extrudovaného (0P) materiálu a materiálu po čtyřech průchodech ECAP (4P). Je jasně vidět, že bimodální struktura je potlačena v materiálu 4P.

V materiálech 1P a 2P byla stále přítomna určitá bimodální struktura ([63]), ale zároveň byla velikost zrn zmenšena. Aby se dosáhlo jednorozměrné parametrizace procesu zjemňování zrn, byla z map EBSD stanovena střední velikost zrn pro každý materiál (střední velikost zrn d). Výsledné hodnoty byly $d_{0P} = 2{,}84\ \mu m$, $d_{1P} = 1{,}11\ \mu m$, $d_{2P} = 0{,}91\ \mu m$, a $d_{4P} = 0{,}72\ \mu m$.

Z těchto materiálů byly připraveny vzorky ve formě malých pravoúhlých rovnoběžnostěnů pro měření RUS 3.1.2. Čtyři z nich (označeny 0P, 1P, 2P a 4P) byly použity pro měření vývoje vnitřního tření a smykového modulu během zahřívání z pokojové teploty na 300 °C. Čtyři vzorky materiálu 4P byly použity pro měření během teplotního cyklu, aby se prozkoumala reverzibilita pozorovaných jevů. Tyto vzorky jsou označeny $4P_{170}$; $4P_{220}$; $4P_{270}$; $4P_{310}$ podle maximální teploty příslušných tepelných cyklů. Přehled rozměrů těchto

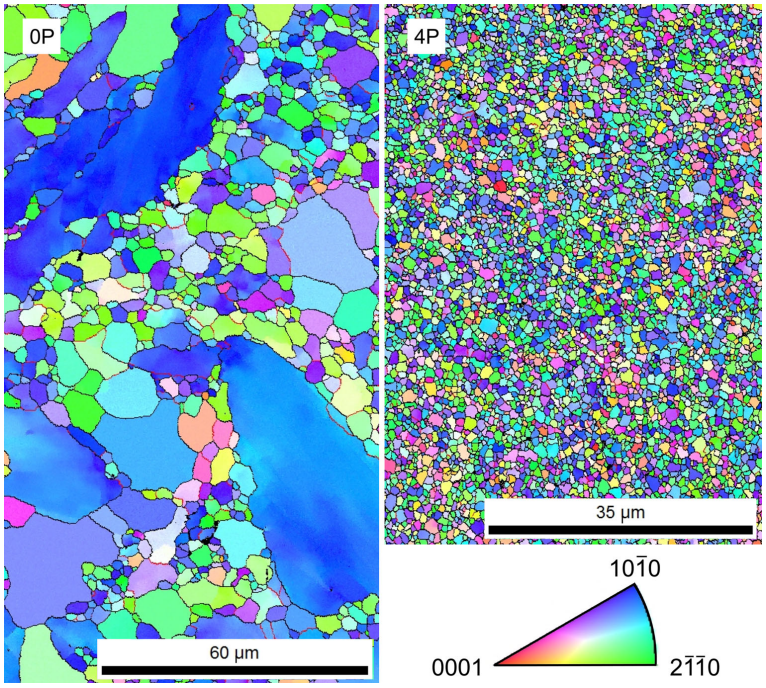

Obrázek 4.5: Orientační mapy EBSD mikrostruktur zkoumaných slitin. Vlevo: počáteční extrudovaný materiál (0P); vpravo: materiál po čtyřech průchodech ECAP (4P). Zobrazené řezy jsou kolmé na směr vytlačování [39]

vzorků a teplotních rozsahů, ve kterých byly vzorky měřeny, je uveden v tab. 4.2. Rychlosti zahřívání a chlazení pro všechny vzorky byly vždy dost malé (1 °C×min^{-1}), aby se zajistila dobrá teplotní stabilita pro každý vzorek a měřicí bod a vyhnuli jsme se vlivu možných dynamických efektů.

Před měřením do vyšších teplot, byla ke stanovení elastických konstant zkoumaných materiálů použita metoda RUS 3.1.1. Jak je ukázáno pro polykrystalickou měď [67], ECAP může vyvolat měřitelnou elastickou anizotropii, která se mění s jednotlivými průchody ECAP. Aby bylo možné zjistit, zda lze podobný účinek pozorovat také pro slitinu AZ31, byly vzorky 0P, 1P, 2P a 4P analyzovány stejným experimentálním postupem jako pro měď v [67]. Pro tato měření byla použita plně bezkontaktní sada RUS 3.1.1.

Pro každý vzorek bylo získáno více než 50 rezonančních frekvencí ve frekvenčním rozsahu 0,3–2,5 MHz; tato data byla doplněna měřením podélných ultrazvukových vln ve směrech kolmých na povrchy vzorků. Elastické konstanty každého materiálu byly poté stanoveny inverzně pomocí postupu popsaného v 2.1.3. Poté byly měřeny vývoje rezonančních spekter všech vzorků s teplotou v teplotních rozsazích uvedených v tab. 4.2.

Tabulka 4.2: Přehled měřených vzorků systémem RUS 3.1.2, PT označuje pokojovou teplotu

Vzorek	Rozměry (mm^3)	Teplotní rozsahy
0P	$1,725 \times 2,642 \times 3,454$	PT $\rightarrow$ 300 °C
1P	$1,725 \times 2,633 \times 3,457$	PT $\rightarrow$ 300 °C
2P	$1,730 \times 2,642 \times 3,458$	PT $\rightarrow$ 300 °C
4P	$1,680 \times 2,760 \times 3,354$	PT $\rightarrow$ 300 °C
$4P_{170}$	$0,575 \times 2,798 \times 3,639$	PT $\rightarrow$ 170 °C; 1h na 170 °C; 170 °C $\rightarrow$ PT
$4P_{220}$	$0,578 \times 2,911 \times 4,007$	PT $\rightarrow$ 220 °C; 1h na 220 °C; 220 °C $\rightarrow$ PT
$4P_{270}$	$0,582 \times 2,533 \times 3,741$	PT $\rightarrow$ 270 °C; 1h na 270 °C; 270 °C $\rightarrow$ PT
$4P_{310}$	$0,565 \times 2,789 \times 3,623$	PT $\rightarrow$ 310 °C; 1h na 310 °C; 310 °C $\rightarrow$ PT

Tato měření byla také prováděna bezkontaktní metodou RUS 3.1.2.

Elastické konstanty materiálů 0P, 1P, 2P a 4P při pokojové teplotě vykazovaly jen velmi malé odchylky od dokonalé elastické izotropie. Na rozdíl od polykrystalické mědi studované stejným přístupem Seiner a kol. [67], ECAP nevyvolával žádné měřitelné změny elastické anizotropie s jednotlivými průchody. Důvodem tohoto rozdílu je pravděpodobně slabá elastická anizotropie hořčíkové mřížky ve srovnání s relativně silnou elastickou anizotropií krychlové mřížky mědi. V důsledku této slabé anizotropie se změny struktury a mikrostruktury způsobené ECAP v případě AZ31 nijak neodrážejí makroskopickými elastickými vlastnostmi polykrystalického agregátu.

Výsledné elastické konstanty za pokojové teploty pro zkoumané materiály jsou uvedeny v tab. 4.3 spolu s koeficienty vnitřního tření stanovenými z nejnižších rezonančních píků pro každý vzorek. Nejvyšší hodnota je u vzorku 4P, což dobře souhlasí s předpokladem, že zjemnění zrna zvyšuje vnitřní tření vyvolané GBS.

Znázornění vývoje smykový modulů G (obr. 4.6) a vnitřních parametrů tření Q^{-1} (obr. 4.7) s ohřevem na 300 °C. Smykové moduly byly vypočteny z detekovatelných rezonančních frekvencí pro každou teplotu pomocí inverzní procedury popsané v 2.1.3, s přihlédnutím ke změnám rozměrů vzorků s teplotou způsobenou tepelnou roztažností (jako koeficient lineární expanze čistého hořčíku byl použit $\alpha = 24,8 \times 10^{-6} K^{-1}$). U všech ma-

Tabulka 4.3: Elastické konstanty zkoumaných materiálů při pokojové teplotě: Youngův modul (E), Smykový modul (G) a Vnitřní tření (Q^{-1}).

Vzorek	E (GPa)	G (GPa)	Q^{-1} (10^{-3})
0P	$44,64 \pm 0,10$	$17,22 \pm 0,06$	$0,05 \pm 0,04$
1P	$44,36 \pm 0,38$	$16,98 \pm 0,27$	$0,04 \pm 0,04$
2P	$44,30 \pm 0,30$	$17,10 \pm 0,24$	$0,08 \pm 0,04$
4P	$44,11 \pm 0,23$	$17,18 \pm 0,29$	$0,15 \pm 0,04$

teriálů vykazují smykové moduly spojitý pokles změkčení, lineární až do přibližně 200 °C a poté se od lineárního trendu mírně odchylují. Rozdíly mezi chováním jednotlivých vzorků jsou minimální, zcela v rozsahu experimentálních chyb. Pro vnitřní parametry tření Q^{-1} se získá úplně jiný obrázek.

Jak je vidět na obr. 4.7, parametry Q^{-1} se zvyšují při zvýšených teplotách o více než dva řády. Zvětšená oblast na obr. 4.7 ukazuje, že počáteční teplota zvýšení vnitřního tření je skutečně závislá na zjemnění zrna: pro 4P začíná nárůst při výrazně nižší teplotě než pro 0P. Vzorky 1P a 2P sledují stejný trend podle počtu ECAP průchodů. Skutečnost, že tato silná zvýšení vnitřního tření u všech materiálů se neodráží žádnými změnami modulů smyku (viz obr. 4.6), potvrzuje předpoklad, že pozorované chování lze dobře popsat vysokofrekvenčním limitem relaxačního tlumení.

Aby se určilo, které ze změn koeficientu vnitřního tření po zahřátí odpovídají nevratným procesům, byla na čtyři různé vzorky materiálu 4P použita sada tepelných cyklů (viz tab. 4.2). Při nejvyšší teplotě pro každý cyklus byl vzorek vždy žíhán po dobu 1h s cílem zjistit možné účinky v časovém měřítku. Výsledné křivky $Q^{-1}(T)$ jsou znázorněny na obr. 4.8. Je vidět, že pro cyklus s maximální teplotou 170 °C je chování vnitřního tření reverzibilní; rozdíly mezi křivkami zahřívání a chlazení jsou pod úrovní experimentální chyby. Rovněž vývoj Q^{-1} v důsledku 1h žíhání při 170 °C je zanedbatelný, což dokazuje, že mikrostruktura odpovědná za vnitřní tření Q^{-1} je v tomto teplotním rozmezí plně stabilní.

V ostrém kontrastu indukuje žíhání při 220 °C měřitelné snížení vnitřního tření a křivka $Q^{-1}(T)$ pro $4P_{220}$ vykazuje širokou hysterezní smyčku. Je zřejmé, že při této teplotě

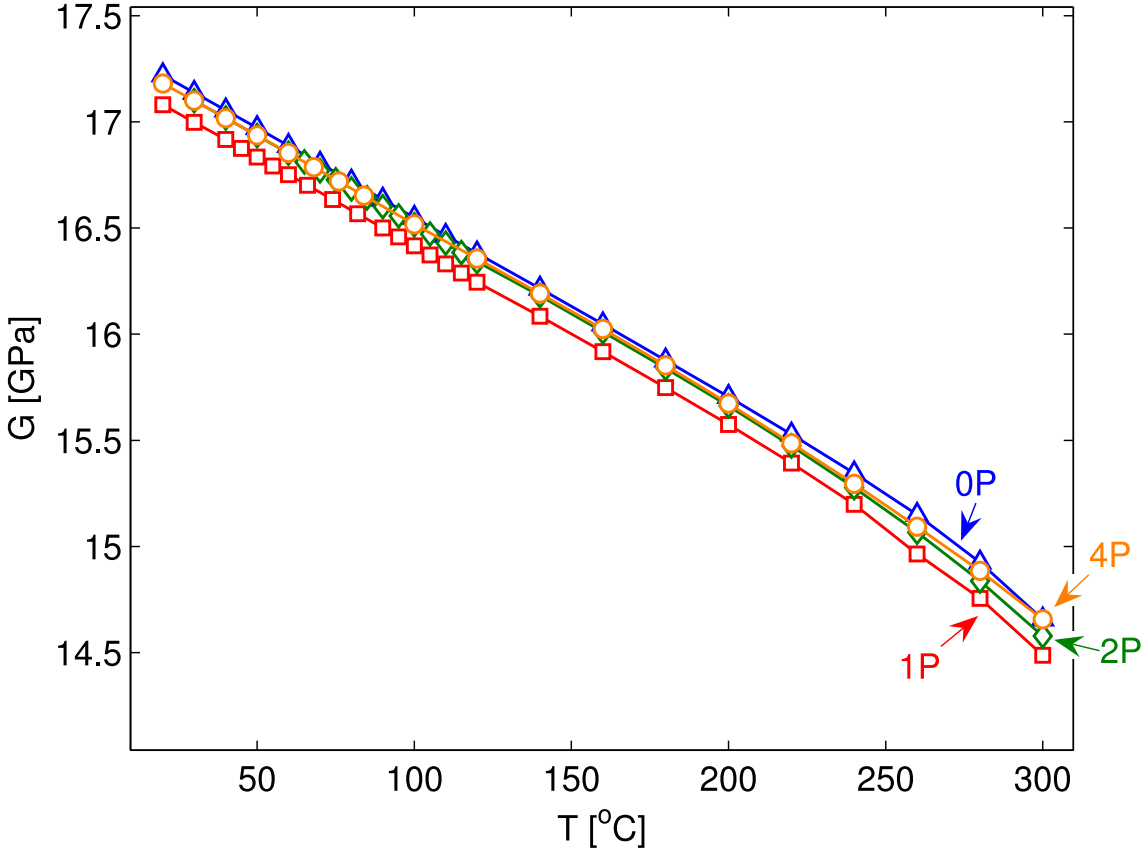

Obrázek 4.6: Vývoj smykových modulů (G) AZ31 materiálů 0P – 4P během žíhání [39]

materiál podléhá nevratným změnám. Hysterezní smyčka se uzavře při přibližně 250 °C, a tak žíhání po dobu 1h při teplotách 270 °C a 310 °C (vzorky $4P_{270}$, respektive $4P_{310}$) nevede k časově závislým změnám vnitřního tření.

Při teplotě nad 250 °C je chování materiálu opět nehysterézní. Protože teplotní rozmezí 200 °C - 250 °C dobře odpovídá rozsahu rekrystalizace struktury ECAPem stanovené z analýz vzorků [65], můžeme dojít k závěru, že pozorovaná hystereze je způsobena rekrystalizací.

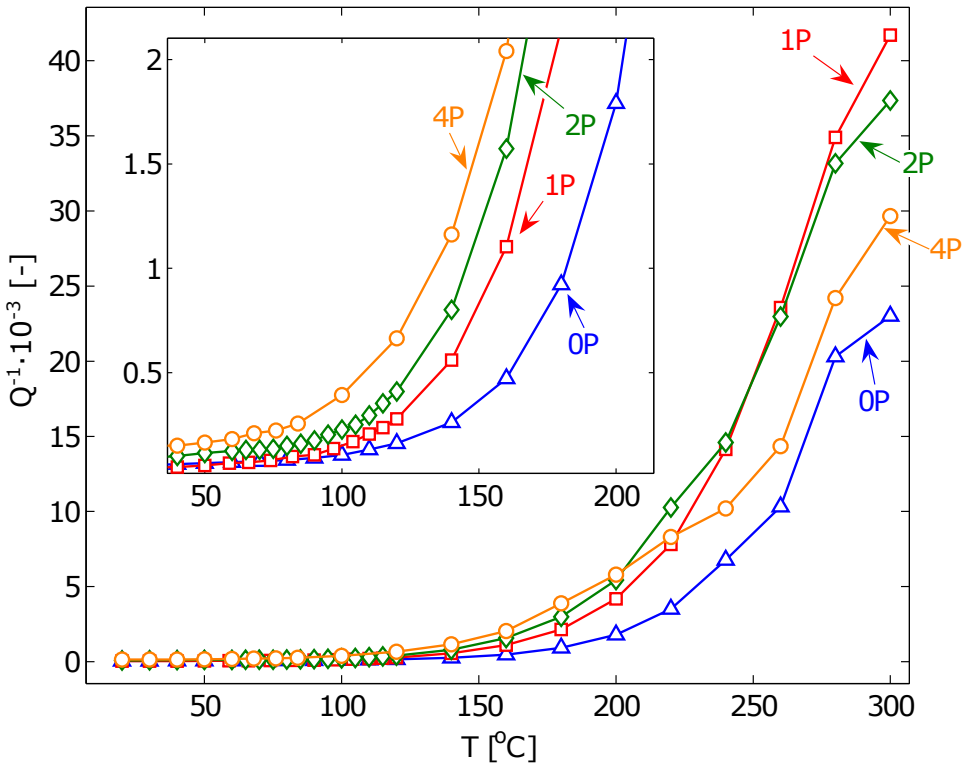

Obrázek 4.7: Vývoj parametrů vnitřního tření Q^{-1} AZ31 materiálů 0P – 4P během žíhání; zvětšená oblast ukazuje teplotní oblast, ve které se začíná Q^{-1} zvyšovat. [39]

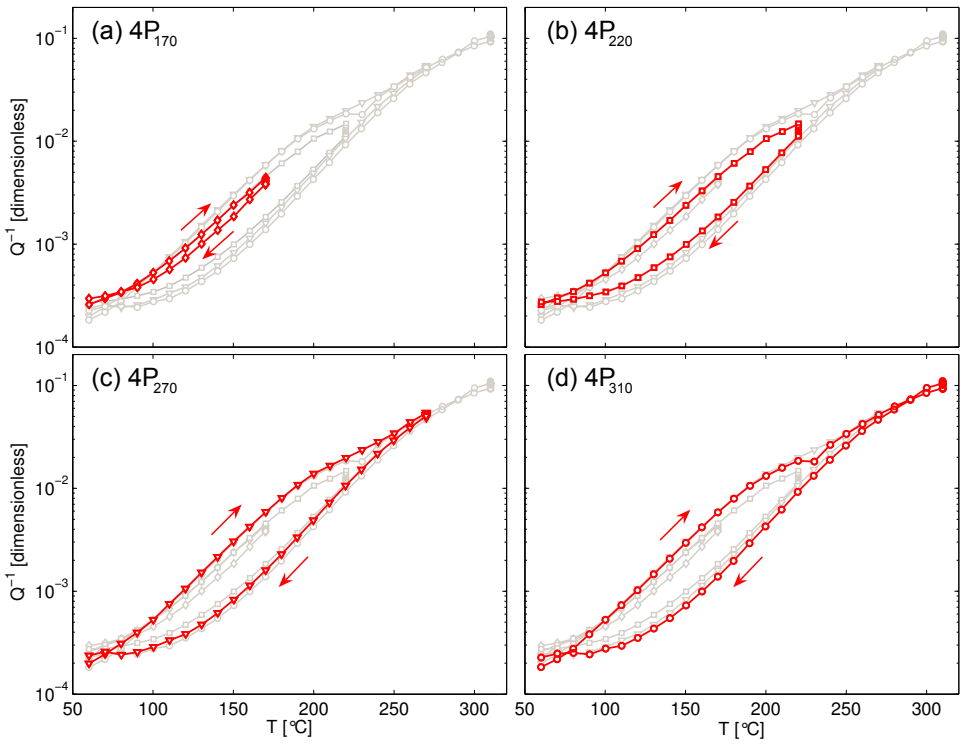

Obrázek 4.8: Vývoj parametru vnitřního tření Q^{-1} AZ31 materiálu 4P (vzorky $4P_{170}$; $4P_{220}$; $4P_{270}$ a $4P_{310}$) s tepelnými cykly. Každá dílčí část ukazuje jeden tepelný cyklus pro jeden vzorek s danou maximální teplotou, při které byl vzorek vždy žíhán po dobu 1 hodiny. Pro srovnání jsou křivky pro zbývající tři vzorky zobrazeny na každém grafu světle šedou barvou. [39]

4.3 Vývoj elastických konstant ve slitině s tvarovou pamětí Fe-Pd pod zatížením

Tato kapitola se bude zabývat studií elastické anizotropie slitiny s tvarovou pamětí Fe-Pd pod zatížením až do $4,3\%$ pomocí ultrazvukových metod. Získá se vývoj úplného tetragonálního tenzoru elastických konstant s přepětím v rozmezí 0 - 200 MPa [68].

Neuspořádané slitiny Fe-Pd s obsahem Pd přibližně 30 % a částečně uspořádané slitiny Fe_3Pd vykazují specifické martenzitické přechody podobné druhému řádu s velmi malou diskontinuitou mřížkových parametrů při teplotě přechodu [69, 70, 71, 72]. V superelastickém režimu, tj. při mechanickém stlačování těsně nad teplotou přechodu, vykazují tyto slitiny reverzibilní, nehysterézní, elastické chování až do 4-6 % deformace, zejména při kompresích podél hlavních $\{100\}$ os. Velikost této napětím indukované tetragonální distorze je zcela srovnatelná s Bainovou distorzí mezi krychlovými (fcc) a tetragonálními (fct) fázemi dosaženými během teplotně indukovaných přechodů pro stejné slitiny. Jako takové se tyto slitiny jeví jako optimální kandidáti pro studium vývoje režimů s měkkými fonony a nestability mřížky. Pozorujeme spojitý vývoj měkkých smykových modulů a souvisejících nízkofrekvenčních limitů fononových režimů během zatěžování a odlehčování a diskutujeme, jak se tento vývoj vztahuje ke strukturní změně materiálu.

Použitým vzorkem byl monokrystal ze slitiny s nominálním složením $Fe - 31,2\%Pd$ vypěstovaného metodou *floating zone method* (další podrobnosti viz odkaz [70]). Monokrystal byl tepelně zpracován při 1373 K po dobu 24 hodin, načež následovalo ponoření do ledové vody. Teplota martenzitického přechodu této slitiny byla stanovena měřením magnetické susceptibility jako $252K$, tj. dostatečně blízko pod pokojovou teplotou (298 K), aby se očekávalo výše uvedené elastické chování. Vzorek geometrie načrtnutý na obr. 4.9a byl připraven z tohoto monokrystalu. Rozměry vzorku byly $4,84 \times 4.07 \times 2,78\ mm^3$, nejdelší hrana byla orientována přibližně podél hlavního směru (001). Na vzorku byly připraveny dva velké boční povrchy orientací přibližně (010) a (340) a vyleštěny; přesná krystalografická orientace byla stanovena Laueho metodou.

Křivka napětí-deformace (obr. 4.9c) pro zkoumaný vzorek byla získána kompresí podél (001)-orientované hrany pomocí elektromechanického testovacího stroje TiraTest 2300 (rozlišení síly 0,1 N, rozlišení deformace 0.1 μm pomocí snímacích senzorů LVDT). Současně

byla měřena expanze materiálu ve směru kolmém na zatížení (zejména (340)) pomocí kontaktních indukčních měničů s rozlišením 0.1 μm, upnutých proti bočním stranám hranolové části vzorku.

Měření napětí-deformace bylo provedeno při pokojové teplotě (298 K, řízeno s přesností $\pm$ 0,25 K) a pro napětí do 210 MPa. Tento limit byl zvolen tak, aby zůstal bezpečně pod kritickým napětím pro ireverzibilní plastickou deformaci vzorku, která měla být 285 MPa [70]).

Měření povrchových akustických vln (obr. 4.9b) bylo provedeno na experimentálním zařízení popsaným v této práci 3.2.3.

Křivka napětí-deformace vzorku při stlačení až do 210 MPa je znázorněno na obr. 4.10. Maximální dosažený axiální tlak byl $4,3\%$. Jak je vidět na obr. 4.10a, křivka napětí-deformace byla přibližně lineární s inflexním bodem při $-\epsilon_{33} = 1,8\ \%(cca80\ MPa)$ a velmi úzkou hysterezí. Z prodloužení vzorku ve směru kolmém na zatížení bylo vypočteno odpovídající maximální tetragonální distorze jako $c/a = 0,94$, což je výrazně silnější než transformační Bainovo napětí $c/a = 0,98$ pozorovaný pro teplotně indukovaný fct martenzit Fe-30Pd v blízkosti teploty přechodu [73]. Obr. 4.10b ukazuje odpovídající vývoj relativní změny objemu; charakter závislosti $\delta V(-\epsilon_{33})$ byl velmi podobný jako u křivky napětí-deformace, s rychlostí změny objemu minimální na $-\epsilon_{33} = 1,5$ %. Maximální změna objemu 0,54 % při axiálním namáhání 4,3 % dává efektivní Poissonův poměr 0,453, což naznačuje téměř dokonalé zachování objemu během zatěžování.

Měřené závislosti napětí SAW rychlostí jsou znázorněny na obr. 4.11 . Podobně jako křivka napětí-deformace vykazovaly rychlosti SAW monotónní trendy s téměř nulovou hysterezí, což potvrzuje, že k tetragonalizaci materiálu došlo postupně, bez vytváření ostrých rozhraní nebo jakýchkoli jiných náhlých nebo nespojitých rysů. Na obou použitých volných površích byla pozorována nejslabší závislost rychlosti SAW na předpětí pro šíření ve směru rovnoběžném se směrem zatížení, zatímco tato závislost byla nejsilnější ve směru kolmém ke směru zatížení. Také rychlosti qL (nejsou zobrazeny) vykazovaly nehysterézní, monotónní nárůst se zvyšující se předpětí.

Jak je vidět na obr. 4.11, pro všechny úrovně mechanického napětí a pro všechny směry šíření se rychlosti získané během zatěžování lišily o méně než 0,07 $mm \times \mu s^{-1}$ od rychlostí získaných při odlehčování, tj. rozdíl byl vždy srovnatelný s experimentální chybou. Proto

se předpokládalo, že také vývoj elastických konstant s mechanickým napětím je nehysterézní, a proto byla pro výpočet elastických konstant použita jedna hodnota rychlosti pro každý směr šíření a každý režim šíření při dané úrovni mechanického napětí (vypočteno jako průměr ze zatěžování a odlehčování) byl použit pro výpočet elastických konstant. Tímto přístupem byl vývoj tenzoru pružnosti dosažen v rozmezí $0MPa - 200MPa$ s krokem $25MPa$. Úplný vývoj elastického tenzoru s mechanickým napětím je znázorněn na obr. 4.12.

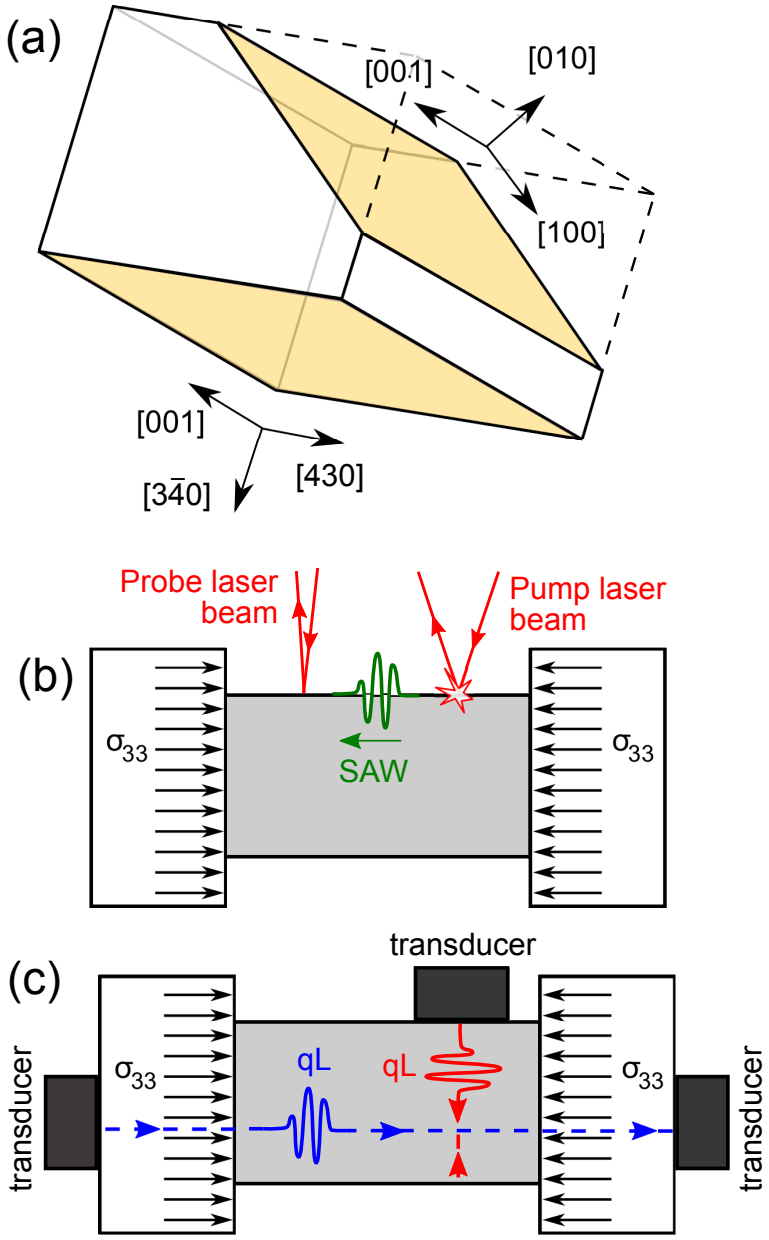

Obrázek 4.9: (a) geometrie vzorku; (b) experimentální uspořádání pro měření SAW; (c) experimentální uspořádání pro měření šíření akustické vlny v bulku [68]

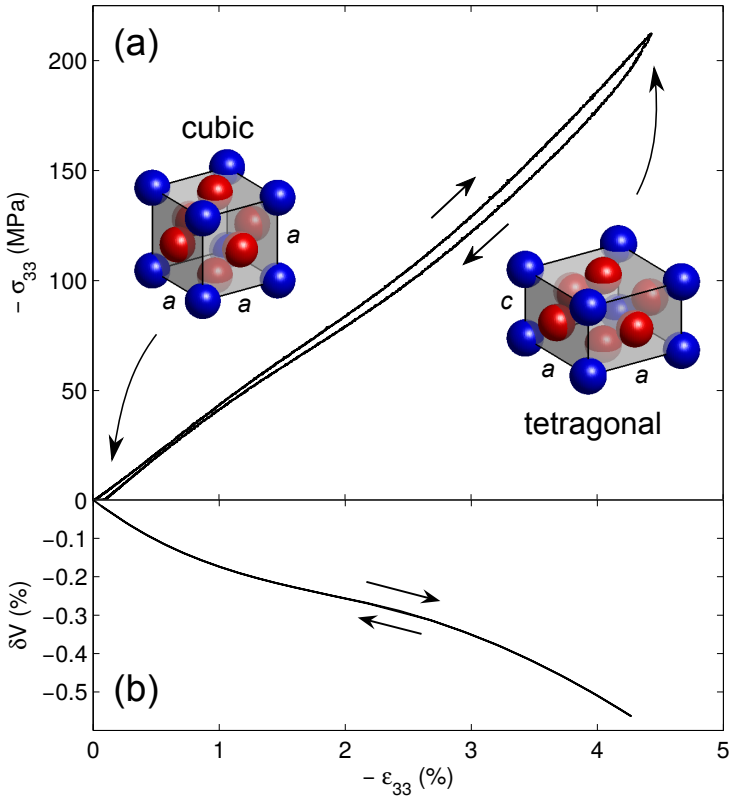

Obrázek 4.10: (a) křivka napětí-deformace zkoumaného monokrystalu Fe-Pd při pokojové teplotě; (b) odpovídající relativní změna objemu stanovená z roztažení vzorku ve směru kolmém na zatížení. [68]

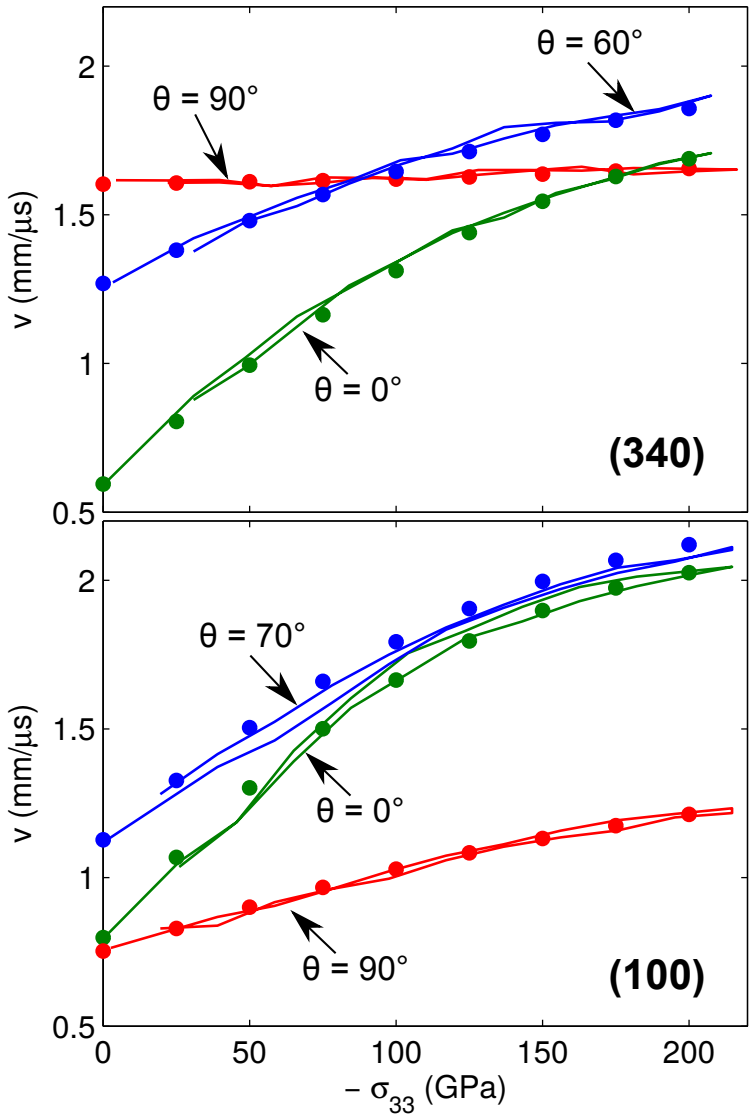

Obrázek 4.11: Ultrazvukové rychlosti SAW měřené na (010) a (340); θ znamená úhel mezi směrem komprese a směrem šíření SAW. [68]

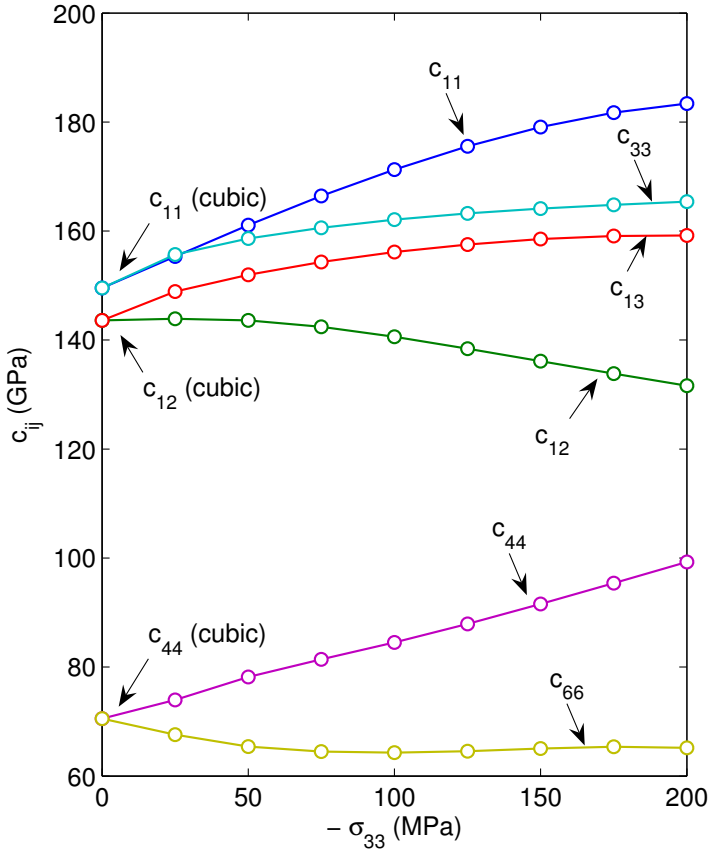

Obrázek 4.12: Vývoj všech nezávislých tetragonálních elastických koeficientů s mechanickým napětím. [68]

4.4 Charakterizace elasticity a fázové transformovace slitiny NiTi s tvarovou pamětí *in situ*

Tato kapitola obsahuje studii vzorku slitiny NiTi s polykrystalickou tvarovou pamětí pod kompresí (SMA) až 5 %, měřenou pomocí laserové ultrazvukové metodiky popsané v kapitole 3.2.3. Vývoj rychlosti šíření povrchové akustické vlny se měří *in situ* během mechanického zatěžování. Inverzní metoda založená na přístupu Ritz – Rayleigh se potom používá k získání vývoje elastických vlastností vzorku, tato metoda byla popsána 2.2. Tento proces umožňuje analýzu vývoje indukované transformace z austenitické na martenzitickou fázi, během mechanického zatěžování, s možností popsat několik fází takové transformace. Mechanické zatěžování způsobuje silnou anizotropii polykrystalického vzorku a postupný přechod na martenzit. [74, 75, 22]

Elastické vlastnosti monokrystalických slitin s tvarovou pamětí jsou obvykle silně anizotropní [76, 77, 78]. V blízkosti teploty přechodu je krystalová mřížka nestabilní kvůli změkčení fononu [79, 80], což ještě více zvyšuje anizotropii. V této kapitole je ukázáno, že makroskopické moduly polykrystalických SMA mohou být za určitých okolností silně anizotropní - v tomto případě po reorientaci martenzitické struktury vyvolané jednoosou kompresí. Je známo, že tyto varianty martenzitu uvnitř jednotlivých zrn, které jsou orientovány v ose zatěžování, rostou rychleji než ostatní [81, 82, 83]. Měření *in situ* nabízí mnohem podrobnější pohled na chování materiálů během mechanického zatěžování s potenciálem přímo popsat probíhající procesy. Elastické konstanty polykrystalického SMA závisí na monokrystalických elastických koeficientech jednotlivých fází, objemových zlomcích těchto fází, krystalografické struktuře austenitu, martenzitické mikrostruktury a vzájemné morfologie austenitu a martenzitu [84].

Studovaný vzorek byl vyroben z komerčně dostupného NiTi (50, 5 % Ni a 49, 5 % Ti). Velikost vzorku byla 5 $times 15 \times 50\ mm^3$, jeden povrch vzorku byl vyleštěn. Při pokojové teplotě je materiál ve stavu austenitu a R-fáze. Transformační teplota je uvedena v [85]. Pro měření rychlosti povrchových akustických vln (SAW) byla použita zrcadlová plocha.

Křivka napětí-deformace zkoumaného vzorku při pokojové teplotě je znázorněna na obr. 4.13. Měření bylo provedeno v 16 různých vzdálenostech mezi excitačním a detekčním místem pro získání rychlosti SAW v konkrétním směru. Toto měření bylo provedeno v 5

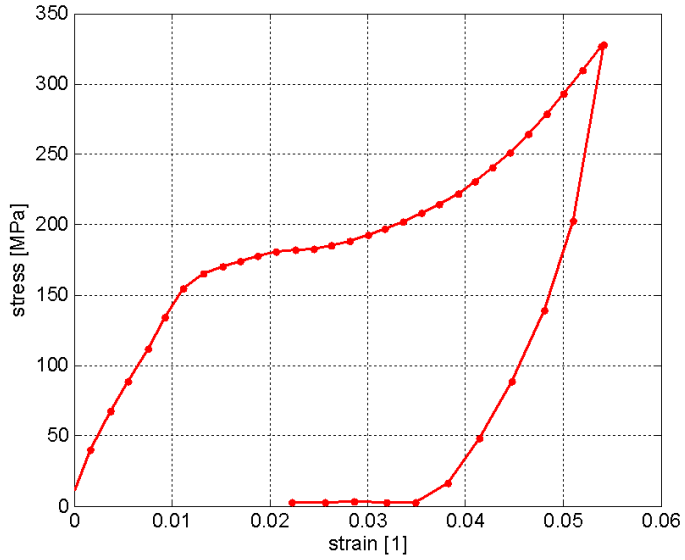

Obrázek 4.13: Křivka napětí-deformace během měření [22]

úhlech mezi šířící se vlnou a osou zatížení ve více než 50 bodech mechanického napětí během zatěžování. Výsledný vývoj rychlostí v různých směrech během zatěžování je znázorněn na obr. 4.14.

Z těchto rychlostí povrchových vln byl pomocí 2.2 vypočten vývoj elastických konstant, zobrazených na obr. 4.15

Křivka napětí-deformace obr. 4.13 ukazuje charakter typický pro paměťové slitiny pod kompresí [86]. Ukazuje počáteční téměř lineární odezvu, pak plato martenzitického přechodu mezi přibližně $1,3$ % a $3,5$ % a následující zatížení martenzitu. Měřené rychlosti SAW (obr. 4.14) a odpovídající smykové moduly (obr. 4.15) dokumentují průběh procesů v materiálu při zatěžování.

V počáteční fázi zatěžování až do začátku martenzitického fázového přechodu nad $1,3$ % vzniká překvapivě silná anizotropie vzorku. S maximem na začátku fázového přechodu dosahuje anizotropie poměr 1,35 mezi moduly pružnosti ve smyku. Předpokládá se, že je to způsobeno indukcí reorientace trigonální R-fáze a bylo ověřeno, že tento proces je plně reverzibilní a lze jej pozorovat pouze během měření *in situ* při mechanickém zatěžování.

Druhá část ukazuje vývoj elastických konstant během mechanickým tlakem indukované transformace martenzitické fáze. Materiál ztuhne ve všech směrech, protože elas-

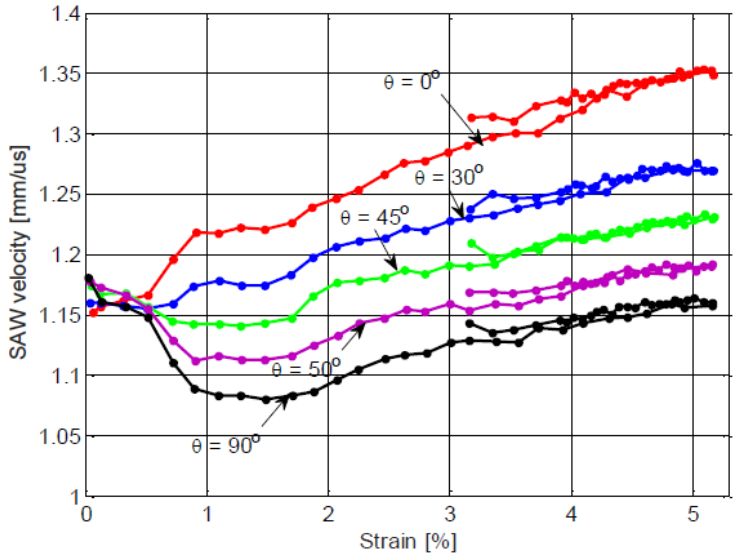

Obrázek 4.14: Experimentálně získané rychlosti SAW v různých úhlech s ohledem na zatížení. [22]

tické konstanty martenzitu jsou vyšší než u R-fáze. Zajímavý je však charakter průběhu - když se c_{44} zvyšuje lineárně, vývoj c_{66} vykazuje určité zakřivení. Z této skutečnosti lze předpokládat, že zatímco na makroskopické úrovni probíhá martenzitický přechod při kompresi homogenně, je heterogenní na úrovni mikrostruktury. Data získaná použitou metodikou jsou bohužel nedostačující pro úplné pochopení heterogenity a samotného procesu, protože většinou obsahují informace o smykovém chování, a proto musí být doprovázena doplňkovými měřeními podélné vlny.

Třetí a poslední část křivky napětí-deformace ukazuje konečné zatížení dominantně martenzitického vzorku. Bylo pozorováno, že elastické koeficienty martenzitu závisí na zatížení plně reverzibilním způsobem. Po odlehčení si orientovaný martenzit zachovává svoji anizotropní elasticitu, což je zcela v souladu s výsledky zjištěnými měřením *ex situ* v [75].

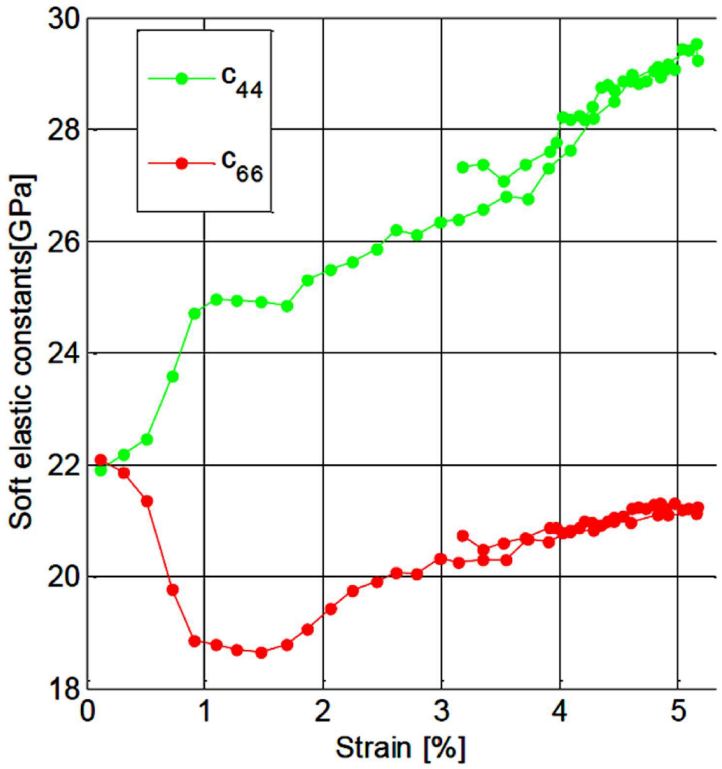

Obrázek 4.15: Výsledné smykové elastické moduly získané inverzní metodou. [74]

5 Závěr

Tato práce si kladla za cíl popsat měřící systémy, na jejichž vývoji se autor podíle. V rámci tohoto popisu byl vždy uveden návrh, vlastní realizace a popis řízení, včetně použitých algoritmů. Díky vyvinutým řídícím a ovládacím mechanismům je nyní možné tyto aparatury provozovat v požadovaných režimech s různou úrovní nastavení. Ovládání těchto systému zvládnou pracovníci oddělení i studenti po krátkém zaškolení. Ke každé měřící aparatuře je k dispozici i podrobný návod, který dotyčnému operátorovi pomůže se základním nastavením a ovládáním.

Tyto aparatury je možné řídit a hlavně kontrolovat pomocí vzdáleného přístupu, což je velmi výhodné zejména u dlouhotrvajících měření (v řádu dní či týdnů). Během těchto dlouhotrvajících měření tedy není nezbytně nutné, aby operátor byl fyzicky přítomen na pracovišti.

V jednotlivých kapitolách (3.1 a 3.2) byly detailně popsány jednotlivé měřící systémy a v kapitolách 4 byly uvedeny příklady aplikací těchto systémů pro různé problémy z oblasti materiálového výzkum. Řada výsledků byla již publikována s autorským podílem autora práce, a další jsou k publikaci aktuálně připravovány.

5.1 Hlavní původní vědecké přínosy disertační práce:

- V rámci této práce jsem navrhnul, postavil, zprovoznil, naprogramoval a otestoval všechny vyvíjené systémy, uvedené v kapitole 3.
- V kapitole 4 jsem uvedl několik příkladů měření, která jsem na těchto systémech provedl
- V příloze C jsou uvedeny publikované výsledky měření, které jsem těmito systémy měřil a podílel se na vyhodnocení.

5.2 Další směr výzkumu

- Vývoj bezkontaktního měření materiálu pod mechanickém zatěžování se změnou teploty a možností měření plné anizotropie.

- Návrh a realizace skenovacího akustického mikroskopu s možností měření distribuce energie v periodických materiálech.
- Vývoj měřicího systému založeného na bezkontaktním měření materiálů ve stacionárním magnetickém poli se změnou teploty.
- Na realizovaných systémech se počítá s dalšími měřeními, která přispějí k lepšímu pochopení dějů vnitřních struktur materiálů.

Seznam obrázků

Seznam tabulek

Reference

[1] A. Migliori and J. Sarrao, *Resonant Ultrasound Spectroscopy : Applications to Physics, Material Measurements and Nondestructive Evaluation.* John Wiley and Sons Ltd, New York, 1997.

[2] A. Migliori, J. Sarrao, W. Visscher, T. Bell, M. Lei, Z. Fisk, and G. Leisure, "Resonant ultrasound spectroscopy techniques for measurements of the elastic moduli of solids," *Physica B*, vol. 183(1-2), pp. 1–24, 1993.

[3] L. Bicanová, "Elastické vlastnosti austenitu a 2h martenzitu slitiny cualni v blízkosti teplot fázových přechodů.," diplomová práce, České vysoké učení technické v Praze, 2007.

[4] M. Landa, H. Seiner, P. Sedlak, L. Bicanova, J. Zidek, and L. Heller, *Resonant ultrasound spectroscopy close to its applicability limits*, vol. 268. Michael Everett and Louis Pedroza, Nova Science Publishers, 2009.

[5] H. Seiner, L. Bodnárová, P. Sedlak, M. Janeček, O. Srba, R. Král, and M. Landa, "Application of ultrasonic methods to determine elastic anisotropy of polycrystalline copper processed by equal-channel angular pressing," vol. 58, pp. 235–247, 2010.

[6] M. Růžek, P. Sedlák, H. Seiner, A. Kruisová, and M. Landa, "Linearized forward and inverse problems of the resonant ultrasound spectroscopy for the evaluation of thin surface layers.," vol. 28, pp. 3426–3437, 2010.

[7] L. Bodnárová, *Vyšetřování elastických vlastností pokročilých materiál multrazvukovými metodami.* Disertační práce, České vysoké učení technické v Praze, 2014.

[8] P. Sedmák, "Měření elasticity a vnitřního tření žárových nástřiků pomocí bezkontaktní rezonanční ultrazvukové spektroskopie.," diplomová práce, České vysoké učení technické v Praze, 2012.

[9] M. Thomasová, "Vývoj elastických konstant polykrystalů slitin s tvarovou pamětí při napěťově indukované reorientaci.," diplomová práce, České vysoké učení technické v Praze, 2016.

[10] P. Sedlak, H. Seiner, M. Landa, V. Novak, P. Sittner, and L. Manosa, "Elastic constants of bcc austenite and 2h orthorhombic martensite in cualni shape memory alloy.," vol. 53, p. 3643–3661, 2005.

[11] D. Royer, S. N. Lyle, and E. Dieulesaint, *Elastic Waves in Solids II: Generation, Acousto-optic Interaction, Applications*. Springer, Berlin Heidelberg, 1999.

[12] B. Pouet, *Modelisation physique par ultrasons laser. Application a la prospection sismique*. 1991.

[13] L. R. F. Rose, "Point-source representation for laser-generated ultrasound.," vol. 75, pp. 723–732, 1984.

[14] J. F. Ready, *Efect of High Power Radiation*. Academic Press, New York,, 1971.

[15] R. J. Smith, W. Li, J. Coulson, M. Clark, M. G. Somekh, and et al., "Spatially resolved acoustic spectroscopy for rapid imaging of material microstructure and grain orientation.," *Measurement Science and Technology*, vol. 25(5), 2014.

[16] A. A. Maznev, K. A. Nelson, and J. A. Rogers, "Optical heterodyne detection of laser-induced gratings.," *Optics Letters*, vol. 23(16), pp. 1319–1321, 1998.

[17] J. Sermeus, R. Sinha, K. Vanstreels, P. M. Vereecken, and C. Glorieux, "Determination of elastic properties of a mno2 coating by surface acoustic wave velocity dispersion analysis.," *Journal of Applied Physics*, vol. 116(2), 2014.

[18] W. Li, *PhD. thesis*. 2012.

[19] S. D. Sharpies, R. A. Light, S. O. Achamfuo-Yeboah, M. Clark, and M. G. Somekh, "The sked: Speckle knife edge detector," *Journal of Physics: Conference Series*, vol. 520(1), 2014.

[20] J. M. Rouvaen, E. Bridoux, N. Gremillet, R. Torguet, and P. Hartemann, "No title.," *Electronics Letters*, vol. 10(15), p. 297, 1974.

[21] T. Kwaaitaal, "Contribution to the interferometric measurement of sub-angstrom vibrations.," *Rev. Sci. Instr.*, vol. 45, pp. 39–41, 1974.

[22] M. Sevcik, T. Grabec, P. Stoklasova, M. Janovska, K. Zoubkova, P. Sedlak, H. Seiner, and M. Landa, "Non-contact characterization of acoustoelastic parameters of advanced materials by laser-ultrasound.," vol. 134(3), pp. 807–810, 2018.

[23] J. Nejezchlebová, H. Seiner, M. Sevcik, M. Landa, and M. Karlik, "Ultrasonic detection of ductile-to-brittle transitions in free-cutting aluminum alloys.," vol. 69, pp. 40–47, 2015.

[24] H. K. Christeson, "Confinement effects on freezing and melting.," vol. 13, pp. 95–133, 2001.

[25] M. Alcoutlabi and G. B. McKenna, "Effects of confinement on material behaviour at the nanometre size scale.," vol. 17, pp. 461–524, 2005.

[26] E. V. Charnaya, "Acoustic studies of phase transitions in crystals and nanocomposites.," vol. 54, pp. 802–813, 2008.

[27] B. F. Borisov, E. V. Chrnaya, W. D. Hoffman, D. Michel, A. V. Sshelypin, and Y. A. Kumzerov, "Nuclear magnetic resonance and acoustic investigations of the melting-freezing phase transition of gallium in a porous glass.," vol. 9, pp. 3377–3386, 1997.

[28] E. V. Charnaya, P. G. Plotnikov, D. Michel, C. Tien, B. F. Borisov, I. G. Sorina, and E. I. Martynova, "Acoustic studies of melting and freezing for mercury embedded into vycor glass.," vol. 299, pp. 56–63, 2001.

[29] B. F. Borisov, E. V. Charnaya, P. G. Plotnikov, W. D. Hoffman, D. Michel, Y. A. Kumzerov, C. Tien, and C. S. Wur, "Solidifcation and melting of mercury in a porous glass as studied by nmr and acoustic techniques.," vol. 58, pp. 5329–5335, 1998.

[30] A. L. Pirozerskii, E. V. Charnaya, E. N. Latysheva, A. I. Nedbai, Y. A. Kumzerov, and A. S. Bugaev, "Acoustic studies of melting and crystalization of indium-gallium alloy in porous glass.," vol. 57, pp. 637–641, 2011.

[31] B. F. Borisov, E. V. Charnaya, Y. A. Kumzerov, A. K. Radzhabov, and A. V. Shelyapin, "Phase transitions for gallium microparticles in a porous glass.," vol. 92, pp. 531–533, 1994.

[32] O. Wouters and J. M. D. Hosson, "Lead induced intergranular fracture in aluminum alloy aa6262," vol. 361, pp. 331–337, 2003.

[33] M. Karlík, J. Faltus, J. Nejezchlebová, P. Haušild, and P. Harcuba, "Characterisation of al-cu and al-mg-si free-cutting alloys," vol. 794, pp. 1181–1186, 2014.

[34] T. Miyagi and H. Koizumi, "Ultrasonic attenuation of polycrystalline aluminum wetted with liquid gallium," vol. 442, pp. 184–186, 2006.

[35] E. M. Elgallad, F. H. Samuel, A. M. Samuel, and H. W. Doty, "Machinability aspects of new al-cu alloys intended for automotive castings," vol. 210, pp. 1754–1766, 2010.

[36] R. L. Smith and W. N. Reynolds, "The correlation of ultrasonic-attenuation, microstructure and ductile to brittle transition-temperature in very low-carbon steels," vol. 17, pp. 1420–1426, 1982.

[37] B. K. Kardashev, A. S. Nefagin, G. N. Ermolaev, M. V. Leont'eva-Smirnova, M. M. Potapenko, and V. A. Chernov, "Internal friction and brittle-ductile transition in structural materials," vol. 32, pp. 799–801, 2006.

[38] G. Vertesy, I. Tomas, S. Takahashi, S. Kobayashi, Y. Kamada, and H. Kikuchi, "Inspection of steel degradation by magnetic adaptive testing," vol. 41, pp. 252–257, 2008.

[39] M. Koller, P. Sedlak, H. Seiner, M. Sevcik, M. Landa, J. Straska, and M. Janecek, "An ultrasonic internal friction study of ultrafine-grained az31 magnesium alloy.," vol. 50, p. 808–818, 2015.

[40] R. Valiev, R. Ismalgaliev, and I. Alexandrov, "Bulk nanostructured materials from severe plastic deformation.," vol. 45, p. 103–189, 2000.

[41] A. Yamashita, Z. Horita, and T. Langdon, "Improving the mechanical properties of magnesium and a magnesium alloy through severe plastic deformation.," vol. 300, p. 142–147, 2001.

[42] S. Kang, Y. Lee, and J. Lee, "Effect of grain refinement of magnesium alloy az31 by severe plastic deformation on material characteristics.," vol. 201, p. 436–440, 2008.

[43] T. Mukai, M. Yamanoi, H. Watanabe, and K. Higashi, "Ductility enhancement in az31 magnesium alloy by controlling its grain structure.," vol. 45, p. 89–94, 2001.

[44] R. Valiev and T. Langdon, "Principles of equal-channel angular pressing as a processing tool for grain refinement.," vol. 51, p. 881–981, 2006.

[45] J. Koike, R. Ohyama, T. Kobayashi, M. Suzuki, and K. Maruyama, "Grain-boundary sliding in az31 magnesium alloys at room temperature to 523 k.," vol. 44, p. 445–451, 2003.

[46] J. Tan and M. Tan, "Superplasticity and grain boundary sliding characteristics in two stage deformation of mg3al1zn alloy sheet.," vol. 339, p. 81–89, 2003.

[47] R. Panicker, A. Chokshi, R. Mishra, R. Verma, and P. Krajewski, "Microstructural evolution and grain boundary sliding in a superplastic magnesium az31 alloy.," vol. 57, p. 3683–3693, 2009.

[48] A. Bussiba, A. B. Artzy, A. Shtechman, S. Ifergan, and M. Kupiec, "Grain refinement of az31 and zk60 mg alloys towards superplasticity studies.," vol. 302, p. 56–62, 2001.

[49] J. Koike, "Enhanced deformation mechanisms by anisotropic plasticity in polycrystalline mg alloys at room temperature.," vol. 36, p. 1689–1696, 2005.

[50] J. Koike, T. Kobayashi, T. Mukai, H. Watanabe, M. Suzuki, K. Maruayama, and K. Higashi, "The activity of non-basal slip systems and dynamic recovery at room temperature in fine-grained az31b magnesium alloys.," vol. 51, p. 2055–2065, 2003.

[51] H. Watanabe, T. Mukai, M. Sugioka, and K. Ishikawa, "Elastic and damping properties from room temperature to 673 k in an az31 magnesium.," vol. 51, p. 291–295, 2004.

[52] D. Mosher and R. Raj, "Use of the internal friction technique to measure rates of grain boundary sliding.," vol. 22, p. 1469–1474, 1974.

[53] G. Pezzotti, H. Kleebe, and K. Ota, "Grain-boundary viscosity of polycrystalline silicon carbides.," vol. 81(12), p. 3293–3299, 1998.

[54] H. Watanabe, A. Owashi, T. Uesugi, Y. Takigawa, and K. Higashi, "Grain boundary relaxation in fine-grained magnesium solid solutions.," vol. 91, p. 4158–4171, 2011.

[55] A. Granato and K. Lucke, "Theory of mechanical damping due to dislocations.," vol. 27, p. 789–805, 1956.

[56] Z. Zhang, X. Zeng, and W. Ding, "The influence of heat treatment on damping response of az91d magnesium alloy.," vol. 392, p. 150–155, 2005.

[57] W. Riehemann and F. A. El-Al, "Influence of ageing on the internal friction of magnesium.," vol. 310, p. 127–130, 2000.

[58] M. No, A. Oleaga, and C. Esnouf, "Internal friction at medium temperatures in high purity magnesium.," vol. 120, p. 419–427, 1990.

[59] A. Nowick and B. Berry, *Anelastic relaxation in crystalline solids.* Academic Press, New York, 1972.

[60] T. Ivleva, J. Goken, I. Golovin, Z. Zuberova, M. Maikranz-Valentin, and K. Steinhoff, "Damping in az31 ecap-processed alloy.," vol. 137, p. 181–188, 2008.

[61] G. Fan, M. Zheng, X. Hu, C. Xu, K. Wu, and I. Golovin, "Effect of heat treatment on internal friction in ecap processed commercial pure mg.," vol. 549, p. 38–45, 2013.

[62] G. Fan, M. Zheng, X. Hu, C. Xu, K. Wu, and I. Golovin, "Improved mechanical property and internal friction of pure mg processed by ecap.," vol. 556, p. 588–594, 2012.

[63] M. Janeček, S. Yi, R. Král, J. Vrátná, and K. Kainer, "Texture and microstructure evolution in ultrafine-grained az31 processed by ex-ecap.," vol. 45, p. 4665–4671, 2010.

[64] M. Janeček, J. Čížek, J. Gubicza, and J. Vrátná, "Microstructure and dislocation density evolutions in mgalzn alloy processed by severe plastic deformation.," vol. 47, p. 7860–7869, 2012.

[65] J. Stráská, M. Janeček, J. Čížek, J. Stráský, and B. Hadzima, "Microstructure stability of ultra-fine grained magnesium alloy az31 processed by extrusion and equal-channel angular pressing (execap).," vol. 94, p. 69–79, 2014.

[66] J. Vrátná, B. Hadzima, M. Bukovina, and M. Janeček, "Room temperature corrosion properties of az31 magnesium alloy processed by extrusion and equal channel angular pressing.," vol. 48, pp. 4510–4516, 2013.

[67] H. Seiner, L. Bodnárová, P. Sedlák, M. Janeček, O. Srba, R. Král, and et al., "Application of ultrasonic methods to determine elastic anisotropy of polycrystalline copper processed by equal-channel angular pressing.," vol. 58, p. 235–247, 2010.

[68] H. Seiner, P. Stoklasova, P. Sedlak, M. Sevcik, M. Janovska, M. Landa, T. Fukuda, T. Yamaguchi, and T. Kakeshita, "Evolution of soft-phonon modes in feepd shape memory alloy under large elastic-like strains.," vol. 105, pp. 182–188, 2016.

[69] F. Xiao, T. Fukuda, and T. Kakeshita, "Critical point of martensitic transformation under stress in an fe-31.2pd (at.%) shape memory alloy," 2015.

[70] F. Xiao, T. Fukuda, and T. Kakeshita, "On the physical nature of high reversible strain in fe-pd single crystals exhibiting lattice softening," vol. 61 (11), pp. 4044–4052, 2013.

[71] T. Yamaguchi, T. Fukuda, T. Kakeshita, S. Harjo, and T. Nakamoto, "Neutron diffraction study on very high elastic strain of 6% in an fe 3pt under compressive stress," vol. 104 (23), 2014.

[72] T. Fukuda and T. Kakeshita, "More than 6% elastic strain realized in a bulk single crystal of an fe 3pt alloy," vol. 69 (1), pp. 89–91, 2013.

[73] M. Matsui, H. Yamada, and K. Adachi, "A new low temperature phase (fct) of fe-pd,"

[74] T. Grabec, K. Zoubkova, P. Stoklasova, M. Sevcik, P. Sedlak, M. Janovska, H. Seiner, and M. Landa, "In situ characterization of the elasticity and stress-induced phase transformation of niti shape-memory alloy.," vol. 134, pp. 811–814, 2018.

[75] M. Thomasova, H. Seiner, P. Sedlak, M. Frost, M. Sevcik, I. Szurman, R. Kocich, J. Drahokoupil, P. Sittner, and M. Landa, "Evolution of macroscopic elastic moduli of martensitic polycrystalline niti and niticu shape memory alloys with pseudoplastic straining.," vol. 123, pp. 146–156, 2017.

[76] T. Brill, S. Mittelbach, W. Assmus, M. Mullner, and B. Luthi, "Elastic properties of niti.," vol. 3, 1991.

[77] P. Sedlák, H. Seiner, M. Landa, V. Novák, P. Šittner, and L. Manosa, "Elastic constants of bcc austenite and 2h orthorhombic martensite in cualni shape memory alloy," vol. 53, 2005.

[78] A. González-Comas, L. Manosa, A. Planes, F. Lovey, J. Pelegrina, and C. Guénin, "Lattice stability and martensitic transition in β-phase cu-based shape memory alloys: Long-wavelength acoustic mode anharmonicity," vol. 56, 1997.

[79] A. Planes and L. Manosa, "Vibrational properties of shape-memory alloys," vol. 55, 2001.

[80] H. Seiner, L. Bicanová, P. Sedlák, M. Landa, L. Heller, and I. Aaltio, "Magnetoelastic attenuation in austenitic phase of ni–mn–ga alloy investigated by ultrasonic methods," vol. 521, 2009.

[81] P. Šittner, D. Neov, P. Lukáš, and D. Toebbens, "Neutron diffraction studies of the stress effect on texture transformations in niti shape memory alloys," vol. 15, 2004.

[82] H.-R. Wenk, I. Lonardelli, and D. Williams, "Texture changes in the hcp $\rightarrow$ bcc $\rightarrow$ hcp transformation of zirconium studied in situ by neutron diffraction," vol. 52, 2004.

[83] P. Šittner, P. Lukáš, V. Novák, M. Daymond, and G. Swallowe, "In situ neutron diffraction studies of martensitic transformations in niti polycrystals under tension and compression stress," vol. 378, 2004.

[84] M. Landa, P. Sedlák, P. Šittner, H. Seiner, and V. Novák, "Temperature dependence of elastic properties of cubic and orthorhombic phases in cu–al–ni shape memory alloy near their stability limits," vol. 462, 2007.

[85] P. Šittner, M. Landa, P. Lukáš, and V. Novák, "R-phase transformation phenomena in thermomechanically loaded niti polycrystals," vol. 38, 2006.

[86] P. Šittner, L. Heller, J. Pilch, C. Curfs, T. Alonso, and D. Favier, "Young's modulus of austenite and martensite phases in superelastic niti wires," vol. 23, 2014.

A Přílohy

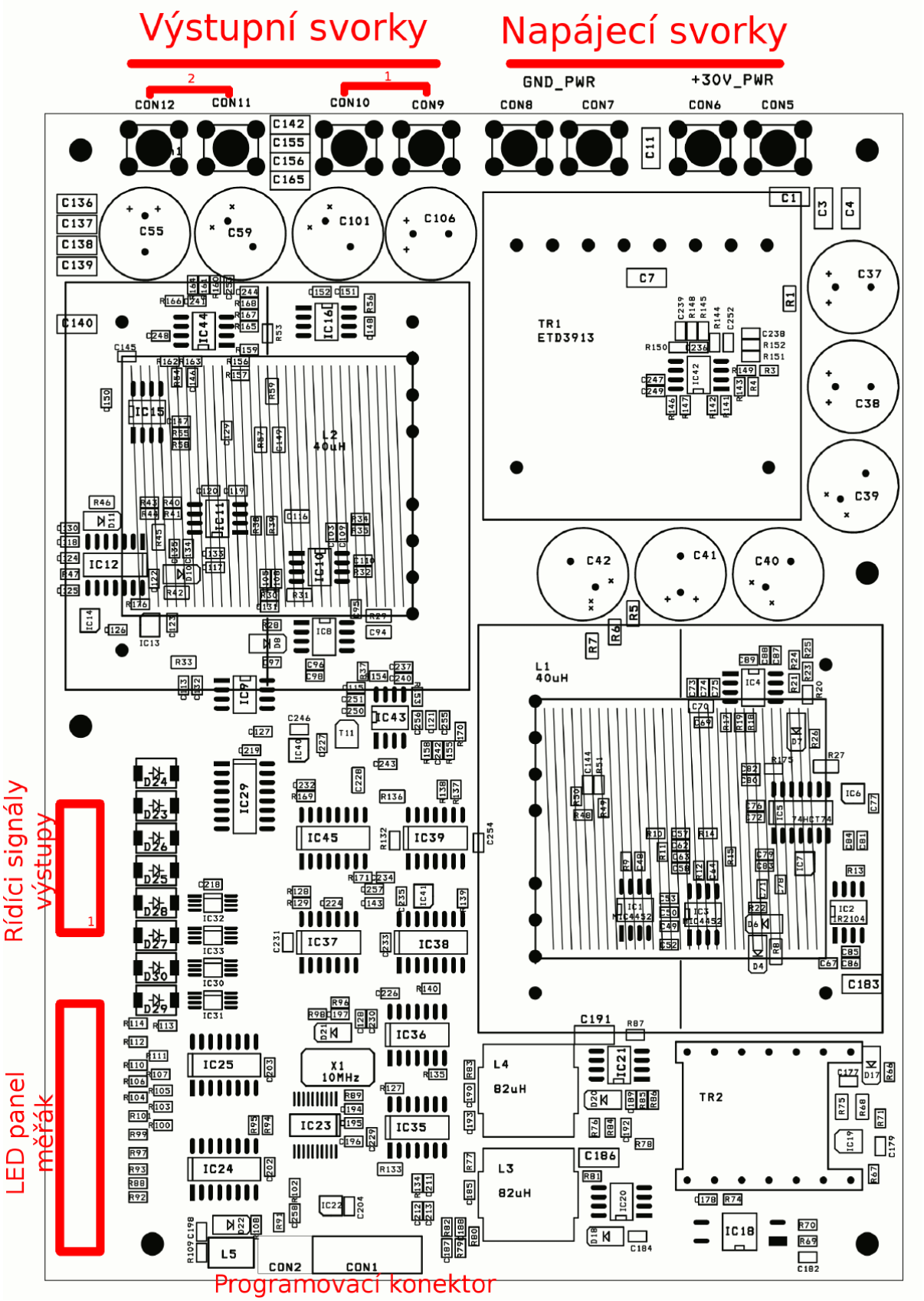

Obrázek A.1: Kontrukce regulačního zdroje pro jeden peltierův článek vyrobený společností Space Research Instruments s.r.o.

B Výpis programu

```
'#Reference {5BF46737-4121-4B92-AF7A-BF07871BDAE3}#1.0#0#C:\Program Files
\Common Files\Polytec\COM\PolyTimer.dll#Polytec PolyTimer Type Library

'#uses "SwitchToAcquisitionMode.bas"
Option Explicit

' Global constants
Const CA_FileFilter = Array("Scan Data (*.svd)|*.svd|All Files (*.*)|*.*|
            |", "Single Point Data (*.pvd)|*.pvd|All Files (*.*)|*.*||")
Const CA_FileExt = Array(".svd", ".pvd")
Const C_FileFilter = "Soubor teplot (*.txt)|*.txt|All Files (*.*)|*.*||"
Const C_FileExt = ".txt"
Const C_Scan% = 0
Const C_SinglePoint% = 1
Const C_Progress$ = "|"
Const C_MaxProgressChar% = 130
'
' Global variables
Dim BackButtonPressed As Boolean
Dim DlgAborted As Boolean
Dim AcqType As Integer
Dim BaseFileName(2) As String
Dim AcqBaseFileName(2) As String
Dim AcqCount As Integer
Dim WaitingTime As Integer
Dim AcqStartTime As Date
Dim AcqStartDirect As Boolean
Dim IsVibSoft As Boolean
Dim oPolyTimer As POLYTIMERLib.Timer
```

```
Dim Nazev_Souboru As String ’nazev souboru pro teploty
Dim teplota() As Integer ’ dynamicke pole teplot

’
Sub Main
’ ------------------------------------------------------------------------
’ Main procedure.
’ ------------------------------------------------------------------------
Call InitGlobalVariables

If Not SwitchToAcquisitionMode() Then GoTo MEnd
If IsVibSoft Then GoTo M1
M1:
Call SelectAcquisitionType
If DlgAborted Then GoTo MEnd
M2:
Call SelectBaseFilename
If DlgAborted Then GoTo MEnd
If BackButtonPressed Then GoTo M1
M3:
Call VyberSouborTeplot
If DlgAborted Then GoTo MEnd
If BackButtonPressed Then GoTo M2


If Dir(Nazev_Souboru) <> "" Then
GoTo M4
Else
MsgBox("Soubor neexistuje, zkuste to znovu")
GoTo M3
End If
```

```
M4:

Call Nacteni_souboru 'nacte soubor teplot a ulozi je do promene
AcqCount = UBound(teplota) 'pocet mereni


Call StartTimedAcquisition
If DlgAborted Then GoTo MEnd
If BackButtonPressed Then GoTo M3

If Not AcqStartDirect Then
Call ShowClock
If DlgAborted Then GoTo MEnd
End If

If AcqStartDirect Then
Call DoAcquisition
End If
MEnd:
MsgBox("Konec makra.", vbOkOnly)
End Sub

Private Sub SelectAcquisitionType
' ------------------------------------------------------------------------
' Select acquisition type.
' ------------------------------------------------------------------------
Begin Dialog UserDialog 400,203,"Priprava mereni",
      .SelectAcquisitionTypeDlgProc
Text 20,7,360,14,"Vyber typ mereni.",.Text1
OptionGroup .AcquisitionType
```

```
OptionButton 60,49,210,14,"*Single shot* mereni",
              .OptionSinglePoint
OptionButton 60,84,160,14,"Scan",.OptionScan
PushButton 290,175,90,21,"Dale >",.NextButton
CancelButton 190,175,90,21
End Dialog
Dim dlg As UserDialog
Dim iRe As Integer
iRe= Dialog (dlg)
If iRe = 0 Then
DlgAborted = True
End If
End Sub

Private Function SelectAcquisitionTypeDlgProc(DlgItem$, Action%,
    SuppValue&) As Boolean
' ------------------------------------------------------------------------
' Select acquisition type.
' ------------------------------------------------------------------------
Select Case Action%
Case 1 ' Dialog box initialization
If AcqType = C_Scan% Then
DlgValue "AcquisitionType" , 1
ElseIf AcqType = C_SinglePoint% Then
DlgValue "AcquisitionType" , 0
End If
Case 2 ' Value changing or button pressed
If DlgItem$ = "NextButton" Then
If DlgValue("AcquisitionType") = 0 Then
AcqType = C_SinglePoint%
ElseIf DlgValue("AcquisitionType") = 1 Then
```

```
AcqType = C_Scan%
End If
End If
Rem SelectAcquisitionTypeDlgProc = True ' Prevent button press
            from closing the dialog box
Case 3 ' TextBox or ComboBox text changed
Case 4 ' Focus changed
Case 5 ' Idle
Rem SelectAcquisitionTypeDlgProc = True ' Continue getting idle
            actions
Case 6 ' Function key
End Select
End Function

Private Sub SelectBaseFilename
' ------------------------------------------------------------------------
' Select filename.
' ------------------------------------------------------------------------
' Declare User Dialog
Begin Dialog UserDialog 400,203,"Priprava mereni",
      .SelectBaseFilenameDlgProc
Text 20,7,360,14,"Vyber zakladni nazev souboru.",.Text1
Text 20,28,350,28,"Mereni bude ulozeno pod zdanym zakladnim
          nazvem souboru zakoncenym poradim mereni.",.Text2
Text 20,70,90,14,"Umisteni:",.Text3
Text 130,70,240,14,"Static",.FilePath
Text 20,105,100,14,"Nazev:",.Text4
TextBox 130,98,240,21,.BaseFilename
PushButton 290,175,90,21,"Dale >",.NextButton
PushButton 20,175,90,21,"< Zpet",.BackButton
CancelButton 190,175,90,21
```

```
PushButton 280,126,90,21,"Hledej...",.BrowseButton
End Dialog
' Show dialog
Dim dlg As UserDialog
Dim iRe As Integer
iRe = Dialog (dlg)
If iRe = 0 Then
DlgAborted = True
End If
End Sub

Private Function SelectBaseFilenameDlgProc(DlgItem$, Action%, SuppValue&)
  As Boolean
' ----------------------------------------------------------------------
' Select filename.
' ----------------------------------------------------------------------
Dim sFilePath As String
Dim sPath As String
Dim sFileName As String
Dim sExt As String

Select Case Action%
Case 1 ' Dialog box initialization
BackButtonPressed = False

sFilePath = AcqBaseFileName(AcqType) + CA_FileExt(AcqType)
Call SplitPath(sFilePath, sPath, sFileName, sExt)

DlgText "BaseFilename", sFileName
DlgText "FilePath", sPath
If IsVibSoft Then
```

```
DlgVisible "BackButton", True
End If
Case 2 ' Value changing or button pressed
If DlgItem$ = "BrowseButton" Then
sFilePath = FileOpenDialog(DlgText ("BaseFilename"),
              CA_FileFilter(AcqType), CA_FileExt(AcqType))
If sFilePath <>"" Then
Call SplitPath(sFilePath, sPath, sFileName, sExt)
DlgText "BaseFilename", sFileName
DlgText "FilePath", sPath
End If
SelectBaseFilenameDlgProc = True
ElseIf DlgItem$ = "NextButton" Or DlgItem$ = "BackButton" Then
sFileName = DlgText("BaseFilename")
sPath = DlgText("FilePath")
sFilePath = sPath + sFileName
Call SplitPath(sFilePath, sPath, sFileName, sExt)
AcqBaseFileName(AcqType) = sPath + sFileName
End If
If DlgItem$ = "BackButton" Then
BackButtonPressed = True
End If

Rem PrepareTimedMeasurementDlg = True ' Prevent button press from
          closing the dialog box
Case 3 ' TextBox or ComboBox text changed
Case 4 ' Focus changed
Case 5 ' Idle
Rem PrepareTimedMeasurementDlg = True ' Continue getting idle
            actions
Case 6 ' Function key
```

```
End Select
End Function

Private Sub VyberSouborTeplot 'vyber souboru teplot
' Declare User Dialog
Begin Dialog UserDialog 400,203,"Nacteni souboru teplot",
      .VyberNazevSouboruTeplot
Text 20,7,360,14,"Nactete soubor teplot, pri kterych chcete
          merit",.Text1
Text 20,70,90,14,"Umisteni:",.Text3
Text 130,70,240,14,"Static",.FilePath
Text 20,105,100,14,"Nazev:",.Text4
TextBox 130,98,240,21,.BaseFilename
PushButton 290,175,90,21,"Dale >",.NextButton
PushButton 20,175,90,21,"< Zpet",.BackButton
CancelButton 190,175,90,21
PushButton 280,126,90,21,"Hledej...",.BrowseButton
End Dialog
' Show dialog
Dim dlg As UserDialog
Dim iRe As Integer
iRe = Dialog (dlg)
If iRe = 0 Then
DlgAborted = True
End If
End Sub

Private Function VyberNazevSouboruTeplot(DlgItem$, Action%, SuppValue&)
  As Boolean
' ----------------------------------------------------------------------
' Select filename.
```

```
' ------------------------------------------------------------------------
Dim sFilePath As String
Dim sPath As String
Dim sFileName As String
Dim sExt As String

Select Case Action%
Case 1 ' Dialog box initialization
BackButtonPressed = False

sFilePath = Nazev_Souboru
Call SplitPath(sFilePath, sPath, sFileName, sExt)

DlgText "BaseFilename", sFileName
DlgText "FilePath", sPath
If IsVibSoft Then
DlgVisible "BackButton", True
End If
Case 2 ' Value changing or button pressed
If DlgItem$ = "BrowseButton" Then
Nazev_Souboru = FileOpenDialog(DlgText ("BaseFilename"),
              C_FileFilter, C_FileExt)
'sFilePath = FileOpenDialog(DlgText ("BaseFilename"),
              C_FileFilter, C_FileExt)
'If sFilePath <>"" Then
'Call SplitPath(sFilePath, sPath, sFileName, sExt)
'DlgText "BaseFilename", sFileName
'DlgText "FilePath", sPath
'End If
'VyberNazevSouboruTeplot = True
'ElseIf DlgItem$ = "NextButton" Or DlgItem$ = "BackButton" Then
```

```
'sFileName = DlgText("BaseFilename")
'sPath = DlgText("FilePath")
'Nazev_Souboru = sPath + sFileName
End If
If DlgItem$ = "BackButton" Then
BackButtonPressed = True
End If

Rem PrepareTimedMeasurementDlg = True ' Prevent button press from
          closing the dialog box
Case 3 ' TextBox or ComboBox text changed
Case 4 ' Focus changed
Case 5 ' Idle
Rem PrepareTimedMeasurementDlg = True ' Continue getting idle
          actions
Case 6 ' Function key
End Select
End Function

Private Sub SelectCountAndTime
' ------------------------------------------------------------------------
' Select count and time.
' ------------------------------------------------------------------------
' Declare User Dialog
Begin Dialog UserDialog 400,203,"Priprava mereni",
      .SelectCountAndTimeDlg
Text 20,7,360,14,"Zadej pocet mereni.",.Text1
Text 20,91,350,14,"Zadej cas cekani mezi dvemi merenimi.",.Text2
TextBox 250,28,90,21,.Count
TextBox 250,112,90,21,.Time
PushButton 290,175,90,21,"Dale >",.NextButton
```

```
PushButton 20,175,90,21,"< Zpet",.BackButton
CancelButton 190,175,90,21
Text 70,35,140,14,"Pocet mereni:",.Text3
Text 70,119,160,14,"Cas cekani (sec.):",.Text4
End Dialog
' Show dialog
Dim dlg As UserDialog
Dim iRe As Integer
iRe = Dialog (dlg)
If iRe = 0 Then
DlgAborted = True
End If
End Sub

Private Function SelectCountAndTimeDlg(DlgItem$, Action%, SuppValue&)
  As Boolean
' ------------------------------------------------------------------------
' Select count and time.
' ------------------------------------------------------------------------
Select Case Action%
Case 1 ' Dialog box initialization
BackButtonPressed = False
DlgText "Count" , CStr$(AcqCount)
DlgText "Time" , CStr$(WaitingTime)
Case 2 ' Value changing or button pressed
If DlgItem$ = "NextButton" Or DlgItem$ = "BackButton" Then
AcqCount = Val(DlgText("Count"))
WaitingTime = Val(DlgText("Time"))
End If
If DlgItem$ = "BackButton" Then
BackButtonPressed = True
```

```
End If
Case 3 ' TextBox or ComboBox text changed
Case 4 ' Focus changed
Case 5 ' Idle
Case 6 ' Function key
End Select
End Function

Private Sub StartTimedAcquisition
' ------------------------------------------------------------------------
' Input start time.
' ------------------------------------------------------------------------
' Declare User Dialog
Begin Dialog UserDialog 400,203,"Zacatek mereni",
      .StartTimedAcquisitionDlg
Text 20,7,360,14,"Veber zacatek mereni.",.Text1
OptionGroup .StartOptions
OptionButton 40,42,320,14,"&Ihned po stlaceni tlacitka Kone",
              .OptionStartDirect
OptionButton 40,84,160,14,"&Zacit mereni v case",
              .OptionStartTimed
PushButton 290,175,90,21,"Konec",.FinishButton
PushButton 20,175,90,21,"< Zpet",.BackButton
CancelButton 190,175,90,21
TextBox 230,77,120,21,.StartTime
End Dialog
' Show dialog
Dim dlg As UserDialog
Dim iRe As Integer
iRe = Dialog (dlg)
If iRe = 0 Then
```

```
DlgAborted = True
End If
End Sub

Private Function StartTimedAcquisitionDlg(DlgItem$, Action%, SuppValue&)
  As Boolean
' ------------------------------------------------------------------------
' Input start time.
' ------------------------------------------------------------------------
Select Case Action%
Case 1 ' Dialog box initialization
BackButtonPressed = False
If AcqStartDirect Then
DlgValue "StartOptions" , 0
Else
DlgValue "StartOptions" , 1
End If
AcqStartTime = Time
DlgText "StartTime", CStr$(AcqStartTime)
Case 2 ' Value changing or button pressed
If DlgItem$ = "FinishButton" Then
If DlgValue("StartOptions") =  0 Then
AcqStartDirect = True
Else
AcqStartDirect = False
End If
AcqStartTime = TimeValue(DlgText("StartTime"))
End If
If DlgItem$ = "BackButton" Then
BackButtonPressed = True
End If
```

```
Case 3 ’ TextBox or ComboBox text changed
Case 4 ’ Focus changed
’ Update Time value if edit box looses the focus
If SuppValue& = DlgNumber("StartTime") Then
AcqStartTime = TimeValue(DlgText("StartTime"))
DlgText "StartTime", CStr$(AcqStartTime)
End If

Case 5 ’ Idle
Case 6 ’ Function key
End Select
End Function

Private Sub ShowClock
’ ------------------------------------------------------------------------
’ Show clock.
’ ------------------------------------------------------------------------
’ Declare User Dialog
Begin Dialog UserDialog 400,84,"Mereni zacne za ...",.ShowClockDlg
GroupBox 20,7,360,35,"",.GroupBox1
Text 120,21,140,14,"2:22",.TimeDiff
CancelButton 150,56,90,21
End Dialog
’ Show dialog
Dim dlg As UserDialog
Dim iRe As Integer
iRe = Dialog (dlg)
If iRe = 0 Then
DlgAborted = True
ElseIf iRe = 1 Then
AcqStartDirect = True
```

```
End If
End Sub

Private Function ShowClockDlg(DlgItem$, Action%, SuppValue&) As Boolean
' ----------------------------------------------------------------------
' Show clock.
' ----------------------------------------------------------------------
Static LastTime
Select Case Action%
Case 1 ' Dialog box initialization
LastTime = Time
DlgText "TimeDiff", TimeSpan(AcqStartTime - LastTime)
Case 2 ' Value changing or button pressed
Case 3 ' TextBox or ComboBox text changed
Case 4 ' Focus changed
Case 5 ' Idle
If LastTime < Time Then
LastTime = Time
If AcqStartTime <= LastTime Then
DlgEnd 1
Else
DlgText "TimeDiff", TimeSpan(AcqStartTime - LastTime)
End If
End If
ShowClockDlg = True
Case 6 ' Function key
End Select
End Function

Private Sub DoAcquisition
' ----------------------------------------------------------------------
```

```
' Acquisition.
' ----------------------------------------------------------------------
' Declare User Dialog
Begin Dialog UserDialog 400,203,"Provadi se mereni",.DoAcquisitionDlg
GroupBox 20,105,360,35,"",.GroupBox2
Text 20,28,100,14,"Mereni cislo:",.Text1
Text 130,28,90,14,"1 of 100",.AcqNo
GroupBox 20,42,360,35,"",.GroupBox1
Text 30,56,340,14,"#####",.AcqProgress
Text 20,91,150,14,"Pro teplotu:",.Text2
Text 30,119,340,14,"0",.teplota
'Text 20,91,150,14,"Cekani...",.Waiting
'Text 30,119,340,14,"#####",.WaitingProgress
PushButton 290,175,90,21,"Stop",.StopButton
End Dialog
' Show dialog
Dim dlg As UserDialog
Dim iRe As Integer
iRe = Dialog (dlg)
If iRe = 0 Then
DlgAborted = True
End If
End Sub

Private Function DoAcquisitionDlg(DlgItem$, Action%, SuppValue&)
  As Boolean
' ----------------------------------------------------------------------
' Acquisition.
' ----------------------------------------------------------------------
Static AcqMode As Integer ' 0 = Start Acquisition , 1 = Acquisition
      in progress, 2 = waiting
```

```
Static AcqNo As Integer
Static WaitingTimer
Static LastTimer
Dim sProgress As String

Select Case Action%
Case 1 ' Dialog box initialization
AcqMode = 0
AcqNo = 1
DlgText "AcqNo" , ""
DlgText "AcqProgress" , ""
'DlgText "WaitingProgress" , ""
Case 2 ' Value changing or button pressed
If Acquisition.State <> ptcAcqStateStopped Then
Acquisition.Stop
End If
Case 3 ' TextBox or ComboBox text changed
Case 4 ' Focus changed
Case 5 ' Idle
If AcqMode = 0 Then ' Start Acquisition
DlgText "AcqProgress" , ""
DlgText "AcqNo" , CStr(AcqNo) + " of " + CStr$(AcqCount)
DlgText "teplota", CStr(teplota(AcqNo))
If AcqType = C_Scan% Then
Acquisition.ScanFileName = AcqBaseFileName(AcqType) + "_"
                    + CStr(AcqNo) + "(" + CStr$(teplota(AcqNo)) + ")" +
                   CA_FileExt(AcqType) 'zmena jmena
Call Mereni 'volani procedury mereni
'Acquisition.Scan ptcScanAll 'mereni bez nastavovani
                   teplot
Else
```

```
Acquisition.Start ptcAcqStartSingle
End If
AcqMode = 1
ElseIf AcqMode = 1 Then
If Acquisition.State = ptcAcqStateStopped Then
If AcqType = C_SinglePoint% Then
Acquisition.Document.SaveAs(AcqBaseFileName(AcqType)
                      + CStr$(AcqNo) + CA_FileExt(AcqType))
End If
AcqNo = AcqNo + 1
If AcqNo > AcqCount Then
DlgEnd 1
End If
AcqMode = 2
WaitingTimer = oPolyTimer.Time + WaitingTime
LastTimer = oPolyTimer.Time + 1
Else
sProgress = DlgText("AcqProgress")
sProgress = sProgress + C_Progress$
If Len(sProgress) > C_MaxProgressChar% Then
sProgress = C_Progress$
End If
DlgText "AcqProgress", sProgress
End If
ElseIf AcqMode = 2 Then
Dim Timer0 As Double
Timer0 = oPolyTimer.Time
If WaitingTimer <= Timer0 Then
'DlgText "WaitingProgress", ""
AcqMode = 0
ElseIf LastTimer <= Timer0 Then
```

```
LastTimer = oPolyTimer.Time + 1
sProgress = DlgText("WaitingProgress")
sProgress = sProgress + C_Progress$
If Len(sProgress) > C_MaxProgressChar% Then
sProgress = C_Progress$
End If
DlgText "WaitingProgress", sProgress
End If
End If
Wait 0.5 ' Give the application time to do the acquisition
DoAcquisitionDlg = True
Case 6 ' Function key
End Select
End Function
'
' ********************************************************************
' * Helper functions and subroutines
' ********************************************************************
Const c_OFN_HIDEREADONLY As Long = 4

Private Function FileOpenDialog(sFileName As String, sFilter As String,
  sAcqType As String) As String
' --------------------------------------------------------------------
' Select file.
' --------------------------------------------------------------------
On Error GoTo MCreateError
Dim fod As Object
Set fod = CreateObject("MSComDlg.CommonDialog")
fod.FileName = sFileName
fod.Filter = sFilter
fod.Flags = c_OFN_HIDEREADONLY
```

```
fod.CancelError = True
On Error GoTo MCancelError
fod.ShowOpen
FileOpenDialog = fod.FileName
GoTo MEnd
MCancelError:
FileOpenDialog = ""
GoTo MEnd
MCreateError:
FileOpenDialog = GetFilePath(sFileName, Right$(sAcqType, 3),CurDir(),
      "Select a base file", 2)
MEnd:
End Function

Private Sub SplitPath(sFilePath As String, sPath As String, sName As
  String, sExt As String)
' ---------------------------------------------------------------------
' Split file.
' ---------------------------------------------------------------------
Dim iBSlash As Integer
Dim iDot As Integer

iBSlash = InStrRev(sFilePath, "\")
If iBSlash > 0 Then
sPath = Left$(sFilePath, iBSlash)
Else
sPath = ".\"
End If

iBSlash = InStrRev(sFilePath, "\")
sName = Right$(sFilePath, Len(sFilePath) - iBSlash)
```

```
iDot = InStrRev(sName, ".")
If iDot > 0 Then
sExt = Right$(sName, Len(sName) - iDot)
sName = Left$(sName, iDot - 1)
Else
sExt = ""
End If
End Sub

Private Function TimeSpan(T As Date) As String
' ------------------------------------------------------------------------
' Get time.
' ------------------------------------------------------------------------
If DatePart("h", T) > 0 Then
TimeSpan = Format(T, "h \h  n \m\i\n")
ElseIf DatePart("n", T) >= 1 Then
TimeSpan = Format(T, "n \m\i\n s \s\e\c")
Else
TimeSpan = Format(T, "s \s\e\c")
End If
End Function

Private Sub Nacteni_souboru() 'procedura pro nacteni teplot do pole
    Dim Counter As Integer 'lokalni promena pro posun v poly
    Dim pomocna As String 'lokalni pomocna promena

    Open Nazev_Souboru For Input As# 1 'otevre soubor pro cteni -
      zjisteni velikosti souboru
    Open Nazev_Souboru For Input As# 2 'otevre soubor pro cteni -
      nacteni teplot
```

```
Counter = 0 ’vychozi hodnota

’timto cyklem zjistime pocet teplot a jestli jsou to pouye cisla
Do While Not EOF(1) ’delej, dokud není konec souboru
     Counter = Counter + 1 ’posun pole o jedna
Input #1, pomocna  ’ulozi promenou do promene String pomocna
If Not IsNumeric(pomocna) Then
MsgBox("V souboru musi byt pouze cisla - konec programu",
              vbOkOnly)
End ’ukonci program
End If
Loop

ReDim teplota(Counter) ’pole dlouhe podle poctu teplot
Counter = 0 ’vychozi hodnota

’timto cyklem nacteme teploty do pole
    Do While Not EOF(2) ’delej, dokud není konec souboru
     Counter = Counter + 1 ’posun pole o jedna
     Input #2, teplota(Counter)  ’cti a uloz promenné do pole
          "TEPLOTA"
Loop

Close ’zavri soubory
End Sub

Private Sub Mereni() ’procedura pro obsluhu nastaveni teploty a mereni
DigitalPorts.Item(ptcDigitalPortOut1).Value=True ’na AUX OUT "1"
Wait 60 ’cekani v secundach

While DigitalPorts.Item(ptcDigitalPortIn1).Value=False ’smycka dokud
```

```
      neni na AUX IN "1"
    Wait 0.0001 'cekani v secundach

    If Acquisition.State <> ptcAcqStateStopped Then
Acquisition.Stop
End If

Wend 'konec while

DigitalPorts.Item(ptcDigitalPortOut1).Value=False 'na AUX OUT "0"

Wait 5 'cekani v secundach

'----------------------------Zacni merit------------------------------
Acquisition.Scan ptcScanAll
'----------------------------Konec merit------------------------------
End Sub


Private Sub InitGlobalVariables
' ------------------------------------------------------------------------
' Initialize variables.
' ------------------------------------------------------------------------
BackButtonPressed = False
DlgAborted = False
AcqBaseFileName(C_Scan%) = CurDir$() + "\Scan"
AcqBaseFileName(C_SinglePoint%) = CurDir$() + "\Analyzer"
Nazev_Souboru = CurDir$() + "\teploty"
WaitingTime = 0
AcqStartTime = Time
AcqStartDirect = True
```

```
IsVibSoft = InStr(Name, "Scanning") = 0
DigitalPorts.Item(ptcDigitalPortOut1).Value=False ’na AUX OUT "0"
’Call Nacteni_souboru ’nacte soubor teplot a ulozi je do promene
’AcqCount = UBound(teplota) ’pocet mereni
If IsVibSoft Then
AcqType = C_SinglePoint%
Else
AcqType = C_Scan%
End If
Set oPolyTimer = New  POLYTIMERLib.Timer
oPolyTimer.Start
End Sub
```

C Seznam publikací v časopisech s IF (včetně jejich kopií)

1. M. Koller, P. Sedlák, H. Seiner, et al., "An ultrasonic internal friction study of ultrafine-grained AZ31 magnesium alloy", *Journal of Material Science*, **Q2**, 2015, počet citací[3]: 6

2. V. Kopecký, O. Perevertov, L. Straka, el al., "Equivalence of Mechanical and Magnetic Force in Magnetic Shape Memory Effect", *Acta Physica Polonica A*, **Q3**, 2015, počet citací[3]: 4

3. J. Nejezchlebová, H. Seiner, M. Ševčík, at al., "Ultrasonic detection of ductile-to-brittle transitions in free-cutting aluminum alloys",*NDT &E International*, **Q1** (2015), počet citací[3]: 3

4. H. Seiner, P. Stoklasová, P. Sedlák, et al., "Evolution of soft-phonon modes in Fe-Pd shape memory alloy under large elastic-like strains", *Acta Materialia*, **Q1**, 2016, počet citací[3]: 7

5. M. Thomasová, H. Seiner, P. Sedlák, et al., "Evolution of macroscopic elastic moduli of martensitic polycrystalline NiTi and NiTiCu shape memory alloys with pseudoplastic straining", *Acta Materialia*, **Q1**, 2017, počet citací[3]: 14

6. E. Buixaderas, P. Bérešová, P. Ondrejkovič, et al. "Acoustic phonons in unfilled tetragonal tungsten-bronze crystals", *Phase Transition*, **Q4**, 2018, počet citací[3]: 2

7. T. Grabec, K. Zoubková, P. Stoklasová, et al., "In Situ Characterization of the Elasticity and Stress-Induced Phase Transformation of NiTi Shape-Memory Alloy", *Acta Physica Polonica A*, **Q3**, 2018, počet citací[3]: 1

8. M. Ševcík, T. Grabec, P. Stoklasová, et al., "Non-Contact Characterization of Acoustoelastic Parameters", *Acta Physica Polonica A*, **Q3**, 2018, počet citací[3]: 1

9. A. Kruisová, M. Ševčík, H. Seiner, et al., "Ultrasonic bandgaps in 3D-printed periodic ceramic microlattices", *Ultrasonics*, **Q2**, 2018, počet citací[3]: 6

10. M. Ševčík, J. Zídek, J. Nejezchlebová, et al., "Crack growth in Fe-Si single crystals on macroscopic and atomistic level", *Results in Physics*, **Q1**, 2019, počet citací[3]: 0

[3]Počet citací z WoS k 25.8.2019

J Mater Sci (2015) 50:808–818
DOI 10.1007/s10853-014-8641-1

An ultrasonic internal friction study of ultrafine-grained AZ31 magnesium alloy

Martin Koller · Petr Sedlák · Hanuš Seiner · Martin Ševčík · Michal Landa · Jitka Stráská · Miloš Janeček

Received: 1 August 2014 / Accepted: 29 September 2014 / Published online: 15 October 2014

Abstract Internal friction in ultrafine-grained AZ31 magnesium alloy is investigated by resonant ultrasound spectroscopy. It is shown that the internal friction significantly increases at elevated temperatures ($\gtrsim 100$ °C), and that this increase can be attributed to grain boundary sliding (GBS). The evolution of this phenomenon with grain refinement is studied by comparing the results obtained for an extruded material and for materials after additional one, two, and four passes of equal channel angular pressing. It is observed that the activation energy for diffusive GBS significantly decreases with decreasing grain size, and so does also the threshold temperature above which this internal friction mechanism is dominant. The results prove that the ultrafine-grained AZ31 alloys exhibit diffusive GBS at temperatures close to the ambient temperature, which is an interesting finding with respect to the possible applications of these alloys in superplastic forming technologies.

M. Koller
Faculty of Nuclear Sciences and Physical Engineering, Czech Technical University in Prague, Trojanova 13, 120 00 Prague 2, Czech Republic

P. Sedlák · H. Seiner (✉) · M. Ševčík · M. Landa
Institute of Thermomechanics, Academy of Sciences of the Czech Republic, Dolejškova 5, 18200 Prague, Czech Republic
e-mail: hseiner@it.cas.cz

J. Stráská · M. Janeček
Department of Physics of Materials, Charles University in Prague, Ke Karlovu 5, 121 16 Prague 2, Czech Republic

Introduction

The ductility of hcp magnesium alloys can be significantly improved by grain refinement, and in particular by severe plastic deformation (SPD) processing [1–4]. This effect partially results from the randomization of the grain orientations due to the SPD, which disturbs the otherwise strong crystallographic texture of the wrought magnesium alloys and suppresses the consequent plastic anisotropy. Additionally, the grain refinement and the corresponding increase of the volume fraction of grain boundaries enable easier plastic flow by the grain boundary sliding (GBS) [5–9], and also by the non-basal dislocation slip, since the activation of the non-basal slip system is enabled by compatibility stresses at the grain boundaries [10, 11]. Both the GBS and the non-basal slip can contribute significantly to the enhanced workability of finely grained magnesium alloys.

In this paper, we present an experimental study of the evolution of internal friction in the AZ31 alloy with a gradual grain refinement given by repetitions of the equal channel angular pressing (ECAP, [5]). The internal friction measurements have been shown many times as a sensitive and reliable tool for detection of GBS [12–15], as well as of the activity of dislocations [16–19], and could be, thus, able to detect the evolution of both these effects due to ECAP. However, as the relaxation strength for GBS is much higher than for the dislocation slip [20], and as the non-basal slip systems in hcp alloys are relatively rigid, it is plausible that the internal friction in finely grained AZ31 is dominantly given by GBS. Ileva et al. [21] reported a rapid increase of internal friction of ECAPed AZ31 upon heating above the room temperature and have shown that this increase can be indeed attributed to GBS. Similar results were obtained by Watanabe et al. [12] who, in

addition, observed the dependence of this increase on the grain size by comparing internal friction results for two different rolled plates and for the as-cast material. Fan et al. [22, 23] reported a very similar increase for finely grained pure magnesium, showing that this increase can be again ascribed to GBS, while a significantly smaller internal friction peak related to the dislocation slip was observed at lower temperatures. Here we bring a comparison of this internal friction increases for extruded AZ31 and AZ31 samples that were, additionally to the extrusion, processed by 1, 2, and 4 ECAP passes. In summary, the main aim of this paper is to show that the internal friction (in particular in the ultrasonic frequency range) is able to monitor sensitively the microstructural processes in ultrafine-grained AZ31, and to contribute, by such observations, to the understanding of the evolution of these processes with grain refinement, temperature, and thermal history of the material.

Theoretical background

Resonant ultrasound spectroscopy for internal friction measurements

The resonant ultrasound spectroscopy (RUS, [24–26]) is an experimental method used mainly for determination of elastic constants of solids. This method is based on measurements of the resonant frequencies of free elastic vibrations of a given small sample with known shape and mass density. From a set of such resonant frequencies (typically several tens of frequencies from the lowest part of the spectrum), the elastic constants are determined inversely by minimizing some objective function

$$F = \sum_{i=1}^{N} \left(f_i^{\mathrm{exp}} - f_i^{\mathrm{calc}}(c_{ij})\right)^2, \tag{1}$$

with respect to the sought elastic constants c_{ij}, where f_i^{exp} and f_i^{calc} are, respectively, the experimentally determined resonant frequencies and the corresponding resonant frequencies calculated for given c_{ij} by a mathematical model. The correct pairing between the measured and calculated frequencies is ensured by comparing the calculated modal shapes of vibrations for the individual involved modes with those detected experimentally using e.g., a scanning laser vibrometer [26, 27]. With sufficiently large number of modes involved, the RUS method is able to determine up to all 21 independent elastic coefficients of a triclinic solid [27]; however, some of the elastic constants are always determined more accurately than the others, since the lowest resonant frequencies involved in the RUS procedure are necessarily related to the softest straining modes of the sample, which are dominantly shears, while the contribution of the elastically stiffer longitudinal and volumetric straining modes is much weaker. If the material is isotropic (with two independent elastic constants, the shear modulus G and the bulk modulus K), the first few peaks in the spectrum are related only to G.

As shown by Sumino et al. [28], besides the determination of the elastic constants, the RUS method can be also employed for the determination of the internal friction. This concept was successfully adopted for various material systems [29–31]. If a small sample of the examined material vibrates at a resonant frequency f, the presence of an internal friction mechanism is represented by an increase of the width of the resonant peak. The internal friction coefficient Q_{exp}^{-1} for a given resonant mode can be defined as $Q_{\mathrm{exp}}^{-1} = \mathrm{FWHM}/f$, where FWHM stands for the full-width-at-half-maximum of the peak, and the subscript exp indicates that this coefficient was determined from an experimentally obtained resonant curve.

The internal friction of a material with a given set of independent elastic constants c_{ij} can be fully described by a corresponding set of internal friction coefficients Q_{ij}^{-1}, assuming that the internal friction exhibits the same symmetry class as the elasticity of the material. For small Q_{ij}^{-1}, the relation between Q_{ij}^{-1} and Q_{exp}^{-1} for a given resonant mode can be derived by a perturbation theory [25, 28] as

$$Q_{\mathrm{exp}}^{-1} = \frac{2}{f} \sum_{ij} c_{ij} \frac{\partial f}{\partial c_{ij}} Q_{ij}^{-1}. \tag{2}$$

If the material is isotropic, this relation simplifies into

$$Q_{\mathrm{exp}}^{-1} = \frac{2}{f} \left(G \frac{\partial f}{\partial G} Q_G^{-1} + K \frac{\partial f}{\partial K} Q_K^{-1} \right), \tag{3}$$

where Q_G^{-1} and Q_K^{-1} are the internal friction coefficients related to shearing and to hydrostatic compression, respectively. As discussed above, the resonant frequencies of the modes from the lowest part of the spectrum are mainly dependent on the shear modulus, i.e.,

$$\left| \frac{\partial f}{\partial G} \right| \gg \left| \frac{\partial f}{\partial K} \right|, \tag{4}$$

so the second term in (3) can be neglected. The assumption that the resonant frequency f depends only on the shear modulus G implicates directly that $G = af^2$, where a is a constant. On substituting such a relation into (3), the terms including f cancel, and the final relation reads $Q_{\mathrm{exp}}^{-1} = Q_G^{-1}$. In other words, the FWHM$/f$ ratios for the first few resonant modes from the RUS spectrum for an isotropic material are directly equal to the shear internal friction coefficient. Hence, for simplicity, we will from hereafter use the symbol Q^{-1} to denote this coefficient, and will not distinguish between whether this coefficient was obtained

as FWHM/f from the experimental spectrum or is a material property.

Internal friction in materials with GBS

Since the GBS is a relaxation process (i.e., a viscous process with some characteristic time scale), the Q^{-1} in the materials with GBS can be expected to exhibit some specific features. In this section, we briefly summarize the main findings of the theory of the relaxation damping in elastic materials [20, 32] with the focus laid on the high-frequency limit, which is relevant for the RUS measurement.

Let us consider an isotropic homogeneous material able to undergo some relaxation process with a characteristic relaxation time τ. The Hooke's law for shear straining of such material can be written as

$$\frac{\partial\sigma}{\partial t}+\frac{\sigma}{\tau}=2G_0\frac{\partial\varepsilon}{\partial t}+2G_R\frac{\varepsilon}{\tau}, \tag{5}$$

where σ is the shear stress, ε is the corresponding strain component, and G_0 and G_R are the instantaneous and the relaxed shear moduli, respectively. Let us further consider a harmonic, planar shear elastic wave traveling in this material at some angular frequency ω. In general, both the phase velocity v_φ and the attenuation coefficient α for such a wave are frequency-dependent. However, in the high-frequency limit ($\omega \gg \tau^{-1}$), the frequency dependence disappears, and the relations for these quantities simplify into

$$v_\varphi=\sqrt{G_0/\rho}, \tag{6}$$

where ρ is the mass density, and

$$\alpha=\frac{1}{2\tau v_\varphi}\left(1-\frac{G_R}{G_0}\right). \tag{7}$$

This means that while the phase velocity is in the high-frequency limit unaffected by the presence of the relaxation process, the attenuation coefficient in this limit is non-vanishing and increases with the difference between G_0 and G_R.

In the RUS measurement, analogously, the resonant frequencies f of the chosen shear modes are independent of G_R and of τ, while the internal friction coefficient Q^{-1} is not. In other words, the shear modulus calculated inversely from the RUS measurements is always the instantaneous shear modulus G_0, while the Q^{-1} value is affected by the presence of the relaxation. In particular, this coefficient is related to the attenuation coefficient of the shear waves by

$$Q^{-1}=\alpha v_\varphi/2\pi f=\frac{1}{4\pi f\tau}\left(1-\frac{G_R}{G_0}\right). \tag{8}$$

Since α is a constant, the FWHMs for all resonant peaks corresponding to the shearing modes are constant as well, since FWHM $= Q^{-1}2\pi f = \alpha v_\varphi$.

If the relaxation process responsible for the damping is thermally activated, the rate of activation increases with increasing temperature, and so the relaxation time decreases. This decrease is exponential, i.e.,

$$\tau=\tau_0\exp\left(\frac{U}{RT}\right), \tag{9}$$

where U is the activation energy, and R is the molar gas constant. Then, the temperature evolution of Q^{-1} can be, in the high-frequency limit, expressed as[1]

$$Q^{-1}=\frac{1}{4\pi f\tau_0}\left(1-\frac{G_R}{G_0}\right)\exp\left(-\frac{U}{RT}\right). \tag{10}$$

For the GBS relaxation in particular, the constant τ_0 is proportional to the grain size and inversely proportional to the grain boundary thickness [20], so with the grain refinement and with thickening of the grain boundaries (which both are expected due to ECAP processing), the internal friction Q^{-1} is expected to increase.

Finally, if the dominant internal friction mechanism changes at some temperature from one to another, this change can be detected as a change in the slope

$$\mathrm{d}(\log Q^{-1})/\mathrm{d}(1/T)=-U/R. \tag{11}$$

The value of the activation energy is given by the micromechanism of the relaxation mechanism, in this particular case by the GBS mechanism. As shown by Koike et al. [6] (see also [9]), the GBS in AZ31 can appear in two different modes. At the room temperature, the dominant mechanism is the *slip-induced GBS*, in which the GBS is coupled with the dislocation slip in basal planes, while at higher temperatures the *pure (diffusion-driven) GBS* dominates. For the rolled AZ31 sheet with the average grain size of 8 μm studied in [6], the temperature limit above which the pure GBS mechanism dominates was 150 °C. This limit can be expected to decrease with decreasing grain size; for nanocrystalline Mg, the pure GBS mechanism was observed already at the room temperature [33]. However, there has not been any systematic study of the relation between the grain size (or other microstructural parameters), temperature, and the dominant GBS mechanism conducted for any magnesium alloy so far, although some qualitative conclusions can be drawn based on the internal friction measurements by Watanabe et al. [12] for AZ31 and by Fan et al. [22, 23] for pure magnesium. The internal friction value Q^{-1} itself cannot directly identify the dominant GBS mechanism at a given temperature, but the temperature evolution of Q^{-1} enables, as shown in this paper, to detect reliably the temperature at which the dominant mechanism

[1] Let us point out that in the high-frequency limit the $Q^{-1}(T)$ does not exhibit any peak behavior common for low-frequency ($\lesssim$ 10 Hz) measurements, cf. Fan et al.[22, 23].

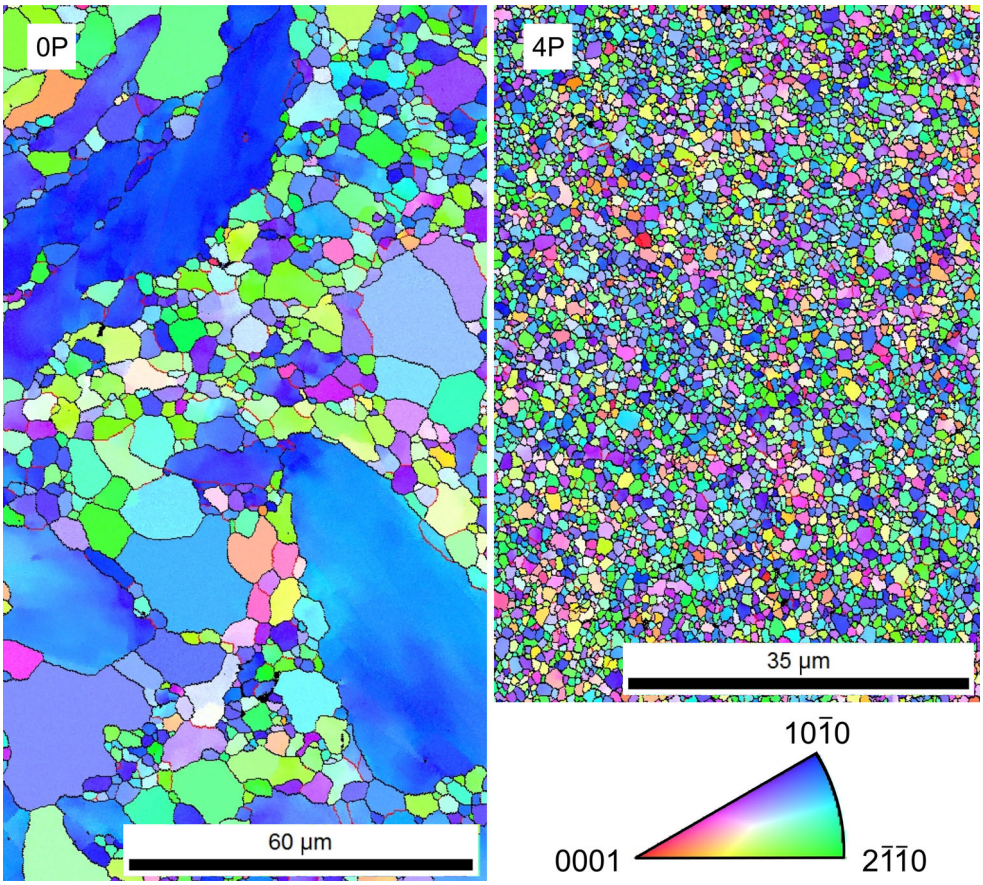

Fig. 1 EBSD orientation maps of the microstructures of the examined alloys. On the *left*: the initial extruded material (0P); on the *right*: the material after four ECAP passes (4P). The shown cuts are perpendicular to the extrusion direction

changes from one to another, providing that their activation energies differ from each other.

Experimental

Examined materials

The examined material was a commercial AZ31 alloy (nominal composition of Mg–3 %Al–1 %Zn). This material, initially in the as-cast condition, was first extruded at 350 °C with an extrusion ratio of 22. Subsequently, it was processed by ECAP performed at 180 °C (see [34] for more details) following route B_C, i.e., rotating the sample by 90° between the individual passes.

Specimens of materials after one (1P), two (2P), and four (4P) passes through the ECAP die were prepared. A detailed information on the properties and microstructural characterization of these materials can be found elsewhere [34–37], here we bring only a brief summary: the initial extruded material (0P) exhibited a bimodal grain size distribution, including simultaneously large grains (diameter 50 µm) and small grains of few micrometers in diameter. The subsequent passes of ECAP led to homogenization of the microstructure and the overall grain refinement. In Fig. 1, the EBSD images of the microstructures of the as-extruded (0P) material and the material after four passes of ECAP (4P) are compared. It is clearly seen that the bimodal structure is suppressed in the 4P material; also the strong $(10\bar{1}0)$ texture observed for the large grains of the 0P material is removed by the ECAP passes. In the 1P and 2P materials, some bimodal structure was still present (not shown in Fig. 1, see [34] for the EBSD micrographs), but both the grain size of the small grains and the volume fraction of the large ones were subsequently reduced. In order to obtain a single-scalar parameterization of the grain refinement process, the *median grain size* for each material was determined from the EBSD maps. (The median grain size is such value $\langle d \rangle$ that the number of grains larger in diameter than $\langle d \rangle$ is equal to the number of grains smaller in diameter than $\langle d \rangle$.) The resulting values were $\langle d \rangle_{0P} = 2.84$ µm, $\langle d \rangle_{1P} = 1.11$ µm, $\langle d \rangle_{2P} = 0.91$ µm, and $\langle d \rangle_{4P} = 0.72$ µm.

From these materials, samples in forms of small rectangular parallelepipeds for the RUS measurements were prepared. Four of them (denoted 0P, 1P, 2P, and 4P according to the material) were used for measurements of the internal friction and shear modulus evolution during heating from RT up to 300 °C. Four samples of the 4P material were used for

Table 1 An overview of samples, their dimensions, and the respective temperature ranges for the RUS measurements

Sample	Dimensions (mm^3)	Measurement temperature range
0P	1.725 × 2.642 × 3.454	RT → 300 °C
1P	1.725 × 2.633 × 3.457	RT → 300 °C
2P	1.730 × 2.642 × 3.458	RT → 300 °C
4P	1.680 × 2.760 × 3.354	RT → 300 °C
$4P_{170}$	0.575 × 2.798 × 3.639	RT → 170 °C; 1 h at 170 °C; 170 °C → RT
$4P_{220}$	0.578 × 2.911 × 4.007	RT → 220 °C; 1 h at 220 °C; 220 °C → RT
$4P_{270}$	0.582 × 2.533 × 3.741	RT → 270 °C; 1 h at 270 °C; 270 °C → RT
$4P_{310}$	0.565 × 2.789 × 3.623	RT → 310 °C; 1 h at 310 °C; 310 °C → RT
Accuracy	±0.005 mm	

All samples were cut such that the largest face was perpendicular to the extrusion direction

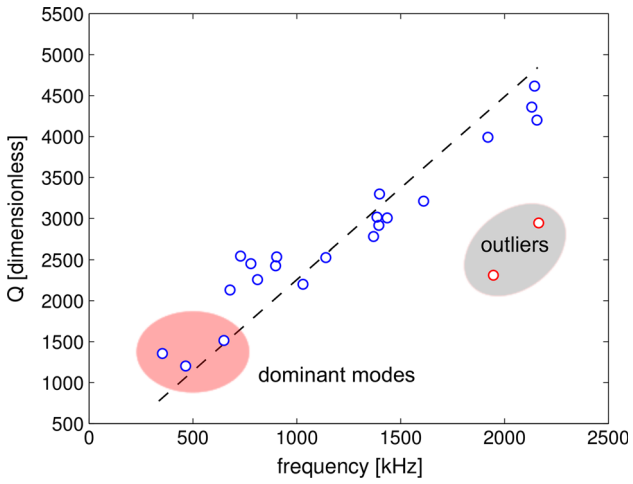

Fig. 2 An example of the frequency evolution of the internal friction (the 4P sample at 125 °C). The *shaded area* on the *left* denotes the dominant modes taken for the calculation of average internal friction, and the *shaded area* on the *right* denotes the outlying modes with higher damping (lower Q) than expected from the linear trend. The *dashed line* outlines the least squares fit by such a linear dependence that $Q = 0$ for $f = 0$, as required by the relation (8)

measurements with thermal cycling, in order to explore the reversibility of the observed phenomena. These samples are denoted $4P_{170}, 4P_{220}, 4P_{270}, 4P_{310}$ accordingly to the maximal temperature of the respective thermal cycles. The overview of the dimensions of these samples and the temperature ranges in which the samples were measured is given in Table 1. The heating and cooling rates for all samples were always quite small (1 K/min) to ensure a good temperature stability for each measurement point and to avoid the influence of possible dynamic effects.

RUS measurements

Prior to the temperature-resolved measurements, the RUS method was used to determine the elastic constants of the examined materials. As shown for polycrystalline copper by Seiner et al. [38], the ECAP can induce a measurable elastic anisotropy that changes with the individual ECAP passes. In order to inspect whether any similar effect can be observed also for the AZ31 alloy, the 0P, 1P, 2P, and 4P samples were analyzed using the same experimental procedure as for copper in [38]. For these measurements, a fully contactless RUS set-up described in details in [27] was used. For each sample, more than 50 resonant frequencies in the frequency range 0.3–2.5 MHz were obtained; these data were complemented by pulse-echo measurements of longitudinal ultrasonic waves in the directions perpendicular to the sample faces. The elastic constants of each material were then determined inversely, using the procedure described in [27].

Then, the evolutions of resonant spectra of all samples with temperature were measured in the temperature ranges given in Table 1. These measurements were also done by a contactless RUS method, with sample placed in a dedicated high-temperature RUS chamber including a heating module able to set the sample temperature up to 650 °C. The vibrations were generated by a Litron Nano S pulse laser (1064 nm, pulse duration 6 ns) and detected by a Polytec OFV 505 laser vibrometer. From the resonant spectrum recorded at each temperature, the resonant frequencies and the FWHM/f ratios for few (3–5) chosen dominant peaks were determined. It was carefully checked that the resonant peaks analyzed in this way for all temperature points for one sample corresponded always to the same set of resonant modes. The chosen peaks belonged in all cases to the lowest part of the spectrum, which means that the corresponding vibrational modes were mainly shearing modes, and thus, the evolutions of these peaks with temperature represent mainly the evolution of the shear modulus and shear internal friction, as discussed in the previous section. The FWHM/f ratios for these dominant peaks at a given temperature always slightly ($\lesssim \pm 10$ %) differed from each other both due to the experimental inaccuracy and due to the expected frequency dependence of the internal friction

(8). However, these differences were incomparably smaller than the increase of Q^{-1} due to heating, so the average value of Q^{-1}s for the chosen modes (always lying in the frequency range 300–800 kHz) was understood as a representative internal friction parameter for the given sample at the given temperature.

For each sample, it was also checked that the internal friction parameters obtained for the attenuated spectra at the elevated temperatures follow the frequency dependence typical for relaxation damping in the high-frequency limit (8), i.e., that $Q = f/\mathrm{FWHM}$ is linearly proportional to f. An example of such frequency dependence is shown in Fig. 2. For all samples, the quality factors Q of all detectable modes followed the linear trends similar to the one shown in Fig. 2, except for few (2–3) outliers, which were always the peaks of the lowest amplitudes (i.e., these modes were not sufficiently excitable by the laser pulses), for which the determination of Q was strongly affected by small signal-to-noise ratios. Hence, the relaxation-like character of the internal friction was confirmed.

Results and discussion

Room temperature elastic constants

The room temperature elastic constants of the 0P, 1P, 2P, and 4P materials exhibited all only very small deviations from perfect elastic isotropy. Unlike for the polycrystalline copper studied by the same approach by Seiner et al. [38], the ECAP did not induce any measurable changes of the elastic anisotropy with the individual passes. The reason for this difference is most probably the weak elastic anisotropy of the hcp magnesium lattice compared with relatively strong elastic anisotropy of the cubic lattice of copper. As a consequence of this weak anisotropy, the changes of texture and microstructure due to ECAP for the case of AZ31 are not anyhow reflected by the macroscopic elastic properties of the polycrystalline aggregate. The resulting room temperature elastic constants for the examined materials are listed in Table 2 along with the internal friction coefficients determined from the lowest resonant peaks for each sample. It is seen that the values of Q^{-1} are very low, of the order 10^{-5}, i.e., comparable to the experimental accuracy. The highest value is obtained for the 4P sample, which agrees well with the assumption that the grain refinement enhances the GBS-induced internal friction. Nevertheless, compared with the increase of the Q^{-1} s for the examined materials upon heating reported in the next paragraph, the differences between the individual materials at the room temperature are rather negligible. There is also a weak systematic decrease of the Young's modulus by the individual passes of ECAP seen in Table 2, which is in agreement with the observations of elastic softening of other ECAPed materials reported in literature (e.g., [39]).

Table 2 Room temperature elastic constants of the examined materials: Young's modulus E, Shear modulus G, and internal friction parameter Q^{-1}

Sample	E (GPa)	G (GPa)	Q^{-1} (10^{-3})
0P	44.64 ± 0.10	17.22 ± 0.06	0.05 ± 0.04
1P	44.36 ± 0.38	16.98 ± 0.27	0.04 ± 0.04
2P	44.30 ± 0.30	17.10 ± 0.24	0.08 ± 0.04
4P	44.11 ± 0.23	17.18 ± 0.29	0.15 ± 0.04

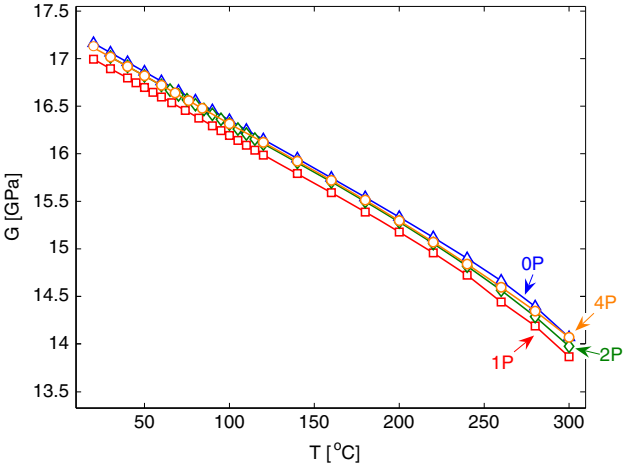

Fig. 3 The evolution of the shear moduli of the 0P–4P materials upon heating

Temperature dependences

The evolutions of the shear moduli G and of the internal friction parameters Q^{-1} with heating up to 300 °C are shown in Figs. 3 and 4, respectively. The shear moduli were calculated from the detectable resonant frequencies for each temperature using the inverse procedure described in [27], taking into account the changes of the dimensions of the samples with temperature due to thermal expansion (the linear expansion coefficient of pure magnesium $\alpha = 24.8 \times 10^{-6}$ K^{-1} was used). For all materials, the shear moduli exhibit smooth softening, linear up to approximately 200 °C and then deviating from the linear trend slightly downwards. The differences between the behaviors of the individual samples are minimal, fully within the range of the experimental errors.

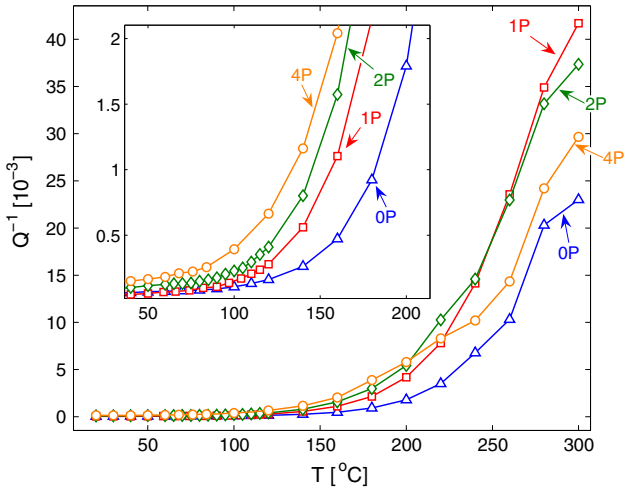

Fig. 4 The evolution of the internal friction parameters Q^{-1} of the 0P–4P materials upon heating; the *zoomed area* shows the temperature region in which the increase of Q^{-1} starts

A completely different picture is obtained for the internal friction parameters. As seen in Fig. 4, the Q^{-1} parameters increase at elevated temperatures by more than two orders of magnitude. The zoomed area in Fig. 4 shows that the onset temperature of the internal friction increase is indeed dependent on the grain refinement: for 4P the increase starts at significantly lower temperature than for 0P. The 1P and 2P samples follow the same trend according to the number of ECAP passes. The fact that these strong increases of the internal friction for all materials are not reflected by any changes of the shear moduli (see Fig. 3) confirms the assumption that the observed behavior can be well described by the high-frequency limit of a relaxation damping model.

The logarithmic plots of Q^{-1} with respect to $1/T$ shown in Fig. 5 reveal that the temperature evolution of the internal friction can be well described by the relation (10), with the slope (11) changing from one constant value to another. (For clarity, only the 0P and 4P samples are shown in Fig. 5; the 1P and 2P samples behave similarly.) The temperatures corresponding to the maximal change of the slope T^* (i.e., the temperatures at which the dominant internal friction mechanisms are changing) are listed in Table 3. The corresponding activation energy U for the high-temperature part of the Q^{-1} curve calculated from the relation (11) is also shown in Table 3; for the low-temperature part, the activation energy was approximately the same for all materials ($\sim$10 kJ/mol), not exhibiting any systematic evolution with the grain refinement. As seen in Table 3, the temperatures of the change of the slope T^* decrease significantly with the number of ECAP passes, and so does the activation energy U.

Table 3 Threshold temperatures T^* for the change of the slope (11) for the 0P–4P materials, and the activation energies corresponding to the internal friction increases above T^*

Sample	T^* (°C)	U (kJ/mol)
0P	127	58
1P	111	52
2P	102	47
4P	96	38
Accuracy	±5	±5

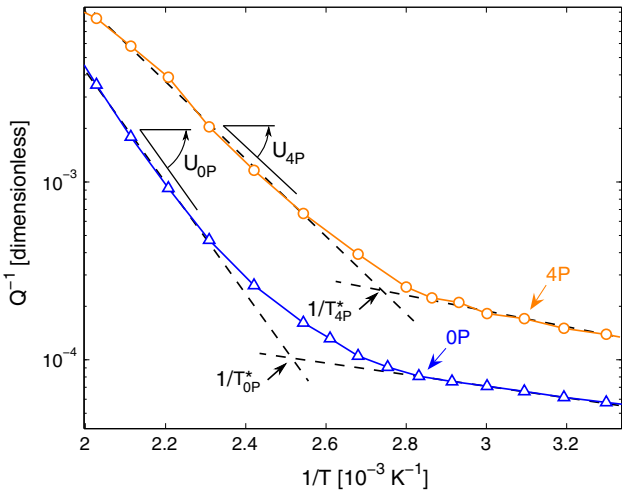

Fig. 5 The change of the slope of the $\log Q^{-1}(1/T)$ curve determining the threshold temperature T^* shown for the 0P and 4P materials. The slope of the curve above T^* (i.e., below $1/T^*$) determines the activation energy U, see the text for more details

There are several indicators that the observed behavior of Q^{-1} is indeed induced by GBS. Most importantly, as shown by the recent positron annihilation measurements [35], the dislocation density in the 4P material is lower than for 2P, so the internal friction resulting from the dislocation activity would not exhibit the systematic behavior seen in Table 3. Moreover, as also known from the positron annihilation measurements [36], the density of the dislocations significantly decreases with heating above 100 °C, while the observed internal friction is rapidly increasing in this temperature range. The recrystallization of the structure can be also disregarded as the source of the internal friction, since the increase of Q^{-1} appears at about 100 °C below the ECAP temperature. Moreover, the behavior of Q^{-1} in the vicinity of the temperatures T^* is reversible, as it will be shown for the 4P material in the next subsection, i.e., the observed internal friction increase cannot be a result of any irreversible process, such as the recrystallization or the recovery.

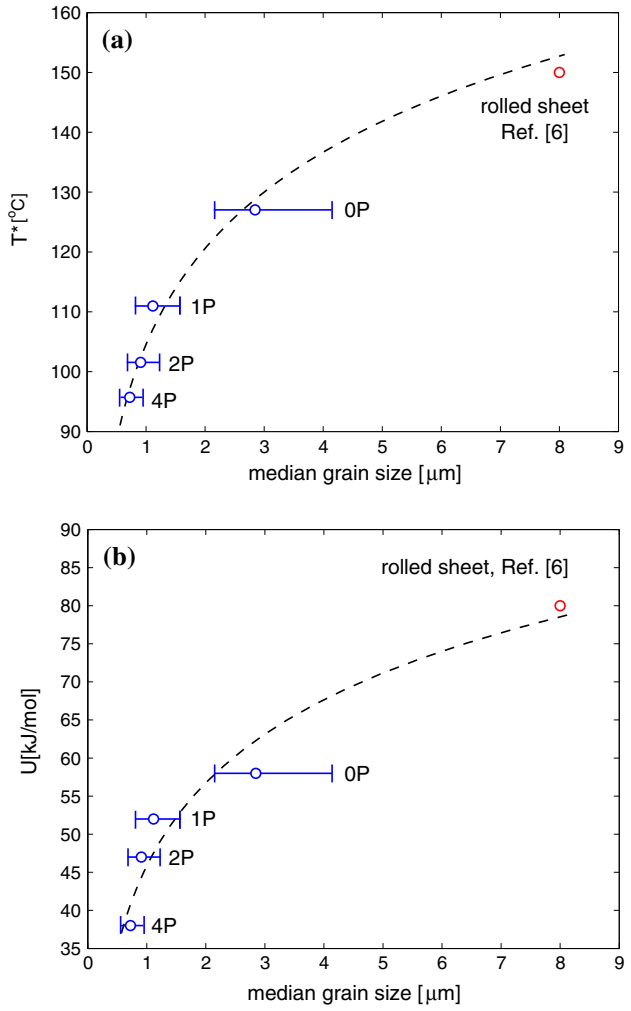

Fig. 6 The dependence of the threshold temperature T^* and the activation energy for diffusive GBS on the grain size. The *error bars* denote the intervals between the lowest (25 %) and the highest (75 %) quartiles for the grain size distribution. The *dashed lines* are just guides for eye obtained by fitting the RUS results (0P–4P) by a logarithmic curve

Quantitatively, the obtained values of the threshold temperature T^* and of the activation energy U are very close to the threshold temperature 150 °C and activation energy $U = 80$ kJ/mol determined by Koike et al. [6] for a rolled sheet with an average grain size of 8 μm. In Fig. 6, the values of T^* and U obtained from RUS measurements are plotted with respect to the median grain size for the extruded and ECAPed materials and compared to the results of [6]. It is seen that the literature data follow the same trend as those obtained by our measurements, which can be understood as an additional confirmation that the observed internal friction is a result of GBS and that the high-temperature part of the $Q^{-1}(T)$ curve corresponds to the diffusion-driven GBS mechanism. The increase of the activation energy U with the grain size is also in a qualitative agreement with the results of Fan et al. [22, 23]; the values of U for pure magnesium reported in [22, 23] are, however, about two times higher than our results and results of Koike et al. [6] for AZ31.

Nevertheless, for the discussion of the quantitative dependence of the activation energy of this GBS mechanism on the grain size, it must be taken into account that the median grain size, used as a parameter of grain refinement in Fig. 6, is not describing fully the evolution of the microstructure with the repetitions of the ECAP. Especially the initial extruded 0P microstructure (and partially also the 1P material) exhibits a strongly bimodal structure, as described in "Examined materials" section, with large variation of the grain size. It is plausible that in such a bimodal structure, the GBS internal friction is dominantly given by mutual slidings of the smallest grains, which has lower activation energy and is activated at lower temperatures. As a result, the activation energy U determined for the 0P material corresponds rather to the smaller grain size than the median value for this material, and, as seen in Fig. 6, appears to be smaller than expected from the trend of the 1P, 2P, and 4P materials. Another consequence of the bimodal structure is seen also in Fig. 5: while for the 4P material the change of the slope is more or less abrupt, for the 0P material it spans over a wide temperature region, corresponding to approximately 30 °C. This can be explained by the fact that the GBS in the 0P material is activated first for the smallest grains at temperatures close to the threshold temperature for the 4P material. Then, upon further heating, the internal friction is subsequently increased by contributions from larger and larger grains. For the 4P material, on contrary, the variation of the grain size is small, so all grains start to contribute to the internal friction with approximately the same activation energy and at approximately the same temperature.

Reversibility and the effect of annealing

In order to determine which of the changes of the internal friction coefficient upon heating are corresponding to irreversible processes, a set of thermal cycles was applied on four different samples of the 4P material (see Table 1). At the highest temperature for each cycle, the sample was always annealed for 1 h with the aim to detect the possible time-scale effects. The resulting $Q^{-1}(T)$ curves are shown in Fig. 7.

It is seen that for a cycle with the maximum temperature of 170 °C, the behavior of the internal friction is reversible; the differences between the heating and cooling curves are below the level of the experimental error. Also the evolution of Q^{-1} due to 1 h annealing at 170 °C is negligible, which proves that the microstructure responsible for the

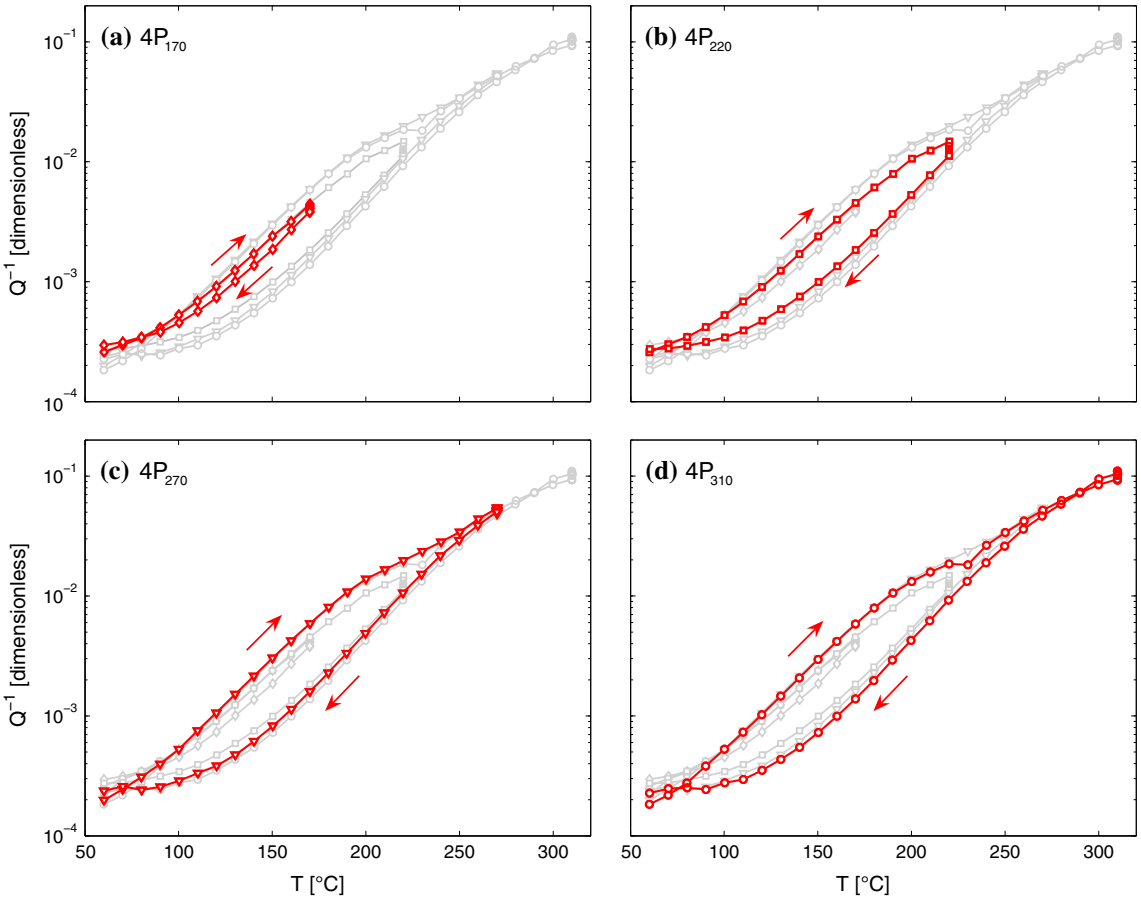

Fig. 7 The evolution of the internal friction parameter of the 4P material (samples $4P_{170}, 4P_{220}, 4P_{270}$, and $4P_{310}$) with thermal cycles. Each subplot shows one thermal cycle for one sample with the given maximal temperature at which the sample was always annealed for 1 h. For comparison, the curves for the remaining three samples are shown in each plot in *light gray*

internal friction is fully stable in this temperature range. In a sharp contrast, annealing at 220 °C induces a measurable decrease of the internal friction, and the $Q^{-1}(T)$ curve for the $4P_{220}$ exhibits a broad hysteresis loop. It is obvious that at this temperature the material undergoes irreversible changes. The hysteresis loop closes at approximately 250 °C, and so the annealing for 1 h at temperatures 270 and 310 °C (samples $4P_{270}$ and $4P_{310}$, respectively) does not lead to any time-dependent changes of the internal friction. Above 250 °C, the behavior of the material is, again, non-hysteretic. As the temperature range 200–250 °C corresponds well to the range of recrystallization of the ECAPed structure determined from *postmortem* analyses of the samples [36], we can conclude that the observed hysteresis is due to recrystallization.

From the cooling curves for the $4P_{270}$ and $4P_{310}$ samples, the threshold temperatures for the activation of the diffusion-driven GBS and the corresponding activation energy of the recrystallized material were determined,

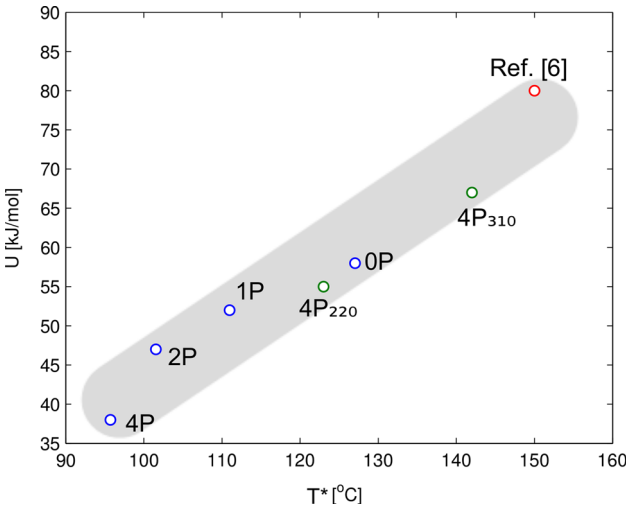

Fig. 8 The relation between the threshold temperature T^* and the activation energy for the diffusive GBS. The *gray area* outlines the possible linear trend

using the same approach as for the 0P–4P materials in the previous section. The results were $U = (66 \pm 5)$ kJ/mol and $T^* = (142 \pm 5)\,^\circ$C for $4P_{270}$, and $U = (67 \pm 5)$ kJ/mol and $T^* = (142 \pm 5)\,^\circ$C for $4P_{310}$. In other words, the grain growth due to recrystallization resulted in an increase of both the activation energy and the threshold temperature for GBS, fully in agreement with the trend outlined in Fig. 6. In the case of the sample $4P_{220}$, the respective values were $U = (55 \pm 3)$ kJ/mol and $T^* = (123 \pm 13)\,^\circ$C, which corresponds to a partially recrystallized structure.

It is again questionable to compare the U and T^* values obtained for the recrystallized samples with those determined during the heating runs for the 0P and 1P materials, since the recrystallized materials do not exhibit such strong bimodal distribution of the grain size. However, there appears to be a well-defined relation between the threshold temperature for the diffusive GBS and its activation energy. As seen in Fig. 8, the relation is approximately linear and describes well the behavior of all materials discussed in this paper (0P, 1P, 2P, 4P, 4P partially recrystallized and 4P fully recrystallized) as well as the literature data. According to this relation, the region of diffusive GBS could be extended toward the vicinity of the room temperature by further decrease of the activation energy.

Conclusions

The results of the internal friction measurements reported in this paper clarify the relations between the temperature, grain size, and the activity of GBS in the AZ31 magnesium alloy. With the gradual grain refinement induced by subsequent repetitions of the ECAP procedure, the threshold temperature T^* above which the diffusive GBS becomes a dominant internal friction mechanism systematically decreases. For the 4P material with the median grain size of $\langle d \rangle_{4P}$ = 0.72 μm, the diffusive GBS is obviously active at temperatures lower than 100 °C, i.e., about 100 °C below the recrystallization temperature for this material. Hence, the grain refinement opens a relatively broad temperature interval in which the superplastic flow can be potentially enabled by the GBS mechanism without any coarsening of the structure or any other irreversible changes to the material. This temperature interval can be important with respect to possible applications of AZ31 for superplastic forming.

Simultaneously with the decrease of the temperature T^*, also a significant decrease of the activation energy for this internal friction mechanism was observed, which indicates that the intergranular diffusion is easier in the finely grained material. A direct relation between the threshold temperature and the activation energy for GBS was found, which is followed by all materials studied in this paper (both the as-ECAPed and recrystallized, as seen in Fig. 8) as well as by the literature data.

Acknowledgements This work has been financially supported by the Czech Science Foundation (Project No. GA13-13616S).

References

1. Valiev RZ, Ismalgaliev RK, Alexandrov IV (2000) Bulk nanostructured materials from severe plastic deformation. Prog Mater Sci 45:103–189
2. Yamashita A, Horita Z, Langdon TG (2001) Improving the mechanical properties of magnesium and a magnesium alloy through severe plastic deformation. Mater Sci Eng A 300: 142–147
3. Kang SH, Lee YS, Lee JH (2008) Effect of grain refinement of magnesium alloy AZ31 by severe plastic deformation on material characteristics. J Mater Process Technol 201:436–440
4. Mukai T, Yamanoi M, Watanabe H, Higashi K (2001) Ductility enhancement in AZ31 magnesium alloy by controlling its grain structure. Scripta Mater 45:89–94
5. Valiev RZ, Langdon TG (2006) Principles of equal-channel angular pressing as a processing tool for grain refinement. Prog Mater Sci 51:881–981
6. Koike J, Ohyama R, Kobayashi T, Suzuki M, Maruyama K (2003) Grain-boundary sliding in AZ31 magnesium alloys at room temperature to 523 K. Mater Trans 44:445–451
7. Tan JC, Tan MJ (2003) Superplasticity and grain boundary sliding characteristics in two stage deformation of Mg3Al1Zn alloy sheet. Mater Sci Eng A 339:81–89
8. Panicker R, Chokshi AH, Mishra RK, Verma R, Krajewski PE (2009) Microstructural evolution and grain boundary sliding in a superplastic magnesium AZ31 alloy. Acta Mater 57:3683–3693
9. Bussiba A, Ben Artzy A, Shtechman A, Ifergan S, Kupiec M (2001) Grain refinement of AZ31 and ZK60 Mg alloys towards superplasticity studies. Mater Sci Eng A 302:56–62
10. Koike J (2005) Enhanced deformation mechanisms by anisotropic plasticity in polycrystalline Mg alloys at room temperature. Metall Mater Trans A 36:1689–1696
11. Koike J, Kobayashi T, Mukai T, Watanabe H, Suzuki M, Maruayama K, Higashi K (2003) The activity of non-basal slip systems and dynamic recovery at room temperature in fine-grained AZ31B magnesium alloys. Acta Mater 51:2055–2065
12. Watanabe H, Mukai T, Sugioka M, Ishikawa K (2004) Elastic and damping properties from room temperature to 673 K in an AZ31 magnesium. Scripta Mater 51:291–295
13. Mosher DR, Raj R (1974) Use of the internal friction technique to measure rates of grain boundary sliding. Acta Metall 22: 1469–1474
14. Pezzotti G, Kleebe HJ, Ota K (1998) Grain-boundary viscosity of polycrystalline silicon carbides. J Am Ceram Soc 81(12): 3293–3299
15. Watanabe H, Owashi A, Uesugi T, Takigawa Y, Higashi K (2011) Grain boundary relaxation in fine-grained magnesium solid solutions. Philos Mag 91:4158–4171
16. Granato AV, Lücke K (1956) Theory of mechanical damping due to dislocations. J Appl Phys 27:789–805
17. Zhang Z, Zeng X, Ding W (2005) The influence of heat treatment on damping response of AZ91D magnesium alloy. Mater Sci Eng A 392:150–155

18. Riehemann W, Abed El-Al F (2000) Influence of ageing on the internal friction of magnesium. J Alloys Compd 310:127–130
19. No ML, Oleaga A, Esnouf C (1990) Internal friction at medium temperatures in high purity magnesium. Phys Statu Solidi (A) 120:419–427
20. Nowick AS, Berry BS (1972) Anelastic relaxation in crystalline solids. Academic Press, New York
21. Ivleva TV, Göken J, Golovin IS, Zuberova Z, Maikranz-Valentin M, Steinhoff K (2008) Damping in AZ31 ECAP-processed alloy. Solid State Phenom 137:181–188
22. Fan GD, Zheng MY, Hu XS, Xu C, Wu K, Golovin IS (2013) Effect of heat treatment on internal friction in ECAP processed commercial pure Mg. J Alloys Compd 549:38–45
23. Fan GD, Zheng MY, Hu XS, Xu C, Wu K, Golovin IS (2012) Improved mechanical property and internal friction of pure Mg processed by ECAP. Mater Sci Eng A 556:588–594
24. Migliori A, Sarrao JL, Visscher WM, Bell TM, Lei M, Fisk Z et al (1993) Resonant ultrasound spectroscopic techniques for measurement of the elastic moduli of solids. Phys B 183:1–24
25. Leisure RG, Willis FA (1997) Resonant ultrasound spectroscopy. J Phys Condens Matter 9:6001–6029
26. Ogi H, Sato K, Asada T, Hirao M (2002) Complete mode identification for resonance ultrasound spectroscopy. J Acoust Soc Am 112:2553–2557
27. Sedlák P, Seiner H, Zídek J, Janovská M, Landa M (2014) Determination of all 21 independent elastic coefficients of generally anisotropic solids by resonant ultrasound spectroscopy: benchmark examples. Exp Mech 54:1073–1085
28. Sumino Y, Ohno I, Goto T, Kumazawa M (1976) Measurement of elastic constants and internal frictions on single-crystal MgO by rectangular parallelepiped resonance. J Phys Earth 24: 263–273
29. Leisure RG, Foster K, Hightower JE, Agosta DS (2004) Internal friction studies by resonant ultrasound spectroscopy. Mater Sci Eng A 370:34–40
30. Bernard S, Grimal Q, Laugier P (2014) Resonant ultrasound spectroscopy for viscoelastic characterization of anisotropic attenuative solid materials. J Acoust Soc Am 135:2601–2613
31. Seiner H, Sedlák P, Koller M, Landa M, Ramírez C, Osendi MI, Belmonte M (2013) Anisotropic elastic moduli and internal friction of graphene nanoplatelets/silicon nitride composites. Compos Sci Technol 75:93–97
32. Truell R, Elbaum C, Chick B (1969) Ultrasonic methods in solid state physics. Academic Press, New York
33. Hwang S, Nishimura C, McCormick PG (2001) Compressive mechanical properties of Mg–Ti–C nanocomposite synthesised by mechanical milling. Scripta Mater 44:1507
34. Janeček M, Yi S, Král R, Vrátná J, Kainer KU (2010) Texture and microstructure evolution in ultrafine-grained AZ31 processed by EX-ECAP. J Mater Sci 45:4665–4671. doi:10.1007/s10853-010-4675-1
35. Janeček M, Čížek J, Gubicza J, Vrátná J (2012) Microstructure and dislocation density evolutions in MgAlZn alloy processed by severe plastic deformation. J Mater Sci 47:7860–7869. doi:10.1007/s10853-012-6538-4
36. Stráská J, Janeček M, Čížek J, Stráský J, Hadzima B (2014) Microstructure stability of ultra-fine grained magnesium alloy AZ31 processed by extrusion and equal-channel angular pressing (EXECAP). Mater Charact 94:69–79
37. Vrátná J, Hadzima B, Bukovina M, Janeček M (2013) Room temperature corrosion properties of AZ31 magnesium alloy processed by extrusion and equal channel angular pressing. J Mater Sci 48:45104516. doi:10.1007/s10853-013-7173-4
38. Seiner H, Bodnárová L, Sedlák P, Janeček M, Srba O, Král R et al (2010) Application of ultrasonic methods to determine elastic anisotropy of polycrystalline copper processed by equal-channel angular pressing. Acta Mater 58:235–247
39. Lebedev AB, Burenko YuA, Romanov AE, Kopylov VI, Filonenko VP, Gryaznov VG (1995) Softening of the elastic modulus in submicrocrystalline copper. Mater Sci Eng A 203:165

Proceedings of the International Symposium on Physics of Materials (ISPMA13)

Equivalence of Mechanical and Magnetic Force in Magnetic Shape Memory Effect

V. Kopecký[a,*], O. Perevertov[a], L. Straka[b], M. Ševčík[c] and O. Heczko[a]

[a]Institute of Physics, ASCR, Na Slovance 2, 182 21 Prague, Czech Republic

[b]Aalto University School of Engineering, Laboratory of Engineering Materials, PL 14200, FIN-00076 Aalto, Finland

[c]Institute of Thermomechanics, ASCR, Dolejškova 5, 182 00 Prague, Czech Republic

High mobility of twin boundary is crucial for magnetic shape memory effect. The twin boundary can be moved by applied magnetic field or mechanical stress. In Ni–Mn–Ga 10M martensite there are two different, field movable, a–c twin boundaries type I and II due to monoclinic lattice. For single twin boundary of both types we experimentally evaluated the equivalence of magnetic and mechanical force and the validity of generally used energy model using direct stress–strain and magnetization measurements. For type II, highly mobile twin boundary, the equivalence seems to be valid and model broadly agrees with measurement. However, for type I the calculated magnetic stress is much larger than mechanical stress needed for twin boundary motion.

DOI: 10.12693/APhysPolA.128.754

PACS: 61.72.Mm, 75.78.Fg, 75.50.Cc, 75.70.Cn, 75.60.Ej, 62.20.D–

1. Introduction

Magnetic shape memory (MSM) effect is a general name for a plethora of the multiferroic effects based on interplay between ferromagnetic order and ferroelasticity [1]. One of the MSM effects is magnetically induced structure reorientation (MIR) that leads to giant deformation (5–12%) in single phase, low-symmetry martensite [2, 3]. Observed giant strain, in contrast to usual magnetostriction, is a result of structure reorientation by growing favourably oriented ferroelastic domain (also called variant) at the expense of other differently oriented domains. These adjacent domains are connected by twin boundary, which is moving easily and thus can be manipulated also by magnetic field [4].

The major representatives of MSM materials are compounds close to stoichiometric Ni_2MnGa. These alloys are also the most investigated [1, 5, 6] as they are the most promising for applications [7–9]. In Ni–Mn–Ga alloy, parental high-temperature cubic phase transforms to various martensites [1, 10]. For composition close to stoichiometry the martensite has 10M modulated structure which can be approximated by monoclinic lattice. The monoclinic structure implies the existence of type I and type II twin boundary [11, 12] that strongly differ by their twinning stress or mobility [13, 14].

Energetic barrier which hinders boundary movement is called twinning stress (σ_{TW}). The stress needed to move twin boundary can be induced mechanically or by magnetic field. In the simplest case the relation between magnetic and twinning stress is described by the Likhachev and Ullakko model [15]. More complex models were suggested, however, the simple equivalence of mechanical and magnetic force is usually retained [16, 17]. In short the model assumes that the twin boundary starts moving when the magnetic energy exceeds the mechanical barrier, which is described by relation

$$\Delta E_{\mathrm{mag}} \geq \sigma_{\mathrm{TW}} \cdot \varepsilon_0 \tag{1}$$

where ΔE_{mag} is difference of magnetic energies of differently oriented variants in magnetic field, strain $\varepsilon_0 = 1 - c/a$ is given by tetragonal lattice distortion for $a \approx b$. Additionally, the model states that the magnetic energy is limited by magnitude of the magnetic anisotropy, K_u, regardless the strength of applied magnetic field [4, 15]. This model can be used to predict existence of MIR and movement of twin boundaries in magnetic field [18, 19].

The model is just phenomenological approximation with no respect to atomic mechanism of twin boundary movement and it was shown to be broadly valid for MIR. However, the movement of individual twin boundaries has never been resolved and the model has never been tested and justified for single twin boundary. Moreover, two types of mobile twin boundaries have not been recognized until recently [13, 14, 20, 21]. To test the validity of the model we directly compare magnetic twinning stress ($\sigma_{\mathrm{mag}} = \Delta E_{\mathrm{mag}}/\varepsilon_0$) and mechanical stress equal to twinning stress (σ_{TW}) induced by compressive loading for single twin boundary of both types.

2. Methods

We used single crystal samples with composition close to stoichiometry Ni_2MnGa produced by Adaptamat Ltd. Samples were rectangular shape with sizes about $20 \times 2 \times 1$ mm^3 cut approximately along {100} planes of the parent phase. Composition of used samples is in the Table. The transformation temperature from austenite to five layered martensite (10M sometimes also 5M) varied from 310 to 340 K as it strongly depends on composition. All experiments were done at room temperature, far enough

*corresponding author; e-mail: kopeckyv@fzu.cz

from transition, i.e. in the region in which the martensitic phase is stable. The lattice parameters only slightly depend on composition and as example for one composition the lattice parameters in the monoclinic approximation are $a = 0.5975$ nm, $b = 0.5944$ nm, $c = 0.5591$ nm, $\alpha = \beta = 90°$, $\gamma = 90.36°$ at room temperature.

TABLE

Comparison of magnetic and mechanical stress. Switching field ($\mu_0 H_{SW}$) is magnitude of magnetic field when twin boundary starts to move. σ_{mag} is calculated magnetic stress using the model and σ_{mech} is mechanical stress given from stress–strain curve. The stress is determined with error less than 10%. Composition error is 0.5 at.%. R is a ratio of stress calculated as $R = \sigma_{\mathrm{mag}}/\sigma_{\mathrm{mech}}$.

sample Ni/Mn/Ga	type	$\mu_0 H_{\mathrm{SW}}$ [T]	σ_{mag} [MPa]	σ_{mech} [MPa]	R
1	I	0.256	1.572	0.865	1.82
49.8/29.0/21.2	II	0.020	0.090	0.086	1.05
2	I	–	–	–	–
49.8/29.0/21.2	II	0.042	0.268	0.311	0.86
3	I	–	–	–	–
49.8/29.4/20.8	II	0.027	0.163	0.111	1.47
4	I	0.354	1.728	1.110	1.56
50/28.5/21.5	II	0.047	0.256	0.241	1.06

Micrographs were taken by optical microscope Zeiss using Nomarski contrast (DIC) which visualizes different tilt of surface planes by different false colors. In our case the tilt originates from various twinning. The angle between two variants connected with a–c twin boundary is given approximately by $\alpha = 90 - 2\arctan(c/a)$. The angle α is usually about 3° which makes twin boundary recognisable from the side of sample where c-axis is out of plane for one of the variants and in-plane for second variant. Different trace orientation of the boundary on the surface helps further to distinguish between type I and II twin boundaries (Fig. 1). To compress the samples

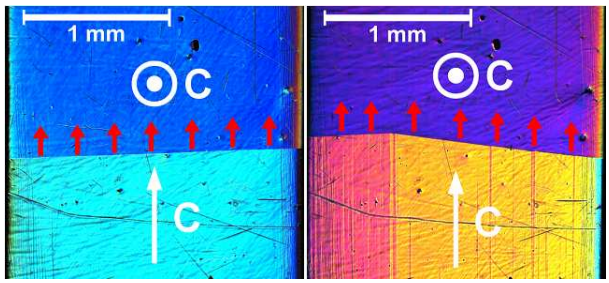

Fig. 1. Optical micrograph of twinning boundary type I (a) and type II (b) taken by optical microscope Zeiss using the Nomarski contrast (DIC). Different colours indicate different tilt of surface. Orientation of c-axis is marked in the figure. When stress or magnetic field along c-axis in plane is applied twin boundary moves as red arrows show. The boundaries are on the same sample and about same place as fiducial marks (scratches, voids) demonstrate.

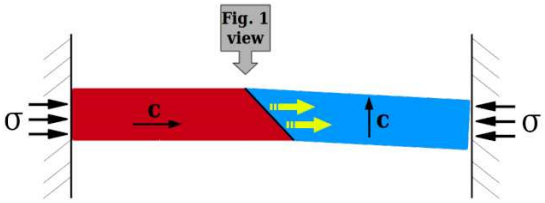

Fig. 2. Mechanical compressive stress inducing the growth of favourable variant (red) at the expense of the other one with c-axis perpendicular to stress by twin boundary motion (yellow arrows) resulting in large strain. The upper arrow points to the place where optical observation of twin boundary (Fig. 1) was made.

we used small custom-made stress-strain machine with step motor and linear transmission that produce continuous movement with constant rate. The sample was put between two parallel flat heads without further fixing to accommodate the large deformation due to twin boundary motion (Fig. 2). The force was measured by sensor which can be loaded up to ±10 N. The deformation strain was calculated from linear shift of the motor and initial sample's dimensions.

The magnetic force or magnetic energy was determined from the magnetization curves. These were measured by vibrating sample magnetometer (VSM) PAR with electromagnet up to 1.4 T. From the magnetization curve of material exhibiting MIR, the field, needed to move twin boundary called switching field, can be determined. The move of twin boundary is indicated by the sharp increase of magnetization [4, 22]. From this switching field the magnetic energy, ΔE_{mag}, was determined as area between magnetization curves of both variants, i.e variants with easy axis along and perpendicular to the field [4]. We neglect the effect of demagnetization as the sample was long and thus the correction is small.

Whole experiment run in several steps. We formed mechanically single twin boundary type I or type II. Using tensile stress we placed the boundary approximately 3 mm from the edge of the sample. Then we did compression stress–strain test. To get the boundary back to the starting position we stretched the sample again. After repeating the procedure few times the last compression run was interrupted. Without increasing forced deformation from the device the twin boundary stopped moving and stayed at the position. We removed the sample from the device and without delay installed into VSM and measured magnetization curve. As the twin boundary was not constrained, the boundary should start to move in the field which corresponds to the last value of compressive stress. After that we formed again the single twin boundary but of different type and repeated the measurement cycle.

3. Results and discussion

Figure 1 shows the optical micrographs of the trace of twin boundary type I and II on (100) surface. Importantly both boundaries were formed in the same sample

and moved to approximately same position. Both twin boundaries are macrotwin boundary between twins with internal twinned structure [12–14]. The type I is straight as it runs along (101) plane but it contains a/b twinning which, though, cannot be resolved in optical microscopy. In contrast, type II boundary is inclined from (101) plane by about four degrees and in addition to a/b twinning it contains also monoclinic twinning. The monoclinic twinning can be readily identified in the variant with c-axis in plane as it forms surface relief, which is equal to twice monoclinic distortion. This twinning changes the orientation of the macrotwin boundary resulting in zigzag line of the boundary as shown in Fig. 1. In addition to much lower twinning stress, this zigzag pattern can serve as easy identification of type II twin boundary [13, 14, 23].

Figure 3 shows the typical compression test for both boundaries. Both boundaries went in the same direction through the approximately same part of the sample, but it was impossible to locate the initial position of the boundary on the exactly same place. Although the boundaries moved across the same sample the stress needed to move the boundary sharply differed and the character of the dependency varied. It is about ten times easier to move type II twin boundary than type I and the mechanical stress is in the range of tenths of MPa. Peaks in the plateau, particularly for twin boundary type I, seems to be connected to surface scratches. The observed fluctuations can be also caused by some internal inhomogeneities. For type II the connections seem to be somehow weaker as the stress–strain curve is mostly flat.

We tried to study movement of both twin boundaries by compression in each sample. Nevertheless, sometimes it was not possible to measure the stress–strain curve of twin boundary type I as the energy needed to move this boundary was larger than energy for nucleation twin boundary type II.

Several cycles of loading were done and all measured curves were roughly similar. The curves were not exactly identical as the movement of twin boundary is a stochastic process. Such behaviour was observed previously [13]. This added some uncertainty to the determination of the twinning stress and to comparison with magnetic force. After several cycles the loading was interrupted in some point and the magnetization curve with the same twin boundary was measured. The interruption points are marked in Fig. 3. From magnetization curves the switching field, i.e. field needed to move twin boundary, was determined. The magnetic energy ΔE_{mag} was calculated and then we obtained equivalent magnetic stress according to Eq. (1). The results from magnetic measurement are collected and compared with mechanical stress–strain testing in the Table. To facilitate the comparison, the ratio of magnetic and mechanic stress is also listed ($R = \sigma_{\mathrm{mag}}/\sigma_{\mathrm{mech}}$).

The Table shows reasonable agreement for type II as the difference is mostly within experimental error. However, for type I the difference is consistently large. The magnetic force exceeds the mechanical one almost up to

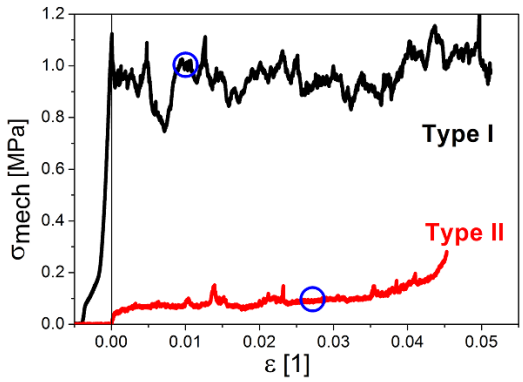

Fig. 3. Stress–strain curves of the same sample utilizing single type I and type II twin boundary movement. Evolution of compressive load affecting the sample with single twin boundary (alloy 1). Several cycles were done for each type of boundary and all of them were roughly similar. Here it is shown one of each as an example. The last cycle was interrupted for magnetic measurement at marked place (blue circle).

factor of two. It suggests that used model is invalid for type I but for disproving widely accepted model much more experiments would be needed. Additionally, the model seems to be valid for type II twin boundary. We can speculate that the model is valid and observed lower mechanical stress compared to magnetic one is due to existence shear stress originated from firm fixture of sample during the test. The forces involved are quite small and thus any additional non-axial loading might affect the measurement (see Fig. 2). In magnetic field there is no such additional force as the field is homogeneous and purely uniaxial. Moreover, the effect of magnetic domains configuration [24] and its interaction with twinning boundary is neglected.

Here, we can only conclude that the observed difference is quite puzzling. For solving this puzzle more experiments are needed which may lead to reformulation of the model. It is not helpful that the mechanism of the twin boundary motion, neither in magnetic field, nor under mechanical stress is known to great detail.

4. Conclusion

We studied the movement of single type I and II twin boundary resulting in structure reorientation in Ni–Mn–Ga magnetic shape memory alloy. We were able to form both boundaries in the same samples and compared their individual behaviour. To evaluate the validity of generally used model, measured mechanical and magnetic forces needed for moving the single boundary were compared. Calculated magnetic and mechanical stress generally agreed for type II, but we registered large error for type I. This somehow puzzling observation leads to some doubt about validity of the model but more detailed measurement is needed.

Acknowledgments

The work was funded by Czech Science Foundation grant to support excellence in research No. 14-36566G.

References

[1] O. Heczko, *J. Mater. Sci.* **30**, 1559 (2014).

[2] K. Ullakko, J.K. Huang, C. Kanter, V.V. Kokorin, R.C. O'Handley, *Appl. Phys. Lett.* **69**, 1966 (1996).

[3] A. Sozinov, N. Lanska, A. Soroka, W. Zou, *Appl. Phys. Lett.* **102**, (2013).

[4] O. Heczko, N. Scheerbaum, O. Gutfleisch, in: *Nanoscale Magnetic Materials and Applications*, Eds. J.P. Liu, E. Fullerton, O. Gutfleisch, D.J. Sellmyer, Springer, 2009, p. 399.

[5] O. Söderberg, I. Aaltio, Y. Ge, O. Heczko, S.-P. Hannula, *Mater. Sci. Eng. A–Struct.* **481**, 80 (2008).

[6] I. Aaltio, X.W. Liu, M. Valden, K. Lahtonen, O. Soderberg, Y. Ge, S-P. Hannula, *J. Alloy Comp.* **577**, S367 (2013).

[7] M. Kohl, M. Gueltig, V. Pinneker, R.Z. Yin, F. Wendler, B. Krevet, *Micromachines* **5**, 1135 (2014).

[8] B. Holz, L. Riccardi, H. Janocha, D. Naso, *Adv. Eng. Mater.* **14**, 668 (2012).

[9] K. Schlüter, B. Holz, A. Raatz, *Adv. Eng. Mater.* **14**, 682 (2012).

[10] J. Pons, V.A. Chernenko, R. Santamarta, E. Cesari, *Acta Mater.* **48**, 3027 (2000).

[11] K. Bhattacharya, *Microstructure of Martensite*, Oxford Univ. Press, New York 2003.

[12] H. Seiner, L. Straka, O. Heczko, *J. Mech. Phys. Solids* **64**, 198 (2014).

[13] L. Straka, O. Heczko, H. Seiner, N. Lanska, J. Drahokoupil, A. Soroka, S. Faehler, H. Haenninen, A. Sozinov, *Acta Mater.* **59**, 7450 (2011).

[14] O. Heczko, L. Straka, H. Seiner, *Acta Mater.* **61**, 622 (2013).

[15] A.A. Likhachev, K. Ullakko, *Phys. Lett. A* **275**, 142 (2000).

[16] X. Chen, Z. Moumni, Y. He, W. Zhang, *J. Mech. Phys. Solids* **64**, 249 (2014).

[17] K. Haldar, D.C. Lagoudas, I. Karaman, *J. Mech. Phys. Solids* **69**, 33 (2014).

[18] L. Straka, O. Heczko, H. Haenninen, *Acta Mater.* **56**, 5492 (2008).

[19] T. Takeshita, T. Fukuda, T. Takeuchi, *Mater. Sci. Eng. A–Struct.* **438**, 12 (2006).

[20] A. Sozinov, N. Lanska, A. Soroka, L. Straka, *Appl. Phys. Lett.* **99**, 124103 (2011).

[21] L. Straka, H. Haenninen, O. Heczko, *Appl. Phys. Lett.* **98**, 141902 (2011).

[22] O. Heczko, A. Sozinov, K. Ullakko, *IEEE Trans. Magn.* **36**, 3266 (2000).

[23] R. Chulist, L. Straka, N. Lanska, A. Soroka, A. Sozinov, W. Skrotzki, *Acta Mater.* 61, 1913 (2013).

[24] Y.L. Ge, O. Heczko, O. Soderberg, S.P. Hannula, *Scr. Mater.* **54**, 2155 (2006).

NDT&E International 69 (2015) 40–47

Contents lists available at ScienceDirect

NDT&E International

journal homepage: www.elsevier.com/locate/ndteint

Ultrasonic detection of ductile-to-brittle transitions in free-cutting aluminum alloys

Jitka Nejezchlebová [a], Hanuš Seiner [b,*], Martin Ševčík [b], Michal Landa [b], Miroslav Karlík [a]

[a] Faculty of Nuclear Sciences and Physical Engineering, Czech Technical University in Prague, Trojanova 13, 12000 Prague, Czech Republic
[b] Institute of Thermomechanics, Academy of Sciences of the Czech Republic, Dolejškova 5, 18200 Prague, Czech Republic

ARTICLE INFO

Article history:
Received 9 June 2014
Received in revised form
17 September 2014
Accepted 23 September 2014
Available online 2 October 2014

Keywords:
Aluminum alloys
Laser ultrasound
Ductile-to-brittle transition
Elastic constants
Resonant ultrasound spectroscopy

ABSTRACT

Resonant ultrasound spectroscopy (RUS) is applied to detect the ductile-to-brittle and brittle-to-ductile transitions in an AA6262 free-cutting aluminum alloy during thermal cycling. It is shown that the RUS method is sensitive enough to detect reliably the melting and solidification temperatures of micro-sized Mg_3Bi_2–Bi eutectic particles responsible for these transitions, although the volume fraction of the particles is very small (~1%) and is even decreasing with the cycling. The proposed RUS approach is compared with differential scanning calorimetry (DSC); the latter method is shown to be unable to detect the transition temperatures especially when transition intervals are broad. The results reveal that the phase transitions of the eutectic particles exhibit a significant hysteresis and pronounced asymmetry between melting and solidification.

1. Introduction

Phase transitions of micro- and nano-sized particles embedded in solid matrices exhibit several differences compared with the transitions of the same materials in bulk [1–3]. For example, the extensive acoustic and nuclear magnetic resonance studies of melting and freezing of various materials in porous glasses [4–9] showed that the transition temperatures of such particles are shifted downwards, and there is always also an observable hysteresis between melting and solidification of the particles. There are, on the other hand, only very few works concerned so far with solid-to-liquid phase transitions of metal particles in metal matrices. Recently, Kuba and Van Aken [10,11] observed melting of indium particles in an aluminum matrix by means of acoustic emission, showing that the transition is accompanied by plastic deformation of the matrix. Earlier, when studying a similar system, Malhotra and Van Aken [12] reported an internal friction peak associated with the melting of the indium particles. In both cases, the shifts of transition temperatures were observed, both upwards and downwards respective to the equilibrium transition temperature of bulk indium, depending on the microstructure and on the thermal history of the material. On the other hand, for nano-sized Pb–Sn particles embedded in an aluminum metallic glass [13], only the shifts downwards were observed.

Among the metal–matrix/metal–particles systems, the AA6262 free-cutting aluminum alloy [14,15] is of apparent interest from the application point of view. This alloy has nominally similar composition as the AA6082 (or AA6061) Al–Mg–Si alloy, but its machinability is enhanced by additions of small amounts of Pb and Bi that form micro-sized particles dispersed in the aluminum matrix. These particles have a rather complex, multi-component structure [16], including also some amount of the Mg_3Bi_2–Bi eutectic. At the melting temperature of this eutectic, the particles partially melt and the alloy undergoes a ductile-to-brittle transition (DBT) due to liquid metal embrittlement. This is advantageous for machining, since the local melting of the Mg_3Bi_2–Bi eutectic close to the cutting tool decreases the strength of the material and results in formation of short and breakable chips. Thus, the knowledge of the DBT temperature is essential for designing the machining process; of similar importance is also the knowledge of the possible evolution of this transition temperature during thermal cycling (i.e. repeated melting and solidification of the eutectic due to temperature oscillations), since it reflects the changes of the properties of the material during machining.

Let us point out that the DBTs in AA6262 and similar alloys (cf. [17,18]) are of a completely different nature than in conventional structural materials such as low-carbon steels, where the embrittlement occurs due to reduction of dislocation slip, and where, thus, the possibilities of ultrasonic non-destructive detection of the DBT temperatures are limited [19–21]. In the case of AA6262, the DBT temperature can be detected indirectly from detecting the melting and freezing points of the embedded particles, for example by differential scanning calorimetry (DSC). However,

* Corresponding author.
E-mail address: hseiner@it.cas.cz (H. Seiner).

http://dx.doi.org/10.1016/j.ndteint.2014.09.007
0963-8695/

due to the small volume fraction of the Pb+Bi particles (~1%), and even smaller volume fraction of the eutectic, the corresponding exo- and endothermic DSC peaks may be small, comparable to the noise level of the DSC apparatus and incomparably smaller than the peaks from various processes in the matrix. A suitable alternative to the DSC measurements in such case can be the detection of the phase transitions from small changes of the elastic moduli of the alloy. These changes can be detected either from pulse-echo measurements of velocities of acoustic waves in the material [3,5], or by resonant ultrasound spectroscopy (RUS, [22–24]), which is a method based on measurements of free elastic vibrations of a given sample of the examined material. This method has been shown as a very sensitive tool for non-destructive detection of several phenomena in materials, for example micro-cracking [25,26], internal stresses [27] or delamination [28], and is also sensitive to structural phase transitions in small volume fractions of materials, e.g. in thin surface layers deposited on non-transforming substrates [29,30]. As observed recently by the current authors and reported briefly in [31], the RUS method is able to detect the melting of the eutectic particles in the free-cutting aluminum alloys AA6262 and AA6023 (which has a very similar composition to AA6262 but with lead partially replaced by tin) during a single heating cycle.

In this paper, we show that the RUS method can be applied for a systematic study of the DBT and reverse (BDT) temperatures in the AA6262 alloy and discuss the evolution of these temperatures due to thermal cycling. In summary, the main aim of this paper is to show that this method is able to provide a detailed information on the DBT and BDT processes in the examined alloy, and to contribute, thus, to the understanding of the response the material to the conditions it is subjected to during machining.

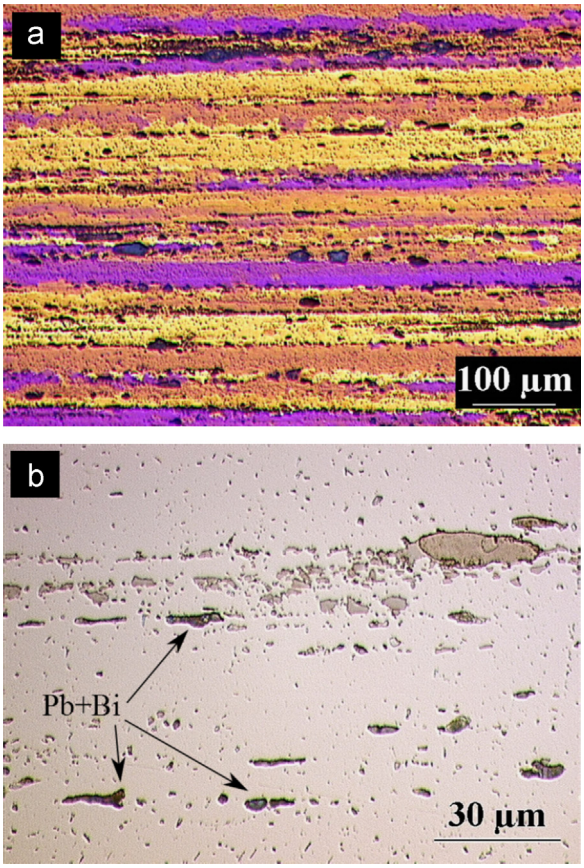

Fig. 1. Microstructure of the studied AA6262 alloy: (a) the fibrous grain structure highlighted by anodizing with Barker's reagent (b) a detail of particles containing lead and bismuth.

2. Experiment

2.1. Material and samples

The examined material was a commercial AA6262 alloy (Constellium Extrustions, Děčín, Czech Republic) fabricated in a form of extruded rods (18.8 mm in diameter). The material was set into the T8 temper (the rods were cold worked into diameter 18.1 mm (reduction 7.3%), artificial aging was performed at 160 °C for 10 h.) The resulting microstructure of the alloy is in Fig. 1: it consists of fibrous grains elongated along the extrusion direction. The particles containing Pb and Bi are dispersed in the matrix and are, as well, elongated along the extrusion direction. The nominal composition (wt.%) of the examined alloy was Al–0.97Mg–0.71Si–0.64Pb–0.60Bi–0.12Mn–0.45Fe. The presence of the DBT in this alloy was determined by Charpy tests (see [16]); the transition temperature was indicated by a sharp drop of the fracture toughness at approximately 250 °C. This temperature corresponds well to the equilibrium melting temperature of bulk Mg_3Bi_2–Bi eutectic, which is $T=260$ °C [32], especially when taking into account the possible shift of the transition temperatures downwards due to the small size of the particles. To obtain some estimates of the evolution of the transition temperatures with thermal cycling prior to the RUS measurements, the AA6262 alloy was studied by DSC, using a DSC8500 (Perkin-Elmer) apparatus (temperature calibrated by tin, indium and lead; heat flow calibrated by melting heat of pure indium; the measurements were performed under a 20 ml/min flow of pure nitrogen). These measurements were performed on a small (~40 mg) sample of this alloy during five subsequent thermal cycles from the room temperature up to 400 °C, at the heating/cooling rates of 10 °C/min. The DSC results (see Section 3.1) were then used as a complement to the RUS measurements and for a comparison of both methods. For the RUS measurement itself, a $2.61 \times 3.21 \times 2.94\ mm^3$ (accuracy ± 0.01 mm) rectangular parallelepiped was prepared with the edges oriented along the processing directions.

In order to enable a comparison of the behavior of the examined AA6262 alloy to some reference material, an additional RUS sample was prepared from a commercial AA6082 alloy (Constellium Extrusions, Děčín, Czech Republic) subjected to the same thermal and mechanical treatment. The AA6082 has nominally very similar composition to AA6262 (Al–0.79Mg–1.08Si–0.44Mn–0.37Fe (wt.%)), but without the Pb and Bi additions, so the difference between the AA6262 and AA6082 RUS spectra evolution can be ascribed solely to the DBT and BDT transitions. The AA6082 sample was a $0.75 \times 2.61 \times 2.79\ mm^3$ (accuracy ± 0.01 mm) rectangular parallelepiped.

2.2. RUS measurements

Prior to the thermal cycling, the room temperature (RT) elastic constants of the above described AA6262 and AA6082 samples were determined by a combination of RUS measurements and conventional pulse-echo technique. The contact-less laser based RUS method was used; this modification of RUS employs a broadband laser pulse for thermoacoustic excitation of the vibrations and a scanning laser vibrometer for detection of the response of the sample and for determination of the individual modal shapes (see [33] for more details on the applied methodology and on the instrumentation). The aim of this preliminary measurement was to investigate whether the fibrous structure induces any measurable elastic anisotropy to the material. Such anisotropy could, consequently, affect the interpretation of the RUS spectra at higher temperatures.

Table 1
Temperature ranges of the thermal cycles applied to the AA6262 and AA6082 samples; RT denotes the room temperature.

Sample	Cycle no.	Temperatures
AA6262	1	RT→290 °C→RT
	2	RT→350 °C→RT
	3	RT→290 °C→RT
	4	RT→350 °C→RT
	5	RT→290 °C→RT
AA6082	1	RT→290 °C→RT
	2	RT→350 °C→RT

After the RT measurements, the samples were subjected to thermal cycling. These measurements were performed in a high-temperature RUS chamber filled with low-pressure nitrogen atmosphere and including a Joule heating module able to set the sample temperature up to 650 °C. The vibrations were generated by a Litron Nano S pulse laser (1064 nm, pulse duration 6 ns) and detected by a Polytec OFV 505 laser vibrometer. The sample of the examined AA6262 alloy was subjected to five thermal cycles, and the reference AA6082 sample was subjected to two cycles with the respective temperature ranges listed in Table 1. The maximal temperatures were for all cycles above the expected DBT temperature for the AA626 alloy (250 °C). For the 2nd and the 4th cycle for the AA6262 alloy, the maximal temperature was chosen above the melting point of Pb ($T_{Pb} = 325$ °C), in order to inspect whether the melting and solidification of Pb inside the Pb+Bi particles has any impact on the DBT and BDT processes.[1] For the reference AA6082 alloy, the second cycle was extended also up to 350 °C to enable a direct comparison with the second cycle for the AA6262 alloy.

During each thermal cycle, the evolution of the resonant spectrum of free elastic vibrations of the sample was measured in the temperature region where the DBTs and the BDTs were expected, i.e. approximately between 150 °C and 300 °C. The temperature steps between individual measurements were chosen between 10 °C (far away from the expected transition temperatures) and 2 °C (close to the expected transition temperatures). The heating and cooling rates were slow (1 °C/min) with an additional 2 min stabilization time at each measurement temperature prior to the RUS measurement itself. This approach was chosen to ensure a homogeneity of temperature over the whole volume of the sample and during the whole period of spectra recording. The spectra were obtained in the frequency range 0.3–2 MHz, which covered approximately 40 resonant peaks at the room temperature. However, with the increasing temperature, a strong increase of the damping was observed, which reduced the number of clearly detectable peaks in the vicinity of the DBT to typically 3–5 dominant ones. As this increase of the damping was observed over the whole temperature ranges and for both the AA6262 and AA6082 samples, this effect was assumed as a property of the matrix, not of the particles, and was further not analyzed in any details.

2.3. RUS data processing

The elevated-temperature RUS data were obtained in the form of sets of resonant spectra for each thermal cycle. At the highest temperatures, only 3–5 resonant peaks were detectable in each spectrum; although such a small number of resonant modes could be in principle sufficient for some form of the inverse analysis of the elastic moduli at these temperatures [34,35], we adopted a simpler approach suggested by Peréz-Landazábal et al. [36] for estimation of temperature evolution of the shear modulus of an isotropic material (see Section 3.2. for justification of the assumption of isotropy). We took few resonant modes from the lowest part of the spectrum and determined the evolution of the corresponding resonant frequencies with temperature. These softest resonant modes are dominantly related to shear vibrations of the material, so that their resonant frequencies are proportional to the shear wave velocity, i.e. $\omega \sim v_{shear} = \sqrt{G/\rho}$, where G is the shear modulus and ρ is the mass density. Thus, the relative evolution of the shear modulus with respect to some reference value $G(T_0)$ is equal to the relative evolution of the resonant frequency squared:

$$[G(T)/G(T_0)] = [\omega(T)/\omega(T_0)]^2, \quad (1)$$

assuming that the density ρ does not change significantly. In our case, however, an additional modification of this approach was necessary. In Fig. 2, an example of the temperature evolution of one chosen peak of the AA6262 alloy during a heating run of one thermal cycle is shown. The quality of the peak rapidly decreases due to the increase of damping mentioned in the previous subsection. It is seen that the peak drifts with nearly constant slope to lower frequencies with the increasing temperature, which indicates a significant softening of the Al–Mg–Si matrix due to heating. The same constant softening was observed also for the AA6082 alloy. Within the shown temperature interval, the resonant frequency decreases from 713 kHz to 690 kHz, which, according to (1), corresponds to an approximately 6.5% decrease of the shear modulus.[2] Since the changes are small compared with the value of G, this decrease of G can be assumed as approximately linear as well. However, the changes of the shear modulus due to melting/solidification of the eutectic particles at the DBT/BDT temperatures are expected to be proportional to the volume fraction of the eutectic ($< 1\%$), and thus, it is necessary to subtract

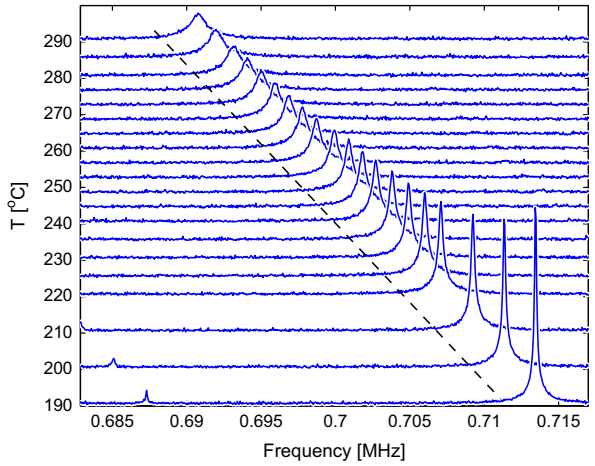

Fig. 2. An example of evolution of one resonant peak with temperature during a heating run for the AA6262 sample. The dashed line outlines the global linear trend (G_0').

[1] In principle, the melting of the Pb components of the particles should also be detectable by the RUS measurements. However, due to the below discussed high damping above approximately 300 °C, such analysis was not possible. As it follows from the Charpy tests, the DBT appears already due to melting of the Mg_3Bi_2–Bi eutectic, so the analysis of further melting of Pb inside the particles is not of any significant importance from the application point of view.

[2] Some part of the drift can also be attributed to the thermal expansion of the material and the consequent changes in the dimensions of the sample and the density. Nevertheless, for the 100 °C temperature increase the corresponding changes of the resonant frequencies calculated for the thermal expansion coefficient of aluminum (2.3×10^{-5} K $^{-1}$) should be approximately 0.1%, i.e. by more than one order of magnitude smaller than those observed experimentally.

the overall linear trend from the $G(T)$ evolution in order to emphasize the localized changes at the transition temperatures. For this reason, the quantity used from hereafter to describe the changes of the shear modulus with the temperature will be

$$\delta G(T) = \frac{G(T) - (T - T_0)G'_0}{G(T_0)} = \frac{[\omega(T)]^2 - G'_0 T}{[\omega(T_0)]^2}, \quad (2)$$

where T_0 is the lowest temperature for each measurement, and G'_0 is the linear slope estimated by fitting the first four values of $G(T)/G(T_0)$ by linear regression. In other words, the quantity δG represents the relative changes of the shear modulus along the heating or cooling run of the given cycle separated from such a global linear trend that $\mathrm{d}\delta G/\mathrm{d}T = 0$ at T_0.

For each run of the measurement, the $\delta G(T)$ curves were determined for three or four different modes. In all cases, these curves did not differ from each other by more than 2–3% of the maximal value of $|\delta G(T)|$. This confirms well our assumptions that the frequencies of these modes correspond dominantly only to the shear modulus G and that the material behaves approximately isotropically, and justifies the use of the parameter (2) for characterization of the changes of elasticity of the examined materials. An additional quantitative analysis of the dominant effect of shear modulus on the lowest resonant frequencies for the chosen samples is given within the discussion of the RT elastic constants in Section 3.2.

3. Results and discussion

3.1. Differential scanning calorimetry

The results of the DSC measurements for the AA6262 alloy are in Fig. 3. The left part of this figure (Fig. 3(a)) shows the evolution of the DSC heating curves with five subsequent thermal cycles from the room temperature up to 400 °C. It can be seen that in the first cycle the DBT induces a small but clearly visible endothermic peak at approximately 257 °C, albeit overlapped with the precipitation peak of the Mg_2Si particles in the matrix. The DBT peak remains similarly pronounced in the second cycle; nevertheless, it appears to be broader and slightly shifted towards lower temperatures. Starting from the third heating run, the DBT peak becomes comparable to the DSC device noise and the exact temperature ranges within which the melting of the particles appears is not detectable. For the cooling runs (Fig. 3(b)), the BDT reverse peaks are even less pronounced than for the heating runs. After the second thermal cycle, the exothermic peak indicating the BDT transition becomes indistinguishable from the noise and it fully disappears in the fourth and fifth cycles. It is clearly seen that the DSC characterization is insufficient for any detailed analysis of the DBT and BDT processes in the examined alloy.

The discussion of why the melting and solidification of the eutectic particles gradually vanishes with thermal cycling falls beyond the scope of this paper and is given elsewhere [16]. Here we mention only that the main mechanism is probably the diffusion of magnesium atoms from the matrix into the molten particles and the consequent increase of the volume fraction Mg_3Bi_2 compound over the Mg_3Bi_2–Bi eutectic in the particles. From the application point of view, it is important to investigate whether the thermal cycling may finally lead to a complete disappearance of the eutectic phase, or whether there may exist some saturated (equilibrium) volume fraction of the eutectic that does not further decrease with further thermal cycling. As shown above, this problem cannot be fully resolved from the DSC measurements; some more sensitive method is required, which, as we show in this paper, can be the resonant ultrasound spectroscopy.

3.2. RT elastic constants

For both the AA6262 and AA6082 samples, it was assumed that the material exhibits a hexagonal symmetry class (sometimes called transversal isotropy) with the anisotropy direction given by the extrusion direction and all direction perpendicular to it being equivalent [37]. The elasticity of such material can be fully described by five independent elastic constants. These are c_{11}, c_{12}, c_{13}, c_{33} and c_{44} (using the shorten Voigt's notation), providing that the anisotropy axis is aligned with the x_3 direction.

Under such assumption, the elastic constants were determined from the RT RUS measurements, using 37 resonant modes and corresponding modal shapes for the AA6262 sample and 19 resonant modes and corresponding modal shapes for the AA6082 sample, in both cases complemented by three pulse-echo measurements of phase velocities of longitudinal waves in directions perpendicular to the faces of the sample. As discussed in detail e.g. in [33], such an additional information from the pulse-echo measurements improves the stability of the inverse procedure used for the calculation of the elastic constants from the RUS spectrum and reduces the experimental errors in certain combinations of the resulting elastic constants.

The results are given in the upper part of Table 2. It is clearly seen that the addition of soft Pb+Bi particles leads to overall deterioration of the elastic stiffness of the AA6262 alloy compared

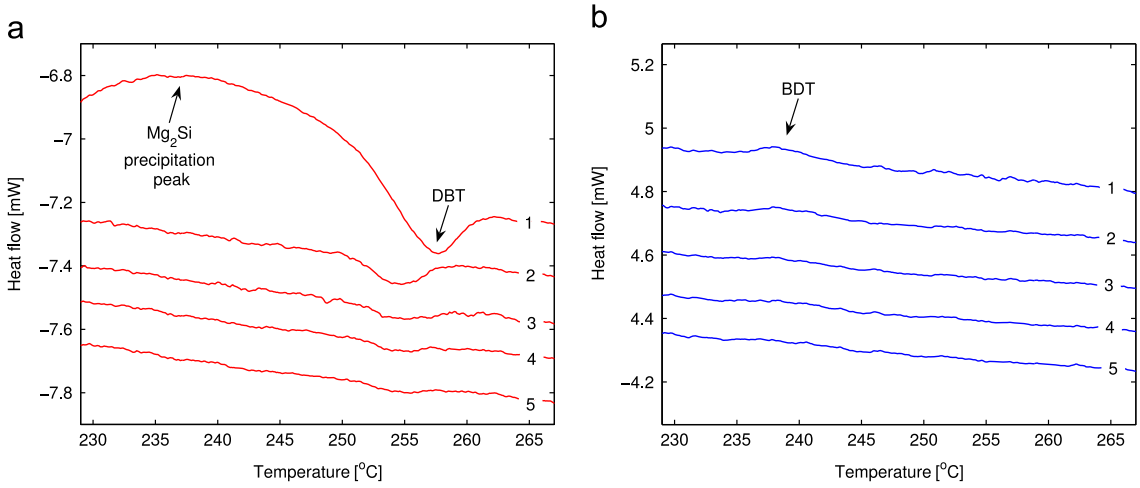

Fig. 3. DSC signals for four five subsequent thermal cycles of the AA6262 alloy. On the left: heating runs; on the right: cooling runs.

with AA6082; the softening is in the range 2–10% for all independent coefficients, which is quite strong with respect to the small volume fraction of the particles.

Nevertheless, both alloys exhibit only very weak deviations from elastic isotropy; the differences $c_{11}-c_{33}$, $c_{12}-c_{13}$ and $c_{44}-c_{66}$ are fully within the range of the respective experimental errors. This means that both samples can be treated approximately elastically isotropic for the high-temperature measurements. In the lower part of Table 2, the closest isotropic elastic constants (the shear modulus G and the bulk modulus K) are given. It is clearly seen that the Pb+Bi particles soften mainly the bulk modulus K, while the shear modulus is nearly unaffected. Since the Pb+Bi particles exhibit very strongly anisotropic spatial arrangement in the microstructure of the AA6262 alloy (see Fig. 1), it is plausible that their melting at the DBT temperature may lead to some additional anisotropization of the material. However, as shown in the next subsection, the changes of the shear modulus accompanying the transitions are smaller than 0.5%, so even above the DBT temperature the deviations from isotropic behavior are rather negligible.

The obtained RT elastic constants for both samples were also used to verify the assumption used for the high-temperature spectra analysis, that the lowest resonant modes are dominantly sensitive to G, while the sensitivity to K is significantly lower. For the first detectable ten modes for both AA6262 and AA6082 samples, the partial derivatives $\partial f/\partial G$ at constant K and $\partial f/\partial K$ at constant G were numerically calculated, where $f=\omega/2\pi$ stands for the resonant frequency of the given mode. The results are summarized in Fig. 4; for each mode, the values of these derivatives are listed together with an estimate of the possible relative error in the evolution of G calculated via the relation (1) when the effect of K is neglected and when assuming that the changes of G and K are comparable. In a linear approximation of the first order, such an error can be calculated as

$$\delta \approx \frac{\left(\frac{\partial f}{\partial K}\right)}{\left(\frac{\partial f}{\partial K}\right)+\left(\frac{\partial f}{\partial G}\right)}. \tag{3}$$

It is clearly seen that the above mentioned assumption is well satisfied, as this error does not exceed 7% for any of the modes, and is lower than 3% for most of the modes. The first mode for both samples is sensitive only to G; there is also one specific modal shape (mode no. 8 for the AA6262 sample and mode no. 3 for the AA6082 sample) where the sensitivity to K is the highest. In summary, the errors given on Fig. 4 are in good agreement with the differences between the $\delta G(T)$ curves for the individual modes mentioned at the end of Section 2.3.

Table 2
Room temperature elastic constants of the examined alloys. In the last two rows, the closest isotropic shear modulus G and bulk modulus K for each material are given.

	AA6262	AA6082
c_{11} (GPa)	110.4 ± 0.9	121.3 ± 1.8
c_{12} (GPa)	57.8 ± 0.9	68.1 ± 1.9
c_{13} (GPa)	56.5 ± 0.8	66.9 ± 1.7
c_{33} (GPa)	108.5 ± 0.7	118.3 ± 1.8
c_{44} (GPa)	26.2 ± 0.1	26.9 ± 0.2
c_{66} (GPa)[a]	26.3 ± 1.3	26.6 ± 2.6
G (GPa)	26.2 ± 0.4	26.8 ± 0.9
K (GPa)	74.5 ± 1.3	84.9 ± 2.0

[a] Calculated as $(c_{11}-c_{12})/2$.

3.3. RUS detection of the transition temperatures

Fig. 5 shows the evolution of δG during heating (a) and cooling (b) runs of two subsequent thermal cycles for the reference AA6082 sample. It is seen that while the cooling curves have a very similar character for both the first and the second cycle, there is a significant increase of δG above 190 °C for the first heating run that fully absents for the second heating run. In agreement with the DSC measurement, this increase can be identified as a result of Mg_2Si precipitation. All other curves are smooth and concave, which indicates that the softening of the matrix is slightly faster than purely linear. However, these deviations from the linear trend are in the order of 10^{-3}, i.e. negligible compared with the linear trend shown in Fig. 2.

The results obtained for the AA6262 sample are shown in Figs. 6 (heating runs) and 7 (cooling runs). For the first heating run, the Mg_2Si precipitation again induces some hardening at above 180 °C, which is however, interrupted at 253 °C by a sharp decrease indicating the melting of the eutectic particles. This decrease of magnitude $\delta G_{DBT}=1.65\times10^{-3}$ is finished at 262 °C.

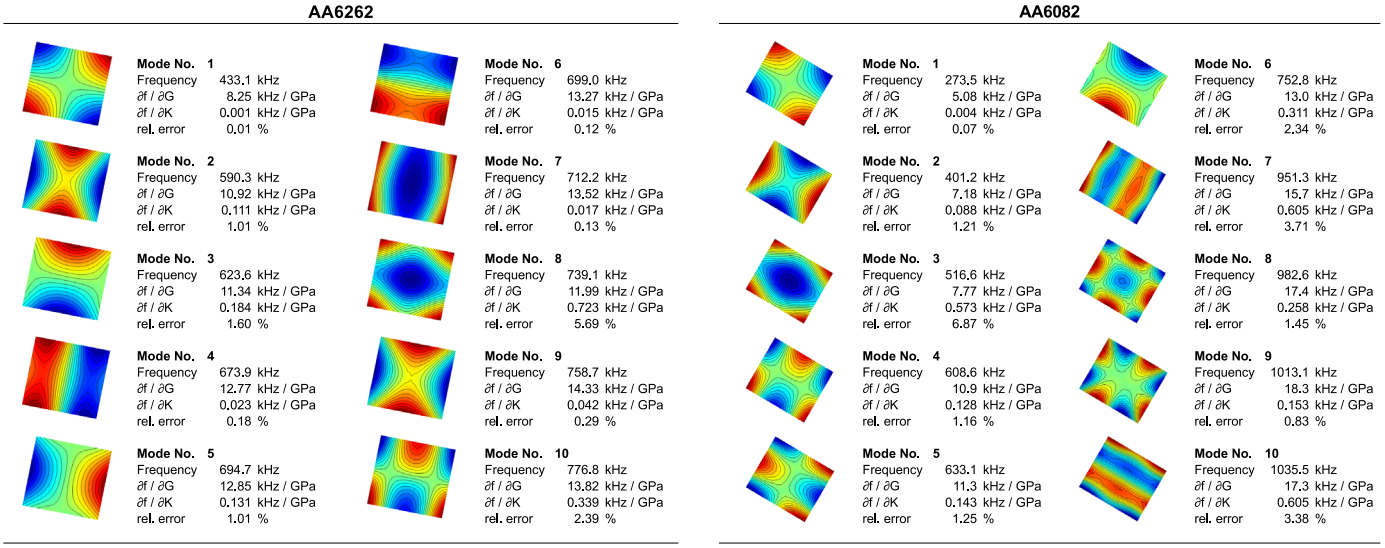

Fig. 4. Sensitivities of the individual resonant modes of the AA6262 sample (on the left) and the AA6082 sample (on the right) to the shear modulus G and the bulk modulus K. The relative errors in $\delta G(T)$ expectable due to neglecting the effect of K on the spectrum are estimated by the formula (3). The modal shapes are represented by contour plots of the out-of-plane displacement field amplitudes at the largest face for each sample.

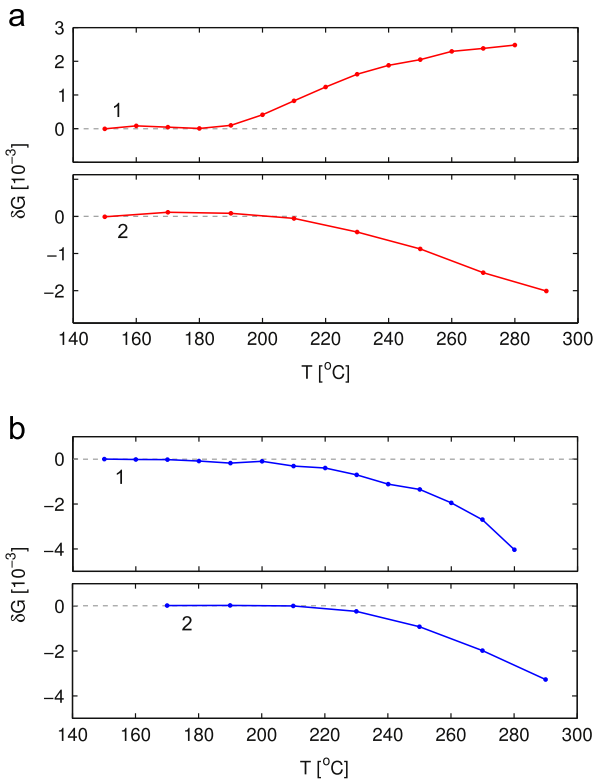

Fig. 5. Evolution of δG with temperature during the heating runs (a) and cooling runs (b) of the AA6082 for two subsequent thermal cycles. The numbers denote the number of the cycle.

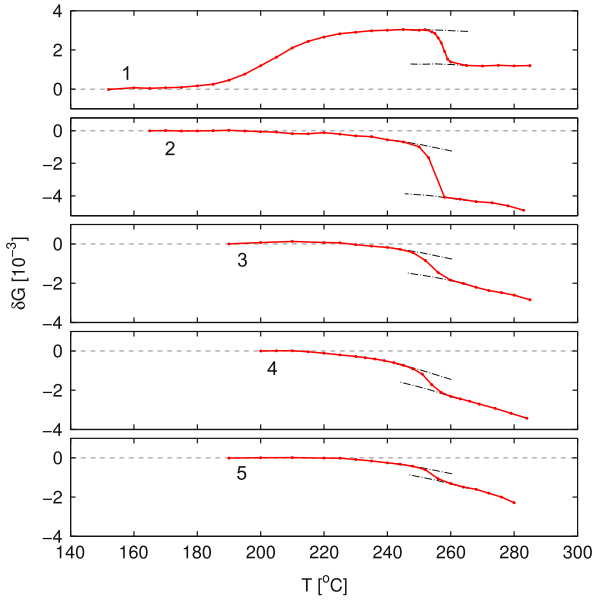

Fig. 6. Evolution of δG with temperature during the heating runs for five subsequent thermal cycles. The numbers 1–5 denote the cycle numbers, the dash-dot lines are guides for eye indicating approximate regions of the BDT transitions.

The maximal slope $\mathrm{d}(\delta G)/\mathrm{d}T$ appears approximately at $T_{\mathrm{DBT}} = 257\ ^{\circ}\mathrm{C}$, which corresponds exactly to the DSC peak. Similarly sharp decreases of δG can be seen also for all other heating runs. The transition temperature for the second cycle is slightly shifted downwards ($T_{\mathrm{DBT}} = 254\ ^{\circ}\mathrm{C}$), which is, again, in agreement with DSC. For the third and further cycles, this temperature remains approximately the same, and so does the width of the transition intervals ($\sim 10\ ^{\circ}\mathrm{C}$). On the contrary, the magnitude of

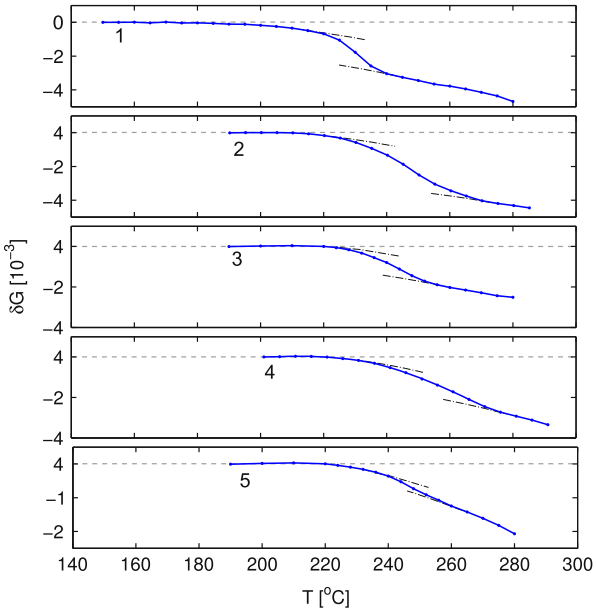

Fig. 7. Evolution of δG with temperature during the cooling runs for five subsequent thermal cycles. The numbers 1–5 denote the cycle numbers, the dash-dot lines are guides for eye indicating approximate regions of the DBT.

the jump associated with the transition (δG_{DBT}) changes significantly due to the cycling. A maximum appears in the second cycle ($\delta G_{\mathrm{DBT}} = 2.9 \times 10^{-3}$ after subtracting the overall concave trend of the curve), which can be, however, affected by the fact that in the first cycle the softening from the DBT still superposes with the stiffening due to the Mg_2Si precipitation. Further on, the value of δG_{DBT} gradually decreases from 1.5×10^{-3} (the third cycle) to 0.6×10^{-3} (the fifth cycle). The evolutions of the DBT temperatures, of the widths of the transition interval and of the δG_{DBT} do not seem to be anyhow affected by the overheating (above T_{Pb}) in the second and the fourth cycle.

A significantly different picture is obtained for the cooling runs (Fig. 7). In the first run, the stiffening appears in a broad temperature interval (from 240 °C to 220 °C) with the magnitude $\delta G_{\mathrm{BDT}} = 2.7 \times 10^{-3}$. The maximal change of the slope indicating the BDT temperature appears approximately at $T_{\mathrm{BDT}} = 235\ ^{\circ}\mathrm{C}$, which is, again in agreement with the DSC prediction. Similar widths of the BDT intervals ($\sim 20\ ^{\circ}\mathrm{C}$, i.e. two times broader than for the DBTs) can also be seen for the third and the fifth thermal cycle, i.e. for those cycles for which the maximal temperature did not exceed T_{Pb}. The BDT temperatures for these cycles systematically increase up to $T_{\mathrm{BDT}} = 250\ ^{\circ}\mathrm{C}$ for the fifth cycle. This means that the hysteresis between the DBT and BDT transition gradually decreases with the increasing number of cycles, while the asymmetry between the widths of the respective transition intervals remains the same. Let us mention that such asymmetry is reversed compared to the one observed by Borisov et al. [9] for gallium particles in porous glasses, where the melting of the particles was quite smooth and within a broad interval, while the freezing appeared abruptly at a certain temperature. The decreasing width of the hysteresis indicates that the material undergoes gradual changes due to thermal cycling; a possible explanation of this effect is that the changes of the density of the eutectic particles during melting and solidification induce cyclic plastic deformation of the matrix (as observed by Kuba and Van Aken [10,11]), and, consequently, the thermal cycling results in an elastic shakedown effect [38]. Such conjecture must be, however, further confirmed by a detailed analysis of the residual stresses in the vicinity of the particles as well as by mathematical modeling of the melting/solidification processes in the given microstructure within the

frame of continuum mechanics, which both fall beyond the scope of this paper.

For the second and the fourth cycle the changes of δG occur in very broad intervals (~40 °C) and are significantly larger than the values of δG_{DBT} in the subsequent heating runs. This means that overheating of the materials above the melting point of Pb significantly affects the BDT process, while the reverse transitions in the next cycles seem to be unaffected. The broad width of the BDT intervals in these two runs gives also a direct explanation of why no corresponding exothermic peaks were detected in the DSC measurements (notice that the maximum temperatures of the cycles for the DSC measurements were all equal to 400 °C).

On the other hand, for such broad temperature intervals the detection of exact temperatures of the initiation and termination of the BDT is necessarily less accurate. The inflection points at the $\delta G(T)$ curves indubitably indicate that these transitions occur, but the changes of the $d(\delta G)/dT$ slope at the limits of the transition interval are much less pronounced, especially at the BDT finish temperature where the effect of the transition superposes with the allover concave character of the $\delta G(T)$ curve for the matrix. In such cases, it is necessary to make a more detailed analysis of the $d(\delta G)/dT$ slope. As known from the AA6082 sample measurements, the $\delta G(T)$ curve for the matrix in the given temperature interval is decreasing, smooth, but not exhibiting any sharp changes of the slope. Let us assume in the sense of Voigt's homogenization scheme that the slope can be expressed as

$$d(\delta G)/dT = (1-\lambda)d(\delta G_{matrix})/dT + \lambda d(\delta G_{particles})/dT, \quad (4)$$

where λ is the volume fraction of the particles, and let us further consider that $d(\delta G_{particles})/dT$ exhibits no significant changes outside the transition interval. Above the transition interval, where the material of the particles is melted, the shear modulus of the liquid can be considered as incomparably smaller than the shear modulus of the particles in the frozen state; consequently, the changes of $G_{particles}$ due to temperature evolution of the viscosity of the melt above the transition should be negligible compared to the $(\delta G_{particles})/dT$ slope in the solid state.

In this sense, the transition interval can be estimated as such an interval outside which the $d(\delta G)/dT$ slope can be fitted by one smooth function $d(\delta G_{matrix})/dT$ plus a finite jump in $d(\delta G_{particles})/dT$. The character of the smooth function is unknown, but can be estimated from the behavior of the $d(\delta G)/dT$ slope for the AA6082 sample in the same temperature range. A comparison of the $d(\delta G)/dT$ slopes for the AA6262 and AA6082 samples in the cooling run of the second thermal cycle is given in Fig. 8. It is clearly seen that up to approximately 220 °C, the $d(\delta G)/dT$ curves are very similar. At higher temperatures, however, the AA6262 slope exhibits a sharp drop with a minimum at approximately 247 °C, and then levels out above 265 °C at some approximately constant value, that is, however, significantly higher for the AA6082 sample. This behavior enables us to estimate the BDT interval as the interval 220–265 °C; outside this interval, the evolution of the slope is smooth and similar as for the AA6082 alloy plus the above discussed finite jump due to melting of the particles.

Nevertheless, although the above given analysis enables some estimation of the transition temperatures even for very broad transition intervals, and gives also some deeper insight into the elasticity changes of the alloy during the transition, the localization of the transition temperatures in such a case is still significantly less accurate than for the heating runs, where the changes are sharp and well detectable. The peak in the $d(\delta G)/dT$ slope seen in Fig. 8 is somehow more pronounced than the corresponding peaks in the DSC measurements. In this case, however, the determination of the transition temperatures from the RUS results requires a relatively extensive processing of the experimental data, so the advantage of the RUS approach over DSC becomes questionable.

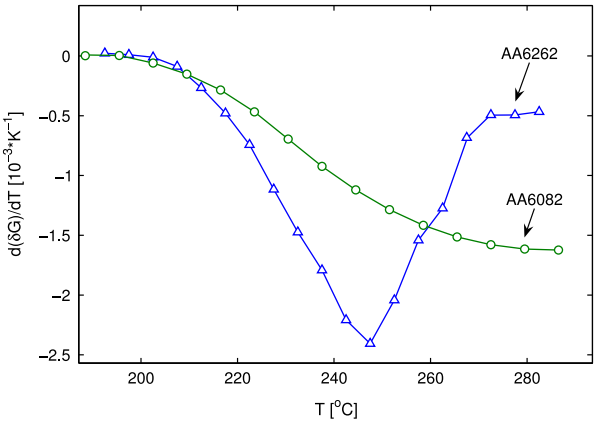

Fig. 8. Temperature evolutions of the $d(\delta G)/dT$ slopes for the AA6262 and AA6082 samples during the cooling runs of the second thermal cycles. For the AA6262 sample the slope was obtained from the experimental data by four-point finite differences, for the AA6082 sample (where the number of the experimental points is lower), the experimental data were fitted by bi-cubic spline functions and the slope was then calculated analytically.

4. Conclusions

The approach proposed in this paper for non-destructive detection of DBTs and BDTs in free-cutting aluminum alloys was shown to be more efficient than the use of DSC especially after two or more thermal cycles, when the volume fraction of the transforming particles decreases below the resolution limit of DSC. As seen for the heating run of the first cycle, the elasticity changes due to the melting of the eutectic particles are fully comparable to those resulting from the structural processes in the Al–Mg–Si matrix (Mg_2Si precipitation). The RUS approach enables to detect also the transitions spread over broad temperature intervals, for which the DSC peaks are absent. In addition, the obtained results enable a semi-quantitative analysis of the DBT and BDT processes by observing the evolution of the δG_{DBT} and δG_{BDT} values and of the resulting widths of the hysteresis and the freezing/melting asymmetries. This analysis indicates that the DBTs and the BDTs in free-cutting aluminum alloys such as AA6262 are complex processes, combining probably the diffusion-driven composition changes and the redistribution of elastic and plastic strains in the vicinity of the particles.

Acknowledgment

This work has been financially supported by the AdMat project of the Czech Science Foundation (14-36566G).

References

[1] Christenson HK. Confinement effects on freezing and melting. J Phys Condens Matter 2001;13:R95–133.
[2] Alcoutlabi M, McKenna GB. Effects of confinement on material behaviour at the nanometre size scale. J Phys Condens Matter 2005;17:R461–524.
[3] Charnaya EV. Acoustic studies of phase transitions in crystals and nanocomposites. Acoust Phys 2008;54:802–13.
[4] Borisov BF, Charnaya EV, Hoffmann WD, Michel D, Shelyapin AV, Kumzerov YA. Nuclear magnetic resonance and acoustic investigations of the melting-freezing phase transition of gallium in a porous glass. J Phys Condens Matter 1997;9:3377–86.
[5] Charnaya EV, Plotnikov PG, Michel D, Tien C, Borisov BF, Sorina IG, et al. Acoustic studies of melting and freezing for mercury embedded into Vycor glass. Phys B 2001;299:56–63.

[6] Borisov BF, Charnaya EV, Plotnikov PG, Hoffmann WD, Michel D, Kumzerov YA, et al. Solidification and melting of mercury in a porous glass as studied by NMR and acoustic techniques. Phys Rev B 1998;58:5329–35.
[7] Pirozerskii AL, Charnaya EV, Latysheva EN, Nedbai AI, Kumzerov YA, Bugaev AS. Acoustic studies of melting and crystallization of indium–gallium alloy in porous glass. Acoust Phys 2011;57:637–41.
[8] Borisov BF, Charnaya EV, Loeser T, Michel D, Tien C, Wur CS, et al. resistance and acoustic studies of the melting-freezing phase transition of gallium in Vycor glass. J Phys Condens Matter 1999;11:10259–68.
[9] Borisov BF, Charnaya EV, Kumzerov YA, Radzhabov AK, Shelyapin AV. Phase-transitions for gallium microparticles in a porous-glass. Solid State Commun 1994;92:531–3.
[10] Kuba MM, Van Aken DC. Analysis of acoustic emission during the melting of embedded indium particles in an aluminum matrix: a study of plastic strain accommodation during phase transformation. Metal Mater Trans A 2013;44A:3444–55.
[11] Kuba MM, Van Aken DC. Plastic strain accommodation and acoustic emission during melting of embedded particles. Mater Lett 2012;77:89–92.
[12] Malhotra AK, Van Aken DC. Experimental and theoretical aspects of internal-friction associated with the melting of embedded particles. Acta Metal Mater 1993;41:1337–46.
[13] Khan PY, Bhattacharya V, Biswas K, Chattopadhyay K. Melting and solidification behavior of Pb–Sn embedded alloy nano-particles. J Nanopart Res 2013;15:2049.
[14] Han Q. The effect of microstructure on the surface finish of extruded 6262 aluminum alloy billet. In: Aluminum Alloys: Fabrication, Characterization and Applications II—TMS 2009 Annual Meeting and Exhibition; San Francisco, CA; United States; 15–19 February 2009; Code 75664, TMS Annual Meeting 2009. p. 95–100.
[15] Wouters O, De Hosson JThM. Lead induced intergranular fracture in aluminum alloy AA6262. Mater Sci Eng A 2003;361:331–7.
[16] Karlík M, Faltus J, Nejezchlebová J, Haušild P, Harcuba P. Characterisation of Al–Cu and Al–Mg–Si Free-Cutting Alloys. Mater Sci Forum 2014;794–796:1181–6.
[17] Miyagi T, Koizumi H. Ultrasonic attenuation of polycrystalline aluminum wetted with liquid gallium. Mater Sci Eng A 2006;442:184–6.
[18] Elgallad EM, Samuel FH, Samuel AM, Doty HW. Machinability aspects of new Al–Cu alloys intended for automotive castings. J Mater Process Technol 2010;210:1754–66.
[19] Smith RL, Reynolds WN. The correlation of ultrasonic-attenuation, microstructure and ductile to brittle transition-temperature in very low-carbon steels. J Mater Sci 1982;17:1420–6.
[20] Kardashev BK, Nefagin AS, Ermolaev GN, Leont'eva-Smirnova MV, Potapenko MM, Chernov VA. Internal friction and brittle–ductile transition in structural materials. Tech Phys Lett 2006;32:799–801.
[21] Vertesy G, Tomas I, Takahashi S, Kobayashi S, Kamada Y, Kikuchi H. Inspection of steel degradation by magnetic adaptive testing. NDT & E Int 2008;41:252–7.
[22] Migliori A, Sarrao JL, Visscher WM, Bell TM, Lei M, Fisk Z, et al. Resonant ultrasound spectroscopic techniques for measurement of the elastic-moduli of solids. Phys B 1993;183:1–24.
[23] Leisure RG, Willis FA. Resonant ultrasound spectroscopy. J Phys Condens Matter 1997;9:6001–29.
[24] Yaoita A, Adachi T, Yamaji A. Determination of elastic moduli for a spherical specimen by resonant ultrasound spectroscopy. NDT & E Int 2005;38:554–60.
[25] Adachi T, Kondo Y, Yamaji A, Yang SH, Yang IY. Nondestructive evaluation of micro-cracks in a ceramic ferrule by resonant ultrasound spectroscopy. NDT & E Int 2005;38:548–53.
[26] Seiner H, Sedlák P, Bodnárová L, Landa M, Stráská J, Janeček M. In-situ detection of surface micro-cracking in ultrafine-grained AZ31 magnesium alloy by resonant ultrasound spectroscopy. Key Eng Mater 2014;606:87–90.
[27] Araki W, Kamikozawa T, Adachi T. Determination of residual stress in spherical balls by resonant ultrasound spectroscopy. NDT & E Int 2008;41:82–7.
[28] Araki W, Uchiki K, Arai Y, Tanaka M. Effects of interface stiffness and delamination on resonant oscillations of metal laminates. NDT & E Int 2010;43:297–304.
[29] Nakamura N, Nakashima T, Oura S, Ogi H, Hirao M. Resonant-ultrasound spectroscopy for studying annealing effect on elastic constant of thin film. Ultrasonics 2010;50:150–4.
[30] Kabla M, Seiner H, Musilová M, Landa M, Shilo D. The relationships between sputter deposition conditions, grain size, and phase transformation temperatures in NiTi thin films. Acta Mater 2014;70:79–91.
[31] Nejezchlebová J, Seiner H, Karlík M. Detection of phase transition in free-cutting Al–Mg–Si alloys by resonant ultrasound spectroscopy. Mater Sci Forum 2014;794–796:21–6.
[32] Hansen M. Constitution of binary alloys. 2nd ed.. New York: McGraw-Hill; 1958.
[33] Sedlák P, Seiner H, Zídek J, Janovská M, Landa M. Determination of all 21 independent elastic coefficients of generally anisotropic solids by resonant ultrasound spectroscopy: benchmark examples. Exp Mech 2014;54:1073–85.
[34] Lebedev AV. Method of linear prediction in the ultrasonic spectroscopy of rock. Acoust Phys 2007;48.
[35] Bernard S, Grimal Q, Laugier P. Resonant ultrasound spectroscopy for viscoelastic characterization of anisotropic attenuative solid materials. J Acoust Soc Am 2014;135:2601–13.
[36] Perez-Landazabal JI, Sanchez-Alarcos V, Gomez-Polo C, Recarte V, Chernenko VA. Vibrational and magnetic behavior of transforming and nontransforming Ni–Mn–Ga alloys. Phys Rev B 2007;76:092101.
[37] Witczak Z, Witczak P, Jemielniak R, Mazur A. Microstructure and mechanical properties of NiAl produced in the SHS process induced by low-temperature hydrostatic extrusion. J Mater Sci 2004;39:5511–5.
[38] König JA. Shakedown of elastic–plastic structures. Amsterdam: Elsevier Sci. Pub.; 1987.

Acta Materialia 105 (2016) 182–188

Contents lists available at ScienceDirect

Acta Materialia

journal homepage: www.elsevier.com/locate/actamat

Full length article

Evolution of soft-phonon modes in Fe–Pd shape memory alloy under large elastic-like strains

Hanuš Seiner [a, *], Pavla Stoklasová [a], Petr Sedlák [a], Martin Ševčík [a], Michaela Janovská [a], Michal Landa [a], Takashi Fukuda [b], Takashi Yamaguchi [b], Tomoyuki Kakeshita [b]

[a] Institute of Thermomechanics, Academy of Sciences of the Czech Republic, Dolejškova 5, 182 00, Prague 8, Czech Republic
[b] Department of Materials Science and Engineering, Graduate School of Engineering, Osaka University, 2-1, Yamada-oka, Suita, Osaka, 565-0871, Japan

ARTICLE INFO

Article history:
Received 18 May 2015
Received in revised form
3 December 2015
Accepted 13 December 2015
Available online 24 December 2015

Keywords:
Ferromagnetic shape memory alloy
Anisotropic elasticity
Single crystal
Phase transitions
Surface acoustic waves (SAW)

ABSTRACT

We study elastic anisotropy of a disordered Fe–Pd alloy under reversible elastic-like strains up to 4.3% by means of ultrasonic methods. The evolution of the full tetragonal tensor of elastic constants with a [001]-prestress ranging from 0 to 200 MPa is obtained, which enables an analysis of the change of the low-frequency limit of the soft-phonon structure. It is observed that while the anisotropy of the elastic moduli further increases, giving rise to an anomalous anisotropy factor of $A > 50$, the phonon branches stiffen. This means that, unlike for conventional shape memory alloys, the tetragonal crystal structure induced by the prestress is more stable than the stress-free cubic structure, although there is no other indication of the stress-induced transition.

1. Introduction

Structural austenite → martensite transitions in shape memory alloys (SMAs) are typically accompanied by anomalous softening of the lowest acoustic phonon branch (TA_2) indicating the shear instability of the lattice [1,2]. This softening is observed both with the temperature decreasing towards the transition temperature [3–6] and under increasing external mechanical loads as a precursor for stress-induced transitions [7–9]. The martensitic transition itself can be then understood as mediated by lattice vibrations (i.e. acoustic phonons) in this soft shearing modes. For the cubic lattice of the austenite phase, the instability can be parametrized by the anisotropy factor $A = c_{44}/c'$, where the elastic constants c_{44} and c' denote the elastic stiffness of the lattice with respect to basal and diagonal shears, respectively. In the vicinity of the transition temperatures, apparently high values of A have been reported for example for Ni–Mn–Al [10] ($A = 6.5$), Cu–Al–Ni [11] ($A = 10.4$), Cu–Zn–Al [7] ($A = 13.2$), Fe–Pd [12] ($A = 14.6$), Ni–Mn–Ga [13] ($A = 18$ after subtracting magneto-elastic effects) and Co–Ni–Al [14] ($A = 25.6$).

However, unlike for structural transition for example in perovskites [15], the complete loss of stability ($A \to \infty$) has never been observed for any SMA, as earlier than this limit is approached the material undergoes the first order martensitic transition related with a discontinuous jump of lattice constants and elastic coefficients. For the same reason, the continuous evolution of the soft-phonon shear modes from austenite to martensite over the transition interval is impossible.

The disordered Fe–Pd alloys with Pd content of approximately 30 at.% and partially ordered Fe_3Pt alloys exhibit specific second-order-like martensitic transitions with very small discontinuity of the lattice parameters at the transition temperature [16–19]. In the superelastic regime, i.e. under mechanical compression close above the transition temperature, these alloys exhibit reversible, non-hysteretic, elastic-like behavior up to 4–6 % of strain, in particular under compressions along the principal {100} axes. The magnitudes of these large, stress-induced tetragonal distortions are fully comparable to the Bain distortion between the cubic (*fcc*) and tetragonal (*fct*) phases achieved during the temperature induced transitions for the same alloys. As such, these alloys appear to be optimal candidates for studying the evolution of the soft-phonon modes and lattice instability with straining along the Bain path. In this paper, we bring results of such an analysis for the Fe–Pd alloy subjected to mechanical prestress. We observe a continuous

* Corresponding author.
E-mail address: hseiner@it.cas.cz (H. Seiner).

http://dx.doi.org/10.1016/j.actamat.2015.12.025
1359-6454/

evolution of the soft shear moduli and related low-frequency limits of the phonon modes during the loading and unloading processes and discuss how this evolution relates to the structural change of the material.

Lattice dynamics of the *fcc* phase of an Fe–Pd alloy with slightly lower Pd content (28 at.%) was studied by Sato et al. [20], who observed significant softening of the low-frequency limit of the lowest acoustic phonon branch with decreasing temperature using neutron inelastic scattering measurements. It was shown that this softening appears in the vicinity of the *fcc* → *fct* transition temperature and is strongly coupled with ferromagnetic ordering, similarly as in the Ni–Mn–Ga alloy [13]. In this paper, we explore the possibility of inducing similarly strong effects on the soft-phonon structure by mechanical prestress applied closely above the transition temperature.

2. Experimental procedures

2.1. Sample preparation and stress-strain measurements

The used sample was a single crystal of an alloy with nominal composition Fe-31.2at.%Pd grown by a floating zone method (see Ref. [17] for more details). The single crystal was heat-treated at 1373 K for 24 h followed by quenching into ice water. The martensitic transition temperature of this alloy was determined by magnetic susceptibility measurements as 252 K, i.e. sufficiently close below room temperature (RT, 298 K) to expect the above mentioned elastic-like behavior. A sample of geometry sketched in Fig. 1 was prepared from this single crystal. The dimensions of the sample were 4.84 × 4.07 × 2.78 mm^3, the longest edge was oriented approximately along a principal [001] direction. Two large lateral surfaces of orientations approximately (010) and (3$\bar{4}$0) were prepared on the sample and mirror-polished; the exact crystallographic orientation of these faces was determined by Laue method.

The stress-strain curve for the examined sample was obtained under compression along the [001]– oriented edge using an electromechanical testing machine TiraTest 2300 (force resolution 0.1 N, displacement resolution 1 μm using LVDT gaging sensors). Simultaneously, the expansion of the material in the direction perpendicular to the loading ([3$\bar{4}$0] in particular) was measured by contact inductive transducers (displacement resolution 1 μm) clamped against the lateral faces of the prismatic part of the sample. Due to the cubic symmetry, it was assumed that the cross-section of the sample parallel to the (001)– plane expands isotropically under the [001]-compression, and so that contraction of the material in the loading direction and its expansion in the [3$\bar{4}$0]– direction are sufficient for calculation of the volume change of the sample upon loading.

The stress-strain measurement was performed at room temperature (RT, 298 K, controlled with precision ±0.25 K) and for stresses up to 210 MPa. This limit was chosen to stay safely beyond the critical stress for the irreversible plastic deformation of the sample, which was expected to be ~ 285 MPa [17].

2.2. Ultrasonic measurements

The two mirror-polished lateral faces of the sample were used for measurements of the velocity of surface acoustic waves (SAWs) under prestress, using a pump-laser line-like source for generation and probe laser for point-like detection of the waves (see Ref. [21] for instrumentation details). This fully contact-less approach enabled accurate measurements of the SAW velocities in different directions without being affected by the changes of the shape of the sample due to the loading; these measurements were performed under prestress along the whole stress-strain curve up to 210 MPa.

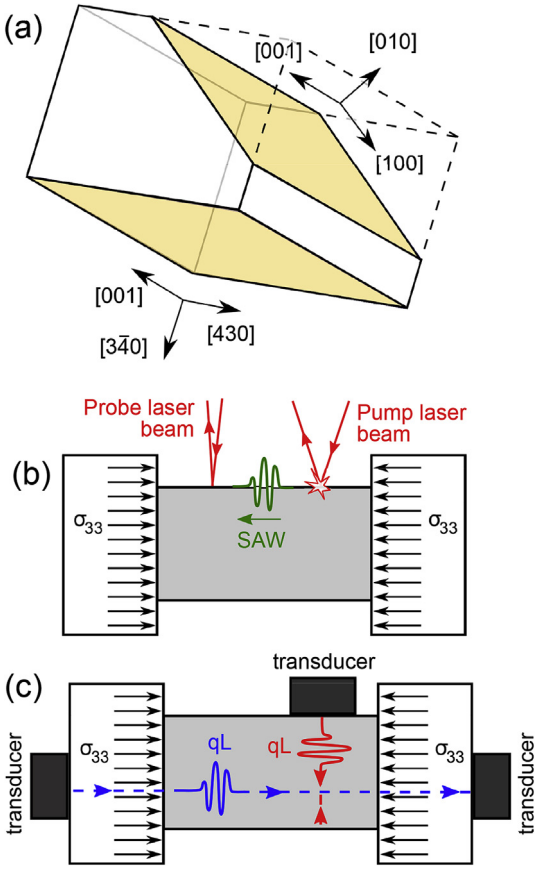

Fig. 1. (a) geometry of the sample; (b) experimental arrangement for SAW measurements; (c) experimental arrangement for qL bulk wave measurement.

For these measurements, the prestress was provided by a small in-house built testing machine (maximal load 5 kN, load resolution 0.1 N); by rotation of the whole testing machine, SAW velocity measurements in different directions were enabled for fixed geometrical configuration of the pump and probe laser beams.

On each of the available free surfaces, the SAW velocity was measured in three directions: along the compression direction (as sketched in Fig. 1(b)), perpendicular to the compression direction, and in a general direction inclined either by 60° (for the (3$\bar{4}$0) surface) or by 70° (for the (010) surface) from the loading direction. Such directions were used that the obtained signals for them enabled easy identification of the SAW arrivals and their tracing during the whole stress cycle. For each direction of propagation and each level of the prestress, SAW signals were obtained for 10 different distances between the line-like source and the point-like detector with an increment of (30 ± 0.1) μm, which was enabled by positioning the probe laser beam by a motorized stage. The velocity was then determined from the linear trend of the SAW signals in dependence on the propagation distance; from the scatter of the data for individual increments, the experimental error of the obtained SAW velocity was estimated as 0.05 mm/μs.

As shown in Ref. [21], the SAW measurements themselves may be insufficient for determination of the whole elasticity tensor, as they are mainly sensitive to the shear elastic constants but not to the longitudinal ones. For this reason, the SAW measurements were complemented by conventional pulse-echo and through-transmission measurements of velocity of quasi-longitudinal (qL) bulk acoustic waves in directions parallel and perpendicular to the loading using the arrangement outlined in Fig. 1(c). Piezoelectric

transducers (5 MHz) were used to generate and detect the waves; the change of the dimensions of the sample due to the prestress was taken into account for the calculation of the velocity from the measured time of flight.

For both SAW and qL waves, strong attenuation of the propagating waves was observed at zero prestress; however, this effect gradually disappeared with the increase of loading above ~ 75 MPa. A possible explanation of this behavior is that the attenuation was caused by magneto-elastic coupling (documented by Sato et al. [20]) that was gradually suppressed by stabilizing the orientation of the magnetization vectors by prestress due to magnetostriction. Both SAW and qL wave measurements were performed at the same conditions as the stress-strain measurements, i.e. under ambient atmosphere and under controlled temperature of (297 ± 0.25) K.

3. Inverse calculation of the elastic constants

The experimentally obtained set of SAW and bulk qL ultrasound velocities was then used for calculation of the full elastic tensors of the material. At zero prestress, this tensor was assumed as cubic (three independent elastic coefficients c_{11}, c_{12} and c_{44}), at non-zero prestress, tetragonal symmetry (point group D_{4h}) with six independent elastic constants c_{11}, c_{33}, c_{12}, c_{13}, c_{44} and c_{66} was assumed, with the tetragonal axis x_3 oriented along the compression direction. For each prestress level, 8 values of velocity (6 for SAW waves and 2 for qL waves) were available.

The inverse calculation was done by the numerical procedure described in Ref. [21]. In this approach, the sought elastic coefficients were obtained by minimization of the error function

$$F(c_{ij}) = \sum_{p} \left(v_p^{\mathrm{cal}}(c_{ij}) - v_p^{\mathrm{exp}} \right)^2, \qquad (1)$$

where c_{ij} represents a set of independent elastic constants, p is the number of the input data ($p = 8$ in this case), and the superscripts exp and cal denote the experimental values of SAW and qL velocities and the corresponding values of these velocities calculated for a given guess of c_{ij}, respectively. A gradient Levenberg–Marquardt method was used for the minimization. For the input of the error function (1), the velocities of qL waves were calculated from the Christoffel's equation [23]. The velocities of SAWs were calculated from resonant frequencies of constrained elastic vibrations of a surface element of the anisotropic material; these resonant frequencies were obtained by the Ritz-Rayleigh approach, see Ref. [21] for more details. For the calculation, the mass density of 9.11 g cm^{-3} was taken at the stress free state, as determined for the examined sample by the Archimedes method; for the non-zero prestress levels, the mass density was always recalculated from the actual volume change of the sample.

As a result, an optimized set of elastic coefficients, i.e. the set that minimizes the error function (1) was obtained for each stress level. The experimental error of this set was estimated by an error analysis procedure described in details in Ref. [22] (see Ref. [21] for the modification of this procedure particularly for SAW measurements). This procedure is based on an eigenvalue analysis of the Hessian matrix $\partial^2 F/\partial c_{ij}\partial c_{ij}$, and was also used for calculation of all experimental errors of soft shear coefficients c' and shear moduli G given in this paper.

4. Results

4.1. Stress-strain behavior

The stress-strain behavior of the sample under compression up to 210 MPa is shown in Fig. 2(a). The maximal reached axial strain was 4.3%. As seen in Fig. 2(a), the stress-strain curve was approximately linear with an inflection point at $-\varepsilon_{33} = 1.8\%$ (~ 80 MPa) and very narrow hysteresis. From the elongation of the sample in the direction perpendicular to the loading, the corresponding maximal tetragonal distortion was calculated as $c/a = 0.94$, which is significantly stronger than the transformation Bain strain $c/a = 0.98$ observed for temperature-induced fct martensite of Fe–30Pd close to the transition temperature [24]. Fig. 2(b) shows the corresponding evolution of the relative volume change; the character of the $\delta V(-\varepsilon_{33})$ dependence was very similar to that of the stress-strain curve with the rate of volume change minimal at $-\varepsilon_{33} = 1.5\%$ and slightly above it. The maximal volume change of 0.54% at axial strain of 4.3% gives the effective Poisson's ratio of 0.453, which indicates nearly perfect volume conservation during the loading.

4.2. Ultrasound velocities

The measured stress-dependencies of the SAW velocities are shown in Fig. 3 (solid lines). Similarly as the stress-strain curve, the SAW velocity data exhibited monotonous trends and nearly zero hysteresis, which confirms that the tetragonalization of the material occurred gradually, without formation of sharp interfaces or any other abrupt or discontinuous features. On both used free surfaces, the weakest dependence of the SAW velocity on the prestress was observed for propagation in direction parallel to the loading direction, while this dependence was the strongest for the direction perpendicular to the loading direction.

Also the qL velocities (not shown) exhibited non-hysteretic, monotonous increases with increasing prestress. In particular, the qL velocity in the [001] (loading) direction exhibited an increase

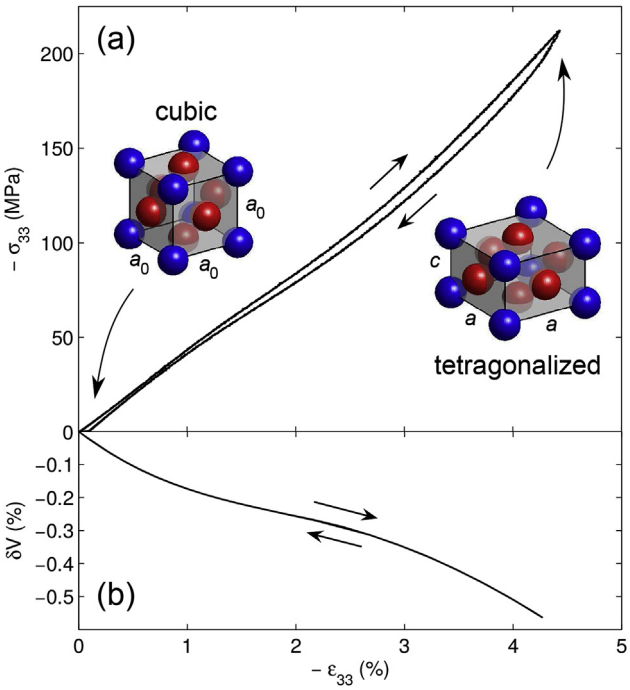

Fig. 2. (a) RT stress-strain curve of the examined Fe–Pd single crystal exhibiting large elastic-like strains; (b) the corresponding relative volume change determined from the expansion of the sample in direction perpendicular to the loading. In the visualizations of the unit cells a_0 denotes the lattice parameter of the cubic unit cell in the stress-free state, and c and a are the lattice parameters of the unit cell tetragonally distorted by the prestress.

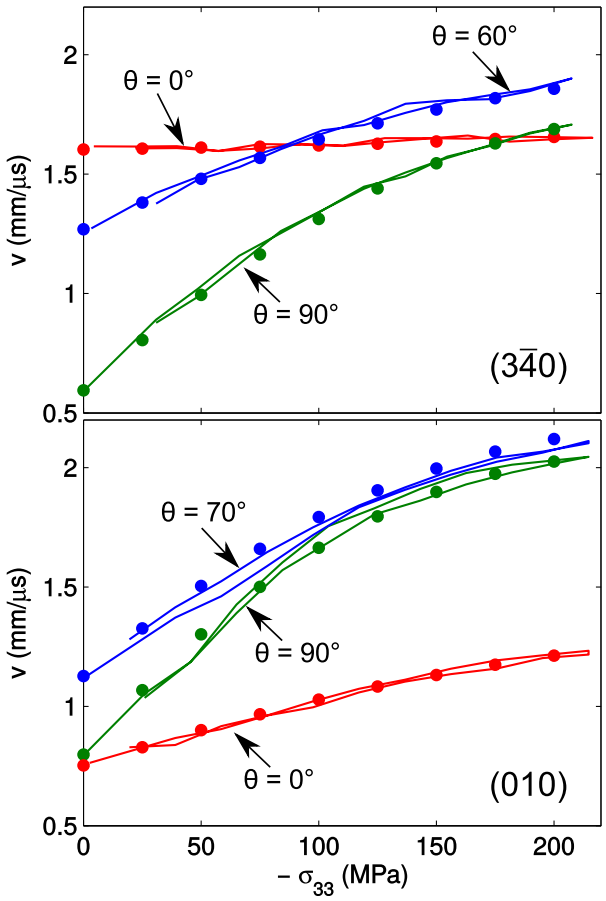

Fig. 3. Ultrasonic SAW velocities measured on the (010)– and (3$\bar{4}$0)– oriented free surfaces of the sample; θ stands for the angle between the compression direction and SAW propagation direction. Solid lines denote the experimental data (during both loading and unloading); the dots denote SAW velocities calculated for the given directions of propagation from the resulting set of elastic constant at each stress level.

from (4.06 ± 0.02) mm/μs to (4.25 ± 0.02) mm/μs at 210 MPa, while the qL velocity in the perpendicular [340] direction exhibited a weaker increase from (4.84 ± 0.02) mm/μs to (4.91 ± 0.02) mm/μs.

4.3. Elastic constants

As seen in Fig. 3, for all levels of the prestress and for all propagation directions the velocities obtained during loading differed by less than 0.07 mm/μs from those obtained during unloading, i.e. the difference was always comparable to the experimental error. Hence, it was assumed that also the evolution of elastic constants with prestress is non-hysteretic, and only one value of velocity for each propagation direction and each propagation mode at the given stress level (calculated as an average from the loading and unloading runs) was taken for the inverse procedure described in Section 3.

By this approach, the evolution of the elasticity tensor was obtained in the range 0 MPa–200 MPa with a 25 MPa step. The results for the upper and lower limits of the cycle are listed in Table 1, the full evolution of the elastic tensor with prestress is shown in Fig. 4. As seen in this figure, the evolution of all six tetragonal constants was continuous and smooth. For the constants c_{12} and c_{66}, a gradual change of the slope was observed between 50 MPa and 100 MPa, which corresponds to the inflection point at the stress-strain curve. This interval also corresponds well to the significant change in the damping of the measured acoustic waves, as mentioned in Section 2.2. Thus, it is plausible that below this stress-level the elastic constants are affected by magneto-elastic coupling reported by Sato et al. [20], while above it the prestress fully suppresses any misorientations of the magnetization vectors and the magneto-elastic effect disappears.

Table 1
RT elastic constants of the examined Fe–Pd single crystal in the stress-free cubic state and under axial prestress of 200 MPa.

Prestress ($-\sigma_{33}$)	0 MPa	200 MPa
Elastic anisotropy	Cubic	Tetragonal
c_{11} (GPa)	149.5 ± 1.6	183.4 ± 1.0
c_{12} (GPa)	143.6 ± 1.7	131.6 ± 1.2
c_{13} (GPa)	$=c_{12}$	159.2 ± 0.8
c_{33} (GPa)	$=c_{11}$	165.4 ± 1.0
c_{44} (GPa)	70.5 ± 0.4	99.3 ± 2.6
c_{66} (GPa)	$=c_{44}$	65.2 ± 2.5

The SAW velocities calculated for these sets of elastic constants at individual prestress levels are in Fig. 3 compared to the experimental input data. It is seen that agreement is satisfactory; the mean deviation of the calculated values from the experimental data in the root-mean-square sense was 0.034 mm/μs for the SAWs and 0.021 mm/μs for the qL waves, which is in both cases comparable to the respective experimental errors.

Let us mention that while the elastic constants c_{ij} determined from the ultrasonic measurement change significantly due to the loading, the stress-strain curve retains an approximately constant slope, i.e. the quasi-static Young's modulus in the loading direction remains unchanged. The evolution of Young's modulus calculated from the experimentally determined elastic constants c_{ij} is given in Fig. 5; in particular, a directional dependence of Young's modulus in the (010) plane is shown. It is seen that the modulus in the [001] direction is indeed only slightly affected by the prestress and remains very small (~ 4 GPa) even at 200 MPa; on contrary, Young's

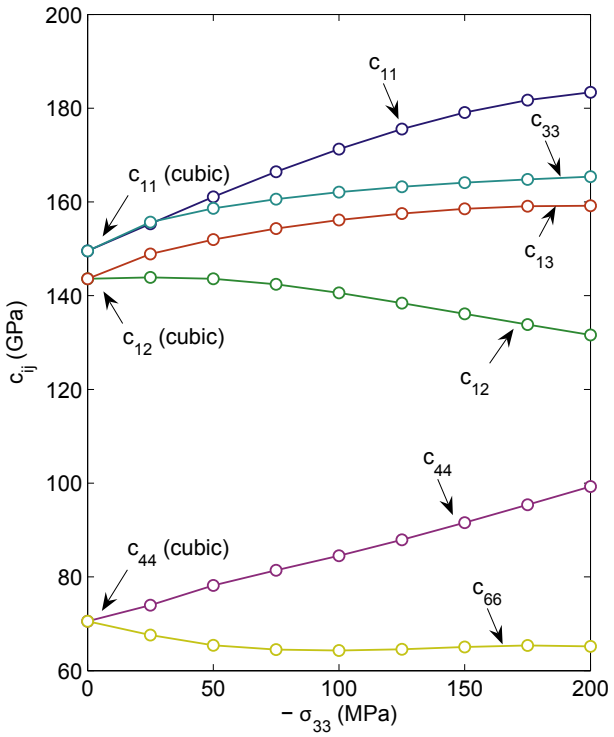

Fig. 4. Evolution of all independent tetragonal elastic coefficients with the applied prestress.

modulus in a direction inclined by approximately 35° from the [010] direction increases nearly five times (from 31 GPa to 149 GPa).

4.4. Elastic anisotropy

Both the stress-free cubic material at 0 MPa and the material at 200 MPa with stress-induced tetragonal elasticity exhibit very high levels of elastic anisotropy. The shear moduli $c' = (2.9 \pm 0.2)$ GPa and $c_{44} = (70.5 \pm 0.4)$ GPa give the anisotropy factor $A = 24.3$ for the stress-free state, which is already a high value indicating the soft-phonon instability related to the $c'-$ shearing modes.

For the material under the compression, the structure of the soft shearing modes further significantly evolves. To analyze the resulting elastic anisotropy, we will use two basic soft moduli $G^{[1\bar{1}0]}_{(110)}$ and $G^{[10\bar{1}]}_{(101)}$, denoting shear moduli for shearing along the (110) and (101) planes, respectively, along the soft ($[1\bar{1}0]$ and $[10\bar{1}]$) directions, see the sketches in Fig. 6 for clarity. Following the conventional definition of a shear modulus, these shear moduli are defined so that if a pure shear loading τ is applied to the material along the prescribed plane and in the prescribed direction, then this loading is related to the corresponding shear strain ε (along the same plane and in the same direction) by

$$\tau = 2G^{[lmn]}_{(ijk)}\varepsilon, \tag{2}$$

where (ijk) is the plane along which is the shearing applied and $[lmn]$ is the lattice vector determining the direction of the shearing. For prescribed (ijk) and $[lmn]$, the corresponding shear modulus can be directly calculated from the elastic constants c_{ij} at each stress level *via* the relation (2).

At zero prestress, these moduli are both equal to c'; their evolution with the prestress is shown in Fig. 6. The $G^{[1\bar{1}0]}_{(110)}$ shears stiffen from (2.9 ± 0.2 GPa) to (25.9 ± 1.1 GPa) and the shear instability fully disappears. The anisotropy of shear moduli for shearing along the planes parallel to the loading direction is then

$$A = G^{[010]}_{(100)} \Big/ G^{[1\bar{1}0]}_{(110)} = c_{66} \Big/ G^{[1\bar{1}0]}_{(110)} = 2.5 \tag{3}$$

at 200 MPa, i.e. comparable to that of copper or iron single crystals.

The $G^{[10\bar{1}]}_{(101)}$ modulus, on the other hand, exhibits moderate continuous softening down to (1.9 ± 0.4) GPa at 200 MPa. The resulting anisotropy of the shears along planes parallel to the [010] (or [100]) direction is then

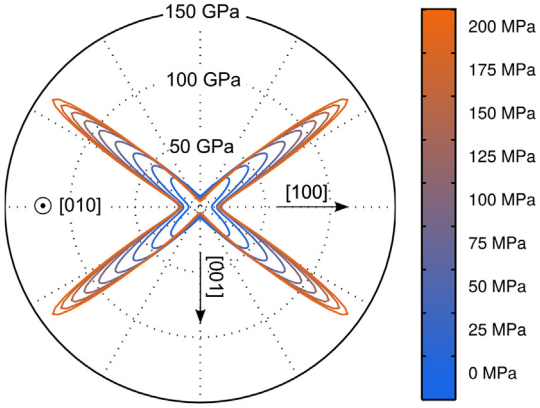

Fig. 5. Evolution of Young's moduli in a (010)– cut; the color scale denotes the level of prestress, the arrows show the orientations of [001] (loading direction) and [100] lattice vectors (For interpretation of the references to colour in this figure legend, the reader is referred to the web version of this article.).

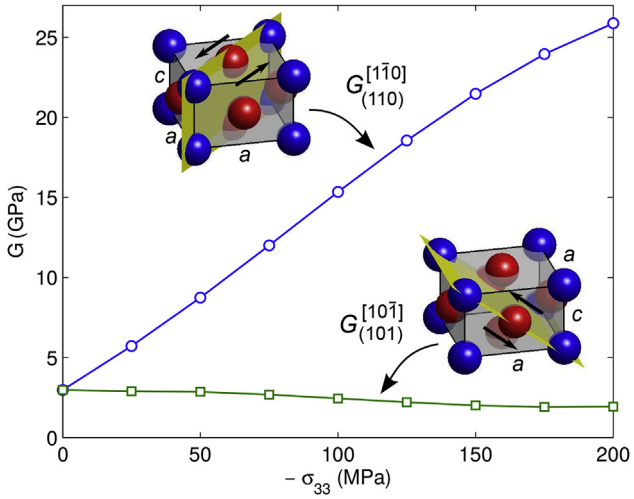

Fig. 6. Evolution of principal shear moduli with the prestress; the arrows in the sketched tetragonal unit cells indicate the directions of the applied shear loads along the highlighted planes.

$$A = G^{[100]}_{(001)} \Big/ G^{[10\bar{1}]}_{(101)} = c_{44} \Big/ G^{[10\bar{1}]}_{(101)} = 52, \tag{4}$$

i.e. two times higher than yet reported for any SMA single crystal; this extremely high value of the anisotropy factor is a result of the softening of the $G^{[10\bar{1}]}_{(101)}$ modulus and simultaneous stiffening of the c_{44} modulus, and it indicates that the [001]-prestressed material at 210 MPa is very unstable with respect to the diagonal shears.

4.5. Soft-phonon structure

As mentioned in the introduction, the martensitic transitions in SMAs are understood as mediated by the softest phonon branches. From this point of view, the anomalous increase of the elastic anisotropy shown in the previous subsection does not directly imply any changes of the stability of the parent phase with straining along the Bain path. To analyze this stability, the soft-phonon structure must be evaluated. The obtained set of elastic constants c_{ij} enables us to calculate the structure of the acoustic phonons in the low-frequency limit, where the relation between the phonon frequency ω and the wave number k is given by the Christoffel's equation [23].

In the stress-free state, the softest acoustic phonons are the shear phonons propagating along {101} directions and polarized in $\{10\bar{1}\}$ directions, i.e. TA_2 phonons, as usual for the high temperature phases of SMAs. The speed of propagation of these phonons is given by

$$v = \omega/k = \sqrt{c'/\rho} = \sqrt{G^{[10\bar{1}]}_{(101)} \Big/ \rho}, \tag{5}$$

where ρ is the mass density. Under the increasing prestress, however, the elasticity of the material becomes tetragonal. Consequently, the slowest acoustic phonons propagating along the {101} may become quasi-shear, i.e. having some small longitudinal component in their polarizations, and the phonons with pure shear polarizations exactly along the $[10\bar{1}]$ direction may not exist; in other words, the extremely soft shear modulus $G^{[10\bar{1}]}_{(101)}$ in the tetragonalized material may not directly correspond to any vibrational mode of the lattice.

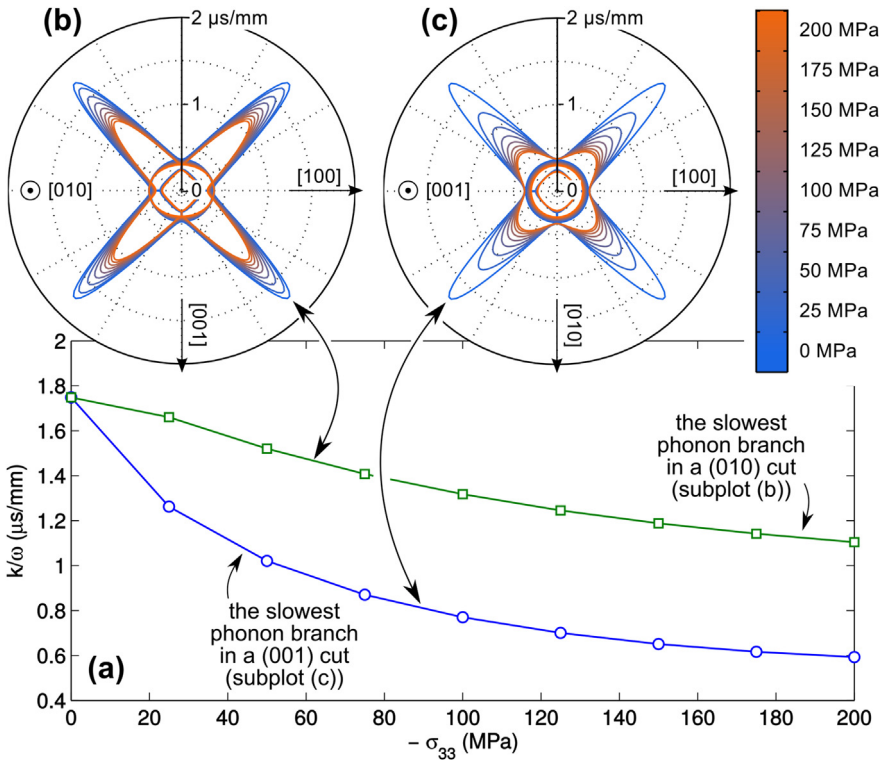

Fig. 7. Phonon slowness k/ω curves for the soft modes (a) and the corresponding cuts of the slowness surfaces by (010) and (001) tetragonal planes (b) and (c).

Fig. 7 shows the calculated evolution of the low-frequency limit of the acoustic phonon structure with prestress. The phonon structure in this figure is depicted in terms of the slowness values $k/\omega = 1/v$ (as usual in the literature, e.g. Ref. [23]). The slowness representation enables clear visualization of the softest phonon branches, as these branches are those with the maximal slowness. The stiffening of a phonon branch can be then observed as a decrease of the slowness value.

In particular, Fig. 7(a) shows the evolution of the slowest TA_2 phonons for directions of propagation oriented along the (010) and (001) planes, i.e. along the principal planes perpendicular to the loading direction and parallel to it, respectively. Obviously, both soft phonon branches are stiffening. Similarly as for the shear moduli, the $[1\bar{1}0]-$ polarized phonons stiffen significantly, while the $[10\bar{1}]-$ polarized phonons keep some instability. Nevertheless, the latter phonon branch does not reflect the increasing anisotropy of the shear moduli; in other words, the extremely soft shear modulus $G^{[10\bar{1}]}_{(101)}$ indeed does not correspond to any of the vibrational modes of the lattice. On the other hand, as seen from the cut of the slowness surface (i.e. the plot of the slowness magnitude with respect to the propagation direction running along a unit sphere) in Fig. 7(b), the phonon structure in the (010) cut remains very similar to that of the unstressed cubic material, with the directions of propagation of the slowest acoustic phonons deviating only slightly (by ~ 1°, approximately in agreement with the inclination of the (101) tetragonal plane) from the cubic {101} directions. This means that the $[10\bar{1}](101)$ phonon branches (TA_2) still retain the soft-mode character, but these soft modes are stiffening with the prestress.

5. Discussion

As seen in Fig. 4, the elastic constants of the examined Fe–Pd single crystal are relatively sensitively dependent to the prestress, as a 25 MPa compressive stress already induces a well-measurable tetragonalization of the elastic anisotropy. Nevertheless, such strong coupling between the stress and the elastic constants is quite common for the high-temperature phases of the SMAs; the magnitudes of $\partial c_{ij}/\partial \varepsilon_{33}$ for the examined material are quantitatively fully comparable with those of the austenite phases of Cu–Al–Ni and Cu–Zn–Al SMAs reported by Černoch et al. [8] and Verlinden et al. [7], respectively.

However, there is a significant qualitative difference between the soft phonon structure of Fe–Pd and the conventional SMAs reported in Refs. [7,8]. These alloys exhibit softening of the TA_2 phonon branch towards the threshold stress for initiation of the first order martensitic transition, which can be understood as a precursor phenomenon for nucleation of the stress-induced martensite. The increase of the phonon instability under external loads has been observed also for NiTi[1] single crystals [9]. In the examined Fe–Pd alloy, on the contrary, the lattice dynamics in the low-frequency limit is getting stabilized by the external prestress. In other words, the soft-phonon picture of the prestressed material resembles rather a stress-induced martensite phase; however, there is no indication of any phase transition seen on the stress strain curve (Fig. 2(a)). The relative volume change (Fig. 2(b)) exhibits some inflection at approximately $-\varepsilon_{33} = 1.8\%$, which we relate to magneto-elastic effects, as commented above, but the stiffening of the soft phonon modes is observed even below this level.

A possible explanation of this behavior may be sought in the theoretical concept of the fcc → fct transition in Fe–Pd recently proposed by Xiao et al. [16]. According to this concept, the large,

[1] For the Ni–Ti–based alloys, however, the soft shear structure is different; the softest phonons are those related to ⟨111⟩ elongations, and their softening is understood as precursor for the transition into the $R-$ phase [25].

non-hysteretic elastic-like strains observed for this alloy above the transition temperature can be interpreted as continuous transitions between the cubic and tetragonal phases, or, more precisely as a behavior of a material above the critical point for the stress induces fcc → fct transition, where the stress-induced fct martensite and the elastically stressed fcc austenite are indistinguishable from each other. The disappearance of anomalously soft phonon branches after the transition into the martensite phase has been reported for both Cu–Al–Ni and Cu–Zn–Al SMAs [11,26]; from this point of view, if the prestressed austenite phase of Fe–Pd can be interpreted as a stress-induced tetragonal phase, it should indeed exhibit phonon stiffening, as we observe experimentally. Furthermore, this interpretation is also consistent with the nearly perfect volume conservation observed of the sample under up to $\gtrsim$4 % of axial strain, which cannot be expected for conventional elastic straining. Anyway, the continuous stiffening of all soft phonon branches under prestress in the parent phase is a phenomenon observed for the first time here for any SMA, and it is plausible that a further experimental and theoretical analysis of this effect would contribute to better understanding to the martensitic transition mechanisms in Fe–Pd.

6. Conclusions

We have shown that the elastic anisotropy and the low-frequency limit of the soft-phonon structure in a Fe–Pd single crystal significantly evolves under mechanical stress applied in the principal direction. Despite of the pronounced change of the elastic coefficients, the Young's modulus in the loading direction remains approximately constant; for this reason the stress-strain curve is linear up to large (>4%) axial strains. The observed evolution of the elastic constants is qualitatively different from the commonly observed non-linear elastic behavior of the high-temperature cubic phases of SMAs, since the soft phonon modes stiffen instead of softening. This indicates that the observed evolution cannot be interpreted as a precursor-like loss of stability of the cubic phase (reported for other SMAs [7,8]), instead, a dynamic stabilization of the lattice by tetragonalization (shearing along the Bain path) is observed. Nevertheless, the resulting stressed material has enormously strong elastic anisotropy, with the anisotropy factor of $A = 52$. This makes the stressed state of Fe–Pd austenite different from the martensite phases of other SMAs, for which the elastic anisotropy is usually weaker than for the corresponding austenite phases [11,26].

Acknowledgment

This work was financially supported by Czech Science Foundation (project No.14-15264S), and by the Japan Society for the Promotion of Science (grant number 26289230).

References

[1] N. Nakanishi, Elastic constants as they relate to lattice properties and martensite formation, Prog. Mater. Sci. 24 (1980) 143–265.
[2] L. Delaey, Diffusionless transformations, in: G. Kostorz (Ed.), Phase Transformations in Materials, Wiley-VCH, Weinheim, 2001, pp. 583–654.
[3] A. Planes, Ll. Mañosa, Vibrational properties of shape-memory alloys, Solid State Phys. 55 (2001) 159–267.
[4] M. Landa, P. Sedlák, P. Šittner, H. Seiner, V. Novák, Temperature dependence of elastic properties of cubic and orthorhombic phases in Cu–Al–Ni shape memory alloy near their stability limits, Mater. Sci. Eng. A 462 (2007) 320–324.
[5] G. Mazzolai, A. Biscarini, R. Campanella, B. Coluzzi, F.M. Mazzolai, Elastic constant softening and martensite nucleation in a CuZnAl single crystal, J. Alloys Compd. 310 (2000) 318–323.
[6] H. Seiner, L. Bicanová, P. Sedlák, M. Landa, L. Heller, I. Aaltio, Magneto-elastic attenuation in austenitic phase of Ni–Mn–Ga alloy investigated by ultrasonic methods, Mater. Sci. Eng. A 521 (2009) 205–208.
[7] B. Verlinden, T. Suzuki, L. Delaey, G. Guenin, Third order elastic constants of β– CuZnAl as a function of the temperature, Scr. Metal. 18 (1984) 975–979.
[8] T. Černoch, M. Landa, V. Novák, P. Sedlák, P. Šittner, Acoustic characterization of the elastic properties of austenite phase and martensitic transformations in CuAlNi shape memory alloy, J. Alloys Compd. 378 (2004) 140–144.
[9] D.Y. Li, X.F. Wu, T. Ko, Effect of stress on soft modes for the phase transformation in a Ti–Ni alloy. I. The stress-induced transformation and soft modes, Philos. Mag. A 63 (1991) 585–601.
[10] X. Moya, Ll. Mañosa, A. Planes, T. Krenke, M. Acet, V.O. Garlea, T.A. Lograsso, D.L. Schlagel, J.L. Zarestky, Lattice dynamics and phonon softening in Ni–Mn–Al Heusler alloys, Phys. Rev. B 73 (2006) 064303.
[11] P. Sedlák, H. Seiner, M. Landa, V. Novák, P. Šittner, Ll. Mañosa, Elastic constants of bcc austenite and 2H orthorhombic martensite in CuAlNi shape memory alloy, Acta Mater 53 (2005) 3643–3661.
[12] R. Oshima, S. Muto, F.E. Fujita, Initiation of fcc-fct thermoelastic martensite transformation from premartensitic state of Fe-30 at% Pd alloys, Mater. Trans. JIM 33 (1992) 197–202.
[13] H. Seiner, O. Heczko, P. Sedlák, L. Bodnárová, M. Novotný, J. Kopeček, M. Landa, Combined effect of structural softening and magneto-elastic coupling on elastic coefficients of NiMnGa austenite, J. Alloys Compd. 577 (2013) S131–S135.
[14] H. Seiner, J. Kopeček, P. Sedlák, L. Bodnárová, M. Landa, P. Sedmák, O. Heczko, Microstructure, martensitic transformation and anomalies in c' – softening in Co–Ni–Al ferromagnetic shape memory alloys, Acta Mater. 61 (2013) 5869–5876.
[15] P.S. Peercy, I.J. Fritz, G.A. Samara, Temperature and pressure dependences of the properties and phase transition in paratellurite (TeO_2: Ultrasonic, dielectric and Raman and Brillouin scattering results, J. Phys. Chem. Sol. 36 (1975) 1105–1122.
[16] F. Xiao, T. Fukuda, T. Kakeshita, Critical point of martensitic transformation under stress in an Fe-31.2Pd (at.%) shape memory alloy, Philos. Mag. 95 (2015) 1390–1398.
[17] F. Xiao, T. Fukuda, T. Kakeshita, On the physical nature of high reversible strain in Fe–Pd single crystals exhibiting lattice softening, Acta Mater 61 (2013) 4044–4052.
[18] T. Yamaguchi, T. Fukuda, T. Kakeshita, S. Harjo, T. Nakamoto, Neutron diffraction study on very high elastic strain of 6% in an Fe3Pt under compressive stress, Appl. Phys. Lett. 104 (2014) 231908.
[19] T. Fukuda, T. Kakeshita, More than 6% elastic strain realized in a bulk single crystal of an Fe 3Pt alloy, Scr. Mater. 69 (2013) 89–91.
[20] M. Sato, B.H. Grier, S.M. Shapiro, H. Miyajima, Effect of magnetic ordering on the lattice dynamics of FCC $Fe_{1-x}Pd_x$, J. Phys. F. Met. Phys. 12 (1982) 2117–2129.
[21] P. Stoklasová, P. Sedlák, H. Seiner, M. Landa, Forward and inverse problems for surface acoustic waves in anisotropic media: a Ritz-Rayleigh method based approach, Ultrasonics 56 (2015) 381–389.
[22] P. Sedlák, H. Seiner, J. Zídek, M. Janovská, M. Landa, Determination of all 21 independent elastic coefficients of generally anisotropic solids by resonant ultrasound spectroscopy: benchmark examples, Exp. Mech. 54 (2014) 1073–1085.
[23] J.P. Wolfe, Imaging Phonons, Cambridge University Press, Cambridge, 1998.
[24] M. Matsui, H. Yamada, K. Adachi, A new low temperature phase (fct) of Fe-Pd invar, J. Phys. Soc. Jpn. 48 (1980) 2161–2162.
[25] X. Ren, K. Otsuka, The role of softening in elastic constant c_{44} in martensitic transformation, Scr. Mater 38 (1998) 1669–1675.
[26] A. Gonzalez-Comas, Ll Manosa, A. Planes, F.C. Lovey, J.L. Pelegrina, G. Guenin, Temperature dependence of the second-order elastic constants of Cu–Zn–Al shape-memory alloy in its and β phases, Phys. Rev. B 56 (1997) 5200–5206.

Acta Materialia 123 (2017) 146–156

Contents lists available at ScienceDirect

Acta Materialia

journal homepage: www.elsevier.com/locate/actamat

Full length article

Evolution of macroscopic elastic moduli of martensitic polycrystalline NiTi and NiTiCu shape memory alloys with pseudoplastic straining

Martina Thomasová [a], Hanuš Seiner [b, *], Petr Sedlák [b], Miroslav Frost [b], Martin Ševčík [b], Ivo Szurman [c], Radim Kocich [c], Jan Drahokoupil [d], Petr Šittner [d], Michal Landa [b]

[a] Faculty of Nuclear Sciences and Physical Engineering, Czech Technical University in Prague, Trojanova 13, 12000 Prague, Czechia
[b] Institute of Thermomechanics, Czech Academy of Sciences, Dolejškova 5, 18200 Prague, Czechia
[c] Regional Materials Science and Technology Centre, VŠB TU Ostrava, 17. listopadu 15, Poruba, 70833 Ostrava, Czechia
[d] Institute of Physics, Czech Academy of Sciences, Na Slovance 2, 18221 Prague 8, Czechia

ARTICLE INFO

Article history:
Received 12 August 2016
Received in revised form
6 October 2016
Accepted 9 October 2016
Available online 24 October 2016

Keywords:
Shape memory alloys
Polycrystals
Elastic behavior
Martensitic phase transformation
Resonant ultrasound spectroscopy

ABSTRACT

Elastic constants of polycrystalline NiTi and NiTiCu shape memory alloys in the martensite phase were determined by resonant ultrasound spectroscopy; the evolution of these constants was studied with subsequent applications of compressive loads inducing reorientation of martensitic variants. While the initial thermally-induced martensite exhibited only weak elastic anisotropy resulting from the underlying crystallographic texture of the parent phase, the materials with oriented martensitic microstructures exhibited strong elastic anisotropy with Young's moduli in different directions differing by several tens of GPa–s. A qualitative difference in behaviors was observed between the monoclinic B19′ martensite in the NiTi alloy and the orthorhombic B19 martensite in the NiTiCu alloy.

1. Introduction

Single crystals of shape memory alloys (SMAs) both in the high-temperature phase (austenite) and in the low-temperature phase (martensite) are known to exhibit very strong elastic anisotropy [1–3]. This anisotropy is even enhanced in the vicinity of the transition temperature, where the crystal lattice is unstable due to phonon softening [4,5]. For polycrystalline aggregates, however, the random orientation of the crystallites leads to isotropization of the homogenized macroscopic elastic constants, and the strong anisotropy at the level of individual grains does not show off at the macro-scale, especially if no strong crystallographic texture is present in the material. For this reason, most of the continuum-level constitutive models of polycrystalline SMAs consider these materials as elastically isotropic, both in the parent phase and in martensite [6–8].

In this paper, we show experimentally that the macroscopic elastic moduli of polycrystalline SMAs can be strongly anisotropic particularly in the martensite phase and, moreover, that this anisotropy depends on the strain state and the loading history. It is generally known that the microstructure of polycrystalline SMAs evolves under mechanical loading: those variants of martensite inside the individual grains that are oriented favorable to the applied stress grow at the expense of the others [16–18]. This process is generally called the *reorientation of martensite*, and is macroscopically observable as an irreversible deformation of the material, sometimes called *pseudoplastic deformation*. In the pseudoplastically strained material, the randomness of the crystallite orientations in the polycrystal is suppressed, and the macroscale elastic constants are dominantly given by micro-scale elastic constants of the preferred variants of martensite.

In general, the macroscale elastic constants of polycrystalline shape memory alloys c_{ij} can depend on four different parameters:

1. the single crystal elastic coefficients C_{ij} of the individual phases, in particular of austenite, martensite, and possibly additional metastable and intermediate phases; these micro-scale elastic constants can be strongly dependent on temperature.
2. the volume fractions of the individual phases present in the polycrystalline aggregate.

* Corresponding author.
E-mail address: hseiner@it.cas.cz (H. Seiner).

http://dx.doi.org/10.1016/j.actamat.2016.10.024
1359-6454/

3. the parent crystallographic texture of the high temperature austenite phase that can be induced by extrusion, drawing, rolling or other mechanical processing; some additional effect can be also attributed to the spatial arrangement of the grain boundaries, characteristic aspect ratios of the grains, etc..
4. the *martensitic microstructure*, i.e. the spatial arrangement of different variants of the low temperature phase, the volume fractions of these variants, and the spatial arrangements of the twin interfaces between them.

In this paper we focus on the case when the first three parameters are fixed. In other words, we examine samples with some given parent texture, being fully (or dominantly) in the martensite phase and at a fixed temperature, so that the single-crystalline elastic constants C_{ij} can be assumed as constant. Under these conditions, we use external mechanical loads to change the fourth parameter, i.e. the microstructure of martensite, and observe its effect on the macro-scale elastic constants c_{ij}. In principle, with the knowledge of all four above listed parameters, the macro-scale elastic constants can be predicted by homogenizing numerical algorithms [19,20]; however, the modern ultrasonic methods, such as resonant ultrasound spectroscopy (RUS, [35–37]) used in this work, enable direct experimental determination of all independent components of the tensor c_{ij}.

In strong contrast to the relatively large variation of elastic constants c_{ij} during thermomechanical loading of NiTi polycrystals, these phenomena are largely neglected in both the experimental and the modelling literature. This is a serious drawback since the macroscopic elastic moduli belong to the essential parameters for designing mechanical applications. The reason is the lack of reliable experimental evidence on the macroscopic elastic moduli and their reversible changes during thermomechanical loads, which is the gap this paper aims to fill. Qui et al. [9] used *in-situ* neutron diffraction to study elastic response of polycrystalline B19′ martensite of NiTi, with the main aim to compare the experimentally observed behavior with predictions of a complex numerical model, using for the individual martensite variants the elastic constants calculated by *ab initio* calculations [10]. The same approach was applied by Stebner et al. [11,12], who, in addition, used the experimental data for determination of some of the monoclinic elastic constants of a single variant of B19′, and proved the necessity of elastic-inelastic strain partitioning for full explanation of the macroscale behavior. However, the macroscale elastic anisotropy of the polycrystalline aggregates was not experimentally analyzed in any of these papers. This issue was partially addressed by Wang and Sehitoglu [13], who showed by first principles calculations that the elastic constants of twinned martensite can be significantly different from those of single variants and pointed out that the evolution of these constants with the reorientation process must be taken into account. Šittner et al. [14] explained why the experimentally measured Young's modulus of strongly [111]-textured thin NiTi wires loaded in tension into fully martensitic state is always relatively low – lower than 50 GPa, while the Young's modulus of the same material loaded into martensite by compression can be up to two times higher [14,15]. The explanation is based on the combination of elastic anisotropy, austenite drawing texture, and different martensite variant selection under tensile and compressive stresses.

In numerical constitutive modelling of polycrystalline SMAs, the anisotropy in behaviours is mostly understood as related only to maximum attainable (macroscopic) strains of martensite and its asymmetry with respect to tensile/compressive loadings. These effects were intensively investigated and documented in textured SMAs of various composition in the last two decades, e.g. Refs. [21–23], and became standard features of many constitutive models [24–27]. For instance, the possibilities to cover tension/compression asymmetry in SMA polycrystals via an enhanced transformation yield surface were pioneered by Qidwai and Lagoudas [28]; Sadjadpour and Bhattacharya [29] modified the set of effective transformation strains so that the transverse isotropy of transformation strain may be easily captured. A very similar approach employing a specific function of tensor invariants was also used in Refs. [30,31]; the latter of these models was recently extended by empirical assumptions of elastic anisotropy of martensite [32] and its evolution with reorientation. One of the aims of this paper is to bring sufficiently detailed and complete experimental data for further improvements of this or similar constitutive models.

2. Materials and methods

2.1. Examined materials and sample preparation

Two different polycrystalline SMAs were used for the reported study: NiTi (a commercially available extruded rod, nominal composition Ni50.5–49.5Ti (at.%)) and NiTiCu (a rod fabricated by rotary forging at Technical University Ostrava, nominal composition Ni40-Ti50-Cu10 (at.%), see Ref. [33] for details on the manufacturing). The transition temperatures of these two alloys were determined by differential scanning calorimetry (DSC); in particular, the martensite start temperature (M_S), the martensite finish temperature (M_F), the austenite start temperature (A_S), and the austenite finish temperature (A_F) were identified as given in Table 1.

To set the materials into a known, well-defined configuration (used then as a reference state for the ultrasonic measurements), both alloys have been heated up to 95 °C, cooled down to −25 °C, and then slowly heated up to room temperature (RT, 22 °C). According to the DSC results, both alloys were in the martensite phase in this state, which was also confirmed by X-ray diffraction. The X-ray measurements were done using a diffractometer X'Pert Pro PANalytical equipped with a cobalt anode ($\lambda = 0.178\ 901$ nm). The semi-focusing Bragg-Brentano geometry was used. The diffraction data were evaluated by Rietveld analysis [34] in program Topas. The results for the reference state are shown in Fig. 1. The dominant structure in the NiTi alloy (Fig. 1(a)) was identified as the monoclinic B19′ martensite; however, additional strong diffraction peaks indicating a significant volume fraction (~30%) of residual austenite or a mixture of austenite and the R-phase, as these two phases were impossible to distinguish from the 2θ scans. The structure of the NiTiCu alloy (Fig. 1(b)) was identified as orthorhombic B19 martensite with some traces of the parent phase as well, but of a negligible volume fraction (less than 5% according to the Rietveld analysis).

From each alloy, a small cuboidal sample was cut such that one edge of the sample was parallel to the axis of the rod, along which the processing texture was expected. One of the faces parallel to this axis was mirror polished to enable measurements of elastic constants by laser-based ultrasonic methods (as described in Subsection 2.3). Hereafter, the direction perpendicular to the

Table 1
Transition temperatures determined for the studied materials by differential scanning calorimetry.

	M_S [°C]	M_F [°C]	A_S [°C]	A_F [°C]
NiTi	39.0	24.7	51.5	70.9
NiTiCu	27.3	13.0	28.7	40.0
Accuracy	±1.0	±1.0	±1.0	±1.0

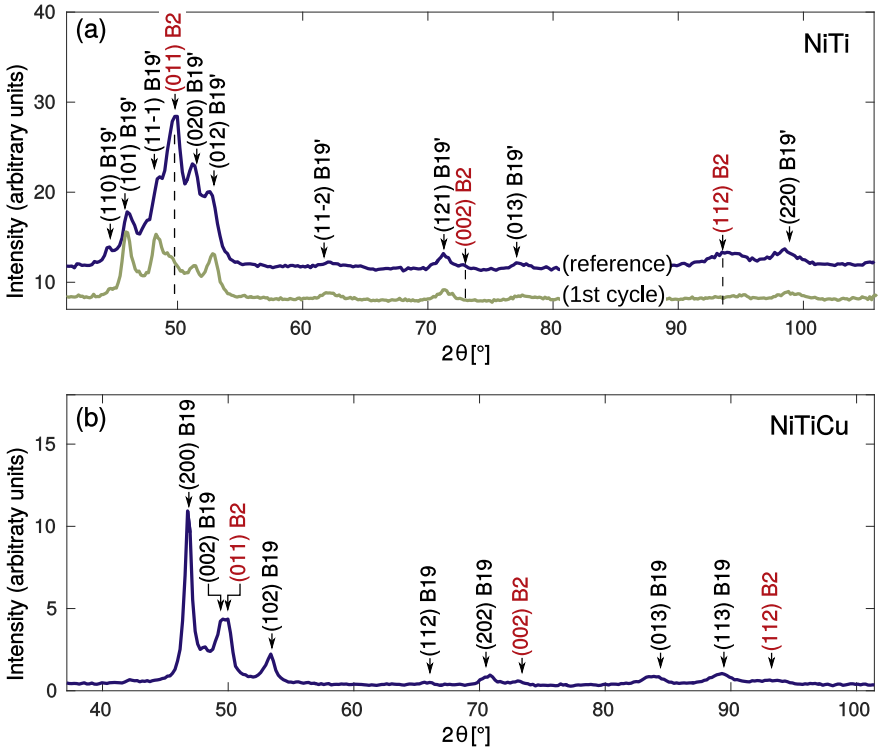

Fig. 1. X-ray diffraction 2θ scans for the examined samples with the locations of the expected dominant peaks for the parent phase (B2) and the martensite phases (B19 and B19′) indexed by arrows: (a) the NiTi alloy, the curve labeled '(reference)' corresponds to the initial reference state, the curve labeled '(1st cycle)' corresponds to the material after the first loading cycle; (b) the NiTiCu alloy in the initial reference state.

polished surface will be denoted as *A*, the processing direction (the direction parallel to the axis of the rod) will be denoted as *B* and the third direction perpendicular to *A* and *B* will be denoted as *C*. The dimensions of the samples are listed in the first row of Table 2.

2.2. Experimental methodology

The elastic constants of each sample were determined in the initial reference state (obtained by a 95 °C → −25 °C → RT thermal cycle), and then at RT in a sequence of pseudoplastically deformed stress-free states. The pseudoplastic deformation was induced by uniaxial compressions performed in a TiraTest 2300 testing machine (force resolution 0.1 N, displacement resolution 1 μm using LVDT gauging sensors). The compressions were applied to maximal loads of −400 MPa for the NiTi sample and −300 MPa for the NiTiCu sample. As it will be shown in Section 3.2, these maximal loads were above the plateau stress for martensite reorientation in compression, i.e. each of the loading cycles induced a reorientation of martensitic variant that remained as a permanent pseudoplastic strain after unloading.

The following sequence was used (see Fig. 2): Firstly, the sample was compressed along the direction of the axis of the initial rod (B). This first compression was expected not to break the rotational symmetry of the properties of the material with respect to the axial direction. Secondly, the compression was applied in direction C, which resulted in a more general strain state of the material, not following the initial symmetry of the rod. Afterwards, the sequence continued by repeating altering compressions along directions B and C, so that the polished surface perpendicular to the direction A remained untouched as necessary for repeated measurements of the elastic constants. Five subsequent compressions (i.e. B-C-B-C-B) were applied for each sample. Between each two compressions, dimensions of the sample were measured by a digital micrometer and the full tensors of elastic constants were determined by ultrasonic methods, as described in the next subsection. During the whole procedure, including sample manipulation and determination of sample dimensions, the sample was held at constant temperature (RT ± 1 °C), the ultrasonic measurements themselves were

Table 2
Dimensions of the NiTi and NiTiCu samples in the initial reference state ($N = 0$) and after application on N loading cycles, and the volume of the sample calculated as $V = d_A \times d_B \times d_C$. The capital letter in parentheses for each N denote the direction along which the compression was applied in the N–th loading cycle.

	NiTi				NiTiCu			
	d_A [mm]	d_B [mm]	d_C [mm]	V [mm^3]	d_A [mm]	d_B [mm]	d_C [mm]	V [mm^3]
$N = 0$	3.925	3.946	3.918	60.68	2.397	3.936	3.408	32.15
$N = 1$ (B)	3.987	3.824	3.982	60.71	2.415	3.877	3.430	32.12
$N = 2$ (C)	4.100	3.886	3.821	60.88	2.453	3.902	3.355	32.11
$N = 3$ (B)	4.109	3.827	3.864	60.76	2.448	3.878	3.377	32.06
$N = 4$ (C)	4.119	3.866	3.825	60.91	2.458	3.897	3.355	32.13
$N = 5$ (B)	4.124	3.838	3.850	60.94	2.452	3.885	3.372	32.12
Accuracy	±0.005	±0.005	±0.005	±0.24	±0.005	±0.005	±0.005	±0.16

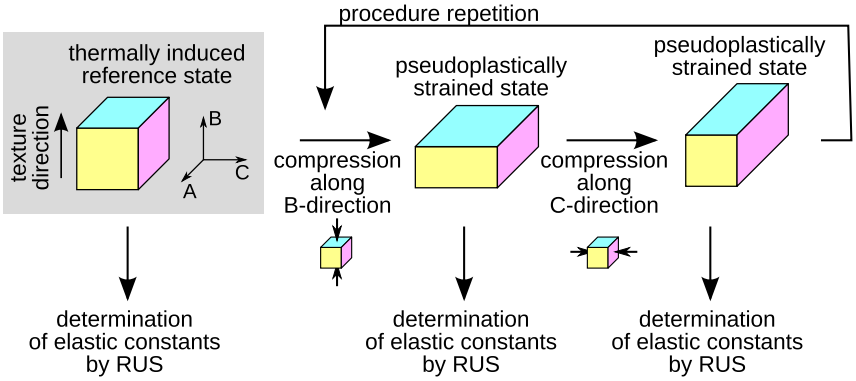

Fig. 2. Outline of the applied experimental procedure: After determination of the elastic constants of thermally induced martensite (the reference state), the sample was pseudoplastically strained by applying uniaxial compressions subsequently in directions C and B; in each stress-free state, the elastic constants were determined. See the text for more details.

performed in a temperature chamber with a ±0.05 °C accuracy.

The chosen sequence of loadings (uniaxial compressions) did not violate the mirror-symmetry of the material with respect to the planes parallel to the faces of the sample, i.e. all achieved pseudoplastic strains states were assumed as describable by a diagonal strain tensor

$$\varepsilon = \begin{pmatrix} \varepsilon_A & 0 & 0 \\ 0 & \varepsilon_B & 0 \\ 0 & 0 & \varepsilon_C \end{pmatrix} \tag{1}$$

with only three non-zero components. Hereafter, we will use the denotation $\varepsilon^0_{A,B,C}$ for total strains with respect to the initial reference state ($\varepsilon^0_A = \varepsilon^0_B = \varepsilon^0_C = 0$ at the beginning of the first loading cycle), and the denotation $\varepsilon_{A,B,C}$ for actual strains in one particular loading cycle, i.e. strains with respect to the starting state in this loading cycle ($\varepsilon_A = \varepsilon_B = \varepsilon_C = 0$ at the beginning of each cycle).

2.3. Ultrasonic measurements

2.3.1. Determination of elastic constants

The elastic constants in the initial temperature-induced state as well as after individual subsequent steps of the loading procedure were measured by resonant ultrasound spectroscopy (RUS, [35–37]). This method is suitable for determination of all independent elastic constants of an anisotropic material available in a form of a small sample of a simple, well-defined shape. The RUS method is based on recording a spectrum of free elastic vibrations of such a sample; the spectrum is then processed by a numerical software in order to determine inversely the elastic constants of the material.

For the measurements reported in this work, the fully non-contact RUS apparatus described in detail in Ref. [37] and the numerical inverse procedure (described *ibid*) were used. In this non-contact arrangement, the elastic vibrations are both generated and detected by lasers, which enables the measurements to be performed in an low-pressure chamber with accurately controlled temperature. In addition, the detection of the vibrations by a laser interferometer allows also for the determination of the modal vibrational shapes corresponding to individual resonant frequencies of the sample. This additional information can be advantageously included in the numerical procedure and significantly improves its robustness and reliability [38]. The RUS measurements were, for each state of the material, complemented by pulse-echo measurements, i.e. by measurements of velocity of longitudinal ultrasonic waves in directions perpendicular to the faces of the samples. As also shown in Ref. [37], the use of additional pulse-echo data compensates the low sensitivity of the RUS method to some of the elastic constants, and is necessary for determination of all sought elastic constants with sufficient accuracy.

For each sample and for each pseudoplastically strained state, the RUS method was applied to determine a full tensor of elastic constants for the assumed symmetry class. In the initial temperature-induced state and after the first compression along the B direction, the material was assumed as rotationally invariant with respect to this direction. Hence, the material was expected to exhibit transversal isotropy with the anisotropy axis oriented along the B-direction and with five independent elastic constants. After the second compression (along the C-direction perpendicular to B), however, the rotational symmetry was lost and the full orthorhombic tensor was assumed.

In particular, for the Cartesian coordinate system oriented so that the triplet (x_1, x_2, x_3) was aligned with the directions (A, B, C), the materials in the initial state and after the first compression were assumed as having the elastic tensor rotationally invariant with respect to the x_2 axis, i.e.

$$c_{ij} = \begin{pmatrix} c_{11} & c_{12} & c_{13} & 0 & 0 & 0 \\ c_{12} & c_{22} & c_{12} & 0 & 0 & 0 \\ c_{13} & c_{12} & c_{11} & 0 & 0 & 0 \\ 0 & 0 & 0 & c_{44} & 0 & 0 \\ 0 & 0 & 0 & 0 & (c_{11}-c_{13})/2 & 0 \\ 0 & 0 & 0 & 0 & 0 & c_{44} \end{pmatrix}, \tag{2}$$

while for the materials after the second loading cycle, orthorhombic elastic anisotropy with nine independent elastic constants c_{11}, c_{22}, c_{33}, c_{44}, c_{55}, c_{66}, c_{23}, c_{13}, and c_{12} was assumed. For all samples, the obtained RUS spectrum and the pulse-echo data were sufficient for determination of all independent elastic coefficients with accuracy better than ±3 GPa (calculated by the sensitivity analysis described in Ref. [37], see Section 3.3 for the experimental errors in the individual coefficients), and the resonant frequencies calculated for the resulting set of elastic constants matched the experimental spectra with accuracy better than 1%. This confirms that the chosen symmetry classes (transversely isotropic and orthorhombic) indeed described well the macro-scale behaviors of the materials. It was also observed from the experimental data that the modal shapes of all measured vibrational resonant modes were mirror-symmetric with respect to the mid-planes parallel to the faces of the sample. This can be understood as an independent confirmation that this symmetry is followed also by the material of the sample.

For a more straightforward interpretation of the results, the

tensors c_{ij} of the elastic constants for each material and in each pseudoplastically deformed state was recalculated into Young's moduli along the directions A, B, and C, i.e. along the edges of the sample. Such Young's moduli can be calculated for each set of elastic constants as $E_A = s_{11}^{-1}$, $E_B = s_{22}^{-1}$ and $E_C = s_{33}^{-1}$, where s_{ij} is the inverse matrix to the matrix c_{ij}. These Young's moduli are used for visualization of the results in Section 3.3.

2.3.2. Verification of transition temperatures

In addition to the measurements of the elastic constants, the RUS method was also used to detect the transition temperatures of the examined materials. This measurement was done in order to confirm that the reference state is below the austenite start A_S temperature, as assumed from the DSC data, and to determine whether the elastic behavior in this reference state is already affected by phonon softening expected due to the vicinity of this temperature. The transition temperatures were detected from temperature evolution of the elastic constants, assuming that the transition temperatures correspond to abrupt changes of the slopes dc_{ij}/dT[39–41]. In particular, the temperature evolution of Young's modulus in the A-direction E_A was analyzed, as this modulus was well determinable from the RUS data in the whole studied temperature range.

The RUS measurements for detection of the transition temperatures were taken before the loading sequence. The measurements were done in a 95 °C → −25 °C → 95 °C cycle, i.e. starting and ending in the austenite phase and covering the whole transition sequence according to the DSC results. In addition, at the end of the thermal cycle, the elastic constants of each sample in the austenite phase at 95 °C were determined, again using a combination of RUS and pulse-echo measurements. Afterwards, the samples were set into the reference state by the above described 95 °C → −25 °C → RT thermal cycle.

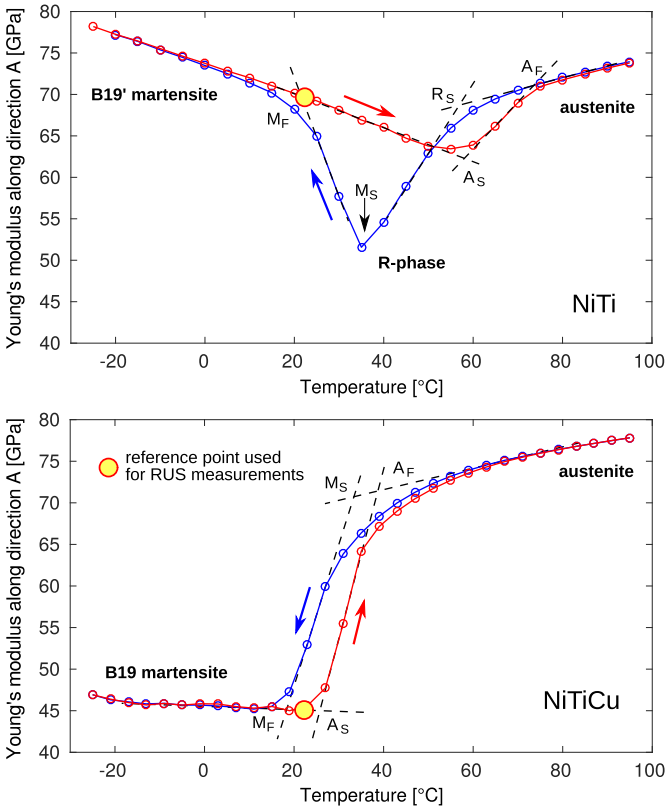

Fig. 3. Evolution of the Young's modulus along the direction A for the NiTi and NiTiCu samples with a thermal cycle. The dashed lines indicate the linear trends in selected segments of the curves, and their intersections give approximate locations of the transition temperatures (cf. Table 1). The larger marker denotes the reference state used as a starting point for ultrasonic measurements.

3. Results and discussion

3.1. Transition temperatures

The evolution of Young's modulus E_A of both the NiTi and the NiTiCu samples with temperature cycles is shown in Fig. 3. It is seen that indeed the chosen temperature cycle covered fully the transitions from the high temperature phase to the studied low temperature phases. The points of maximal change of the slope (outlined by intersections of the linear trends in Fig. 3) are in approximate agreement with the DSC results, although some shift between these two temperature sets can be observed. This shift is given by the fact that the RUS and DSC methods are differently sensitive to the changes of volume fractions of the phases in the material. As shown by Nejezchelbová et al. [42], the RUS method is able to reliably detect phase transitions in volume fractions smaller than 1%, which is at the resolution limit of DSC.

For the NiTi sample, the RUS data reveal that the transition from austenite to martensite is preceded by formation of the R-phase, which was not detected by the DSC measurements. The R-phase start temperature (R_S) is accompanied by a significant drop in Young's modulus, that is, however, overwritten by a steep increase upon further cooling starting from M_S, as the material transforms to B19′ martensite. In the heating run, the transition to the R-phase is absent, and direct transition between B19′ and the austenite is observed in a relatively narrow temperature interval. This behavior of the macroscale elastic modulus is very typical for polycrystalline NiTi, and was observed for both bulk polycrystals [43] and nanocrystalline sputtered NiTi films [44].

For the NiTiCu alloy, no evidence of the R-phase or any other intermediate phase is observed. Upon cooling, the elastic response of the austenite phase continuously softens and this softening rapidly accelerates close to the transition temperatures. After the transition, on the contrary, the stiffening of the B19 martensite upon further cooling is very small. Let us point out, however, that the relative change in E_A for the NiTiCu alloy corresponding to the austenite → B19 is even larger than the one corresponding to the formation of the R-phase in NiTi, and is not compensated by further cooling. In other words, the difference between the elastic modulus of austenite and martensite phases in NiTiCu is significantly larger than in NiTi.

As also seen in Fig. 3, the chosen reference point in the heating run is for both alloys below the transition temperature A_S, albeit it is very close to this temperature for the NiTiCu sample. Nevertheless, by applications of the reorientation sequence, the A_S temperature can be expected to shift upwards due to the *stabilization of martensite by detwinning*[45,46]. Hence, if there was any small amount of the austenite phase nuclei (indicated by the X-ray measurements) in the reference state due to the vicinity of the A_S temperature, after the first pseudoplastic straining the material would be transformed fully to martensite. Similarly, for the NiTi sample, for which a significant amount of residual high-temperature phases in the reference state was detected by the X-ray diffraction, the first pseudoplastic straining can be expected to transform the material fully to martensite. This assumption was fully confirmed by additional X-ray diffraction measurement done for the NiTi sample at RT after the first loading cycle (see Fig. 1(a), the curve labeled as '(1st cycle)'); the results proved that the sample after the first loading cycle contained less than 5% of the residual phases, which is comparable to the resolution limit of the used method.

Moreover, it is seen in Fig. 3 that there is no significant softening in the elastic response neither of the NiTi sample, nor of the NiTiCu sample close to the reference points, the $E_A(T)$ curves at these points follow the low-temperature linear trends for both materials. In other words, the behavior of the materials in these reference points can be understood as representative for the martensite phase, regardless of the vicinity of the transition temperatures.

3.2. Stress-strain behaviors

Figs. 4 and 5 show the stress-strain curves recorded during the reorientation sequence for the NiTi and NiTiCu samples, respectively. In both cases, the first application of the uniaxial compression (along the direction denoted as B) induced a significant pseudoplastic deformation (~3.5% strain for NiTi and ~1.5% strain for NiTiCu), and the corresponding stress-strain curves have the expected shapes with gradual plateaus, typical for polycrystalline SMAs under compression [14]. The maximal pseudoplastic strain is, however, achieved in the second loading cycle (~5% for NiTi and ~2.5% for NiTiCu), with even more clearly visible stress plateaus for both alloys. This behavior is fully expectable: the first compression along the B-direction induces such reorientation of the martensitic variants that the sample expands in the A- and C-directions, and thus the second loading cycle (along the C-direction) is applied already to a material oriented unfavorably to the loading, and so larger reorientation strains can be achieved.

Starting from the third repetition of the loading cycle, the achieved pseudoplastic strains are being reduced and the plateau-like behavior disappears. Some indication of the plateau can be seen for the 4th loading cycle for the NiTiCu alloy, although in this case rather a gradual change of the stress-strain slope during the loading run is observed.

This gradual suppressing of the reorientation can be explained by the fact that the sample after the second loading cycle is already significantly extended in the A-direction (which is not compressed in the sequence), and the microstructure of martensitic variants is mostly unaffected by further compressions along the B- and C-directions. However, there is a difference observed between the behaviors of the NiTi and NiTiCu samples, most clearly visible from the evolutions of the total strains of the samples (Figs. 4(f) and 5(f)). While the NiTi sample weakly but continuously expands along the A-direction with the fourth and the fifth loading cycle, the A-dimension of the NiTiCu sample rather oscillates with the loading sequence. The corresponding evolutions of dimensions of the NiTi and NiTiCu samples during the loading sequence is given in Table 2, where for each sample at each stage also the volume is enumerated. It is seen that all the induced pseudoplastic strains are, as expected, of a purely deviatoric nature, as the volume of the sample varies only within the range of the experimental error.

After completing the whole loading sequence, both samples were subjected to the same thermal cycle as at the beginning, i.e. 95 °C → −25 °C → RT, in order to analyze the reversibility of the straining process. The dimensions after this thermal cycle were compared to those in the initial reference state of each sample. It was observed that both samples retained some irreversible part of the strains. In particular, irreversible strains of $\varepsilon_A = 2.46\%$, $\varepsilon_B = -1.41\%$, and $\varepsilon_C = -0.83\%$ were determined for the NiTi sample, and irreversible strains of $\varepsilon_A = 0.54\%$, $\varepsilon_B = -0.24\%$, and $\varepsilon_C = -0.14\%$ were determined for the NiTiCu sample. These irreversible parts of strains may be attributed mainly to the plastic deformation occurring during the loading sequence; some part of it, however, may also follow from initiation of the two-wave memory effect, as the dislocations and other defects induced to the samples during the loading sequence may affect the formation of the thermally induced martensitic microstructure. As expected, the results indicate that the plastic slip in the NiTi sample is more pronounced than in the NiTiCu sample. For the analysis of the elastic constants given in the next subsection, it will not be distinguished between those parts of the strain induced by reorientation and those related to plastic slip; it is assumed that the dislocations do not affect significantly the elastic constants, except of the fact that the microstructures forming in the sample during the loading cycle follow from some interplay between the dislocations and the reorientation.

3.3. Evolution of elastic constants during the sequence of compressive loadings

Table 3 gives the elastic constants c_{ij} of the NiTi and NiTiCu samples in the parent austenite phase (at 95 °C) and in the

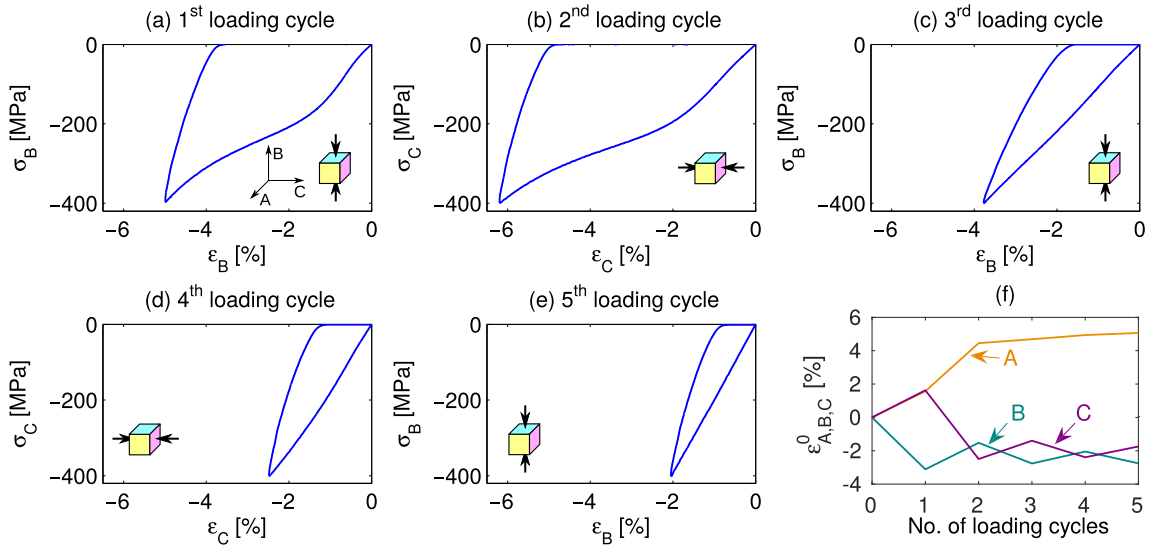

Fig. 4. Mechanical responses of the NiTi sample during the loading sequence: (a)–(e) stress-strain curves in the individual loading cycles, the orientation of the applied load is outlined by a sketch in each plot area; (f) corresponding evolution of the macroscopic strains of the sample. In (a)–(e), $\varepsilon_{B,C}$ refers to measured strains in the given loading cycle; in (f), $\varepsilon^0_{A,B,C}$ refers to total strains with respect to the original shape of the sample.

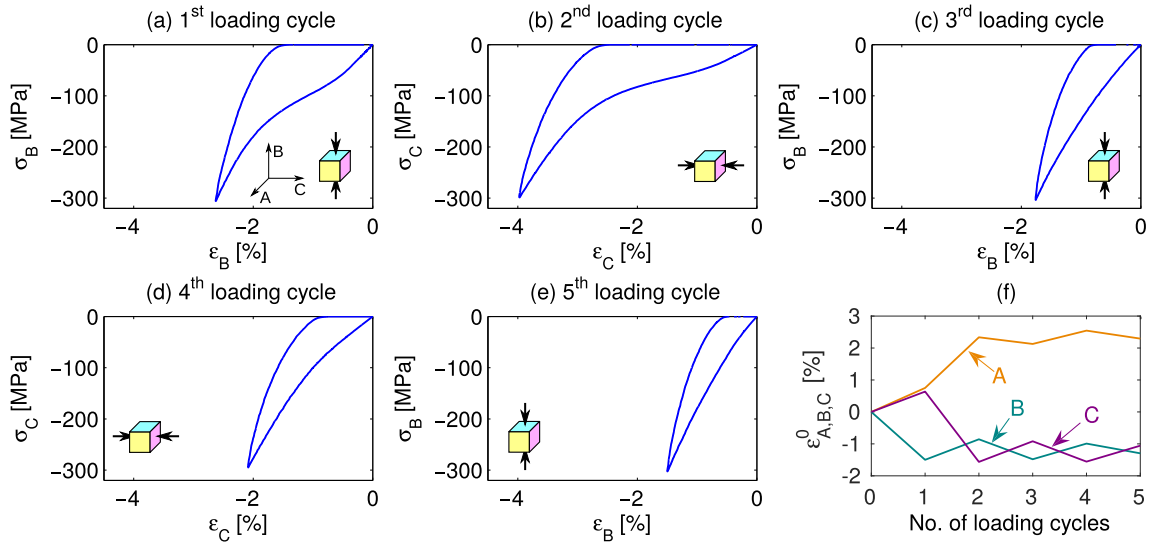

Fig. 5. Mechanical responses of the NiTiCu sample during the loading sequence: (a)–(e) stress-strain curves in the individual loading cycles, the orientation of the applied load is outlined by a sketch in each plot area; (f) corresponding evolution of the macroscopic strains of the sample. In (a)–(e), $\varepsilon_{B,C}$ refers to measured strains in the given loading cycle; in (f), $\varepsilon^0_{A,B,C}$ refers to total strains with respect to the original shape of the sample.

Table 3
Elastic constants c_{ij} of the NiTi and NiTiCu samples in the parent phase at 95 °C and the reference state (thermally induced martensite). The last column gives the resulting anisotropy factor A.

	c_{11} [GPa]	c_{22} [GPa]	c_{44} [GPa]	c_{55} [GPa]	c_{23} [GPa]	c_{13} [GPa]	A [1]
Austenite at 95 °C							
NiTi	186.7	184.7	24.1	26.0[a]	130.5	134.6	1.15
NiTiCu	182.1	187.7	23.3	27.0[a]	126.1	128.2	1.25
Martensite at RT							
NiTi (B19′)	174.9	175.1	25.9	25.8[a]	124.8	123.2	1.02
NiTiCu (B19)	163.9	168.0	15.5	15.0[a]	132.0	133.8	1.12
Error	±1.3	±1.4	±2.1	±0.7	±1.9	±2.4	±0.04

[a] calculated as $(c_{11} - c_{13})/2$.

reference state prior to the start of the loading sequence. In addition to the values of c_{ij}, the generalized anisotropy factor A is given for each material. The anisotropy factor measures the strength of anisotropy of shear elastic properties of each material. For cubic materials, the classical (non-generalized) anisotropy factor is defined as $A = 2c_{44}/(c_{11} - c_{12})$; for lower symmetry classes, this definition can be generalized as [47].

$$A = \left(\max\left(v^2_{\text{shear}}\right) \Big/ \min\left(v^2_{\text{shear}}\right)\right), \tag{3}$$

where v_{shear} is a set of shear (or quasi-shear) elastic waves propagating in all possible directions in the material. Hence, the anisotropy factor is calculated as a ratio between the maximal such velocity and the minimal such velocity squared, which gives $A = 1$ for isotropic materials and $A = 2c_{44}/(c_{11} - c_{12})$ for cubic materials with $2c_{44} > c_{11} - c_{12}$. For lower symmetry than cubic, the generalized anisotropy factor given by relation (3) cannot be directly expressed in terms of the elastic constants c_{ij}.

For the austenite phases, both samples exhibit measurable elastic anisotropy ($A = 1.15$ for NiTi and $A = 1.25$ for NiTiCu) resulting from the texture induced by initial extrusion and rotary forging, respectively. Let us point out that as the elastic anisotropy of NiTi and NiTiCu austenite single crystals is relatively strong, and so even weak crystallographic texture may induce pronounced anisotropy of the macroscale elastic constants of the polycrystalline aggregate. Upon cooling to thermally induced martensite, the elastic anisotropy significantly reduces; this indicates that the formation of the self-accommodated twinned structure in the reference state suppresses the effect of the texture.

The elastic constants listed in Table 3 also confirm the difference between NiTi and NiTiCu samples observed already in Fig. 3. While in the parent phase all elastic constants c_{ij} are very similar for NiTi and NiTiCu, those of the NiTiCu sample exhibit a much stronger decrease upon the thermally induced transition into martensite. In particular, all diagonal elastic constants (c_{11}, c_{22}, c_{44} and c_{55}) for NiTiCu are significantly lower than for NiTi, while the off-diagonal constants (c_{12} and c_{13}) are higher, which means that the shear elastic stiffness of NiTiCu is lower in all directions.

Tables 4 and 5 summarize the evolutions of all independent (orthorhombic) elastic coefficients in the NiTi and NiTiCu samples, respectively, in the martensite phase with the reorientation sequences. In addition to the elastic constants and the anisotropy factor A, also the bulk modulus K is given for each material and each stage of the reorientation sequence. The bulk modulus K is determined as a parameter of proportionality between a hydrostatic compression applied to the material and the elastic volume change of the material. For polycrystalline aggregates this parameter can be expected as approximately independent of the crystallographic texture or the spatial arrangement of the microstructure, and thus, the conservation of this parameter along the reorientation sequence can be understood as an independent confirmation that the obtained sets of elastic constants describe the same material

Table 4
Elastic constants c_{ij} of the NiTi sample and their evolution with the number of reorientations N. $N = 0$ denotes the reference state (thermally induced martensite). The last two columns give the resulting anisotropy factor A and the bulk modulus K for each N.

	c_{11} [GPa]	c_{22} [GPa]	c_{33} [GPa]	c_{44} [GPa]	c_{55} [GPa]	c_{66} [GPa]	c_{23} [GPa]	c_{13} [GPa]	c_{12} [GPa]	A [1]	K [GPa]
$N = 0$	174.9	175.1	–	25.9	25.8[a]	–	124.8	123.2	–	1.02	141.2
$N = 1$	175.2	193.4	–	36.9	27.1[a]	–	126.8	120.9	–	1.34	142.9
$N = 2$	173.4	187.8	189.1	36.9	28.2	30.9	120.1	125.4	117.5	1.32	141.5
$N = 3$	173.5	198.0	186.4	36.4	28.5	33.9	121.4	122.6	124.1	1.28	143.3
$N = 4$	173.1	192.3	189.4	36.4	30.2	32.9	119.4	124.0	120.9	1.28	142.3
$N = 5$	174.1	197.1	187.6	38.9	28.7	32.9	118.3	123.6	121.9	1.37	142.6
Error	±1.3	±1.4	±1.4	±2.1	±0.7	±0.9	±1.9	±2.4	±2.6	±0.04	±2.4

[a] calculated as $(c_{11} - c_{13})/2$.

Table 5
Elastic constants c_{ij} of the NiTiCu sample and their evolution with the number of reorientations N.

	c_{11} [GPa]	c_{22} [GPa]	c_{33} [GPa]	c_{44} [GPa]	c_{55} [GPa]	c_{66} [GPa]	c_{23} [GPa]	c_{13} [GPa]	c_{12} [GPa]	A [1]	K [GPa]
$N = 0$	163.9	168.0	–	15.5	15.0[a]	–	132.0	133.8	–	1.12	143.5
$N = 1$	161.0	173.0	–	16.6	13.0[a]	–	127.6	134.9	–	1.49	141.7
$N = 2$	157.6	170.6	164.8	20.6	12.9	14.0	122.5	131.9	132.7	1.74	140.7
$N = 3$	157.7	174.4	164.3	21.8	12.4	13.9	121.4	133.2	130.8	1.98	140.7
$N = 4$	157.4	172.2	165.5	22.0	12.7	14.1	121.9	131.1	133.1	1.82	140.7
$N = 5$	157.8	175.5	165.1	24.1	12.4	13.2	119.9	133.4	129.7	2.02	140.4
Error	±1.3	±1.3	±1.3	±0.6	±0.5	±1.1	±1.3	±1.5	±2.3	±0.04	±2.6

[a] calculated as $(c_{11} - c_{13})/2$.

only with different arrangements of the martensitic variants. As seen in Tables 4 and 5, the values of K for the martensite phases stay constant (or vary within the respective experimental error) for both examined materials. For NiTi, moreover, the average value of K for $N = 0, \ldots, 5$, which is $K = 142.3$ GPa, is in a perfect agreement with $K = 142$ GPa predicted for B19′ martensite by *ab initio* calculations by Wagner and Windl [10].

It is further observed that with the application of the loading cycles, the anisotropy factors A of the NiTi and NiTiCu samples show slightly different behaviors. For NiTi, the anisotropy factor increases after the first loading cycle to 1.34, and then stays within the range 1.28–1.37. For NiTiCu, the increase in the strength of anisotropy of the material is more pronounced. The first loading cycle induces the increase in A to 1.49, but with further repetition of the reorientation sequence A increases up to $A = 2.02$, which is nearly comparable to the strength of anisotropy of nickel single crystals [49].

In Figs. 6 and 7, the evolutions of the elastic constants with the reorientation sequences are visualized by plots of Young's moduli in the principal directions of the sample. It is clearly seen that these moduli evolve from approximately isotropic to significantly anisotropic.

For the NiTi sample, the first loading cycle induces a pronounced increase in the direction of the applied loading (B), but also a slight increase in the perpendicular directions. After the second loading cycle, an increase is observed both in direction C (loading direction) and the direction B. In other words, the reorientation processes within these first two cycles lead to an increase of the Young's moduli, especially in the loading directions; from $E_A \approx E_B \approx E_C \approx 70$ GPa, the Young's moduli of the material change to $E_A \approx 75$ GPa, $E_B \approx 95$ GPa and $E_C \approx 85$ GPa without any detectable change of the bulk modulus K. With the third loading

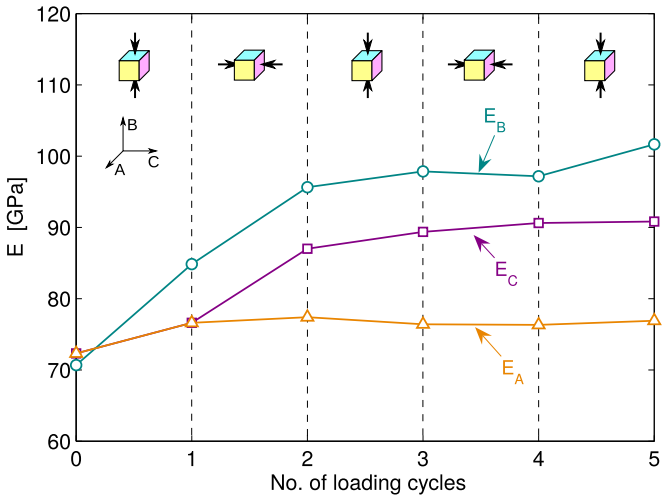

Fig. 6. Young's moduli evolution of the NiTi sample with the reorientation sequence. The orientations of the applied loads within the sequence are outlined in the upper part of the plot area.

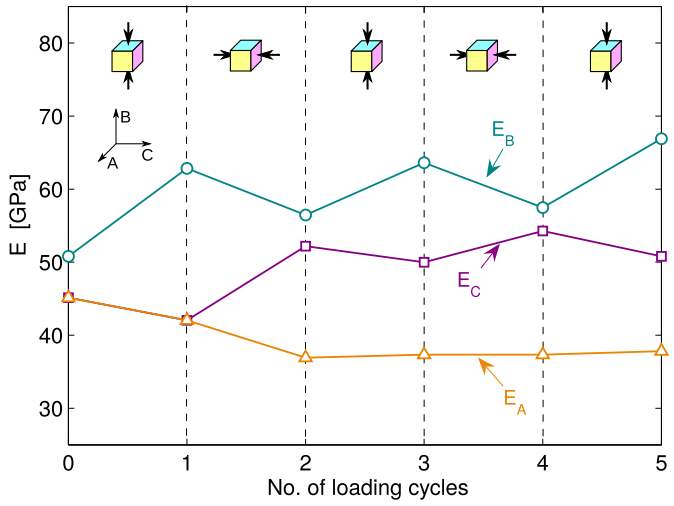

Fig. 7. Young's moduli evolution of the NiTiCu sample with the reorientation sequence. The orientations of the applied loads within the sequence are outlined in the upper part of the plot area.

cycle as well as with the rest of the loading sequence, the Young's moduli remain approximately constant. A slight decrease is observed for the A-direction, while the moduli in the B- and C-directions slightly increase.

For the first loading cycle, the allover increase in Young's moduli can be explained by reduction of the volume fraction of the residual austenite and R-phase; as mentioned in Section 3.1, it was confirmed by X-ray measurements that this reduction takes place during the first cycle. However, the continuation of this increase in the rest of the loading sequence indicates that there is an additional microstructural mechanism that enables elastic stiffening of the material in the direction of the applied compressive stress without inducing pronounced elastic softening in the perpendicular directions. According the Šittner et al. [48], the direction of maximal transformation strain ε^{tr}_{max} for B19′, i.e. the direction of maximal elongation of the lattice due to the austenite → martensite transition, is a direction corresponding to one of the $\{111\}_P$ lattice directions in austenite (the subscript P denotes the parent phase). A shown by *ab initio* calculations by Wagner and Windl [10], this is also the direction of minimal Young's modulus of a B19′ martensite single crystal. Hence, the results obtained here indicate that these soft directions with ε^{tr}_{max} are driven out from the B and C directions by the applied loading cycles, but not reoriented into the directions perpendicular to the loadings. It is obvious that a martensitic variant with the ε^{tr}_{max} strain oriented along the compression direction can reorient only into variants with the ε^{tr}_{max} strains inclined by approximately $\pi/6$ from the plane perpendicular to the loading direction, as the angle contained by two body diagonals (i.e. two $\{111\}_P$ directions in austenite) is equal to $\pi/6$. Thus the elastically soft directions of the reoriented variants may not contribute that much to the elasticity in directions perpendicular to the loading axis.

In summary, our results for NiTi are fully consistent with the finding of Wang and Sehitoglu [13], that the thermally induced microstructure of self-accommodated twins exhibits effectively smaller Young's moduli than the oriented, detwinned martensites. On the other hand, even though the NiTi sample in the direction A is significantly extended ($\varepsilon_A \sim 5\%$), the Young's modulus E_A is incomparably larger that the Young's modulus of thin NiTi wire oriented by tension reported by Šittner et al. in Ref. [14] (~40 GPa). However, the experiments documented in Ref. [14] were done on wires with probably much stronger [111]-texture than one in the examined NiTi sample; moreover, these results were obtained in the superelastic regime, i.e. above the A_F temperature. As seen in Fig. 3, the elastic modulus of the martensite significantly decreases with increasing temperature, and so it is plausible that the stress-induced martensite in the superelastic regime may exhibit somehow lower elastic moduli than the thermally induced one. Nevertheless, Šittner et al. [14] determined the Young's modulus of the wire at only approximately 20 °C above the A_F, but extrapolating the linear trend of dE/dT for NiTi martensite in Fig. 3(b) to $A_F + 20$ °C still gives an estimate of more than 50 GPa. Hence, there must be an additional reason for the discrepancy between our results and [14]. Either the dE/dT slope becomes more steep at elevated temperatures, or there is some microstructural difference or difference in mechanical properties between the thermally induced and stress induced B19′ martensites in NiTi. To analyze in more details the low elastic modulus of stress-induced martensite, measurements of elastic anisotropy under external prestress would be necessary. The RUS method used in this paper is, in principle, unsuitable for such measurements, as it requires free elastic vibrations of the examined sample; as shown recently by Seiner et al. [50] for the Fe-Pd ferromagnetic shape memory alloy, such an issue can be successfully resolved by use of surface acoustic waves.

A somehow different picture is obtained for the NiTiCu sample. The first loading cycle induces an increase in Young's modulus in the loading direction (B), while the Young's moduli in the perpendicular directions decrease. With the second loading cycle (direction C), the Young's modulus in the loading direction increases again, but E_A and E_B decrease. With further repetition of the loading cycles the value of E_A becomes constant, but the Young's moduli in the loading directions B and C oscillate, without showing any tendency to reach a saturated state as observed for the NiTi sample. To analyze this behavior, one additional repetition of the loading sequence was applied to the NiTiCu sample (i.e. the sample was compressed once more along the C-direction and then along the B-direction), and the same oscillations of E_B and E_C were observed.

The observed behavior of the NiTiCu sample probably follows from the orthorhombic structure of B19 martensite. Unlike for the monoclinic B19′, the maximal transformation strain of an orthorhombic martensite must be always aligned with one of the principal directions, and so the reorientation of a B19 unit cell always results in rotation of all elastic properties by $\pi/2$. Consequently, if some elastically soft directions of this unit cell are driven out from the loading direction by reorientation, some softening must appear in the perpendicular directions. Moreover, the orthorhombic B19 martensite can form only three types of twins, while monoclinic B19′ can form up to five types of different twins [51], and so probably the monoclinic martensite can more easily accommodate in complex microstructures under the sequence of applied loadings. As a result, the NiTi sample may subsequently attain a microstructure that is stable under loadings in both B- and C-directions, while for the NiTiCu sample such a microstructure may not exist. The tendency of the NiTiCu polycrystals not to form such microstructures may follow also from the higher mobility (i.e. lower twinning stress) for this alloy.

Regardless of the differences between the evolutions for NiTi and NiTiCu, the relations between Young's moduli E_A, E_B and E_C for both materials after finishing the reorientation sequence is strikingly similar. The maximal Young's modulus E_B is by approximately 30 GPa larger than the minimal Young's modulus E_A, while the value of E_C is approximately in between these two extremes. Nevertheless, further analysis of the directional dependence of the Young's modulus reveals additional differences between the

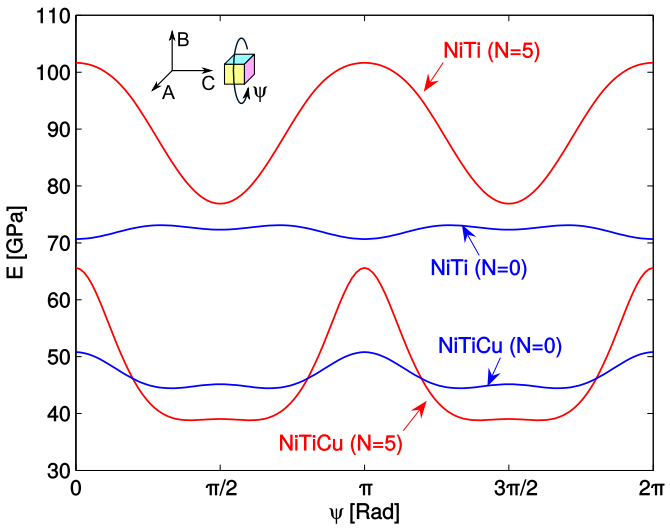

Fig. 8. Directional dependences of Young's moduli of the NiTi and NiTiCu alloy in the A-B plane, plotted for the thermally induced state ($N = 0$) and the maximally reoriented state ($N = 5$). The angle ψ represents the rotation about the C-direction with $\psi = 0$ corresponding the B-direction.

behaviors of the studied alloys (Fig. 8). Young's modulus of the fully reoriented NiTi sample exhibits approximately harmonic evolution with the loading direction with well-defined minima along the A-direction. For NiTiCu, sharp maxima appear along the B-direction, while the minima are broad and flat and the minimum value of E is attained not exactly for the A-direction (the difference is, however, within the range of the experimental error, ±3 GPa). The less smooth character of the $E(\psi)$ curve for the NiTiCu alloy agrees well with the higher value of the anisotropy factor A for this material.

It can be thus concluded that the elastic anisotropy evolves quite differently with the reorientation process in the two examined alloys; in other words, the character of this anisotropy is not determined by the loading procedure, which was the same for both samples, but most probably by the particular microstructure of martensitic variants in the polycrystalline aggregate. Again, the higher number of possible martensitic variants and the higher number of possible twinning systems in the NiTi alloy can be responsible for the less anisotropic macroscale behavior of this alloy compared with NiTiCu. Alternatively, this difference might be explained by a stronger elastic anisotropy of the B19 unit cell, which is, however, not supported by any available experimental data. From the *ab initio* calculations by Windl and Wagner [10], the elastic anisotropy of the B19 and B19′ unit cells seems to be comparable.

The obtained full sets of elastic constants for the polycrystalline NiTi and NiTiCu SMAs may be subjected to further theoretical analysis. As a result of the used experimental methodology, these sets of macroscopic elastic constants correspond to several different pseudoplastically deformed states. When complemented by structural analysis and determination of the orientation distribution functions (ODFs) for the martensitic single variants for each of these deformed states, the obtained data would enable inverse calculation of the elastic constants of a single variant of martensite, as done for example for $\omega-$ titanium by Tane et al. [52].

4. Conclusions

The ultrasonic measurements presented in this work confirm that polycrystalline shape memory alloys can exhibit significant elastic anisotropy (anisotropy factors A ~ 1.5 for NiT and A ~ 2 for NiTiCu) due to reorientation of martensitic variants, and that this anisotropy depends of the pseudoplastic straining history of the material. For both examined alloys, it was observed that Young's modulus in the direction oriented along the applied loading significantly increases when the reorientation is induced by uniaxial compression. Young's moduli in perpendicular directions may either also slightly increase (in the case of NiTi) or slightly decrease (in the case of NiTiCu), probably depending on the particular reoriented martensitic microstructure forming in the material and on the crystal structure of martensite.

The obtained data are not sufficient yet for any reliable analysis of general relations between the pseudoplastic strains and the elastic constants of an SMA polycrystal. To map fully the space of possible strains, imposing tensile and shear deformations onto the materials would be necessary; however, our results indicate that such relations must be particular for each alloy, as there are observable qualitative differences between behaviors of the NiTi and NiTiCu samples.

Full sets of macroscopic elastic constants for the polycrystalline NiTi and NiTiCu SMAs in martensite state were experimentally determined for various deformation states obtained by compression of prism shaped samples and loading histories. These results may be potentially confronted with mechanics model predictions of macroscopic moduli if weak austenite drawing texture of NiTi sample is assumed.

Acknowledgement

Dr. J. Kopeček (Institute of Physics, Czech Academy of Sciences, Prague) is acknowledged for the DSC measurements. This work has been financially supported by Czech Science Foundation (CSF) projects Nos. 14-15264S and 14-28306P.

References

[1] T.M. Brill, S. Mittelbach, W. Assmus, M. Mullner, B. Luthi, Elastic properties of NiTi, J. Phys. Condens. Mat. 3 (1991) 9621–9627.
[2] A. González-Comas, L. Mañosa, A. Planes, F.C. Lovey, J.L. Pelegrina, G. Guénin, Temperature dependence of the second-order elastic constants of Cu-Zn-Al shape-memory alloy in its martensitic and β phases, Phys. Rev. B 56 (1997) 5200–5206.
[3] P. Sedlák, H. Seiner, M. Landa, V. Novák, P. Šittner, L. Mañosa, Elastic constants of bcc austenite and 2H orthorhombic martensite in CuAlNi shape memory alloy, Acta Mater. 53 (2005) 3643–3661.
[4] N. Nakanishi, Elastic constants as they relate to lattice properties and martensite formation, Prog. Mater. Sci. 24 (1980) 143–265.
[5] J. Zhang, X. Ren, K. Otsuka, K. Tanaka, Yu.I. Chumlyakov, M. Asai, Elastic constants of Ti-48at%Ni-2at%Fe single crystal prior to B2 → R transformation, Mater. Trans. 40 (1999) 385–388.
[6] M. Panico, L.C. Brinson, A Three-dimensional Phenomenological Model for Martensite Reorientation in Shape Memory Alloys, vol. 55, 2007, pp. 2491–2511.
[7] L. Saint-Sulpice, S. Arbab Chirani, S. Calloch, A 3D super-elastic model for shape memory alloys taking into account progressive strain under cyclic loadings, Mech. Mater. 41 (2009) 12–26.
[8] F. Auricchio, E. Bonetti, G. Scalet, F. Ubertini, Theoretical and numerical modeling of shape memory alloys accounting for multiple phase transformations and martensite reorientation, Int. J. Plast. 59 (2014) 30–54.
[9] S. Qiu, B. Clausen, S.A.P. Ii, R.D. Noebe, R. Vaidyanathan, On elastic moduli and elastic anisotropy in polycrystalline martensitic NiTi, Acta Mater. 59 (2011) 5055–5066.
[10] M.F.X. Wagner, W. Windl, Lattice stability, elastic constants and macroscopic moduli of NiTi martensites from first principles, Acta Mater. 56 (2008) 6232–6245.
[11] A.P. Stebner, D.W. Brown, L.C. Brinson, Young's modulus evolution and texture-based elastic-inelastic strain partitioning during large uniaxial deformations of monoclinic nickel-titanium, Acta Mater. 61 (2013) 1944–1956.
[12] A.P. Stebner, D.W. Brown, L.C. Brinson, Measurement of elastic constants of monoclinic nickel-titanium and validation of first principles calculations, Appl. Phys. Lett. 102 (1–6) (2013) 211908, http://dx.doi.org/10.1063/1.4808040.
[13] J. Wang, H. Sehitoglu, Martensite modulus dilemma in monoclinic NiTi-theory and experiments, Int. J. Plast. 61 (2014) 17–31.
[14] P. Šittner, L. Heller, J. Pilch, C. Curfs, T. Alonso, D. Favier, Young's modulus of austenite and martensite phases in superelastic NiTi wires, J. Mater. Eng. Perform. 23 (2014) 2303–2314.
[15] B. Reedlunn, C.B. Churchill, E.E. Nelson, J.A. Shaw, S.H. Daly, Tension, compression, and bending of superelastic shape memory alloy tubes, J. Mech. Phys. Solids 63 (2014) 506–537.
[16] P. Šittner, D. Neov, P. Lukás, D.M. Toebbens, Neutron diffraction studies of the stress effect on texture transformations in NiTi shape memory alloys, J. Neutron Res. 12 (2004) 15–20.
[17] H.-R. Wenk, I. Lonardelli, D. Williams, Texture changes in the hcp - bcc - hcp transformation of zirconium studied in situ by neutron diffraction, Acta Mater. 52 (2004) 1899–1907.
[18] P. Šittner, P. Lukáš, V. Novák, M.R. Daymond, G.M. Swallowe, In Situ Neutron Diffraction Studies of Martensitic Transformations in NiTi Polycrystals under Tension and Compression Stress, vol. 378, 2004, pp. 97–104.
[19] M. Kamaya, A procedure for estimating Young's modulus of textured polycrystalline materials, Int. J. Solids Struct. 46 (2009) 2642–2649.
[20] T. Iwakuma, S. Koyama, An estimate of average elastic moduli of composites and polycrystals, Mech. Mater. 37 (2005) 459–472.
[21] K. Gall, H. Sehitoglu, Yu I. Chumlyakov, I.V. Kireeva, Tension-compression asymmetry of the stress-strain response in aged single crystal and polycrystalline NiTi, Acta Mater. 47 (1999) 1203–1217.
[22] Q.-P. Sun, Z.-Q. Li, Phase transformation in superelastic NiTi polycrystalline micro-tubes under tension and torsion - from localization to homogeneous deformation, Int. J. Solids Struct. 39 (2002) 3797–3809.
[23] K. Taillard, S.A. Chirani, S. Calloch, Equivalent transformation strain and its relation with martensite volume fraction for isotropic and anisotropic shape memory alloys, Mech. Mater. 40 (2008) 151–170.
[24] F. Auricchio, L. Petrini, A three-dimensional model describing stress-temperature induced solid phase transformations : solution algorithm and boundary value problems, Int. J. Numer. Methods Eng. 61 (2004) 807–836.
[25] W. Zaki, An approach to modeling tensile-compressive asymmetry for martensitic shape memory alloys, Smart Mater. Struct. 19 (1–7) (2010) 025009.
[26] Y. Chemisky, A. Duval, E. Patoor, Constitutive model for shape memory alloys

including phase transformation, martensitic reorientation and twins accommodation, Mech. Mater. 43 (2016) 361–376.
[27] A.F. Saleeb, S.A.P. Ii, A. Kumar, A multi-axial, multimechanism based constitutive model for the comprehensive representation of the evolutionary response of SMAs under general thermomechanical loading conditions, Int. J. Plast. 27 (2011) 655–687.
[28] M.A. Qidwai, D.C. Lagoudas, On thermomechanics and transformation surfaces of polycrystalline NiTi shape memory alloy material, Int. J. Plast. 16 (2000) 1309–1343.
[29] A. Sadjadpour, K. Bhattacharya, A micromechanics-inspired constitutive model for shape-memory alloys, Smart Mater. Struct. 16 (2007) 1751–1765.
[30] S. Stupkiewicz, H. Petryk, A robust model of pseudoelasticity in shape memory alloys, Int. J. Numer. Methods Eng. (2012) 747–769.
[31] P. Sedlák, M. Frost, B. Benešová, T. Ben Zineb, P. Šittner, Thermomechanical model for NiTi-based shape memory alloys including R-phase and material anisotropy under multi-axial loadings, Int. J. Plast. 39 (2012) 132–151.
[32] M. Frost, P. Sedlák, L. Kadeřávek, L. Heller, P. Šittner, Modeling of mechanical response of NiTi shape memory alloy subjected to combined thermal and non-proportional mechanical loading: a case study on helical spring actuator, J. Intell. Mater. Syst. Struct. 27 (2015) 1927–1938.
[33] R. Kocich, M. Kursa, I. Szurman, The influence of imposed strain on the development of microstructure and transformation characteristics of Ni-Ti shape memory alloys, J. Alloys Compd. 509 (2011) 2716–2722.
[34] R.J. Hill, C.J. Howard, Quantitative phase analysis from neutron powder diffraction data using the Rietveld method, J. Appl. Cryst. 20 (1987) 467–474.
[35] R.G. Leisure, F.A. Willis, Resonant ultrasound spectroscopy, J. Phys. Condens. Mat. 9 (1997) 6001–6029.
[36] J. Maynard, Resonant ultrasound spectroscopy, Phys. Today 49 (1996) 26–31.
[37] P. Sedlák, H. Seiner, J. Zídek, M. Janovská, M. Landa, Determination of all 21 independent elastic coefficients of generally anisotropic solids by resonant ultrasound spectroscopy: benchmark examples, Exp. Mech. 54 (2014) 1073–1085.
[38] M. Landa, P. Sedlák, H. Seiner, L. Bicanová, P. Šittner, Modal resonant ultrasound spectroscopy for ferroelastics, Appl. Phys. A 96 (2009) 557–567.
[39] R.E.A. Mcknight, B.J. Kennedy, Q. Zhou, M.A. Carpenter, Elastic anomalies associated with transformation sequences in perovskites: II. The strontium zirconate-titanate Sr(Zr,Ti)O(3) solid solution series, J. Phys. Condens. Matter 21 (2009) 015902.
[40] P. Ctibor, H. Seiner, J. Sedláček, Z. Pala, P. Vaňek, Phase stabilization in plasma sprayed BaTiO3, Ceram. Int. 39 (2013) 5039–5048.
[41] M. Kabla, H. Seiner, M. Musilova, M. Landa, D. Shilo, The relationships between sputter deposition conditions, grain size, and phase transformation temperatures in NiTi thin films, Acta Mater. 70 (2014) 79–91.
[42] J. Nejezchlebová, H. Seiner, M. Ševčík, M. Landa, M. Karlík, Ultrasonic detection of ductile-to-brittle transitions in free-cutting aluminum alloys, NDT E Int. 69 (2015) 40–47, http://dx.doi.org/10.1016/j.ndteint.2014.09.007.
[43] P. Šittner, M. Landa, P. Lukáš, V. Novák, R-phase transformation phenomena in thermomechanically loaded NiTi polycrystals, Mech. Mater. 38 (2006) 475–492.
[44] M. Thomasová, P. Sedlák, H. Seiner, M. Janovská, M. Kabla, D. Shilo, M. Landa, Young's moduli of sputter-deposited NiTi films determined by resonant ultrasound spectroscopy: austenite, R-phase, and martensite, Scr. Mater. 101 (2016) 24–27.
[45] Y. Liu, D. Favier, Stabilisation of martensite due to shear deformation via variant reorientation in polycrystalline NiTi, Acta Mater. 48 (2000) 3489–3499.
[46] G. Tan, Y. Liu, Comparative study of deformation-induced martensite stabilisation via martensite reorientation and stress-induced martensitic transformation in NiTi, Intermetallics 12 (2004) 373–381.
[47] H. Seiner, L. Bodnárová, P. Sedlák, M. Janeček, O. Srba, R. Král, M. Landa, Application of ultrasonic methods to determine elastic anisotropy of polycrystalline copper processed by equal-channel angular pressing, Acta Mater. 58 (2010) 235–247.
[48] P. Šittner, V. Novák, Anisotropy of martensitic transformations in modeling of shape memory alloy polycrystals, Int. J. Plast. 16 (2000) 1243–1268.
[49] M.J.P. Musgrave, Crystal Acoustics, Holden-Day, San Fransisco, 1970.
[50] H. Seiner, P. Stoklasová, P. Sedlák, M. Ševčík, M. Janovská, M. Landa, T. Fukuda, T. Yamaguchi, T. Kakeshita, Evolution of soft-phonon modes in FePd shape memory alloy under large elastic-like strains, Acta Mater. 105 (2016) 182–188.
[51] K. Bhattacharya, Microstructure of Martensite, Oxford University Press, New York, 2003.
[52] M. Tane, Y. Okuda, Y. Todaka, H. Ogi, A. Nagakubo, Elastic properties of single-crystalline x phase in titanium, Acta Mater. 61 (2013) 7543–7554.

PHASE TRANSITIONS
https://doi.org/10.1080/01411594.2018.1499914

Taylor & Francis
Taylor & Francis Group

Acoustic phonons in unfilled tetragonal tungsten-bronze crystals

E. Buixaderas[a], P. Bérešová[a], P. Ondrejkovič[a], P. Vaněk[a], M. Savinov[a], P. Bednyakov[a], J. Dec[b], D. Mareš[c], M. Ševčík[c] and M. Landa[c]

[a]Czech Academy of Sciences, Institute of Physics, Prague, Czech Republic; [b]Institute of Materials Science, University of Silesia, Katowice, Poland; [c]Czech Academy of Sciences, Institute of Thermomechanics, Prague, Czech Republic

ABSTRACT

We have studied several unfilled tetragonal tungsten-bronze crystals (SBN-35, CBN-28, CBN-30, CBN-32) by differential scanning calorimetry, Brillouin spectroscopy and piezoresponse-force microscopy. The Brillouin backscattering configuration in the c-plates revealed the longitudinal acoustic phonon, which has a frequency near 50 GHz and displays softening when approaching the phase transition in all crystals. The ferroelectric domain structure and the domain size are dependent on the Sr/Ba or Ca/Ba ratios, and on the occupation rate in the channels as shown by the piezoresponse-force microscopy images. A splitting of the longitudinal acoustic phonon was found in SBN-35 in the multidomain sample, but poling of the crystal removed this splitting and just left the phonon with higher frequency.

ARTICLE HISTORY
Received 18 May 2018
Accepted 9 July 2018

KEYWORDS
Acoustic phonons; tetragonal tungsten-bronzes; piezoresponse-force microscopy; ferroelectric domains

1. Introduction

Tetragonal tungsten-bronzes (TTBs) with the general chemical formula $(A1)_2(A2)_4(C)_4(B)_{10}O_{30}$ conform a whole structural family with versatile properties caused by cationic substitution in the crystallographic sites. The structure is formed by a network of interconnected BO_6 octahedra forming three types of channels along the *c* axis: squared (A1 site), pentagonal (A2 site) and triangular ones (C site). Different cations can occupy A1, A2, B and C sites, which provide the structure with versatile properties. We have focused on niobium based unfilled TTBs with the formulae $(Sr_xBa_{1-x})_5Nb_{10}O_{30}$ (SBN-100*x*) and $(Ca_xBa_{1-x})_5Nb_{10}O_{30}$ (CBN-100*x*). Ca and Sr atoms share the squared and pentagonal channels, Ba is located only in pentagonal channels and triangular ones remain empty. In their structure, only five out of six available A-sites are occupied. Thus, the empty A-sites, being random, create an inherent disorder in the structure. Dielectric properties, mainly T_C and the maximum value of permittivity, change according to the amount of Sr or Ca present in the structure [1,2], and besides, SBN crystals show a perfect tuning between ferroelectric and relaxor behaviour.

Regarding the acoustic and elastic properties of these crystals, several studies have already been conducted in SBN, but mainly in the compositions displaying relaxor behaviour. In SBN-61 the Brillouin scattering in several geometries was already studied, showing the frequency of longitudinal and transverse acoustic modes [3]. Later, it was shown that an electric field applied during the measurements of the Brillouin spectra increased substantially the frequency of the longitudinal acoustic (LA) mode showing an intermediate region with two peaks [4]. The lower frequency peak was related to the LA mode travelling along polar nano regions (PNRs) in this relaxor sample, and the high frequency one to the LA mode of the poled crystal. In ferroelectric

CONTACT E. Buixaderas buixader@fzu.cz

SBN-40 [5] the effect of the field on the Brillouin spectra was also increasing the frequency of the LA mode. In this crystal, the effect of the coexistence of two LA peaks was attributed to the existence of nano and macro domains, and the evolution from the nanodomain state to the macro- or single domain state by the application of the electric field, similarly to SBN-61. The Brillouin scattering of CBN was also studied [6,7]. The LA mode was found to have similar frequencies to those in SBN and it softens towards T_C. The same field-effect on the LA frequency on heating and cooling was found for CBN-30 [8].

The purpose of this study is to investigate the phase transitions of several ferroelectric TTB crystals with different techniques (calorimetry, Brillouin spectroscopy, piezo-force microscopy) and compare the behaviour of the LA modes in a wide temperature range (~200–570 K) on heating and cooling, also in relation to the distribution of the ferroelectric domains and poling of the crystals.

2. Experimental details

Crystals were grown by the Czochralski method, as explained elsewhere [1]. From the transparent bulk crystals, samples were cut in the form of plates (about $4.5 \times 4.5 \times 0.8$ mm^3) with the polar axis perpendicular to the surface, i.e. *c*-plates. The structure of a TTB crystal in the ferroelectric phase is depicted in Figure 1, where the unit cell is marked by red lines. Grey coloured octahedra contain Nb atoms in special positions, and green octahedra correspond to octahedra containing Nb in general positions. Multi-occupation in the channels and atomic disorder is marked by the presence of several atoms in the same site.

Differential scanning calorimetry (DSC) was carried out with a PerkinElmer DSC 8000 differential scanning calorimeter. The samples were heated from room temperature to at least 500 K at a rate of 5 K/min for SBN and 10 K/min for CBN, and cooled at the same rate after holding at the highest temperature for one minute. The calorimetric sample holder was purged by nitrogen at 20 ml/min. PerkinElmer Pyris 13.1 software was used for control and evaluation. Three measurements of the same crystals were performed to check reproducibility.

Piezoresponse -force microscopy (PFM) studies were carried out using a Ntegra atomic force microscope. The measurements were performed using a conductive *n*-doped Si cantilevers (HQ: NSC35/Pt and TESP-V2) in a contact mode at room temperature. The frequency of the alternating

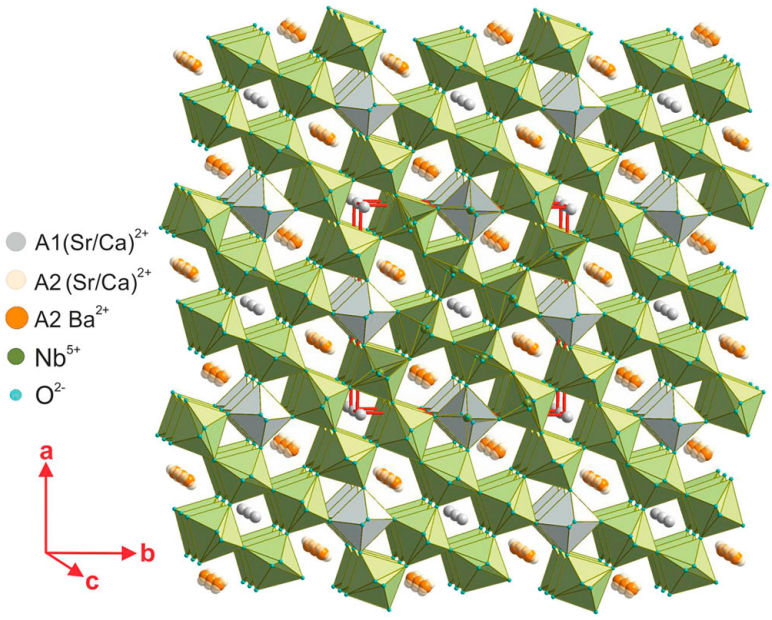

Figure 1. Tetragonal tungsten-bronze structure at room temperature.

voltage was set to 25 and 34 kHz and the amplitude to 4 5 V. The vertical PFM signals were amplified and analysed with an external SR830 DSP Lock-In Amplifier.

Brillouin scattering measurements were done with a tandem Fabry-Pérot interferometer TFP-2 HC in combination with a solid state single longitudinal mode laser source LCX-532S (wavelength of 532 nm and power of 200 mW). The optical arrangement of this interferometer is a tandem arrangement of two triple pass interferometers. A spatial filter separates the two interferometers and, thus, eliminates any cross-talk between the first and last passes. The coupling between passes is eliminated using quarter wave antireflection techniques. In this way, the transmission peaks remain completely symmetrical. Because the multiple reflections between passes are totally eliminated, a contrast of at least 1015 was achieved.

3. Results and discussion

3.1 Calorimetric results and piezoresponse-force microscopy

Three crystals were measured by DSC: SBN-35, CBN-28 and CBN-32. Figure 2 shows the normalized calorimetric curves on heating and cooling at 5 K/min (SBN-35) and 10 K/min (CBN-28 and CBN-32). After heating, the samples were held one minute at the maximum temperature and then cooled down at the same rate. The ferroelectric phase transition is clearly seen in all crystals and shows a small thermal hysteresis. The highest T_C corresponds to CBN-28. The calculated enthalpy shows values near 0.4 J/g for the CBN crystals and 0.35 for SBN-35 (see Table 1), although peaks for CBN crystals are wider than the one for SBN-35. This widening could be due to the quicker heating/cooling rate for CBN, which allows different kinetics at the phase transition. But also it could mean that CBN samples have a certain diffusive character, showing some traces of starting/developing relaxor behaviour. Due to the shape of the peaks, the phase transition can be considered of *weak* first order.

The TTB crystals were checked by PFM to see the distribution of the ferroelectric domains. The biggest domains are present in SBN-35, with sub-micron size, irregular distribution, and clear 180° domain walls, as seen in Figure 3(a) (amplitude) and Figure 3(b) (phase). The grey and red colours in the phase images correspond to domains with polarization oriented upwards and downwards, respectively. CBN crystals show smaller domains with grainy-like texture, especially in CBN-32. The domain size decreases with increasing Ca/Ba concentration and 180° domain walls become more jagged in agreement with ref. [9].

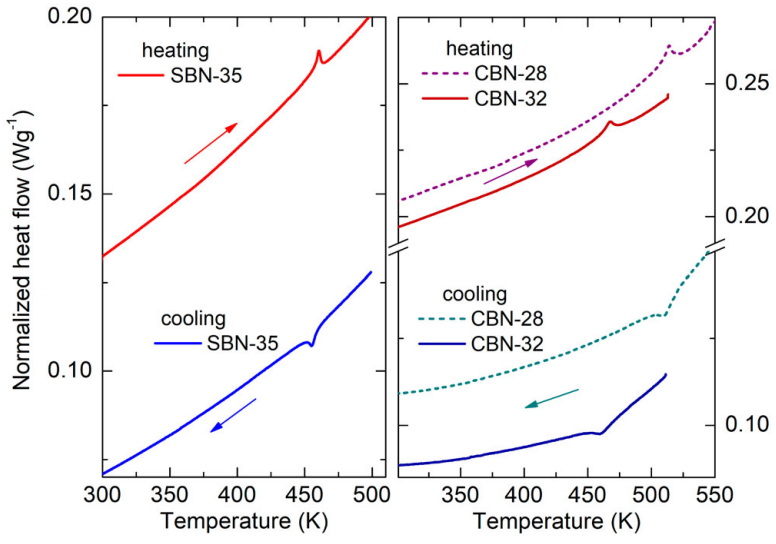

Figure 2. Calorimetric curves on heating and cooling for SBN and CBN crystals.

Table 1. Obtained transition temperatures by Brillouin scattering and differential scanning calorimetry (together with the change of enthalpy) on several TTB crystals.

TTB crystal	T_C (Br) heating/cooling (K)	T_C (DSC) heating/cooling (K)	ΔH (J/g)
SBN-35	475/455	460/455	0.35
CBN-28	527/521	513/510	0.4
CBN-32	473/461	468/460	0.4

3.2 Brillouin scattering

Results of Brillouin scattering from all the crystals at room temperature in two runs (during the first heating and the subsequent cooling) are shown in Figure 4. In the measured configuration (backward scattering) on *c*-plates just longitudinal acoustic (LA) modes are shown. In all the crystals the frequency of LA mode is about 50 GHz. However, in SBN-35, this mode is split, which is somehow unusual, because there is just one LA mode allowed.

The Raman tensors of polar modes A_1 and E of the tetragonal group 4 mm are

$$A_1(z) = \begin{pmatrix} a & 0 & 0 \\ 0 & a & 0 \\ 0 & 0 & b \end{pmatrix}, E(x,y) = \begin{pmatrix} 0 & 0 & e \\ 0 & 0 & e \\ e & e & 0 \end{pmatrix}$$

As the selection rules for the acoustic modes are the same as in Raman, in the *c*-plates (polar axis along z direction) and in $z(xx)\bar{z}$ configuration only longitudinal A_1 modes are allowed; therefore the mode detected by the Brillouin scattering is the longitudinal acoustic A_1LA near 50 GHz. The small feature seen at 32 GHz could be an artefact from the glass cover of the temperature chamber or a weak leakage of the A_1TA mode due to a non-perfect orientation of the crystal and polarizators.

In CBN samples, the spectra at room temperature taken on heating and on cooling are practically the same, just in CBN-32 there is a small asymmetry of the peak. However, in SBN-35, the splitting is evident. A similar effect was found in SBN-61 and CBN-30 with the application of an electric field [4,8]. In Figure 4 we added the spectra of SBN-35 after poling, where the doubled peak has disappeared, although the position of the peak changes after the heating and subsequent cooling.

In Figure 5 we show the behaviour of the A_1LA mode on heating and on cooling for CBN-28 and CBN-32 crystals. The phase transition is seen by a change in the shift of the peak. The spectra in

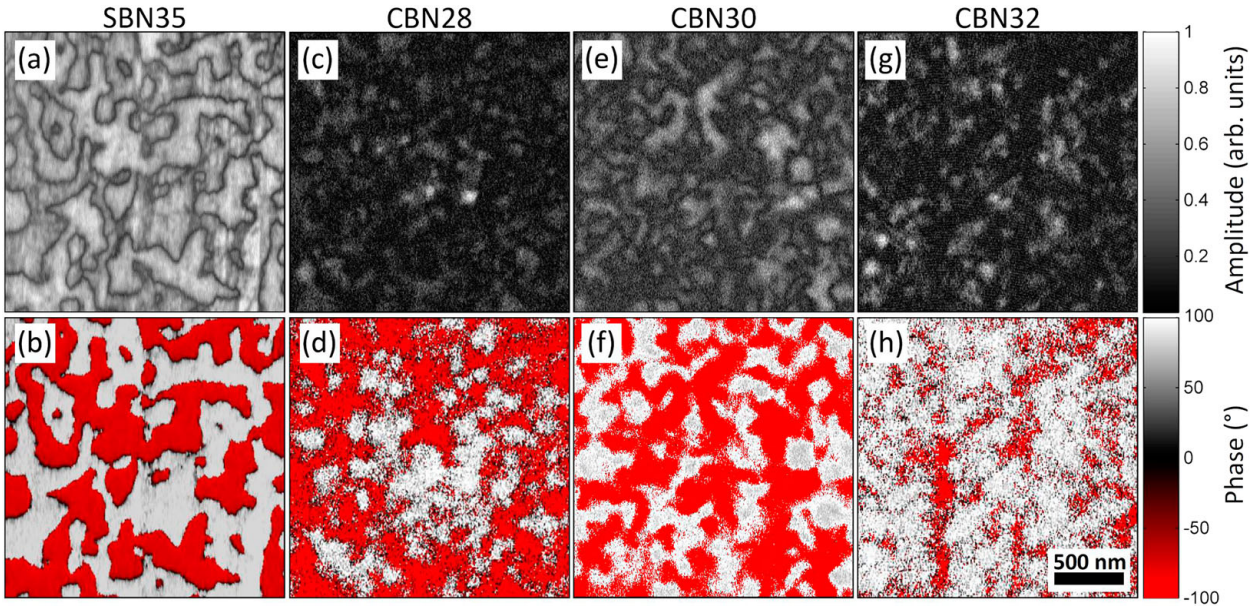

Figure 3. Amplitude (first row) and phase (second row) images of vertical PFM signal measured on the (001) cut of SBN and CBN crystals.

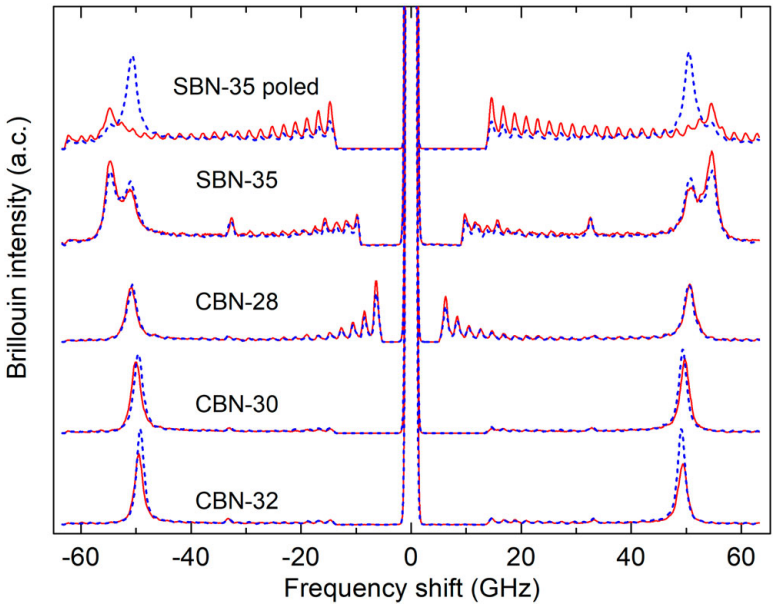

Figure 4. Brillouin scattering spectra at room temperature in *c*-plates, $z(xx)\bar{z}$ configuration. The solid and dashed lines correspond to data measured during heating and cooling.

Figure 5 were fitted to a simple Lorentzian curve whose parameters – frequency ν_B and width (FWHM) – are plotted in Figure 5(c,d) as a function of temperature. The softening of the A_1LA mode towards the phase transition is clear in both samples and the transition temperatures are found to be well consistent with the calorimetric results (see Table 1). There is a thermal hysteresis of several degrees in the value of T_C for the crystals, but the behaviour of ν_B is asymmetric for heating and cooling in a wide temperature range below T_C (for more than 100°), evidenced also in the temperature dependence of its width. This rather indicates 'global thermal hysteresis', as it was found in SBN-61 [10] and in other incommensurate materials [11]. The velocity of propagation of A_1LA, the longitudinal sound waves in the *c*-plates, was calculated according to the formula $v_{LA} = \lambda\nu_B/2n_e$, using the wavelength of the laser, $\lambda = 532$ nm, and an approximate index of refraction of the extraordinary ray for both samples $n_e = 2.28$ [12].

The strongest thermal hysteresis is present in SBN-35, where the difference in T_C on heating and cooling is $\Delta T_{h\text{-}c} = 20$ K (see Figure 6 and Table 1), and the shape of the LA mode changes substantially between heating and cooling Brillouin measurements.

To check the influence of the domain configuration on the Brillouin scattering of SBN-35 and find out whether the doublet found in SBN-35 is related to the distribution or density of ferroelectric domains, we poled the crystal and checked the Brillouin signal again. The sample was poled by applying a voltage of 5 kV at 60°C for two weeks. Results of the Brillouin scattering measured of heating and on cooling before and after the poling of the crystal are shown in Figure 6, together with the frequency of the A_1LA mode and the associated sound velocity, using $n_e = 2.31$ [13].

Before the poling, the sample showed a double peak (the frequencies of the two maxima at room temperature are ν_{B1}~51 and ν_{B2}~55 GHz). On heating up to T_C, the doublet persists, although the higher frequency mode ν_{B2} loses its strength and then disappears in the paraelectric phase, where just one mode is present up to 573 K. On cooling from this temperature and passing through T_C again, the two-mode state is recovered in the same fashion, the higher frequency one ν_{B2} is weaker. This means that the domain state was essentially not changed.

After the poling of the crystal, the spectra showed just one peak, a little asymmetric, located at ν_{B2}~55 GHz (see Figure 6(c)). This mode displays an important softening towards T_C on heating up to 573 K, and during the subsequent cooling, it again softened towards T_C. However, below T_C, the frequency was different, and the mode hardened only to ν_{B1}~51 GHz. The change of behaviour with poling seems to suggest that the multidomain character of the crystal was responsible for

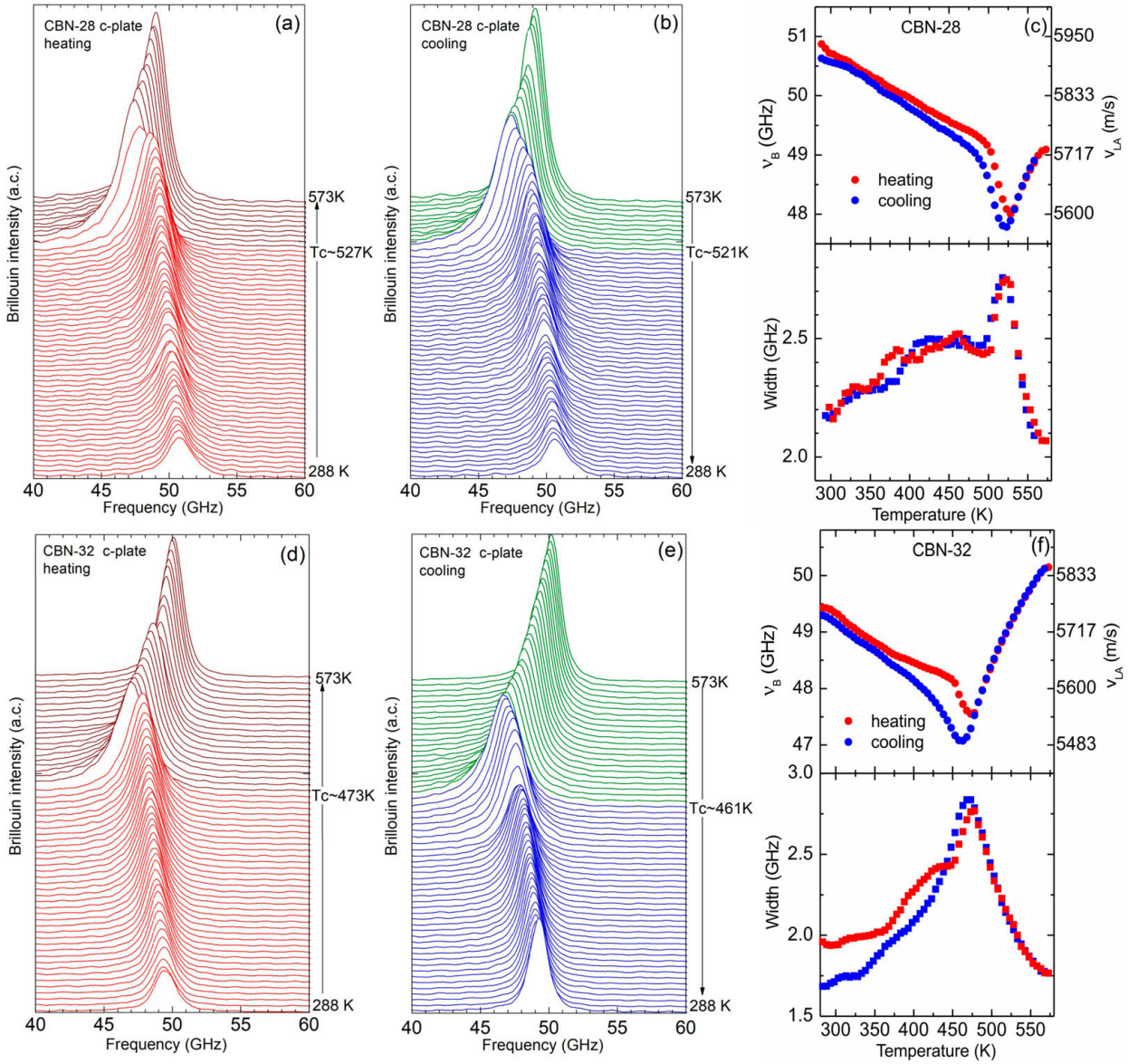

Figure 5. A_1LA modes of CBN-28 and CBN-32 on heating and cooling. Temperature dependences of the frequency and width (FWHM) of the LA peak.

the double LA peak in Brillouin scattering. A simple explanation could be that the LA waves travel at different speed along the domains and the domain walls.

The effect of the electric field in situ on the Brillouin signal of SBN-61, SBN-40 and CBN-30 was already studied [4,5,8]. The electric field applied during the Brillouin experiment changes the intensity of the LA mode and induces its shift to higher frequencies. This effect was related to the coexistence of ferroelectric macro domains and PNRs (for SBN-61) or nanodomains (in SBN-40 and CBN-30). This seems to suggest, that the higher frequency Brillouin peak is related to the ferroelectric bulk state in the crystal. This is in agreement with our measurements: after the poling of the crystals, we also observed the LA mode at higher frequencies.

In SBN-35 there are no PNRs (this crystal shows an utmost ferroelectric behaviour). When the crystal was poled, the sample was in almost single domain state and the volume fraction of the domain walls was much smaller, therefore the high frequency peak ν_{B2}, related to the bulk, was revealed. On the subsequent cooling we practically just found the low-frequency peak ν_{B1}. This peak could, in principle, be related to the presence of either small ferroelectric domains or domain walls. In order to solve this question we checked the state of the poled crystal at room temperature

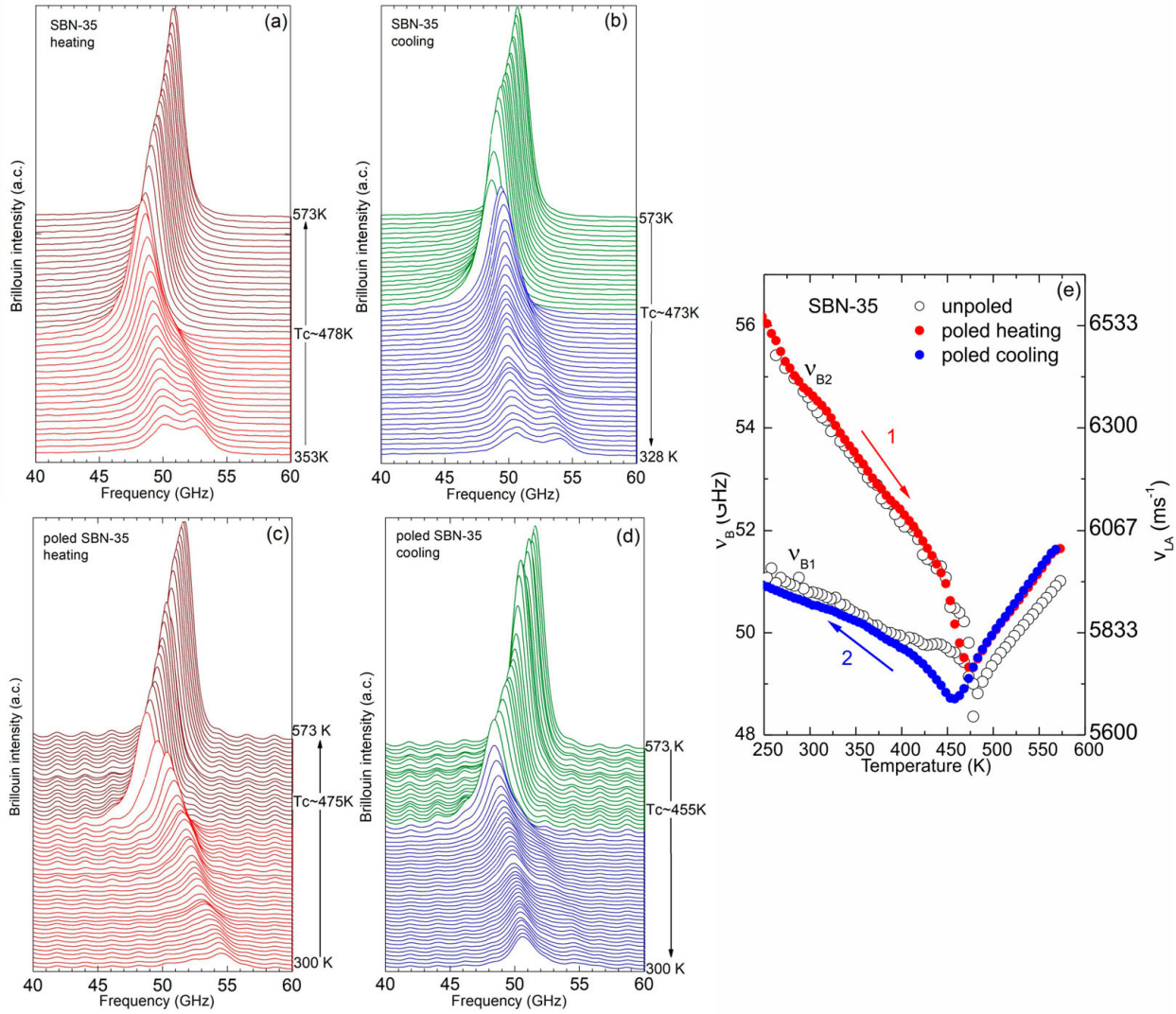

Figure 6. (a–b): A_1LA mode on heating and cooling for SBN-35 before poling (with the domain distribution shown in Figure 3); (c–d): after poling (single domain state); (e): temperature dependences of the frequency of the A_1LA peak.

after the measurements (heating and cooling runs) by PFM technique and the sample still showed the single domain state.

The fact that the split acoustic mode is seen in both relaxor and ferroelectric compounds (SBN-61 and SBN-35) means that the splitting cannot be related simply to the coexistence of different types of domains and PRNs; it rather suggests that the antiparallel domain boundaries clamp the electromechanical contribution to the elasticity in the bulk. This effect calls for further investigation.

4. Conclusions

The behaviour of the longitudinal acoustic mode has been investigated in several TTB crystals (SBN-35, CBN-28, CBN-30 and CBN-32) by Brillouin scattering in a wide temperature range (~200–570 K) and in a backwards configuration in *c*-plates. The transition temperatures were compared with those found by DSC, and PFM studies were performed at room temperature to check the distribution of the ferroelectric domains. Poling of SBN-35 shown that the domain arrangement of the crystal has an influence on the Brillouin scattering and the frequency of the longitudinal acoustic waves. The single domain state shows a longitudinal acoustic mode with higher frequency, whereas in the multidomain crystal this mode coexists with another mode of lower frequency. The relationship of this lower frequency mode with the high density of smaller domains or domain walls remains still unclear.

Disclosure statement

No potential conflict of interest was reported by the authors.

Funding

This work was supported by Czech Science Foundation (Grantová Agentura České Republiky): [grant number: 16-09142S].

References

[1] Lukasiewicz T, Swirkowicz MA, Dec J, et al. Strontium–barium niobate single crystals, growth and ferroelectric properties. *J Cryst Growth*. 2008;310:1464–1469.
[2] Malyshkina OV, Lisitsin VS, Dec J, et al. Pyroelectric and dielectric properties of calcium barium niobate single crystals. *Phys Solid State*. 2014;56(9):1763–1766.
[3] Jiang FM, Ko JH, Kojima S. Central peaks and Brillouin scattering in uniaxial relaxor single crystals of Sr0.61Ba0.39Nb2O6. Phys Rev B. 2002;66:184301(1)–184301(7).
[4] Matsumoto K, Kojima S. Electric field on uniaxial relaxor ferroelectric strontium barium niobate. *Jap J Appl Phys*. 2015;54:10NC04(1)–10NC04(4).
[5] Aftabuzzaman M, Helal MA, Paszkowski R, et al. Electric field and aging effects of uniaxial ferroelectrics $Sr_xBa_{1-x}Nb_2O_6$ probed by Brillouin scattering. *Sci Rep*. 2017;7:11615(1)–11615(9).
[6] Suzuki K, Matsumoto K, Dec J, et al. Composition variation of elastic anomalies in uniaxial relaxor $Ca_xBa_{1-x}Nb_2O_6$ crystals. *Proc Symp Ultras Electr*. 2013;34:29–30.
[7] Suzuki K, Matsumoto K, Dec J, et al. Critical slowing down and elastic anomaly of uniaxial ferroelectric $Ca_{0.28}Ba_{0.72}Nb_2O_6$ crystals with tungsten bronze structure. *Phys Rev B*. 2014;90:064110(1)–064110(4).
[8] Aftabuzzaman M, Dec J, Kleemann W, et al. Field dependent elastic anomaly in uniaxial tungsten bronze relaxors. *J Appl Phys Jap*. 2016;55:10TC01(1)–10TC01(6).
[9] Shvartsman VV, Gobeljic D, Dec J, et al. A piezoresponse force microscopy study of $Ca_xBa_{1-x}Nb_2O_6$ single crystals. *Materials (Basel)*. 2017;10:1032(1)–1032(7).
[10] Ondrejkovic P, Kempa M, Savinov M, et al. Electric-field influence on the neutron diffuse scattering near the ferroelectric transition of $Sr_{0.61}Ba_{0.39}Nb_2O_6$. *Phase Transitions*. 2016;89:808–816.
[11] Hernandez O, Hlinka J, Quilichini M. Study of the global thermal hysteresis in D-BCCD with elastic neutron scattering. *J Phys I*. 1996;6:231–236.
[12] Esser M, Burianek M, Held P, et al. Optical characterization and crystal structure of the novel bronze type $Ca_xBa_{1-x}Nb_2O_6$ (x = 0.28; CBN-28). *Cryst Res Technol*. 2003;38(6):457–464.
[13] Venturini EL, Spencer EG, Lenzo PV, et al. Refractive indices of strontium barium niobate. *J Appl Phys*. 1968;39:343–344.

Proceedings of the International Symposium on Physics of Materials (ISPMA 14), September 10–15, 2017, Prague

In Situ Characterization of the Elasticity and Stress-Induced Phase Transformation of NiTi Shape-Memory Alloy

T. Grabec[a,*], K. Zoubková[b], P. Stoklasová[c], M. Ševčík[c], P. Sedlák[c], M. Janovská[c], H. Seiner[c] and M. Landa[c]

[a]Nuclear Physics Institute, Academy of Sciences of the Czech Republic, Řež 130, 250 68 Řež, Czech Republic
[b]Faculty of Nuclear Sciences and Physical Engineering, Czech Technical University in Prague, Trojanova 13, 120 00 Prague 2, Czech Republic
[c]Institute of Thermomechanics, Academy of Sciences of the Czech Republic, Dolejškova 5, 182 00 Prague 8, Czech Republic

In the presented paper, a sample of polycrystalline shape-memory NiTi alloy is studied under compression up to 5% by the means of laser-excited and laser-detected ultrasound waves. The evolution of a propagation velocity of the surface acoustic wave is measured *in situ* during mechanical loading. An inverse method based on the Ritz–Rayleigh numerical approach is then used to obtain the development of elastic properties of the sample. This process enables an analysis of the evolution of stress-induced transformation from the austenitic to the martensitic phase with the possibility to describe several stages of such transformation, i.e., the transformation to full R-phase, its reorientation causing strong anisotropy of the polycrystalline sample, and consecutive gradual transition to martensite.

DOI: 10.12693/APhysPolA.134.811
PACS/topics: 43.20.+g, 81.05.Bx, 62.20.fg

1. Introduction

Elastic properties of single crystals of shape-memory alloys (SMAs) are usually strongly anisotropic [1–3]. Near the transition temperature, the crystal lattice is unstable due to phonon softening [4–6], which increases the anisotropy even further. Laser-ultrasound measurements, such as the resonant ultrasound spectroscopy (RUS) comprise a great tool to study the highly anisotropic materials [7] and the temperature-dependent behavior of materials [8]. Recently, Thomasová et al. [9] presented an *ex situ* study of the strain-dependence of elastic properties of martensitic structures in polycrystalline NiTi. It was shown in this work that the macroscopic moduli of polycrystalline SMAs can be strongly anisotropic under certain circumstances — in this particular case after stress-induced reorientation of martensitic structure by a uniaxial compression. It is known that those variants of martensite inside the individual grains oriented to the applied stress in an advantageous way grow more than the others [10–12]. It is shown in this study that the *in situ* measurement offers much more detailed insight into the behavior of the material under stress, with a potential to directly describe the ongoing processes.

The elastic constants of a polycrystalline SMA depend on single-crystal elastic coefficients of the individual phases present in the aggregate, the volume fractions of these phases, on the crystallographic texture of austenite, the martensitic microstructure, and the mutual morphology of austenite and martensite [9]. In this work, the development of elastic properties and overall anisotropy of a sample undergoing a compressional loading is studied. The changes in the velocity of the Rayleigh waves during the loading are observed by laser-based ultrasound measurement. To obtain the changes in elasticity coefficients out of the SAW velocities, an inverse procedure utilizing a Ritz–Rayleigh approach as the forward method is presented. It is shown that the originally almost-isotropic compound of R-phase and austenite is transformed to full R-phase, which then reorients, and thus induces strong anisotropy of the sample. During the following loading, the sample undergoes a martensitic phase-transformation. It can be observed from the presented results that the transformation is heterogeneous on microscale. In the last phase of the loading, the stiffening of martensitic phase can be seen, followed by reversible softening during the unloading, thus proving a stress-dependence of elastic properties of the martensite.

2. Sample and experimental method

The studied sample was made from a commercially available NiTi with the nominal composition of 50.5 at.%Ni and 49.5 at.%Ti. The sample size is $5 \times 15 \times 50$ mm^3, one surface of the sample was polished. At room temperature, the material is in a state of austenite and R-phase. The transformation temperatures can be found in [13].

*corresponding author; e-mail: grabec@ujf.cas.cz

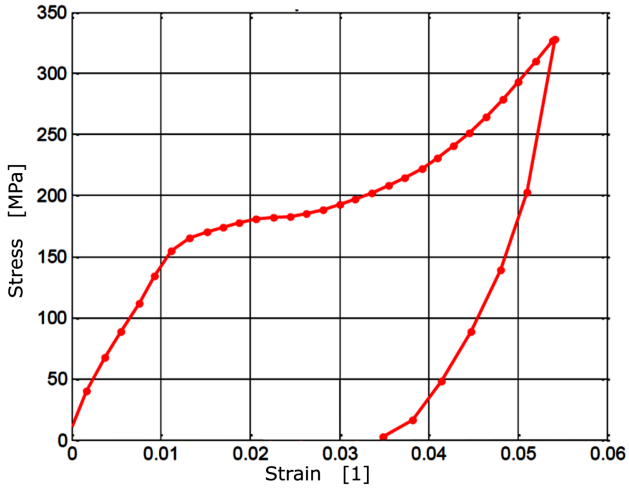

Fig. 1. Stress–strain curve obtained during the measurement (note that the stress is compressional and correspondingly the strain is negative) [14].

A mirror-polished face was used for measurement of the velocity of surface acoustic waves (SAWs). For the excitation, a Nd:YAG laser (1064 nm, 400 ps pulses) focused through a cylindrical lens in order to create a line source was used. The emergent waves were detected by a laser vibrometer (532 nm, cw). The sample was mounted on a small in-house built testing machine (maximal load 5 kN). The testing machine can rotate in order to allow the measurement of the SAW velocity in different directions with respect to the loading. The stress–strain curve of the examined sample at room temperature is shown in Fig. 1. The measurement was conducted in 16 different distances between the excitation and detection spot to obtain the SAW velocity in particular direction. This measurement was made in 5 angles between the propagating wave and loading axis in over 50 strain stages during loading. The resulting evolution of velocities in different directions during the loading is shown in Fig. 2. More details about the experimental setup can be found in [14].

3. Inverse calculation of the elastic constants

The experimentally determined SAW velocities were processed by numerical inverse procedure based on the Ritz–Rayleigh approach introduced in [15]:

$$F\left(c_{ij}\right) = \sum\nolimits_{p} \left(v_p^{\mathrm{cal}}\left(c_{ij}\right) - v_p^{\mathrm{exp}}\right)^2 . \qquad (1)$$

The Ritz–Rayleigh approach offers a fast and robust forward procedure capable of calculation of the velocity of SAW propagating in any direction through a generally anisotropic material with the elastic given. The approach is based on Hamilton's principle, according to which the resonant frequencies and the corresponding modal shape can be found as stationary points of a Lagrangian energy of a harmonically vibrating body, i.e. a computational domain with the constraints chosen in a way to suit the problem solved. To find these stationary points, a discretization of the displacement field into the Legendre polynomials is considered. The solution then contains both bulk and surface resonances of the domain, which can be easily distinguished, e.g. based on the modal shape. The inverse procedure is then based on an iterative process of changing the initial set of elastic constants. The set of corresponding SAW velocities obtained from the forward procedure is then compared to the experimental value via the objective function where p goes through all measured angles, and the superscripts exp and cal denote the calculated and experimental velocity, respectively. For the minimization of this function, a gradient Levenberg–Marquardt method is used. The numerical inverse procedure depicted briefly here was described in more detail by Stoklasová et al. [15]. It was shown that in addition to the spatial dispersion calculated in this case, the method can be modified for calculations of a frequency dispersion in a layered system [16].

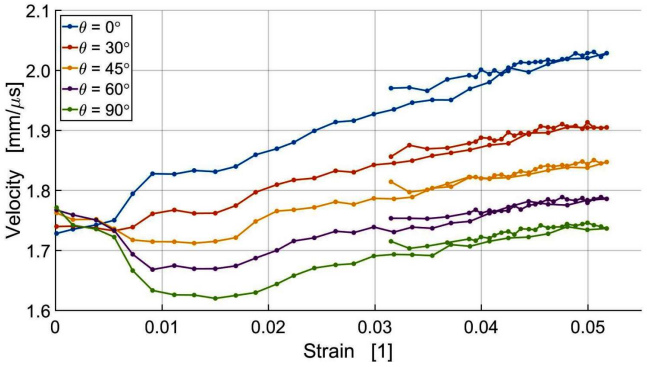

Fig. 2. Experimentally obtained SAW velocities in different angles with respect to strain.

The result of the inverse procedure is a set of elastic constants minimizing the objective function. Considering the nature of the experiment, i.e. the initial isotropy and uniaxial loading, the material is assumed to adopt the transversely isotropic character. As such, it exhibits hexagonal symmetry with 5 independent elastic constants: c_{11}, c_{33}, c_{13}, c_{44}, and c_{66}. Considering the geometry of the experiment, the direction of the symmetry is assumed to be aligned with x_3 axis. This set was calculated for each stress level. The error of this set can be estimated by an error-analysis procedure described in detail in Ref. [7]. However, given the informative character of the results presented in this paper, the error is not calculated here. The mass density taken for the calculations was 6.45 g/cm^3.

4. Results

Experimental stress–strain curve (Fig. 1) shows a character typical for memory alloys under compression [17]. It shows the initial almost-linear response, then the plateau of martensitic transition between around 1.3% and 3.5%, and then the following loading of martensite. The measured velocities of SAWs (Fig. 2) and corresponding shear elastic moduli (Fig. 3) document arguably rather peculiar behavior of the material during this compression test.

In the initial phase of loading up to the start of the martensitic phase transition above 1.3%, a surprisingly strong anisotropy of the sample arises. With a maximum at the beginning of the phase transition, the anisotropy peaks a ratio of 1.35 between the shear elastic moduli. This is believed to be caused by the induction of the reorientation of the trigonal R-phase, and it was checked that this process is fully reversible and can be observed only during *in situ* measurement under applied stress.

The second part shows the development of elastic constants during the stress-induced martensitic phase transformation. The material stiffens in all directions, as the elastic constants of martensite are higher than the ones of R-phase. However, there is an interesting observation in the character of the progress — whereas c_{44} increases linearly, the c_{66}-evolution shows a certain curvature. From this fact, it can be assumed that whereas on a macroscopic level, the martensitic transition in compression proceeds homogeneously, it is heterogeneous on the level of microstructure. The data obtained by SAWs are unfortunately insufficient to obtain a full understanding of the heterogeneity and the process itself, as they mostly carry the information about the shear behavior, and thus must be accompanied by supplement measurements of the longitudinal wave.

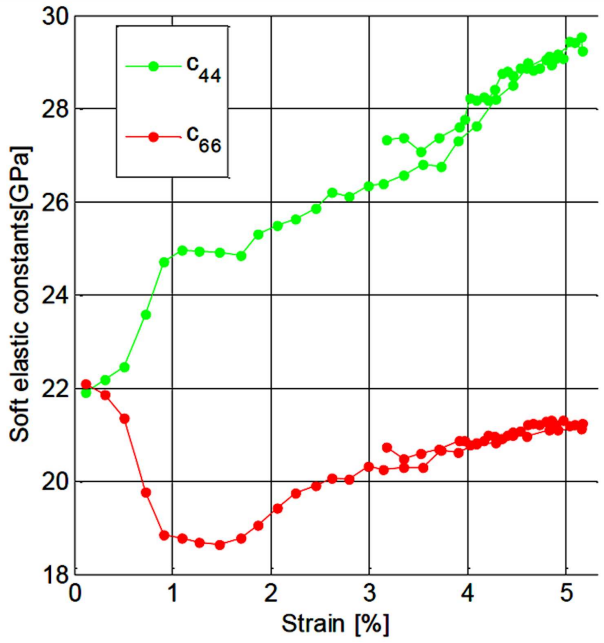

Fig. 3. Resulting shear elastic moduli obtained by the inverse procedure.

The third and last part of the stress–strain curve shows the final loading of a dominantly martensitic sample. It was observed that the elastic coefficients of martensite depend on stress in a fully reversible manner. After unloading, the oriented martensite retains its anisotropic elasticity, which is entirely in compliance with the results found by *ex situ* measurement presented by Thomasová et al. [9].

5. Conclusions

The contribution presented illustrates the evolution of elastic properties of polycrystalline NiTi undergoing a compressional loading, observed *in situ* by the laser-based ultrasound method focused on surface acoustic waves. It is shown that the *in situ* measurement has great potential to increase the understanding of the processes in the material in such a case.

The measurement of SAW velocities and their spatial distribution can be realized during the loading. Velocities obtained are then used to determine the development of elasticity coefficients by the inverse procedure based on the Ritz–Rayleigh approach. Since SAWs carry mostly information about the shear behavior, only the shear constants c_{44} and c_{66} can be determined with sufficient accuracy.

Based on the development of the identified elastic constants, several remarks on the stress-dependent behavior of the material can be made. Firstly, the reorientation of R-phase introduces a surprisingly large anisotropy to the sample. The character of the anisotropy remains similar even after the full martensitic phase-transformation. However, the development of the constants is uneven, suggesting a heterogeneous character of transition between the R-phase and martensite. Unfortunately, the presented measurement does not offer sufficient data to completely reveal this character and supplementary experimental data are necessary. One of the possibilities is to combine the SAW with a pulse-echo measurement during the loading.

Acknowledgments

This work has been supported by OP RDE, MEYS, under the project ESS — SCANDINAVIA — CZ — PROJECT CZ.02.1.01/0.0/0.0/16_013/0001794, and the CSF project of the Research Center AdMAT (14-36566G).

References

[1] T.M. Brill, S. Mittelbach, W. Assmus, M. Mullner, B. Luthi, *J. Phys. Condens. Matter* **3**, 9621 (1991).

[2] P. Sedlák, H. Seiner, M. Landa, V. Novák, P. Šittner, L. Manosa, *Acta Mater.* **53**, 3643 (2005).

[3] A. González-Comas, L. Manosa, A. Planes, F.C. Lovey, J.L. Pelegrina, C. Guénin, *Phys. Rev. B* **56**, 5200 (1997).

[4] H. Seiner, P. Stoklasová, P. Sedlák, M. Ševčík, M. Janovská, M. Landa, T. Fukuda, T. Yamaguchi, T. Kakeshita, *Acta Mater.* **105**, 182 (2016).

[5] A. Planes, Ll. Manosa, *Solid State Phys.* **55**, 159 (2001).

[6] H. Seiner, L. Bicanová, P. Sedlák, M. Landa, L. Heller, I. Aaltio, *Mater. Sci. Eng. A* **521**, 205 (2009).

[7] P. Sedlák, H. Seiner, J. Zídek, M. Janovská, M. Landa, *Exp. Mech.* **54**, 1073 (2014).

[8] M. Landa, P. Sedlák, P. Šittner, H. Seiner, V. Novák, *Mater. Sci. Eng. A* **462**, 320 (2007).

[9] M. Thomasová, H. Seiner, P. Sedlák, M. Frost, M. Ševčík, I. Szurman, R. Kocich, J. Drahokoupil, P. Šittner, M. Landa, *Acta Mater.* **123**, 145 (2017).

[10] P. Šittner, D. Neov, P. Lukáš, D.M. Toebbens, *J. Neutron Res.* **12**, 15 (2004).

[11] H.-R. Wenk, I. Lonardelli, D. Williams, *Acta Mater.* **52**, 1899 (2004).

[12] P. Šittner, P. Lukáš, V. Novák, M.R. Daymond, G.M. Swallowe, *Mater. Sci. Eng. A* **378**, 97 (2004).

[13] P. Šittner, M. Landa, P. Lukáš, V. Novák, *Mech. Mater.* **38**, 475 (2006).

[14] M. Ševčík, T. Grabec, P. Stoklasová, M. Janovská, K. Zoubková, P. Sedlák, H. Seiner, M. Landa, *Acta Phys. Pol. A* **134**, 807 (2018).

[15] P. Stoklasová, P. Sedlák, H. Seiner, M. Landa, *Ultrasonics* **56**, 381 (2015).

[16] T. Grabec, P. Sedlák, P. Stoklasová, M. Thomasová, D. Shilo, M. Kabla, H. Seiner, M. Landa, *Smart. Mater. Struct.* **25**, 127002 (2016).

[17] P. Šittner, L. Heller, J. Pilch, C. Curfs, T. Alonso, D. Favier, *J. Mater. Eng. Perform.* **23**, 2303 (2014).

Proceedings of the International Symposium on Physics of Materials (ISPMA), September 10–15, 2017, Prague

Non-Contact Characterization of Acoustoelastic Parameters of Advanced Materials by Laser-Ultrasound

M. Ševčík[a,*], T. Grabec[b], P. Stoklasová[c], M. Janovská[c], K. Zoubková[c], P. Sedlák[c], H. Seiner[c] and M. Landa[c]

[a]Faculty of Electrical Engineering, Czech Technical University in Prague, Technická 2, Praha 6, 16627, Czech Republic

[b]Nuclear Physics Institute of The Czech Academy of Science, Řež, 25068, Czech Republic

[c]Institute of Thermomechanics of The Czech Academy of Science, Dolejškova 1405/5, Praha 9, 18200, Czech Republic

In advanced functional materials, where the prestress can initialize phase transitions or other structural changes, the effect of the increasing load on an acoustic wave velocity is substantial and can provide important information on the undergoing physical phenomena. In this paper, a novel method for contactless measurements of acousto-elastic parameters is presented. The contactless arrangement, based on the concept of laser-ultrasound, enables an accurate detection of small changes of the velocities of surface acoustic waves in various directions. Because of this contactless arrangement, the changes of the sample shape during the loading do not affect the results, which can be assumed as the main source of inaccuracy for classical contact methods. The experimental device and its control system is described in detail, and its application possibilities and limits are shown on examples of shape memory alloys.

DOI: 10.12693/APhysPolA.134.805

PACS/topics: 81.40.Jj, 81.70.Cv, 43.35.Yb

1. Introduction

Acoustoelastic effect refers to the dependence of the acoustic wave velocity on stress or strain. The interest in acoustoelasticity has been stimulated by measurements of residual stresses in polycrystalline materials [1] and the study of anharmonic behaviour of long-wavelength acoustic modes in single crystals [2].

Since the acoustoelastic coupling (stress-induced anisotropy) is very weak in structural polycrystalline materials, other factors such as temperature, microinhomogeneity, texture, which are usually neglected in engineering applications of the theory of elasticity, cannot be neglected in the study of acoustoelasticity. For this reason, the ultrasonic methods for measuring residual stresses have not been fully developed yet [3].

However, in advanced functional materials, where the prestress can initialize phase transitions or other structural changes, the evolution of acoustic wave velocity with increase of load can be substantial and can provide an important information on the undergoing physical phenomena.

The semi-linearized theory, first published by Thurston and Brugger in [4], enables to develop methods for determination of third-order elastic constants from the change of wave velocities in crystals under the influence of initial stresses. This approach was used for study of lattice stability and martensitic transformation in Cu-based shape memory alloys by Gonzalez-Comas and Manosa in [5], where complete set of third-order elastic constants of the SMAs single crystals are a function of temperature. This method for the characterization of stress-induced phase transition brings two difficulties [6]. Firstly, theory of Thurston and Brugger supposed a small difference between instantaneous and stress-free acoustic wave propagation velocities. This condition cannot be fulfilled in the case of stress-induced transformations [7]. This problem can be solved by evaluation of second-order elastic constants as a function of the applied stress. It means that in each loading step, the inverse procedure for determination of complete elastic tensor [8] will be applied, and hence softening phonon modes can be identified. Secondly, the time of flight measurement of wave velocity by the contact approach is influenced by the change of sample size and shape due to applied strain.

In this paper, both optical part and the control system of the experimental arrangement is presented. The suggested method is based on measurements of velocities of surface acoustic wave propagation along the specimen surface in various directions with respect to the loading direction. Due to the fully contactless approach, the geometrical changes of the sample do not affect the velocity measurement.

2. Experiment

The propagation of the planar surface acoustic waves (SAW) along the flat surface of isotropic homogeneous material exhibit minimal dispersion effect and the SAW

*corresponding author; e-mail: sevcik@it.cas.cz

velocity gives information on mechanical properties in the propagation direction. The penetration depth of the SAW corresponds to the acoustic wavelength that is large enough for the inspection of the bulk properties. Although the SAW propagation on anisotropic solids is more complex [9], the detection of the SAW propagation in various direction on the specimen surface allows to map the instantaneous anisotropic properties of tested material. The SAW propagation is constrained only on one side of the specimen and rest of the sample surface can be exposed to the external loading.

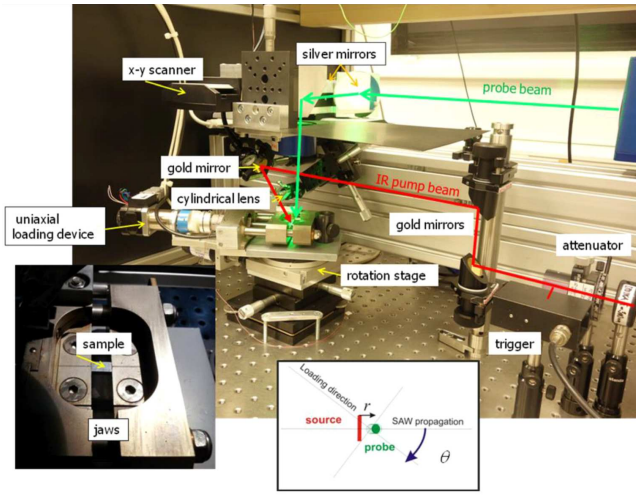

Fig. 1. The experimental setup of laser-based ultrasonic SAW method for *in situ* material characterization under uniaxial mechanical loading.

The applied laser technique is similar to the system described in [10]. In the presented experimental setup (Fig. 1), the SAW was excited thermoelastically by the impact of an infrared laser pulse. A beam of the Nd:YAG laser (1064 nm, pulse energy $>$ 100 μJ, pulse width 500 ps and 1 kHz repeating frequency) was focused via a cylindrical lens into a line-like source on the sample surface. The line source provides the generation of planar SAWs. The surface vibration was detected at variable pump–probe distances by a homodyne laser interferometer (532 nm) with an adaptive beam combiner, using two-wave mixing in a photorefractive crystal. The signal which is proportional to the instantaneous out-of-plane displacement of the surface was recorded. The frequency bandwidth of the interferometer output was restricted to 100 MHz. The spot size of the probe laser beam was less than 10 μm. The pump-line-source spot is fixed and the point-probe spot is translated along the sample surface. This arrangement protects the sample surface from the potential damage caused by an infrared laser source. The higher level of energy density of the pump laser can cause a localized melting of the exposed surface. This effect is dependent on the properties of a tested material. The energy level is usually decreased below the melting limit and the signal-to-noise ratio of the recorded signal is attained by averaging of repeated shots in an acquisition scope card. Since the higher averaging number increases measuring time, the adjustment of the laser power and averaging number must be balanced. The averaging over 1000 shots for high speed scope card NI – PXIe 5162 10bits/5GS/s was found optimal. The optical large aperture beam (50 mm in diameter), outgoing from the interferometric system, is nearly collimated. Motorized translators with a pair of large silver mirrors (3 inch in diameter) and the objective lens with focus length 100 mm were used for precise positioning and focusing of the probe beam on the sample surface. The repeatable precision of the probe beam position is better than 0.1 μm. Typical translation step in the scan of pump-probe distance was 30 μm in the range 200–900 μm. The minimal value (200 μm) of the pump-probe distance was found ideal for the elimination of the near-field effects of the acoustic source.

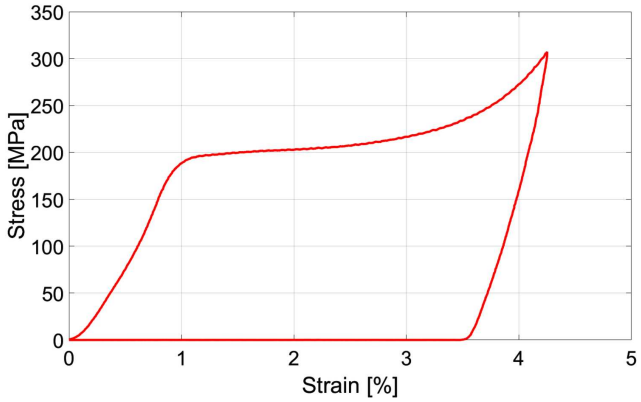

Fig. 2. Typical stress–strain dependence of stress-induced martensitic transformation in Ni–Ti.

The prismatic specimens of advanced functional materials were placed in the laboratory-made uniaxial loading two-guide-rod micro machine working in compression mode. The force was measured from strain measurement on both guide rods by the calibrated full bridge of semiconductive strain gauges with temperature compensation with precision 0.5 N in the range up to 6 kN. Typical stress–strain dependence of stress-induced martensitic transformation in Ni–Ti sample can be seen in Fig. 2. The displacement was measured by inductive transducer (LVDT) with free movable plunger (linearity better than ± 3 μm in the range of 10 mm). The stress–strain control of loading is available. The temperature was monitored by the miniature thermocouple (0.3 mm in diameter) placed near to the specimen. The testing micromachine was rotated by the motorized rotation stage with high precision (0.3 degree).

The measuring process starts with the setting of the stress loading and then the SAW signals are recorded for each defined pump-probe distance in all given angular positions of the sample.

3. Results and discussion

Typical signal data set for given loading levels and for the SAW propagation in a loading direction (theta = 0) is shown in Fig. 3. Owing to the imperfect stabilization of the interferometric setup the signal phase was changing and thus poor results were obtained after averaging. For better results, the absolute values of signals were averaged. Despite the fact that the signals in Fig. 3 are in their absolute values the arrivals of SAW and also skimming surface longitudinal waves (SSLW) are observable. A SSLW is a surface longitudinal wave that exhibits strong dispersion (with comparison to the SAW) because SSLW generates a transverse wave (TW) propagating from the surface into a bulk of the sample. Since SSLW acts as a supersonic movable source of a TW, the determination of a SSLW arrival is influenced by velocity of a transversal wave and strongly depends on spatial distribution of the finite acoustic source. Precise analysis of the SSLW waveform and evaluation of its velocity needs a more realistic model of the acoustic source and a wave propagation model. At the present time, the determined SSLW velocity can be used for the rough estimation of velocity of a longitudinal wave (LW) propagating in the bulk. By contrast to the evaluation of SSLW, the SAW velocity can be evaluated more precisely because of the perfect detectability of a wave arrival and neglectable dispersion. The presented specimen was cut from the rod of fine-grained material of Ni–49.5Ti (50.5 at.%Ni–49.5 at.%Ti), for details see [11].

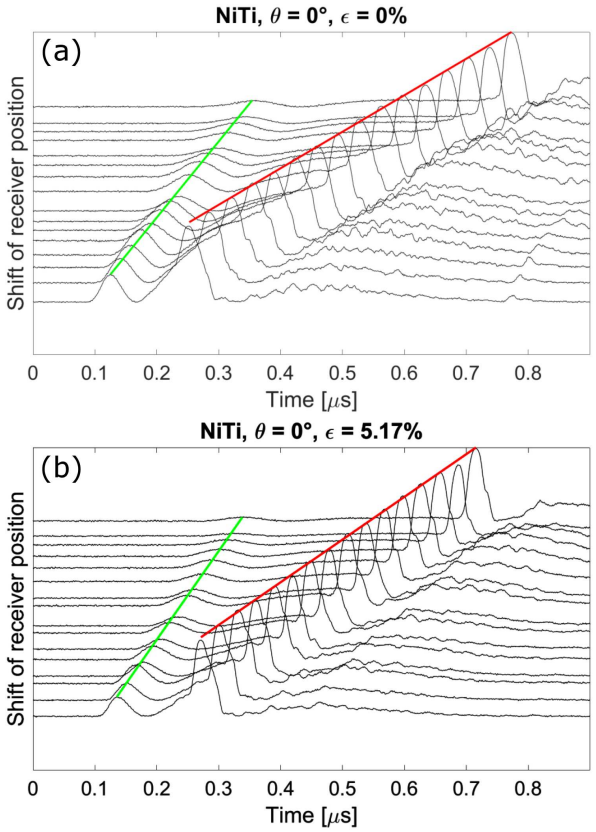

Fig. 3. Ultrasonic signal set for stress free (a) and max loaded (b) state of the Ni–49.5Ti sample, red = SAW, green = SSLW.

Evolution of SAW velocities at various directions of propagation starts from common origin at stress-free state (Fig. 4). The SAW at the compression direction rapidly increases its velocity from 0.5% of strain whereas SAW velocities decrease with increase of the propagation angle. Minimal value of velocity is at perpendicular direction to the loading. This anisotropization can be explained by elasticity softening at R-phase transformation [11]. Following martensitic transformation and martensitic reorientation causes increase of the SAW velocity. During unloading of the final martensite, the SAW velocity decreases along the loading curve without hysteresis.

Detailed context with microstructural processes is possible to discuss after evaluation of elastic properties by inversion of acoustic data in [8]. In this paper, the described example illustrates potential of the laser-based ultrasonic method for *in situ* material characterization during mechanical testing.

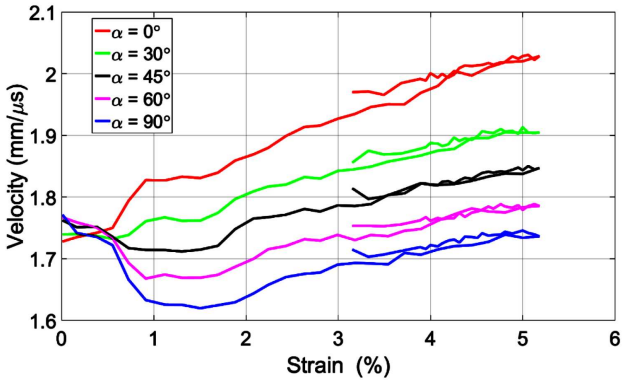

Fig. 4. SAWs velocities different directions with respect to loading.

4. Conclusion

A novel method for acoustoelastic characterization of functional materials was presented. The contactless arrangement, based on the concept of laser-ultrasound, enables accurate detection of small changes of the surface velocities and estimation of bulk acoustic waves in various directions on a small sample loaded uniaxially in a testing machine. Due to this arrangement, the changes of the shape of the sample during the loading do not affect the results, which can be assumed as the main source of inaccuracy for classical contact methods. The experimental device and its control system was described in detail, and its applicability was shown on Ni–49.5Ti sample. The described experimental technique has a great potential for *in situ* non-destructive characterization of microstructural processes during material testing.

Acknowledgments

This work has been supported by the project of the Czech Science Foundation (17-04871S), and by OP RDE, MEYS, under the project ESS — SCANDINAVIA — CZ — PROJECT CZ.02.1.01/0.0/0.0/16_013/0001794.

References

[1] Y.H. Pao, W. Sachse, H. Fukuoka, in: *Physical Acoustics*, Vol. XVII, Eds. W.P. Mason, R.N. Thurston, Academic Press, London 1984, p. 62.

[2] M.A. Breazeale, J. Philip, in Ref. [1], p. 2.

[3] E. Schneider, in: *Structural and Residual Stress Analysis by Non-Destructive Methods*, Ed. V. Hauk, Elsevier Sci. B, Amsterdam 1997.

[4] R.N. Thurston, K. Brugger, *Phys. Rev.* **135**, A1604 (1964).

[5] A. Gonzales-Comas, Ll. Manosa, *Philos. Mag. A* **80**, 1681 (2009).

[6] T. Černoch, M. Landa, V. Novák, P. Sedlák, P. Šittner,*J. Alloys Comp.* **378**, 140 (2004).

[7] H. Seiner, P. Stoklasová, P. Sedlák, M. Ševčík, M. Janovská, M. Landa, T. Fukuda, T. Yamaguchi, T. Kakeshita, *Acta Mater.* **105**, 182 (2016).

[8] T. Grabec, K. Zoubková, P. Stoklasová, M. Ševčík, P. Sedlák, M. Janovská, H. Seiner, M. Landa, *Acta Phys. Pol. A* **134**, 809 (2018).

[9] D. Royer, E. Dieulesaint, *J. Acoust. Soc. Am.* **76**, 1438 (1984).

[10] P. Stoklasová, P. Sedlák, H. Seiner, M. Landa, *Ultrasonics* **56**, 381 (2015).

[11] M. Thomasová, H. Seiner, P. Sedlák, M. Frost, M. Ševčík, I. Szurman, R. Kocich, J. Drahokoupil, P. Šittner, M. Landa, *Acta Mater.* **123**, 146 (2017).

Ultrasonics 82 (2018) 91–100

Contents lists available at ScienceDirect

Ultrasonics

journal homepage: www.elsevier.com/locate/ultras

Ultrasonic bandgaps in 3D-printed periodic ceramic microlattices

Alena Kruisová [a], Martin Ševčík [a], Hanuš Seiner [a,*], Petr Sedlák [a], Benito Román-Manso [b], Pilar Miranzo [c], Manuel Belmonte [c], Michal Landa [a]

[a] Institute of Thermomechanics, Czech Academy of Sciences, Dolejškova 5, 18200 Prague, Czech Republic
[b] School of Engineering and Applied Sciences, Harvard University, 52 Oxford St, 02138 Cambridge, MA, USA
[c] Institute of Ceramics and Glass (ICV-CSIC), Campus de Cantoblanco, Kelsen 5, 28049 Madrid, Spain

ARTICLE INFO

Article history:
Received 13 March 2017
Received in revised form 21 July 2017
Accepted 27 July 2017
Available online 29 July 2017

Keywords:
Phononic crystals
Ceramics
Additive manufacturing
Bandgaps
Wave propagation
Finite elements method

ABSTRACT

The transmission of longitudinal ultrasonic waves through periodic ceramic microlattices fabricated by Robocasting was measured in the 2–12 MHz frequency range. It was observed that these structures (scaffolds of tetragonal and hexagonal spatial arrangements with periodicity at length-scales of ~100 μm) exhibit well-detectable acoustic band structures with bandgaps. The locations of these gaps at relatively high frequencies were shown to be in close agreement with the predictions of numerical models, especially for tetragonal scaffolds. For hexagonal scaffolds, a mixing between longitudinal and shear polarizations of the propagation modes was observed in the model, which blurred the matching of the calculated band structures with the experimentally measured bandgaps.

1. Introduction

Robocasting [1–3] is an additive manufacturing technique that enables fabrication of micro-architectured three-dimensional (3D) scaffolds consisting of ceramic micro-rods in periodic spatial arrangements. These scaffolds are typically developed for particular applications such as bone tissue engineering [4,5] or advanced liquid filtering [6]; however, the high acoustic performance of dense ceramic materials in combination with the periodicity of the micro-architecture of the scaffold predetermine the robocast structures also for applications in acoustics.

As previously shown by the current authors [7], tetragonal robocast scaffolds exhibit extremely strong elastic anisotropy, accompanied by equivalently anisotropic effects in the acoustic wave propagation. In addition, due to the periodicity, a pronounced frequency-dependence of the acoustic wave propagation can be expected, arising from a combination of internal resonances of the unit cells of the structure and Bragg scattering effects resulting from the periodic arrangement of these cells. In particular, the existence of the so-called frequency bandgaps (BGs) typical for acoustic meta-materials [8–10] or phononic crystals [11–15] can be theoretically expected for the scaffolds. Indeed, the appearance of these gaps in tetragonal robocast structures was recently predicted by finite elements calculations [7,16].

In this paper, we give experimental evidence of the existence of acoustic BGs for silicon carbide (SiC) scaffolds of various micro-architectures and symmetry classes. We show that the BG structure can be reliably predicted by finite elements calculations, especially for scaffolds with highly symmetric (tetragonal) spatial arrangements. The main aim of this paper is, however, to show experimentally that the acoustic energy transmission through a robocast scaffold is strongly dependent on the micro-architecture, which opens the possibility of tuning this architecture in order to achieve the desired acoustic filtering properties. As known from theoretical models [17–22], the structure and width of acoustic BGs of a porous material with geometrically ordered pores are strongly dependent on the shape of the pores and their volume fraction, which opens space for topological optimization. The additive manufacturing methods are, in general, understood as particularly suitable tools for fabrication of phononic crystals [23–26], as they enable fine tailoring of both the porosity and the geometry of pores. The Robocasting method enables this approach to be utilized for ceramic materials.

There have been several experimental demonstrations of phononic crystals reported in the literature so far, typically exhibiting bandgaps either in a 100 Hz–100 kHz frequency range [27–30], in the case when the spatial periodicity in these structures appeared at the millimeter (or even longer) length-scales, or in a

* Corresponding author.
E-mail address: hseiner@it.cas.cz (H. Seiner).

http://dx.doi.org/10.1016/j.ultras.2017.07.017
0041-624X/

200 MHz–10 GHz range for structures with ~1–10 μm spatial periodicity (e.g. [31–34]). In contrast, the robocast scaffolds reported in this paper have the characteristic length-scales of 200–700 μm; this, together with the high acoustic impedance of fully dense ceramics, enables the robocast materials to exhibit BGs and other metamaterial-like features at ultrasonic frequencies ~5–10 MHz, which has rarely been reported in the literature yet [35].

2. Experiment

2.1. Materials

The examined SiC micro-scaffolds were fabricated by Robocasting using a similar additive manufacturing process as described in [3,36]. In brief, an aqueous colloidal paste (containing attrition milled SiC powders with 7 wt.% Al_2O_3 and Y_2O_3 sintering additives plus organic additives) was printed through a robotically controlled nozzle into an oil bath, so that a regular architecture was obtained layer-by-layer, consisting of a linear array of parallel filaments in each layer. By different mutual rotations between these layers and different spacings between the rods, four different micro-architectures were obtained, according to CAD computer designs shown in Fig. 1(a). Two samples were of tetragonal symmetry (LS and SS), differing only in the in-plane spacings between the rods; similarly, two samples were of hexagonal arrangements (LH and SH). Hereafter, we will use the acronyms (LS, SS, LH, and SH) to denote the samples; the acronyms were chosen according to the in plane shape of the unit cell for each material, i.e. small square, large square, small hexagon, large hexagon.

Each structure was then slowly dried at room temperature and subsequently heat treated at 600 °C to burn out the organic additives. As a final step, the 3D structures were densified by pressureless Spark Plasma Sintering (SPS) at 1700 °C in Ar. As shown in [36], these sintering conditions led to full densification of the ceramic materials. Scanning Electron Microscopy (SEM) images and optical micrographs of the final sintered micro-lattices are shown in Fig. 1 (b) and (c), respectively. From the four prepared micro-architectures, samples for ultrasonic measurement were prepared by cutting out the non-periodic parts (the frames) of the scaffolds (Fig. 1(d)). Prior to the sintering, the dimensions of all samples were approximately $10 \times 10 \times 3$ mm^3. After sintering and after cutting out the non-periodic parts, the resulting samples were all approximately $8.5 \times 8.5 \times 2.8$ mm^3.

2.2. Experimental methodology

The acoustic properties of the samples were studied using a through-transmission method (see Fig. 2 for an outline). Each sample was contacted by a CrystalBond wax onto two 0.5 mm thin glass plates to ensure flat co-planar faces for an adequate contacting of ultrasonic probes.

Then, narrow-band longitudinal ultrasonic pulses were sent through the sample, each consisting of ten harmonic periods at given frequency inside of an amplitude-envelope ('input signal' curve shown in Fig. 2). The narrow band excitation allowed satisfactory signal-to-noise ratio, enabled time-resolved analysis of the output signals, and, at the same time, would reveal possible nonlinearities in the measurement system (which were not observed). The glass plates were always glued onto two lateral faces of the sample and oriented such that they enabled measurements of waves propagating along one of the orientations of the rods. According to the coordinate system outlined in Fig. 1, the measurements were performed in the x_1 direction for all samples.

For the generation of the input signals and the acquisition of the transmitted signals, a National Instruments NI-PXI card system was used, including a functional generation card 5422 (16 bits/40 MHz) employed for burst signal generation, and an acquisition card 5122 (14 bits/100 MHz) for signal recording. The generated as well as the recorded signals were amplified by a high power ultrasonic system Ritec RAM 5000. This system was equipped by a gated amplifier (nominal frequency range 50 kHz–22 MHz, output RMS power 5 kW at 50 ohms/2.5 MHz) and a broadband receiver (frequency band 40 kHz– 80 MHz/72 dB gain).

A $LiNbO_3$ single crystal (central frequency 20 MHz) glued on a 10 mm Homosil substrate was used as an emitting transducer. A commercial delayed ultrasonic probe Panametric V206 (0.12″, 20 MHz) was employed as a receiver. Propylenglycol was used for acoustic coupling.

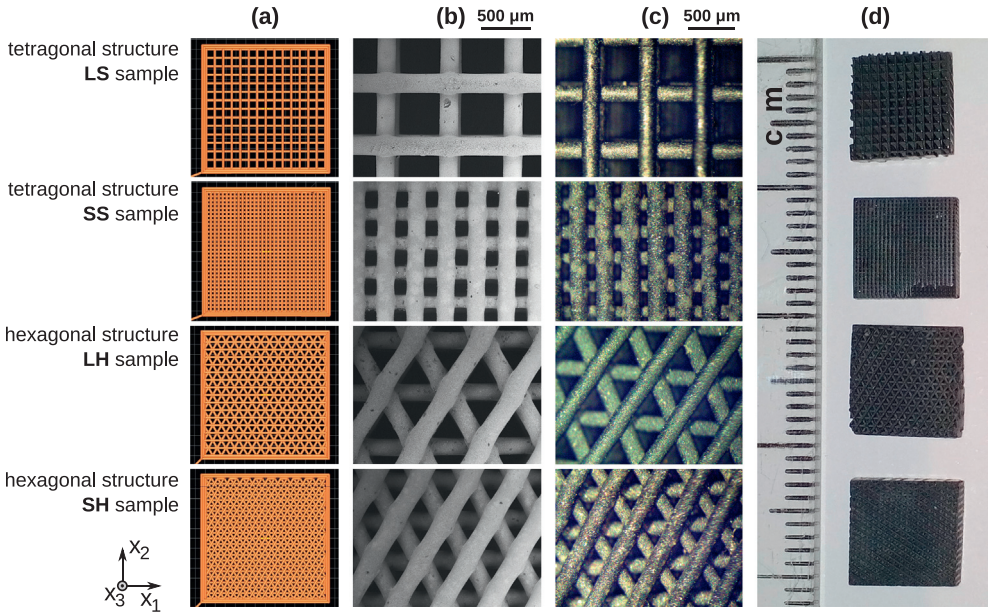

Fig. 1. The four different micro-architectures used in the experiments: (a) initial computer CAD designs; (b) SEM images of the resulting sintered architectures; (c) optical micrographs of these architectures; (d) samples for ultrasonic measurements cut from the central parts of the robocast structures.

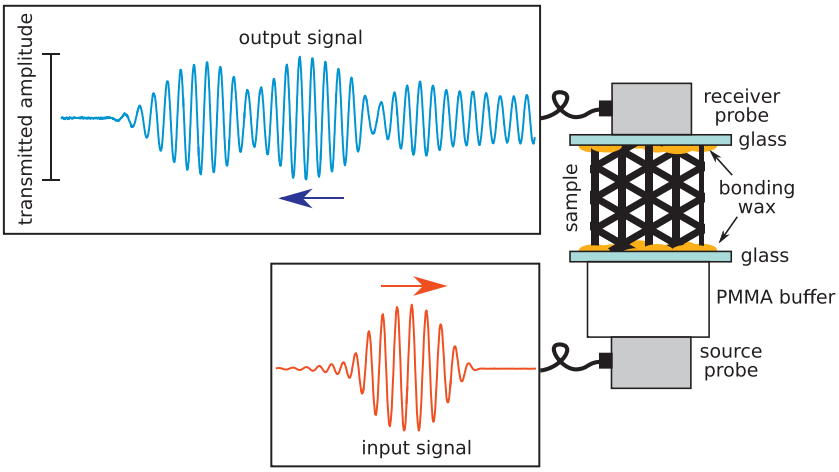

Fig. 2. Outline of the experimental set-up of the through-transmission acoustic tests.

Input burst pulses with nominal frequencies (f_{in}) between 2 MHz and 12 MHz were used; this frequency range was scanned with a 0.1 MHz step.

While the input signal was a compact burst wave-packet, the transmitted signal was much more general (as, for example, the 'output signal' curve in Fig. 2). For each nominal frequency of the input signal, two basic parameters of the output signal were determined: (1) the maximal transmitted amplitude, and (2) the dominant frequency (f_{out}) determined by Fast Fourier Transform (FFT) of the output signal. It was checked that for a reference sample (a 10 mm thick bulk plexiglass) the transmitted amplitude was monotonously increasing with frequency for the whole used frequency range, and that

$$f_{in} = f_{out} \tag{1}$$

in the given frequency range. This result is visualized in Fig. 3 as a plot of the transmitted amplitude with respect to the input frequency f_{in} (solid line) and the output frequency f_{out} (vertical bars). The amplitude is normalized with respect to its maximum value (reached at 12 MHz). It is seen that the amplitude decreased below 3 MHz due to low sensitivity of the detection probe to such low frequencies; in the rest of the used frequency range, the amplitude was increasing due to approaching the vicinity of the resonant frequencies of both emitting and receiving probes. This reference measurement confirmed that any localized sharp decreases in the transmitted amplitude obtained for the robocast samples must follow from the interactions of the propagating waves with the microarchitecture.

In the rest of the paper, we will use the same representation of the acoustic energy transmission through the robocast samples as the one used in Fig. 3 for the bulk plexiglass sample, i.e. two plots of the transmitted amplitude, the first one with respect to the input frequency (f_{in}) and the second one with respect to the dominant frequency of the output signal (f_{out}). The lowest amplitude transmitted through the bulk plexiglass sample was obtained at 2 MHz, where the output signal was by two orders of magnitude (i.e. −40 dB) lower than that at 12 MHz. For the robocast samples, we decided to consider the frequency intervals in which the attenuation becomes even by one order of magnitude stronger (i.e. −60 dB) as regions of possible BGs; the −60 dB cut-off frequencies will be indicated in all experimental results in the rest of the paper. With the used averaging (100×) and the nominal signal-to-noise ratio of the acquisition system, the resulting signal-to-noise ratio of the recorded signal was higher than 80 dB.

3. FEM calculations

In addition to the experiment, the wave propagation in the examined scaffolds was studied by numerical modelling, in particular by the finite elements method (FEM). The calculations were

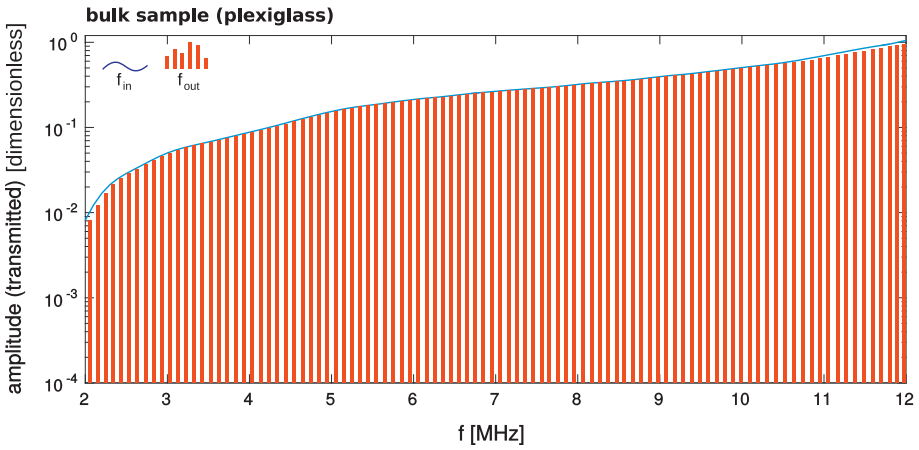

Fig. 3. Results of a preliminary reference measurement for a bulk plexiglass sample. The solid (blue) line is a plot the transmitted amplitude with respect to the set input frequency f_{in} of the transmitter probe, the vertical (red) bars represent the plot of the same amplitude with respect to the dominant frequency of the output signal f_{out}. The amplitude is normalized with respect to its maximum value. (For interpretation of the references to colour in this figure legend, the reader is referred to the web version of this article.)

performed on representative unit cells of the scaffolds shown in Fig. 4. For both tetragonal and hexagonal scaffolds these unit cells are representative building blocks that repeat periodically along the three spatial directions (x_1, x_2 and x_3). However, while for the tetragonal structures this building block is directly equivalent to the smallest (irreducible) unit cell of the scaffold, for the hexagonal structures the cell used for the calculation is composed of two mirror-reflected irreducible unit cells, each of them periodically repeating in the structure along the directions $x_2 = \pm\sqrt{3}x_1$.

The unit cells were meshed by tetrahedral Lagrangian elements, and the corresponding wave-propagation problem was solved using COMSOL Multiphysics computational environment [37]. The dimensions of the unit cells, i.e. the out-of-plane spacing of the rods h, the in-plane spacing of the rods l, and the rod diameter d, were obtained from optical micrographs of the scaffolds (both axial views and cross-sectional cuts); the results are listed in Table 1. A relatively large scatter (up to ±20 μm) was observed in the micrographs for all parameters. Hence, the results of the FEM calculations must be understood just as idealized approximations of the behaviors of the real scaffolds. The material parameters of robocast SiC for the calculations were taken from [7] as follows: the density $\rho = 3.34\ \mathrm{g\,cm^{-3}}$, Young's modulus $E = 305$ GPa, and Poisson's ratio $\nu = 0.19$.

As usual for wave propagation in periodic media with spatial periodicity described by a translational vector **a** [27,38,39], the displacement field of the sought solution was assumed in form of a planar wave of frequency ω

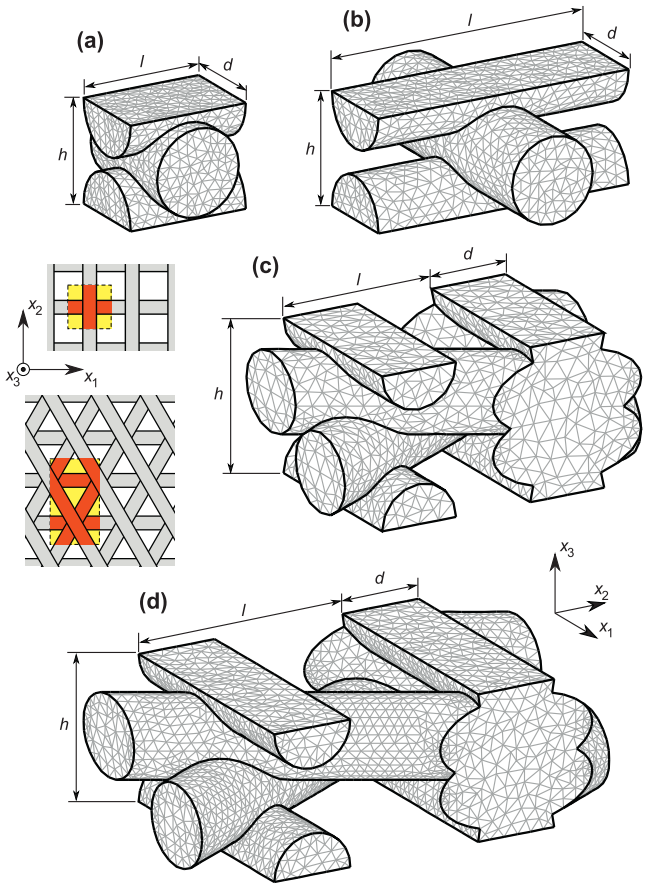

Fig. 4. Geometries and FEM meshes used for calculations of the band structure of the studied scaffolds: (a) SS structure; (b) LS structure; (c) SH structure; (d) LH structure. Schematic sketches on the left show the placements of the unit cells in tetragonal (a,b) and hexagonal (c,d) structures in the x_1-x_2 plane.

Table 1
Geometric parameters of the calculation domains for FEM calculations; see Fig. 4 for the meaning of individual parameters.

Sample	l [μm]	d [μm]	h [μm]
LS	650	210	275
SS	308	219	261
LH	576	215	385
SH	420	210	405

$$\mathbf{u}(\mathbf{x}, t) = \mathbf{U}_{\mathrm{B}}(\mathbf{x}, \mathbf{k}) \exp[i(\mathbf{k}\cdot\mathbf{x} - \omega t)], \tag{2}$$

where

$$\mathbf{U}_{\mathrm{B}}(\mathbf{x}, \mathbf{k}) = \mathbf{U}_{\mathrm{B}}(\mathbf{x} + \mathbf{a}, \mathbf{k}) \tag{3}$$

is the Bloch waveform [40,41] having the same spatial periodicity as the scaffold, and **k** is the wave vector, that can always be mapped into the first irreducible Brillouin zone. In particular, planar waves propagating along the symmetry direction x_1 were assumed in all cases; in this direction, the spatial period of the scaffolds was $a = l$ for the tetragonal structures and $a = 2l/\sqrt{3}$ for the hexagonal structures. The calculations were done for sets of wave numbers $k = |\mathbf{k}| \in [0, \pi/a]$ for the tetragonal structures, and $k = |\mathbf{k}| \in [0, 2\pi/a]$ for the hexagonal ones.

The Bloch wave solution was determined by calculating eigenfrequencies and eigenmodes of elastic vibrations of the unit cell with the complex phase-shift boundary condition

$$\mathbf{u}(x_1 = 0, x_2, x_3, t) = \mathbf{u}(x_1 = a, x_2, x_3, t) \exp(ika) \tag{4}$$

in the direction x_1 and periodic boundary conditions in the x_2 and x_3 directions. For the tetragonal scaffolds, this calculation gave directly the full band structure for the wave propagation in direction x_1. For the hexagonal scaffolds, the solutions were duplicate due to the fact that the used computational unit cell consisted of two irreducible unit cells of the structure; i.e. for each $k \in [0, 2\pi/a]$, also solutions for $\tilde{k} = (2\pi/a) - k$ were obtained. The separation of these two sets was done by checking the phase shifts between corresponding points at planes $x_1 = 0$ and $x_1 = a/2$.

For each solution, the displacement amplitudes u_1 (i.e. along the propagation direction), u_2 and u_3 at the faces perpendicular to x_1 were compared, which enabled identification of waves with dominantly longitudinal polarizations. For a more detailed analysis of the individual modal shapes, visualizations of the corresponding solutions on supercells consisting of four unit cells repeating along the propagation direction were constructed from the solutions on single cells.

4. Results

4.1. Tetragonal structures

The plots of the transmitted amplitudes with respect to input and output frequencies for the LS and SS samples are shown in Fig. 5, being significantly different from what was observed for the reference bulk sample (Fig. 3). Some energy is transmitted through the LS and SS structures for all input frequencies, however, it is clearly seen that in some frequency ranges this transmission is only due to the finite spectral width of the input signals. In the spectrum of the output signals (f_{out}, vertical bars), broad BGs are clearly observed; the locations of these gaps are summarized in the first two columns of Table 2.

For the LS sample, the transmitted amplitude starts rapidly decreasing above 3 MHz, reaching a −60 dB attenuation at approximately 3.3 MHz. Then, in the 3.5–4.9 MHz interval a BG is observed, and above it the transmitted amplitude increases again. Similarly, the second −60 dB cut-off frequency emerges at

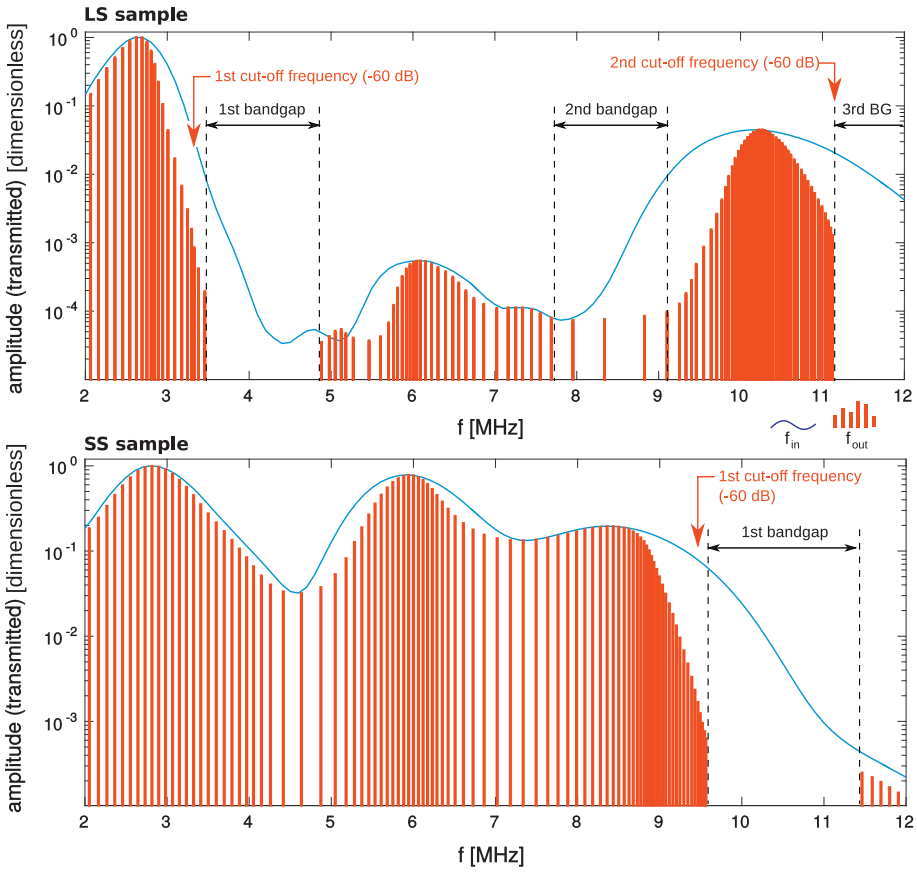

Fig. 5. Experimental results for the tetragonal scaffolds LS (upper plot) and SS (lower plot). The solid line is the plot of the transmitted amplitude with respect to the input frequency; the vertical bars are the plot with respect to the dominant frequency of the output signal. For each sample, the amplitude is normalized with respect to its maximum output value. For the f_{out} plot, approximate locations of the BGs are outlined by the dashed lines; broken arrows denote the locations of the drops of the normalized amplitude beyond 10^{-3} (i.e. −60 dB).

Table 2
Cut-off (−60 dB) frequencies and BGs of the examined samples. All values are in MHz (experimental data with accuracy ±0.1 MHz).

Sample	LS	SS	LH	SH
1st cut-off freq. [MHz]	3.3	9.5	3.8	6.1
2nd cut-off freq. [MHz]	11.1		6.1	
1st BG location [MHz]				
Experimental	3.5–4.9	9.6–11.5	4.3–5.4	6.1–7.8
Calculated	3.2–4.5	From 10.1	3.8–5.4	5.7–7.9
2nd BG location [MHz]				
Experimental	7.7–9.1		6.3–8.5	From 11.0
Calculated	6.9–7.8		6.2–7.9	9.8–10.6
3rd BG location [MHz]				
Experimental	From 11.1		9.6–11.5	
Calculated	From 11.6		9.7–9.8	

11.1 MHz, which is followed again by a sharp BG. Between these two sharp BGs, an additional minimum of the transmitted amplitude appears, corresponding to the output frequency range denoted as '2nd bandgap' in Fig. 5.

For the SS sample, a shallow local minimum is observed at about 4.5 MHz, but there is no real gap in the transmitted frequencies related to this minimum. A strong decrease in the transmitted amplitude is then seen at above 9 MHz, reaching a −60 dB cut-off frequency at 9.5 MHz. A sharp BG for the SS structure is localized between 9.8 and 10.6 MHz. The decreases of the amplitudes around the BGs are gradual rather than abrupt for both samples, which is probably due to the irregularities of the real structure mentioned in Section 3, that leads to some blurring of the BG edges.

The observed band structure for the LS and SS samples can easily be interpreted based on the results of the FEM modeling shown in Fig. 6. For the LS sample, the FEM model predicts that there are three longitudinal modes appearing in the studied frequency range. Two of them with positive group velocity ($\partial\omega/\partial k > 0$, modes denoted by capital letters C–C′ and D–D′ in Fig. 6) and one with negative group velocity ($\partial\omega/\partial k < 0$, mode G–G′). Fig. 7 shows the modal shapes of the chosen modes for two different values of the k-vector: in the middle between the center and the edge of the 1st Brillouin zone ($k = a/2\pi$) and at the edge of the 1st Brillouin zone ($k = a/\pi$), where the size of the unit cell corresponds to one half of the wavelength. It is observed

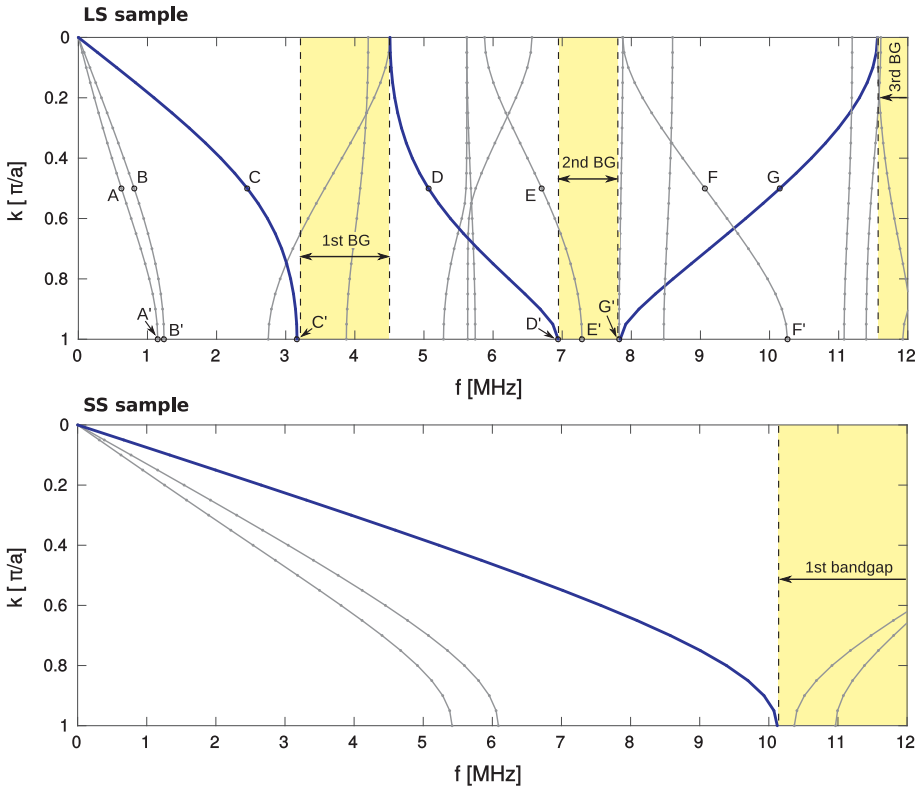

Fig. 6. Band structure of the tetragonal scaffolds LS (upper plot) and SS (lower plot) calculated by FEM. The thick (blue) lines denote the modes with dominant longitudinal component; the shaded (yellow) areas denote the gaps between these modes. In the upper plot, the capital letters A,. . .,G and A′, . . ., G′ labeling the individual modes refer to Fig. 7. (For interpretation of the references to colour in this figure legend, the reader is referred to the web version of this article.)

that the geometry of the modes for these two values of k is essentially the same, up to the change in the wavelength.

From these mode visualizations, it is clearly shown that these three modes represent purely longitudinal straining of the scaffold, while all other modes have dominantly shear polarizations related to bending of the rods oriented along the propagation direction. The high symmetry class of the scaffold enabled clear distinguishing between the shear and the longitudinal modes, according to

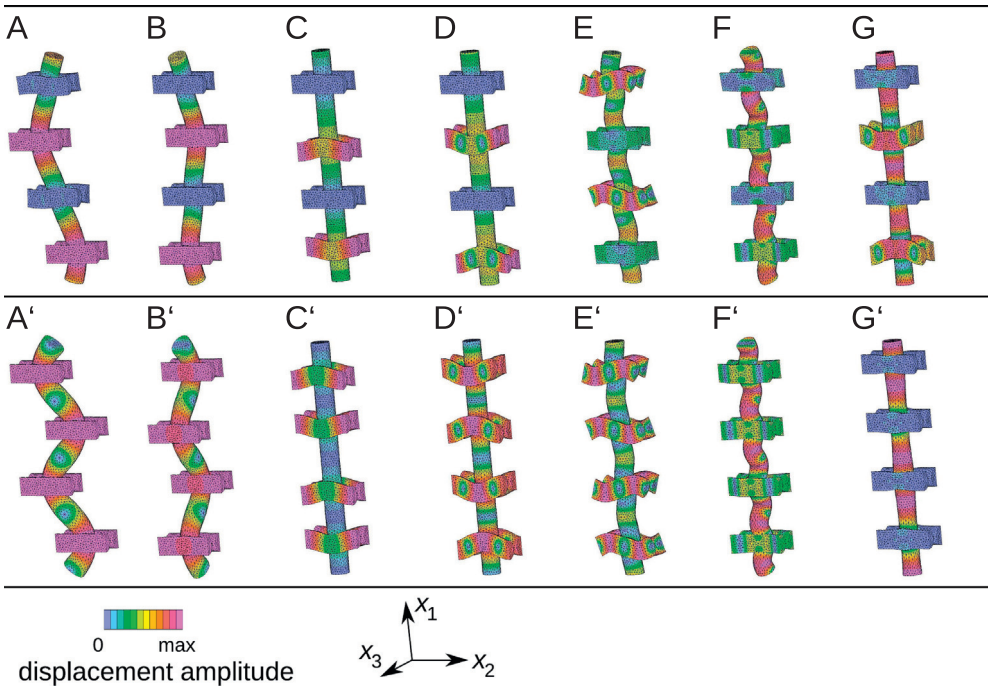

Fig. 7. Visualizations of the selected propagation modes (see the labels in Fig. 6) for the LS structure. Modal shapes A,. . .,G correspond to $k = \pi/2a$, modal shapes A′, . . ., G′ to $k = \pi/a$. The color-scale represents the instantaneous displacement amplitude (normalized into a [0;1] interval) for fixed phase angle ωt.

the symmetry components of the structure. In summary, there is a good quantitative agreement between the gaps separating the modes C–C′, D–D′ and G–G′ and the experimentally observed BGs.

For the SS sample, the FEM calculation predicts only one BG within the measured frequency range, starting above the edge of the first longitudinal mode and denoted by a thick line in the lower plot of Fig. 6. This mode is geometrically equivalent to the C–C′ mode in the LS structure. The quantitative agreement between the FEM prediction of the location of this BG and the experimental value is also satisfactory, especially when taking into account that for higher frequencies (shorter wavelengths) the local imperfections in the geometry of the structure, i.e. deviations of the real geometry of the scaffold from the idealized geometry of the FEM unit cell, may have a more pronounced effect. The FEM model also confirms that there should be no BG around 4 MHz, i.e. that the first local minimum on the amplitude curve of the SS sample is artificial. As this minimum was observed neither for any other robocast sample nor for the bulk sample, its appearance cannot be ascribed to any internal resonances of the experimental arrangement; a possible explanation is that there was a localized heterogeneity or other imperfection in the structure of this sample.

4.2. Hexagonal structures

For the hexagonal LH and SH samples, the experimental results are shown in Fig. 8, presenting localized decreases in the amplitude followed by broad BGs. The frequency ranges of these gaps are summarized in the third and the fourth columns of Table 2. For the LH sample, a sharp BG is observed between 6.3 and 8.5 MHz, while for the SH sample the BGs are detected between 6.1 and 7.8 MHz and above 11.0 MHz. For the LH sample, two less pronounced minima of the transmitted amplitude can also be seen. The first one appears above the first −60 dB cut-off frequency (3.8 MHz) and corresponds to the f_{out} frequency range denoted as '1st BG' in Fig. 8. The second minimum ('3rd BG') is very shallow, located approximately between 9.6 and 11.5 MHz. It is not clear from the experimental results whether the latter minimum can be assigned to some real BG.

The interpretation of the observed band structure for hexagonal samples by FEM calculations (Fig. 9) is much less straightforward than for the tetragonal structures. Most importantly, the propagation along the x_1 direction in the hexagonal structure does not correspond to a single direction on the 1st Brillouin zone, but to a path from the center of the zone (Γ) to its corner (point K) and then to its edge (point M, see the sketch in Fig. 9), where the notation Γ, M and K is adopted from phonon mechanics [41]. Due to this complex path, the $\omega(k)$ curves for most of the propagation modes are non-monotonous, exhibiting local stationary points ($\partial\omega/\partial k = 0$) for various values of $k \leq 2\pi/a$.

The visualizations of the selected propagation modes (see the labels in Fig. 9) for the LH structure are depicted in Fig. 10 for $k = \pi/2a$, $k = \pi/a$ and $k = 2\pi/a$. Among the three lowest (acoustic) modes, two shear modes (A–A′–A″, B–B′–B″) and one longitudinal mode (C–C′–C″) can be distinguished based on the modal shapes, although the latter intersects with a higher-order shear mode D–D′–D″. The longitudinal mode has a stationary point at approximately $k = 0.6(2\pi/a)$, i.e. neither in the corner of the zone (but close to it), nor at its edge. Simultaneously, the longitudinal mode C–C′–C″ intersects in the K-point with the dominantly shear mode D–D′–D″, neither of them having zero group velocity $\partial f/\partial k$ at

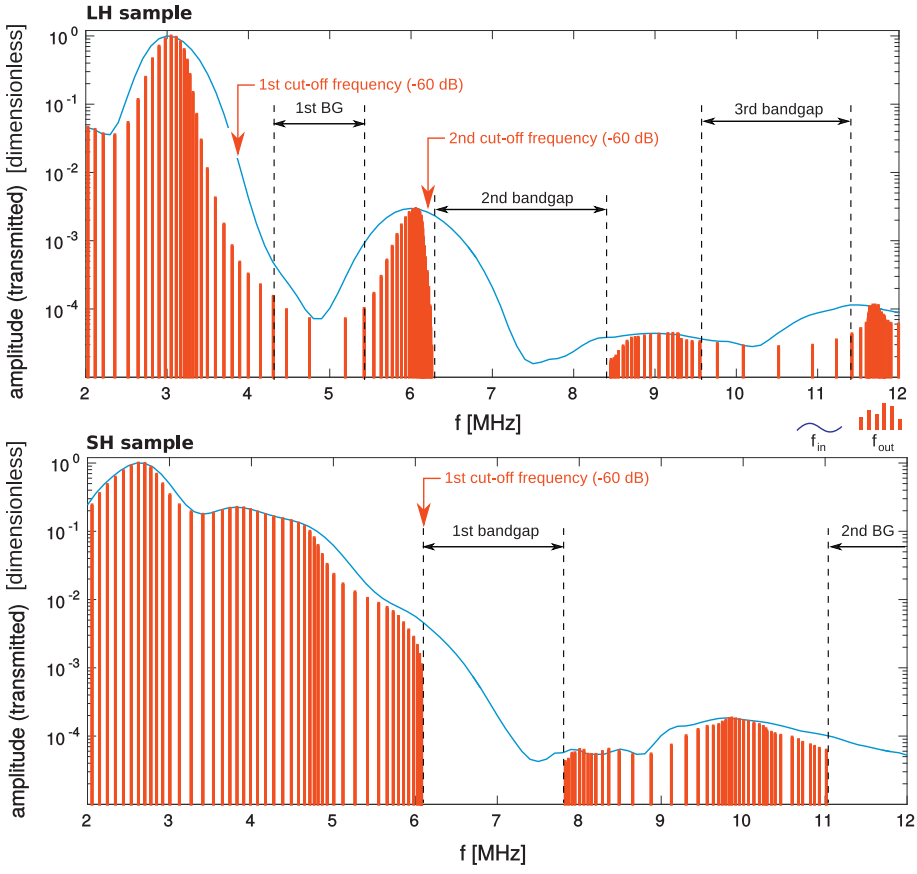

Fig. 8. Experimental results for the hexagonal scaffolds LH (upper plot) and SH (lower plot), showing the dependences of the transmitted signal amplitude on the input frequency (f_{in}) and on the dominant frequency of the output signal (f_{out}); see Fig. 5 for a detailed legend. For each sample, the amplitude is normalized with respect to its maximum output value.

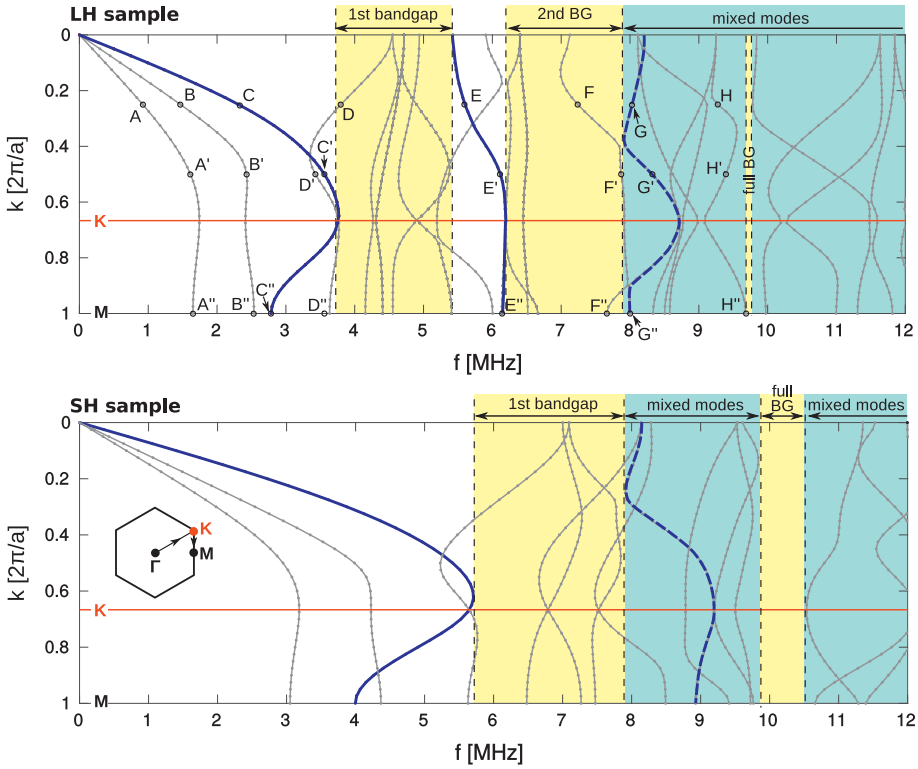

Fig. 9. Band structure of the hexagonal scaffolds LH (upper plot) and SH (lower plot) calculated by FEM. The thick (blue) lines denote the modes with dominant longitudinal component, the thick dashed lines denote modes with mixed polarizations but having a dominant longitudinal component in some segments. The shaded region labeled as 'Mixed modes' covers the modes among which a distinguishing between dominantly longitudinal a dominantly shear ones is impossible. In the upper plot, the capital letters A,. . .,H″ refer to Fig. 10; within the lower plot area, the first Brillouin zone of the hexagonal environment is sketched, with marked points Γ (center), K and M. (For interpretation of the references to colour in this figure legend, the reader is referred to the web version of this article.)

this point (this situation is more clearly seen for the corresponding modes for the SH sample). This indicates degeneracy of these two modes and their mutual conversion by Bragg scattering.

The stationary point of the C–C′–C″ mode, nevertheless, corresponds well to the experimentally observed first cut-off frequency and the start of the first BG. The polarizations of the modes appearing above this point are dominantly shear, except of the mode E–E′–E″, which is a propagating longitudinal mode between points Γ and K, but turns into a non-propagating mode ($\partial\omega/\partial k = 0$) between K and M. The upper edge frequency of this mode corresponds well to the start of the second experimentally observed BG in the LH structure. At higher frequencies, nevertheless, any clear distinguishing between longitudinal and shear modes becomes impossible. Unlike tetragonal scaffolds, hexagonal scaffolds do not impose any particular symmetry to the modal shapes except the mirror symmetry about the $x_3 = 0$ plane; hence, the mixing of in-plane shears and longitudinal strains is not anyhow constrained. The mode F–F′–F″ is dominantly shear for $k \sim 0.4(2\pi/a)$ while the mode G–G′–G″ is dominantly longitudinal in this region (see visualizations F and G). However, when the curves for these two modes nearly touch each other at $k \sim 0.45(2\pi/a)$, their polarizations interchange (see visualizations F′ and G′), which occurs again at $k \sim 0.9(2\pi/a)$, and so the mode F–F′–F″ is purely shear again at the edge of the Brillouin zone (visualization F″), while the mode G–G′–G″ is purely longitudinal at this point. The lowest frequency of the longitudinal polarization of these two modes corresponds well to the end of the second experimentally obtained BG, so it can be concluded that although the mode G–G′–G″ is of the above described mixed polarization, this mode enables some energy transmission through the structure.

All higher modes exhibit similar switching between longitudinal and shear polarizations, or even more complex modal shapes (such as H–H′–H″) in which the longitudinal and shear components are fully comparable. Hence, it is difficult to find the origin of the third experimental BG for the LH structure. The calculations predict a narrow BG for both longitudinal and shear modes at 9.7–9.8 MHz, but the relation of this calculated BG and the broad observed minimum of the transmitted amplitude is questionable.

Similarly, for the SH sample, the FEM calculation enables a straightforward interpretation only for the lowest modes. The start of the first BG again corresponds to the stationary point of the longitudinal acoustic mode. The end of this BG then probably corresponds to the mode denoted by the dashed line in the lower subplot of Fig. 9. This mode is geometrically similar to the mode G–G′–G″ of the LH structure, and exhibits similar switching of polarizations. However, at higher frequencies the agreement between the model and experiment deteriorates. The FEM calculations predict a BG for both longitudinal and shear modes between 9.8 and 10.6 MHz, which cannot be seen in the experimental results. On the contrary, the experiment gives a local maximum of the transmitted amplitude in this interval. It is plausible that this theoretically predicted BG may correspond to the measured BG at above 11.0 MHz, and the discrepancy follows from the deviations of the real micro-morphology of the scaffold from the geometry of the FEM model. Similarly as for the tetragonal scaffolds, the agreement between the model and the experiment at high frequencies is worse for the denser structure. As it can be partially seen from the optical micrographs in Fig. 1, the rods in these dense structures (SS and SH) appear more wavy due to the inherent overlapping between layers, exhibiting less constant diameter over the

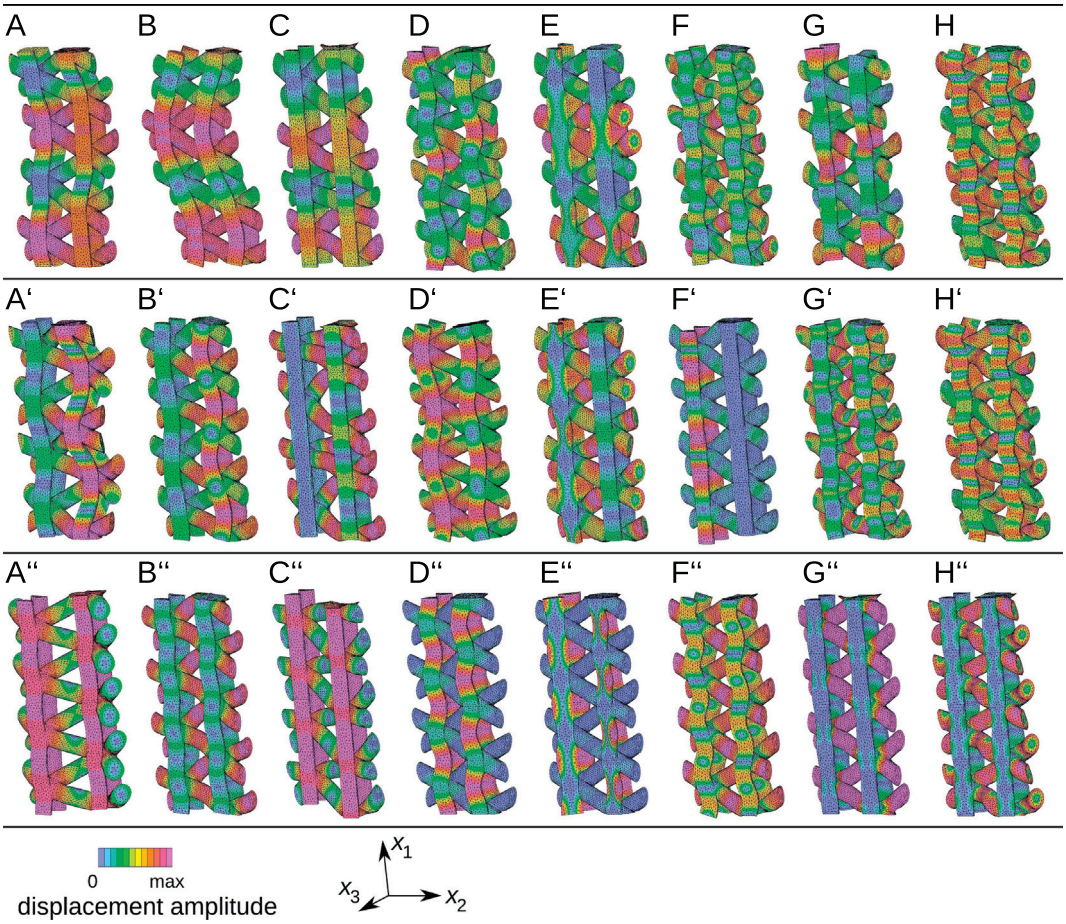

Fig. 10. Visualizations of the selected propagation modes (see the labels in Fig. 9) for the LH structure. The color-scale represents the instantaneous displacement amplitude (normalized into a [0;1] interval) for fixed phase angle ωt. (For interpretation of the references to colour in this figure legend, the reader is referred to the web version of this article.)

structure; hence, a stronger disagreement with the model could be expected.

5. Conclusions

Both experimental results and FEM calculations in the present paper confirm that ceramic microlattices fabricated by Robocasting exhibit band structures for longitudinal ultrasonic wave propagation with acoustic bandgaps. For the fine robocast scaffolds studied, the lowest BGs appear above 3 MHz. Broad BGs were observed for both tetragonal and hexagonal structures, the spectral width of these gaps being between ~1 MHz and ~2 MHz in both cases. Robocasting, as a 3D printing method, is proved to be a versatile tool for rapid prototyping of phononic crystals with a prescribed acoustic band structure and bandgaps that block acoustic energy propagation at frequency ranges of as high as 5–10 MHz.

The results presented in this paper also show the limitations for FEM modeling of the wave propagation in real robocast structures. For increasing frequencies, the geometric imperfections and/or boundary defects of the real structures may lead to significant shifts between the predicted locations of the bandgaps and the real frequency ranges in which the transmitted energy is lowered. Despite this quantitative mismatch at high frequencies, FEM calculations were shown efficient for the interpretation of the experimentally observed band structures, and enabled also a deeper insight into the acoustic wave propagation in the scaffolds, especially for the hexagonal symmetry class where mixing of shear and longitudinal polarizations appears.

Acknowledgment

This work was financially supported by the Czech Science Foundation (Grant No. 17-01618S) and MINECO (Spain)/FEDER (UE) under project MAT2015-67437-R.

References

[1] J.E. Smay, G. Gratson, R. Shepherd, J. Cesarano, J.A. Lewis, Directed colloidal assembly of 3D periodic structures, Adv. Mater. 14 (2002) 1279–1283.
[2] J.E. Smay, J.A. Lewis, Solid free-form fabrication of 3-D ceramic structures, in: N.P. Bansal, A.R. Boccaccini (Eds.), Ceramics and Composites Processing Methods, John Wiley and Sons, Hoboken, 2012, pp. 459–484.
[3] K. Cai, B. Román-Manso, J.E. Smay, J. Zhou, M.I. Osendi, M. Belmonte, P. Miranzo, Geometrically complex silicon carbide structures fabricated by robocasting, J. Am. Ceram. Soc. 95 (2012) 2660–2666.
[4] P. Miranda, E. Saiz, K. Gryn, A.P. Tomsia, Sintering and robocasting of β-tricalcium phosphate scaffolds for orthopaedic applications, Acta Biomater. 2 (2006) 457–466.
[5] D.L. Cohen, J.I. Lipton, L.J. Bonassar, H. Lipson, Additive manufacturing for in situ repair of osteochondral defects, Biofabrication 2 (2010) 035004.
[6] B. Román-Manso, S.M. Vega-Díaz, A. Morelos-Goméz, M. Terrones, P. Miranzo, M. Belmonte, Aligned carbon nanotube/silicon carbide hybrid materials with high electrical conductivity, superhydrophobicity and superoleophilicity, Carbon 80 (2014) 120–126.
[7] A. Kruisová, H. Seiner, P. Sedlák, M. Landa, B. Román-Manso, P. Miranzo, M. Belmonte, Metamaterial behavior of three-dimensional periodic architectures assembled by robocasting, Appl. Phys. Lett. 105 (2014) 211904.

[8] R.V. Craster, S. Guenneau (Eds.), Acoustic Metamaterials: Negative Refraction, Imaging, Lensing and Cloaking, Springer Series in Materials Science, vol. 166, Springer, London, 2013.
[9] S. Guenneau, A. Movchan, G. Petursson, S.A. Ramakrishna, Acoustic metamaterials for sound focusing and confinement, New J. Phys. 9 (2007) 399.
[10] J.-H. Lee, C.Y. Koh, J.P. Singer, S.-J. Jeon, M. Maldovan, O. Stein, E.L. Thomas, 25th Anniversary article: ordered polymer structures for the engineering of photons and phonons, Adv. Mater. 26 (2014) 532–569.
[11] T. Gorishnyy, M. Maldovan, C. Ullal, E.L. Thomas, Sound ideas, Phys. World 18 (2005) 24–29.
[12] S. Yang, J.H. Page, Z. Liu, M.L. Cowan, C.T. Chan, P. Sheng, Focusing of sound in a 3D phononic crystal, Phys. Rev. Lett. 93 (2004) 024301.
[13] X. Zhang, Z. Liu, Negative refraction of acoustic waves in two-dimensional phononic crystals, Appl. Phys. Lett. 85 (2004) 341–343.
[14] H. Zhao, Y. Liu, D. Yu, G. Wang, J. Wen, X. Wen, Absorptive properties of three-dimensional phononic crystal, J. Sound Vib. 303 (2007) 185–194.
[15] D. Mousanezhad, S. Babaee, R. Ghosh, E. Mahdi, K. Bertoldi, A. Vaziri, Honeycomb phononic crystals with self-similar hierarchy, Phys. Rev. B 92 (2015) 104304.
[16] A. Kruisová, H. Seiner, P. Sedlák, M. Landa, B. Román-Manso, P. Miranzo, M. Belmonte, Finite elements modeling of mechanical and acoustic properties of a ceramic metamaterial assembled by robocasting, Appl. Mech. Mater. 821 (2016) 364–371.
[17] O. Sigmund, J.S. Jensen, Systematic design of phononic band-gap materials and structures by topology optimization, Phil. Trans. Roy. Soc. A 361 (2003) 1001–1019.
[18] Y. Li, X. Huang, F. Meng, S. Zhou, Evolutionary topological design for phononic band gap crystals, Struct. Multidiscipl. Optim. 54 (2016) 595–617.
[19] S. Hedayatrasa, K. Abhary, M. Uddin, C.-T. Ng, Optimum design of phononic crystal perforated plate structures for widest bandgap of fundamental guided wave modes and maximized in-plane stiffness, J. Mech. Phys. Solids 89 (2016) 31–58.
[20] Y. Liu, J.-Y. Su, Y.-L. Xu, X.-C. Zhang, The influence of pore shapes on the band structures in phononic crystals with periodic distributed void pores, Ultrasonics 49 (2009) 276–280.
[21] Y. Liu, J.-Y. Su, L. Gao, The influence of the micro-topology on the phononic bandgaps in 2D porous phononic crystals, Phys. Lett. A 372 (2008) 6784–6789.
[22] Z. Hou, Y. Liu, The effects of shapes and symmetries of scatterers on the phononic band gap in 2D phononic crystals, Phys. Lett. A 332 (2004) 481–490.
[23] L. D'Alessandro, E. Belloni, R. Ardito, A. Corigliano, F. Braghin, Modeling and experimental verification of an ultra-wide bandgap in 3D phononic crystal, Appl. Phys. Lett. 109 (2016) 221907.
[24] E.P. Furlani, H.S. Jee, H.S. Oh, A. Baev, P.N. Prasad, Laser writing of multiscale chiral polymer metamaterials, Adv. Optoelectron. 2012 (2012) 861569.
[25] K.H. Matlack, A. Bauhofer, S. Krödel, A. Palermo, C. Daraio, Composite 3D-printed metastructures for lowfrequency and broadband vibration absorption, Proc. Natl. Acad. Sci. USA 113 (2016) 8386–8390.
[26] S. Laureti, O. Akanji, L.A.J. Davis, S.J. Leigh, D.A. Hutchins, M. Ricci, Design and characterization of 3D-printed phononic crystals for sub-MHz ultrasound manipulation, in: 2015 IEEE International Ultrasonics Symposium, IUS 2015, 2015, 7329403.
[27] M. Miniaci, A. Marzani, N. Testoni, L.D. Marchi, Complete bandgaps in a polyvinyl chloride (pvc) phononic plate with cross-like holes: numerical design and experimental verification, Ultrasonics 56 (2015) 251–259.
[28] P. Celli, S. Gonella, Laser-enabled experimental wavefield reconstruction in two-dimensional phononic crystals, J. Sound Vib. 333 (2014) 114–123.
[29] O. Yuksel, C. Yilmaz, Shape optimization of phononic band gap structures incorporating inertial amplification mechanisms, J. Sound Vib. 355 (2015) 232–245.
[30] J.O. Vasseur, P.A. Deymier, B. Chenni, B. Djafari-Rouhani, L. Dobrzynski, D. Prevost, Experimental and theoretical evidence for the existence of absolute acoustic band gaps in two-dimensional solid phononic crystals, Phys. Rev. Lett. 86 (2001) 3012–3015.
[31] B. Bonello, L. Belliard, J. Pierre, J.O. Vasseur, B. Perrin, O. Boyko, Negative refraction of surface acoustic waves in the subgigahertz range, Phys. Rev. B 82 (2010) 104109.
[32] P.H. Otsuka, K. Nanri, O. Matsuda, M. Tomoda, D.M. Profunser, I.A. Veres, S. Danworaphong, A. Khelif, S. Benchabane, V. Laude, B.O. Wright, Broadband evolution of phononic-crystal-waveguide eigenstates in real- and k-spaces, Sci. Rep. 3 (2013) 3351.
[33] H. Ogi, S. Masuda, A. Nagakubo, N. Nakamura, M. Hirao, K. Kondou, T. Ono, Impact of interface stiffness in surface-wave resonances on nanostrip-attached substrates, Phys. Rev. B 93 (2016) 024112.
[34] N.-K. Kuo, G. Piazza, Ultra high frequency resonant cavity in Aluminum Nitride phononic crystals, in: 2012 IEEE International Ultrasonics Symposium, IUS 2012, 2012, 6562306.
[35] M. Torres, F.R. Montero de Espinosa, Ultrasonic bandgaps and negative refraction, Ultrasonics 42 (2004) 787–790.
[36] B. Román-Manso, Á. de Pablos, M. Belmonte, M.I. Osendi, P. Miranzo, Microstructural designs of spark-plasma sintered silicon carbide ceramic scaffolds, Bol. Soc. Esp. Ceram. Vidr. 53 (2014) 93–100.
[37] Comsol Inc., Comsol Multiphysics version 3.5, 2007.
[38] Y. Liu, X.Z. Sun, S.T. Chen, Band gap structures in two-dimensional super porous phononic crystals, Ultrasonics 53 (2013) 518–524.
[39] Y.-F. Wang, Y.-S. Wang, X.-X. Su, Large bandgaps of two-dimensional phononic crystals with cross-like holes, J. Appl. Phys. 110 (2011) 113520.
[40] F. Bloch, Quantum mechanics of electrons in crystal lattices, Z. Phys. 53 (1928) 555–600.
[41] C. Kittel, Introduction to the Solid State Physics, eighth ed., Wiley, New York, 2005.

Results in Physics 14 (2019) 102450

Contents lists available at ScienceDirect

Results in Physics

journal homepage: www.elsevier.com/locate/rinp

Crack growth in Fe-Si (2 wt%) single crystals on macroscopic and atomistic level

Martin Ševčík[a,b], Jan Zídek[a], Jitka Nejezchlebová[a], Jan Štefan[a], Anna Machová[a,*], Hanuš Seiner[a], Alena Uhnáková[a], Jaroslav Čapek[c], Pavel Lejček[c]

[a] Institute of Thermomechanics AS CR, Dolejškova 5, 18200 Prague 8, Czech Republic
[b] Faculty of Electrical Engineering, CTU, Technicka 2, 16627 Prague 6, Czech Republic
[c] Institute of Physics AS CR, Na Slovance 2, 18221 Prague 8, Czech Republic

ARTICLE INFO

Keywords:
Fe-Si single crystals
Experiments
Fracture
T-stress
Molecular dynamics
Bcc iron

ABSTRACT

This paper is dedicated to experimental and atomistic study of the influence of so called *T*-stress (acting along the crack plane) on fracture processes in bcc iron. We analyze experimental results from fracture tests performed at room temperature on bcc iron-silicon single crystals with a long edge crack $(\bar{1}\,1\,0)[1\,1\,0]$ (crack plane/crack front). The specimens were loaded in tension mode I under different border conditions inducing different sign of the *T*-stress. The brittle-ductile behavior at the crack front was monitored on-line via optical microscopy together with external force and prolongation of the specimens. Topology of the specimens has been investigated before and after the fracture tests via the white light interferometer. The microscopic processes produced by the crack itself were studied at 300 K via 3D molecular dynamic (MD) simulations in bcc iron under equivalent boundary conditions and the *T*-stress was examined by means of stress calculations on the atomistic level. The experimental and atomistic results show that the sign of the *T*-stress affects the fracture behavior. MD simulations reveal that positive *T*-stress makes the emission of blunting dislocations $\langle 1\,1\,1\rangle\{1\,1\,2\}$ from the crack front more difficult. As a consequence, higher external loading is needed for crack blunting in the experimental specimens with $T > 0$ in comparison with the specimen having $T < 0$.

Introduction

The brittle-ductile response of bcc iron single crystals with a low content of silicon is often studied experimentally, see e.g. [1–11], since it is a good model material to understand crack behavior in structural ferritic steels which is important topic in many engineering applications, e.g. for reactor steels [12]. The experimental studies reveal that the brittle-ductile behavior depends on temperature [1–3] loading (strain) rate [4], crack orientation [9,10] and type of loading [5–7,11].

Continuum analyses based on linear fracture mechanics (*LFM*) and Peirls-Nabarro (*PN*) model for dislocations [13,14] enabled to introduce a criterion for the brittle vs. ductile behavior of cracks by means of the stress intensity factor *K* describing the near stress field at the crack front and utilized also for evaluation of fracture tests. Beltz and coworkers [15] incorporated into the Rice model [13] for isotropic continuum also so called *T*-stress, i.e. the nonsingular constant term acting along the crack plane. Extension of this model (including both *K*-factor and *T*-stress) to anisotropic continuum and comparison with atomistic simulations in bcc iron under bi-axial loading in mode I is presented in [16]. The study [16] shows that the brittle-ductile behavior is influenced by the change of the *T*-stress under bi-axial loading. Recent 3D atomistic studies [17] with a short and long edge cracks $(\bar{1}\,1\,0)[1\,1\,0]$ (crack plane/crack front) reveal that the brittle-ductile transition under uniaxial tension in mode I at low temperature ($\sim$0 K) can be caused also by the crack length or by different boundary conditions due to the change of the sign of the *T*-stress. This was our motivation for new fracture experiments presented in the paper.

Previous fracture experiments [9] on Fe-Si single crystals with a relatively short narrow edge notch $a/W = 0.3$ (a means the crack length and W the sample width) of the orientation $(\bar{1}\,1\,0)[1\,1\,0]$ loaded in mode I were only performed under the constant displacements boundary conditions and they showed that the behavior at the crack front was ductile.

In this paper we present the results of new fracture tests on single crystals of α-Fe (2.1 wt%Si) with a narrow long edge notch $a/W = 0.8$ of the type $(\bar{1}\,1\,0)[1\,1\,0]$ loaded in mode I under two different border conditions leading to the different sign of the *T*-stress by continuum treatment. Because the relative ratio a/c (crack length/crack opening)

* Corresponding author.
E-mail address: machova@it.cas.cz (A. Machová).

https://doi.org/10.1016/j.rinp.2019.102450
Received 16 February 2019; Received in revised form 13 June 2019; Accepted 13 June 2019
Available online 27 June 2019

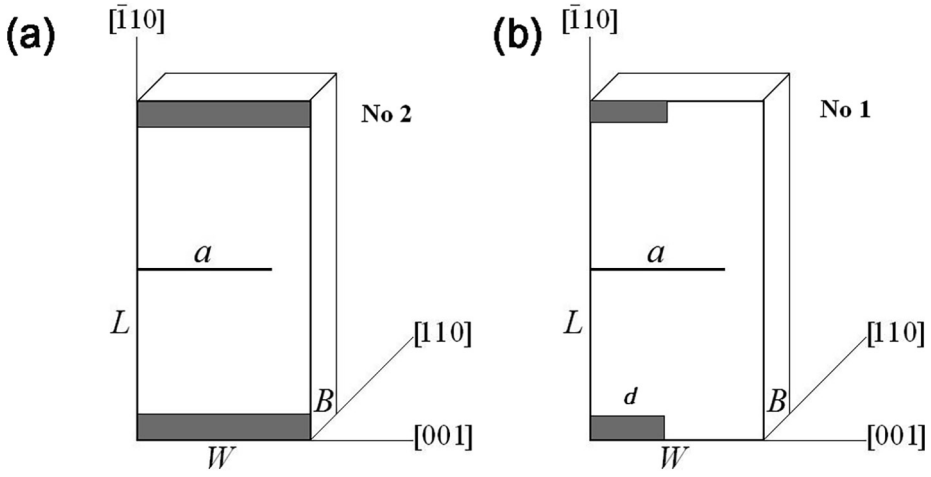

Fig. 1. Geometry and crystallographic orientation of the specimens with edge crack (1̄ 1 0)[1 1 0] (crack plane/crack front). The grey area indicates type of loading induced by the gripper: a/ constant displacements at the borders (specimen No2); b/ partial loading by constant stress along the distance *d* (specimens No1, No3).

exceeds 20, the notch (with $a/c \approx 80$) can be considered according to the Goodier solution for elliptical cavities as a narrow crack and treated by *LFM*, similar to [9]. The shape and orientation of the experimental specimens is shown in Fig. 1. The experiments include also ultrasonic measurements of the velocity of the elastic waves in the anisotropic Fe-Si (2.1 wt%) crystals to determine the unknown elastic constants for the given content of silicon. They are needed for evaluation of fracture tests. The edge crack in fracture experiments was loaded under uniaxial mode I at room temperature. The experimental results are accompanied with new MD simulations at room temperature utilizing 3D atomistic samples of similar geometry as in Fig. 1 (i.e. with the same ratios *a/W*, *L/W* and *B/W* as in experiment). This means that the boundary corrections factors F_I and f_I staying at the *K*-factor [18,20] and *T*-stress [19,21] are the same in MD and as well in experiments. In other words, this study utilizes the self-similar character of fracture mechanics. Our question is how the sign of the *T*-stress (determined by the border conditions) affects the brittle-ductile behavior at the crack front.

As pointed out in [22], any fracture process ultimately involves the rupture of interatomic bonds and therefore, the processes on the atomic scale critically influence overall fracture behavior. It concerns also the crack induced generation of dislocations or stacking faults, where the exchange of interatomic bonds plays the role. This activity is decisive for crack stability or mechanisms of crack extension [23].

Although direct (quantitative) comparison of MD crack simulations in bcc iron with fracture experiments on iron silicon crystals is impossible for many reasons (pre-existing dislocations, dilute Si atoms, different strain rates, etc), we believe that a qualitative assessment of the *T*-effect on the brittle-ductile behavior at the crack front is possible, as shown below.

Experiments

Crystal preparation

Rod-like single crystals of a Fe–2.1 wt% Si alloy (diameter of 12 mm; length of 60 mm) with the axis oriented in the ⟨1 1 0⟩ direction were grown by the floating zone melting technique at the Institute of Physics, Academy of Sciences of the Czech Republic (AS CR) using the apparatus FZ-T-12000-X-VI-VP (Crystal Systems Corp., Japan) [24]. A molten zone was established in the material located in a common focal point of light beams produced by focusing the light beams of four Xe lamps located in focal points of semi-ellipsoidal mirrors. The growth procedure was done using an oriented seed crystal in argon atmosphere in the course of moving the material along the material axis at a rate of 10 mm/h. Simultaneously, both the seed (later being grown crystal) and the materials were rotated in opposite directions by the rate of 10 rev/min. After checking the crystallographic orientation via an x-ray Laue back-scattering technique, rectangular samples of length *L* of about 50 mm, width *W* of about 10 mm, and thickness *B* of about 1.85 mm were prepared by electrospark cutting. The shape and crystallography of the samples are schematically shown in Fig. 1. The deformed layer was removed by grinding and by chemical polishing in dilute mixture of HF and H_2O_2. After this procedure, a narrow edge notch of the length *a* of about 8 mm was electrospark cut using a thin tungsten wire of diameter of 50 μm. After cutting, the initial crack opening $COD = 2c$ was about ~0.2 mm. More precise values are given in Table 1. Note that while the specimens No1 and No2 were of rectangular shape, the sample No3 was rather of a trapezoidal (conic) shape after the cutting from the original circular rod of the single crystal. The basic values *W* given in Table 1 are valid for the middle of the specimen where the notch of the length *a* was cut.

The orientation of the main surface *LW* of the sample in Fig. 1 is (1 1 0), the side surface *LB* is (0 0 1) and *BW* surfaces possess the orientation (1̄ 1 0). The crack is parallel to the (1̄ 1 0) plane; the crack front is oriented in the [1 1 0] direction; and the potential direction of crack extension is [0 0 1].

Precise chemical analysis from the single crystal has been shown that Si content is 2.1 wt% Si. The content of other impurities corresponds to about C ~ 0.003, P ~ 0.01, S ~ 0.01, Mn ~ 0.01 (in wt%) and other 0.02 wt%.

Ultrasonic measurements

Since experimental values of the elastic constants for the present content of silicon are not known, we performed in IT AS CR ultrasonic measurements of the velocity of the longitudinal (L) and transverse (T) shear waves in the [1 1 0] direction (the thickness B) and in the [0 0 1] direction (the width *W*) of the specimen viewed in Fig. 1. Pulse-echo method and PZT transducers with nominal frequency 30 MHz have been used for the measurements of L-waves through the thickness B,

Table 1
Dimensions of three experimental specimens from the Fe-2 wt%Si single crystal corresponding to scheme in Fig. 1. Note that $c = COD/2$.

No.	*L* mm	*W* mm	*B* mm	*a* mm	*COD* mm	*a/c*	*a/W*
1	49.71	9.92–3	1.83–5	7.98	0.195	81.9	0.80
2	49.72	9.88–9	1.83–5	7.96	0.194	82.1	0.80
3	50.66	11.42 ± 1	1.86–8	8.07	0.196	82.3	0.71

while the through-transmission method and transducers at 20 MHz were used for the measurements of L-waves in the [0 0 1] direction (along the width *W*). Additional measurements of propagation of the shear T-waves through the thickness B have been performed using transducers at 20 MHz. The transducers were glued either on the extended free surface *LW* of the specimen in Fig. 1 or on the side narrow surface *LB*.

For our crystal orientation the elastic constants can be determined e.g. from the relations given in [25]:

$$C_{11} = \rho(V_{L[001]})^2, \quad {}'C_{110} = \rho(V_{L[110]})^2, \quad C_{44} = \rho(V_{T2[110]})^2,$$
$$(C_{11} - C_{12})/2 = \rho(V_{T1[110]})^2,$$

where the index $_{T2[110]}$ means the transverse (shear) waves polarized in the direction $[\bar{1}\,1\,0]$ (in the basic cubic orientation the displacements $U_1 \neq 0$, $U_2 \neq 0$, $U_3 = 0$), while the index $_{T1[110]}$ means the T-waves polarized in the [0 0 1] direction (where only $U_3 \neq 0$). The average velocities were determined from 5 or 7 measurements in each case on the rectangular specimens No1 a No2 (see Table 1) and the results are following:

$$V_{L[001]} = 5341\ \text{m/s}, \quad V_{L[110]} = 6235\ \text{m/s}, \quad V_{T2[110]} = 3960\ \text{m/s},$$
$$V_{T1[110]} = 2360\ \text{m/s}.$$

The density ρ of the iron crystal with the content 2.1 wt%Si has been determined to be $\rho = 7.783 \times 10^3\ \text{kg/m}^3$ from the relation $\rho = 0.021\rho(\text{Si}) + 0.979\ \rho(\text{Fe})$ with the densities $\rho(\text{Si}) = 2.329 \times 10^3\ \text{kg/m}^3$ for pure Si and $\rho(\text{Fe}) = 7.9 \times 10^3\ \text{kg/m}^3$ for pure bcc Fe. The content 2.1 wt%Si corresponds to 4.09 at% Si. The numerical value $\rho = 7.783 \times 10^3\ \text{kg/m}^3$ fits well with the experimental and theoretical dependencies ρ vs. at% Si for the iron-silicon single crystals presented in Fig. 1 in [26]. Utilizing the values above for determination of the elastic constants we obtain

$$C_{11} = 2.22 \times 10^{11}\ \text{N/m}^2, \quad {}'C_{110} = 3.03 \times 10^{11}\ \text{N/m}^2,$$
$$C_{44} = 1.22 \times 10^{11}\ \text{N/m}^2, \quad C_{12} = 1.35 \times 10^{11}\ \text{N/m}^2.$$

The largest scattering of data was monitored in the case of $V_{L[001]}$, which concerns evaluation of C_{11}. Due to the narrow LB cross section the measurement of the velocity of the L-waves in the [0 0 1] direction was not very precise since the side lateral wave reflections from LW surfaces make difficult a precise measurement of the transit time. If we use the more precise measurements of $V_{L[110]}$, i.e. the value of $'C_{110} = (C_{11} + C_{12} + 2C_{44})/2$ and the value C_{44} given above for the evaluation of C_{11}, we obtain $C_{11} = 2.24 \times 10^{11}\ \text{N/m}^2$ and consequently $C_{12} = 1.38 \times 10^{11}\ \text{N/m}^2$. The new values differ from the previous by about 1% and 2.2% respectively, which approximately represents the accuracy of evaluation of the elastic constants in the present study. For further treatment we will consider a set $C_{11} = 2.24 \times 10^{11}\ \text{N/m}^2$. $C_{12} = 1.35 \times 10^{11}\ \text{N/m}^2$ and $C_{44} = 1.22 \times 10^{11}\ \text{N/m}^2$. It complies well with the experimental data on the elastic constants of Fe-Si single crystals in the region of low content of silicon, viewed in Fig. 2 in [26]. For comparison, the room temperature data for pure bcc iron from ultrasonic measurements [27] are $C_{11} = 2.33$, $C_{12} = 1.35$ and $C_{44} = 1.18 \times 10^{11}\ \text{N/m}^2$. It may be seen that the elastic constants of Fe-Si single crystals with low content of silicon do not differ significantly from pure bcc iron. It complies with quantum mechanical treatment [28] of the elastic constants in dilute Fe-Si alloys, where just a week dependence on Si content is valid up to ~9 at% Si.

The presented results will be utilized in the next part of the study for evaluation of the effective elastic stiffness coefficient C binding the energy release rate G with the stress intensity factor *K* in anisotropic crystals via the relation $G = C{\cdot}K^2$. It needs to know the matrix of the elastic constants ‘Cij and of the compliance constants ‘Sij for our crystal orientation shown in Fig. 1. If the coordination system according to LFM is utilized, i.e. the axis $x = x_1 = [0\,0\,1]$, $y = x_2 = [\bar{1}\,1\,0]$, $z = x_3 = [1\,1\,0]$, then the individual elements of the matrix are given

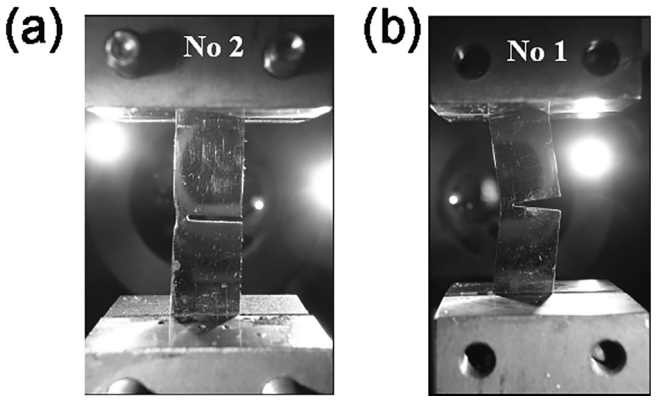

Fig. 2. Experimental arrangement for tension mode I: a/ constant displacements at the borders (specimen No2); b/ the grippers enabling bending (specimens No1, No3). The distance between the grippers corresponds to the active sample length *La*.

by the relations: $'C_{11} = C_{11}$; $'C_{12} = 'C_{13} = C_{12}$; $'C_{22} = 'C_{33} = (C_{11} + C_{12} + 2\ C_{44})/2$; $'C_{23} = (C_{11} + C_{12} - 2\ C_{44})/2$ … $'C_{44} = (C_{11} - C_{12})/2$; $'C_{55} = 'C_{66} = C_{44}$. Numerically the matrix is given by

$$\begin{matrix} 2.24 & 1.35 & 1.35 & 0 & 0 & 0 \\ 1.35 & 3.03 & 0.585 & 0 & 0 & 0 \\ 1.35 & 0.585 & 3.03 & 0 & 0 & 0 \\ & & & 0.434 & 0 & 0 \\ & & & & 1.22 & 0 \\ & & & & & 1.22 \end{matrix} \quad \text{in units of } 10^{11}\ \text{N/m}^2.$$

The compliance constants ‘S_{ij} are determined by inversion of the C-matrix given above for Fe-2.1 wt%Si. In this case the S-matrix is:

$$\begin{matrix} 0.813 & -0.304 & -0.304 & 0 & 0 & 0 \\ -0.304 & 0.457 & 0.047 & 0 & 0 & 0 \\ -0.304 & 0.047 & 0.457 & 0 & 0 & 0 \\ & & & 2.304 & 0 & 0 \\ & & & & 0.820 & 0 \\ & & & & & 0.820 \end{matrix} \quad \text{in units of } 10^{-11}\ \text{m}^2/\text{N}.$$

Fracture tests

The crystals were loaded by uniaxial tension in the direction parallel to the sample length *L*, i.e., the crack was loaded in tension mode I. The fracture experiments were performed at the Institute of Thermomechanics, Academy of Sciences of the Czech Republic (AS CR), using the electromechanical testing machine TiraTest 2300 (force resolution 0.1 N, displacement resolution 1 μm using LVDT gaging sensors) equipped with special grippers modeling the different border conditions: i/ with the prescribed constant end displacements (Figs. 1a and 2a) and ii/ with a partial stress loading on an area *d B*, enabling bending (Figs. 1b and 2b). The total shape of the specimens in Fig. 2 was recorded during the tests by means of uEye UI-2250-C CCD camera (chip size 1/1.8″) with full 1600 × 1200 pts. Crack behavior was observed (with using the same magnification for each crystal) by an OLYMPUS SZ60 optical stereo microscope installed on the test machine and monitored on line by a video recorder. The active sample length (between the grippers) was about $L_a \approx 28$ mm in the case of the samples No1 and No2, while for No3 it was $L_a \approx 24$ mm. During the fracture tests, the loading force P(t), the crosshead displacement ΔL, and the crack tip opening displacements CTOD were recorded simultaneously (on-line) by means of the optical microscope records. The camera enabled to detect also the maximum crack opening COD at the edge of the crack during loading in mode I.

The stress intensity factor was determined from the known relation

$$K_I = F_I \sigma_A (\pi\, a)^{\frac{1}{2}} \text{ where } \sigma_A = P/BW$$

is the applied stress and F_I is the boundary correction factor depending on relative sample dimensions and the boundary conditions.

For the sample No2, the same grippers as in [3] were used with prescribed end displacements (Figs. 1a and 2a) and the shape function $F_I\ (a/W)$ has been determined by Harris [20] from the relation

$$F_I(a/W) = 5/[20 - 13\,a/W - 7(a/W)^2]^{1/2},$$

similar to [3].

For the samples No1 and No3, the new grippers were used, enabling bending in the *LW* plane (Figs. 1b and 2b) under a momentum M. In this case we utilize the boundary corrections and stress intensity factors suggested in [18] that can be written [33] as:

$$F_2(a/W) = [(2W/\pi a)\tan(\pi a/2W)]^{1/2}[0.923 + 0.199(1 - \sin(\pi a/2W))^4] /\cos(\pi a/2W),$$

$$K_1 = F_2\sigma_M(\pi\ a)^{1/2},\ \text{where}\ \sigma_M = 6\,M/BW^2.$$

We suppose that along the distance d in Fig. 1b a constant stress distribution acts in the grippers. It leads to the resulting force P acting at the distance $d_1 = d/2$ and to the momentum $M = P{\cdot}d_1$. In the case of the sample Vz1 the distance $d = 4$ mm and $d_1 = 0.2$ W, so that $\sigma_M = 6{*}0.2WP/BW^2 = 1.2P/BW = 1.2\sigma_A$ and we may use the standard formulation for *K*-factor given above with $F_I = 1.2\ F2$ and $F2 = 4.71$ for $a/W = 0.8$. In the case Vz3, the distance $d = 6$ mm and d_1 corresponded to 0.25 W, i.e. $F_I = 1.5\ F2$ with $F2 = 2.72$ for $a/W = 0.7$. The needed data on the relative ratio a/W, further on M and F_I are included in Table 2, including the used crosshead speed VE = 1 mm/min (at No1 and No2) and VE = 0.2 mm/min for the specimen No3.

In the case of the most favored inclined slip system ⟨1 1 1⟩{1 1 2} viewed in Fig. 3 the Burgers vectors lie in the observation *LW* plane (1 1 0) and so, no slip traces are expected on the surface planes *LW* in the perpendicular *z*-direction. Activity of the slip system leads only to surface steps on the right free surface of the specimen (in front of the crack). This is visible as an extension or contraction in W-direction.

For the reasons mentioned above, the fracture test with the sample No2 was interrupted behind the maximum of the loading force *P(t)* and the topography of the sample No2 has been evaluated after the fracture test by white-light interferometry using the topography module of the Polytec MSA-500 Micro System Analyzer.

MD simulations

The same sample geometry (i.e. the same ratios a/W, L/W, B/W), the same crack orientation as in Fig. 1 and the same type of loading as in fracture experiments on the specimens No2 and No1 have been used for 3D atomistic simulations in bcc iron via molecular dynamics technique. Stress calculations have been performed at temperature of 0 K and 300 K, while the brittle vs. ductile behavior was examined at room temperature of 300 K, relevant to experiments.

Atomistic samples consisted of 440 atomic planes ($\bar{1}$ 1 0) in *L*-direction, 220 planes (0 0 1) in *W*-direction and 30 planes (1 1 0) in *B*-direction along the crack front. The total number of atoms in the 3D crystal was $NPOIN = 1\,452\,000$.

The initial edge crack has been created by cutting interatomic bonds across the crack faces and interatomic interactions across the initial crack faces have not been allowed during MD simulations. The initial crack length in the [0 0 1] direction (see Fig. 1) corresponds to $a = 88$ ao, where ao = 2.8665 Å is the lattice parameter in bcc iron by the potential in use. It corresponds to the ratio $a/W = 0.8$, relevant for fracture experiments with the specimens No1 and No2. The crack is atomically sharp with initial ratio $a/c \approx 124$.

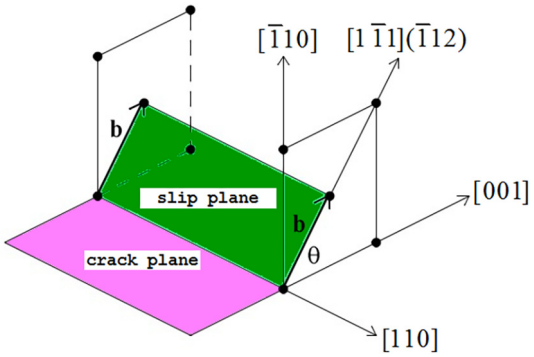

Fig. 3. Orientation of the crack plane and available inclined slip system: the letter b denotes the Burgers vector oriented in the direction [$\bar{1}$ 1 1], lying in the plane (1 1 0) and as well in the slip plane ($\bar{1}$ 1 2). Orientation of the crack front is [1 1 0]. Observation planes in MD and in experiment are the LW planes (1 1 0) perpendicular to the crack front.

Surface relaxation has been performed before the loading to avoid its influence on crack tip processes. No periodic boundary conditions were applied. Newtonian equations of motion for individual atoms were solved in all three directions by a central difference method using stable time integration step h = 1E-14s.

In simulations at temperature of 300 K, random atomic velocities were prescribed initially for all the atoms in the crystal according to Maxwell-Boltzman distribution in classical thermodynamics and the crystal was heated for some period without any loading. When a steady state was reached in the system with an average value of the kinetic energy corresponding to temperature of 300 K (i.e. $E_{kin} = 3/2\ NPOIN\ k_B$ (300 K)), we started with loading of the crystal. It was after the time step 268 in the presented study (i.e. from t = 269 h).

Similar to our previous work, we use our in-house Fortran sequence code for MD simulations and the same N-body potential [35] for bcc iron, tested successfully in many applications. MD simulations are completed by additional stress calculations on the atomistic level for purposes of the comparison atomistic versus continuum predictions. The stress calculations on the atomistic level were performed using the concept of the so-called interplanar stress [36], since it is able to adequately describe the stress gradient arising when straining is inhomogeneous in the range of the interatomic interactions, e.g. at interfaces and free surfaces or during dislocation generation. Comparison with other concepts is discussed in detail in [36]. The fracture characteristics for the potential in use are given in [16], as well as in [17]. (Theoretical values of the Griffith stress intensity factor for the potential in use are $K_G = 0.906$ MPa m$^{1/2}$ for plane strain and $K_G = 0.886$ MPa m$^{1/2}$ for plane stress conditions.)

To model the crack behavior in the specimen No2, the atomistic sample was loaded with prescribed end displacements V_A on 6 surface

Table 2
Results of fracture tests at room temperature: $\sigma_{cr} = P_{cr}/BW$, $H = La/2$, $K_{Icr} = F_I\ \sigma_{cr}\ (\pi\ a)^{1/2}$. The crosshead speed during the tests was V_E = 1 mm/min for the specimens No1 and No2, and for No3 it was V_E = 0.2 mm/min. The values T/σ and biaxiality ratio $\beta = (\pi a)^{1/2}\ T/K_I$ are taken from ref. a/, d/. References: [b]Harris [20]; [a]Fett [21]; [c]Marchand [33]; [d]Sherry [19].

No	P_{cr} (kN)	ΔL_cr (mm)	ΔL_k (mm)	σ_{cr} (MPa)	Boundary con.	H/W	a/W	F_I	K_{Icr} (MPa m$^{1/2}$)	T/σ	β
No1	1.80	2.89	4.25	98.52	M = 0.20 WP[c]	1.4	0.80	5.65	88.12	+1.92[a]	+0.85[d]
No2	1.37	0.60	/	75.5	V_A[b]	1.4	0.80	2.24[b]	26.75	−0.78[a]	−0.98[a]
No3	2.42	1.94	3.87	108	σ_A, d = 0.5 W[a]	1.0	0.71	5.23[a]	89.92	+1.96[a]	+0.38[a]
No3	2.42	1.94	3.87	108	M = 0.25 WP[c]	1.0	0.71	4.07	70.05	+1.96[a]	+0.60[d]

BW layers at the bottom and the top of the sample in Fig. 1a, loaded in *L*-direction. The surface atoms with prescribed displacements do not enter the time integration scheme.

To study the crack behavior in the specimen No1, the atomistic sample has been loaded with prescribed external forces at the top and bottom of the sample in the directions ⟨1̄ 1 0⟩. The external forces were distributed to 6 surface *BW* layers up to the distance $d = 0.4\,W$ (see Fig. 1b), which corresponds to the experiment. The applied stress σ_A and the external force per one atom are related via simple relations $F_{ext} = A_{110}{}^{*}\sigma_A$ where $A_{110} = (ao)^2/\sqrt{2}$ is the area per 1 atom in the ⟨1 1 0⟩ direction where ao is the lattice parameter in bcc iron. When F_{ext} is distributed into 6 layers in *L*-direction then the force acting at one atom in 1ayer is $F(1) = F_{ext}/6$. This distribution is used to avoid failure at the loaded surfaces and to transfer well external loading toward the crack.

During the simulations we monitored each time step the global energy balance (*WEXT*, *EPOT*, *EKIN*), the total number of the interactions in the system *LINT,* further the relative shear displacement *U10* at the crack tip, the maximum crack opening displacements (*COD*) and also the crack advance in the middle of the crystal (i.e. at *B*/2). At selected time steps, the coordinates *X(li), Y(li), Z(li),* the local kinetic energy *Ekin(li)* and the coordination numbers *KNT(li)* of all the individual atoms *li* in the system are recorded for purposes of the graphical treatment of MD results. We use our in-house Fortran sequence code for MD simulations. For visualization of the results in 3D we utilize graphical codes written in the commercial computing environment Matlab. We can scan the situation in all the individual (1 1 0) planes along the crack front and in the perpendicular planes (0 0 1) and (1̄ 1 0) as well, if needed.

Static stress calculations have been performed to see how *LFM* works on the atomistic level at temperature of 0 K and the dynamic simulations under higher level of loading discover the micromechanics of crack growth at temperature of 300 K. Here, 2D visualization of defects is in gray scale while 3D visualization is in color.

Results and discussions

Experimental results and continuum predictions

In cubic anisotropic crystals the relation between the energy release rate G and K factor at the crack front is given [18] by

$$G = C\cdot K^2, \quad \text{where} \quad C = (A_{11}A_{22}/2)^{1/2}\{(A_{22}/A_{11})^{1/2} + (2A_{12} + A_{66})/2A_{11}\}^{1/2}.$$

The elastic compliance coefficients A_{ij} follows from the known strain-stress relations $\varepsilon_i = S_{ij}\,\sigma_j$.

Under plane strain conditions at the crack front ($\varepsilon_3 = \varepsilon_{31} = \varepsilon_{32} = 0$), the needed A_{ij} constants are given by a relation $A_{ij} = S_{ij} - S_{3i}\,S_{j3}/S_{33}$ which leads to $A_{11} = 0.5698$, $A_{12} = -0.2664$, $A_{22} = 0.4470$, $A_{66} = 0.8621$ and $C = 0.387 \times 10^{-11}\,m^2/N$. The last value for Fe-2.1 wt%Si differs only slightly from the value $C = 0.386 \times 10^{-11}\,m^2/N$ determined for pure bcc iron in [16]. Under plane stress conditions the Aij coefficients are replaced by the Sij constants from the matrix above and $C = 0.403 \times 10^{-11}\,m^2/N$ in the Fe (2.1 wt%Si) crystals.

LEFM utilizes also the effective elastic constant describing pure tension, Young modulus. Considering simple tension of a perfect crystal (i.e. Fig. 1 without the crack) in the *L* direction [1̄ 1 0] in Fig. 1, Young modulus under plane stress condition in the *B*-direction [1 1 0] of the Fe (Si)crystals is given by the relation $E = 1/s_{22} = 2.189 \times 10^{11}\,N/m^2$. Under plane strain condition in the [1 1 0] direction $E = 1/A_{22} = 2.237 \times 10^{11}\,N/m^2$, which is the same as in bcc iron.

When cleavage crack growth is expected then $G = 2\gamma$ where γ is the surface formation energy for given crack orientation and the corresponding *K*-factor needed for cleavage is called as Griffith stress intensity factor $K_G = (2\,\gamma/C)^{1/2}$.

The experimental value of γ for our crack orientation in pure bcc iron can be estimated from [29] by relation $\gamma_0 - n_{110}\cdot k_B T$. Here $\gamma_0 = 2.550\,J/m^2$ is the value for 0 K extrapolated by Miedema [29a] from high temperature data on surface tension in liquid state of iron and the second term is a temperature correction by Tyson [29b] where $n_{110} = 1/a_0{}^2\,\sqrt{2}$ is the number of atoms per unit area on (1 1 0) plane, $a_0 = 2.866$ Å is the lattice parameter and k_B is the Boltzmann constant. For temperature of 300 K and pure bcc iron it gives $\gamma_{110} = 2.48\,J/m^2$, i.e. $2\,\gamma_{110} = 4.96\,J/m^2$. MD simulations in [16] indicated at the front of the crack (1̄ 1 0)[1 1 0] the strain energy $W_{110} = 2\,\gamma_{110} = 3.85\,J/m^2$ is needed for cleavage in pure bcc iron under bi-axial tension. The weak anisotropy of γ in bcc Fe is discussed in [29c].

As to Fe-Si crystals, some data for low content of Si (3%) can be found in [4] and [30], but only for crack orientation on a {0 0 1} plane. Large scattering of low temperature data $\gamma_{100} = 1.36$–$28\,J/m^2$ is reported by Gilman in [30] while $K_{IC} = 0.9\,MPa\,m^{1/2}$ close to Griffith value was reported in [4] at room temperature. It corresponds to about $G = C\;K_{IC}{}^2 = 2\gamma_{001} = 3.53\,J/m^2$ using $C = 0.436 \times 10^{-11}\,m^2/N$ for the crack orientation (0 0 1)[1 1 0] tested in [4]. By continuum treatment (e.g. in the model by Orowan or in [31]), the surface cleavage energy $2\gamma_{hkl}$ is calculated as the work done by the stress, needed to separate two given surfaces and it is proportional to an effective elastic constant (Cij or E) acting in the crystallographic direction [*h k l*]. It means, for Fe-Si crystals we may estimate it from a relation $2\gamma_{110} = (`C_{11}/C_{11})\;2\gamma_{001}$. Utilizing the elastic constant given above we obtain an experimental estimate $2\gamma_{110} = 4.78\,J/m^2$ for temperature of 300 K. It complies well with the experimental estimate $4.96\,J/m^2$ for pure bcc iron presented above. The expected Griffith stress intensity for cleavage initiation of the crack (1̄ 1 0)[1 1 0] in Fe-2 wt%Si could be $K_G(1\,1\,0) = 1.11$–$1.13\,MPa\,m^{1/2}$ for plane strain and $K_G = 1.09$–$1.11\,MPa\,m^{1/2}$ for plane stress. It follows from the experimental estimates of γ_{110} for pure bcc Fe and Fe-3 wt%Si and from the different C-coefficients for plane strain and plane stress.

The tested crack (1̄ 1 0)[1 1 0] loaded in mode I at room temperatures is usually ductile (see [9,11,16]) and extends slowly via blunting mechanism caused by dislocation emission into the inclined ⟨1 1 1⟩{1 1 2} slip systems. It is because the available slip system ⟨1 1 1⟩{1 1 2} (Fig. 3) has the largest Schmid factor 0.47 (so that the shear stress τ_A acting in the slip system and coming from the applied tension stress σ_A is $\tau_A = 0.47\,\sigma_A$). Moreover, the slip system in this case is oriented in the hard anti-twinning direction [16]. As a consequence, the crack itself does not generate twins and prefers dislocation emission, leading to crack blunting. The second possibility is an oblique slip system ⟨1 1 1⟩{1 1 0} with Schmid factor 0.41. The activity of this slip system at the short crack $a/W = 0.3$ was observed experimentally before but only under cyclic [11] loading in mode I, not under monotonic tension. An activity of the third possible slip system ⟨1 1 1⟩{1 2 3} in bcc is not probable in our case because of a very low Schmid factor (≈0.15, i.e. sqrt(2/3)*1/sqrt(28)).

When dislocation emission on inclined slip systems is expected, then by the Rice isotropic model [13] including only *K*-factor, the energy release rate can be expressed in a simple form $G_{disl} = \gamma_{us}\,f(\theta)$ where $f(\theta) = 8/(1 + \cos\theta)\sin^2\theta$ and γ_{us} is so called unstable stacking fault energy, which is the energy barrier that has to be overcome during dislocation generation in an available slip system, inclined to the crack plane under an angle θ. The model [13] is based on Peierls-Nabarro (PN) model for dislocations. Atomistic simulations [32] have been shown that the values of G_{disl} and $K_{disl} = (G_{disl}/C)^{1/2}$ by [13] are significantly overestimated. Beltz and coworkers [15,16] has been shown that *T*-stress can significantly decreases the value G_{disl} and consequently K_{disl}. There is no simple (analytical) relation including *T*-stress into the expression for *G* or *K* needed for dislocation generation. The PN equations occurring in the Beltz-Rice model [15,16] have to be solved numerically. As an example of the *T*-effect may serve one case in [16] concerning the central crack (1̄ 1 0)[1 1 0] in the extended crystal of bcc

iron loaded uni-axially with applied stress σ_A in mode I. The inclination angle of the available slip systems ⟨1 1 1⟩{1 1 2} for dislocation emission is $\theta = 54.7°$ (precisely tg $(\theta) = \sqrt{2}$ in bcc lattice) and thus by Rice model [13] including only *K*-factor in isotropic continuum $G_{disl}/\gamma_{us} = 7.612$. Including $T = -\sigma_A$ into the isotropic model [15] then $G_{disl}/\gamma_{us} = 4.27$. In our anisotropic case with $T = \mathrm{Re}(\mu_1\mu_2)\,\sigma_A = -0.8857\,\sigma_A$ one obtains $G_{disl}/\gamma_{us} = 4.09$ which means a drop almost 50% (with respect to 7.612) caused by the *T*-stress. Further decrease comes from normal relaxation in the slip system and the final material parameter $K_{disl} = 0.892\ \mathrm{MPa\,m^{1/2}}$ has been found to be smaller than $K_G = 0.906\ \mathrm{MPa\,m^{1/2}}$ with the used potential [33] for bcc iron. In agreement with the Beltz-Rice prediction, the expected dislocation emission on ⟨1 1 1⟩{1 1 2} slip systems was really monitored by MD in [16] in this case. The recent MD study [17] confirmed that the Beltz-Rice model [16] is applicable as well for edge cracks in finite samples when the boundary correction factors staying at *K*-factor and *T*-stress are included into consideration. Since the unstable stacking fault energy γ_{us} for Fe-Si alloys is not known, we will utilize the value $K_{disl} = 0.892\ \mathrm{MPa\,m^{1/2}}$ which is a reasonable estimate since the elastic properties of the dilute Fe-2.1 wt%Si alloy are very close to pure bcc iron. The value can be utilized to determine the yield stress from the relation $\sigma_{ys} = K_{disl}/(\pi\ a)^{1/2} = 5.63\ \mathrm{MPa}$ considering the crack length $a = 8$ mm in an extended crystal.

The direct results of the fracture tests i.e. the diagrams *P*-Δ*L* and *P*-*t* for the individual samples are shown in Fig. 4a and in Fig. 4b respectively. Evaluation of fracture toughness is presented in Table 2, including the shape functions F_I with corresponding references. The maximum force from the tension diagrams is denoted as P_{cr} and similarly the further corresponding quantities: prolongation of the sample ΔL_{cr}, $\sigma_{cr} = P_{cr}/BW$ and $K_{cr} = F_I\,\sigma_{cr}\,(\pi\ a)^{1/2}$. The quantity ΔL_k denotes the final prolongation of the fractured sample. Fig. 4c presents the stress–strain diagrams for the specimens No1 and No2. It was recalculated from Fig. 4a,b as $\sigma = P/WB$ and $\varepsilon = \Delta L/L_a$ where the active sample length is $L_a = 28$ mm and the dimensions *W, B* correspond to average values following from Table 1. The stress-strain diagram was not evaluated in the case of the specimen No 3 because of its variable cross section *WB* along the length *L* – see Table 1. (The specimen has been prepared from the remaining part of the cylindrical single crystal and it served rather for testing of the new bending grippers.)

Table 2 also includes the biaxiality ratio $\beta = T\,(\pi\ a)^{1/2}/K_I$ from the compendium [19], often used instead of *T* in engineering applications (e.g. in [37]), and as well *T*-stress from the compendium of the elastic solutions by Fett [21].

For the finite geometry associated with our samples loaded under mode I, the *T*-stress can be approximated by a relation [21]: $T/\sigma = f\,(a/W, H/W)$ where σ is a characteristic stress for given type of loading. For constant displacements V_A applied at the borders in mode I it is by [21] $\sigma = \sigma_o = E\,V_A/H$ where *E* is Young modulus. For the boundary condition with the applied constant stress at the borders the characteristic stress is $\sigma = \sigma_A$. In this case the biaxiality ratio can also be written as $\beta = f/F$ where *F* is the geometric (shape) function in definition $K = \sigma_o\,F\,(\pi\ a)^{1/2}$ presented in [21].

In the case of partially applied stress acting along a distance d_1 it can be written [21] generally as $T/\sigma = f(a/W, H/W, d_1/W)$. The tabulated values of the shape function *f* from [21] for the individual specimens are included in Table 2.

The problem is that while the elastic solutions by Fett for constant displacement boundary condition [21] can be successfully used in a low elastic region of loading, the solutions lost their validity in nonlinear and elasto-plastic region of loading. The characteristic stress σ_o for the specimen No2 at the maximum of the tension diagram *P*-Δ*L*, i.e. at $\Delta L_{cr} = 0.6$ mm reaches a very high level $\sigma_o = E\ \Delta L_{cr}/L_a = 2.189 \times 10^{11}\ \mathrm{N/m^2}{*}(0.6/28) = 4.69\ \mathrm{GPa}$, exceeding the conventional yield stress limit $\mathrm{Rp_{02}} = E{*}0.002 = 440\ \mathrm{MPa}$, representing a

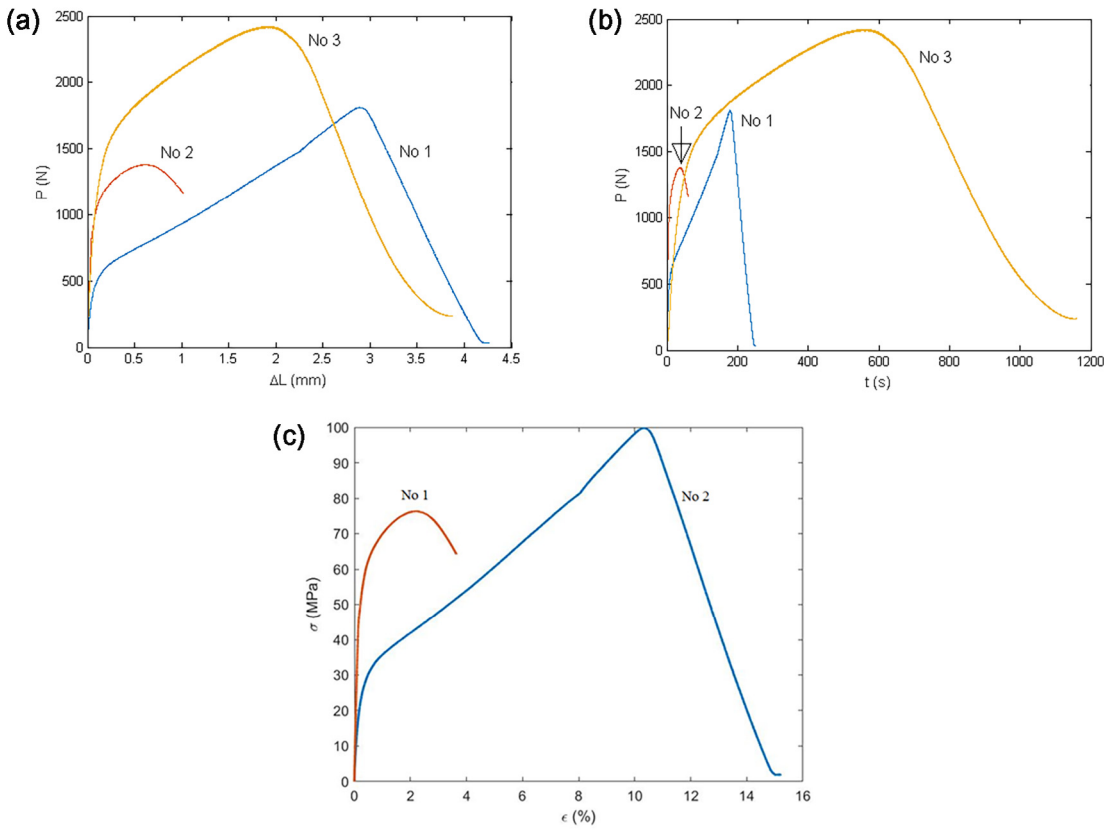

Fig. 4. Records from the fracture tests: a/ total force P vs. prolongation ΔL; b/ total force P vs. time. Crosshead speed VE = 1 mm/min was used for the specimens No1 and No2 and VE = 0.2 mm/min for the specimen No3; c/ stress-strain diagrams for the specimens No1 and No2.

limit for using LFM in practical applications with technical ductile materials. To avoid the problem, we utilize the boundary correction factor by Harris [20] and the characteristic stress $\sigma = P/WB$ for K-factor. The reasons are explained more in detail in Section "MD results".

Moreover, the value K_{cr} for No2 was checked in two ways: an R-curve [9,12] was constructed in the same way as in [9]: at selected values $P(t)$, the crack tip opening ($CTOD$) was measured from the video records, the effective crack length was defined as $a_{eff} = a + a_{blunt}$ where $a_{blunt} = CTOD/2$ and the effective K-factor was determined according to the relation $R_{max} = C\ K^2_{eff}$, where R_{max} denotes the maximum of the curve $R = C\ K^2(a_{eff})$ and C is the elastic coefficient for plane stress or plane strain. The maximum of the R-curve corresponds to fracture toughness $K_{eff} = 30.2\ \mathrm{MPa\,m^{1/}}2$. Another check was the determination of the crack driving force according to the relation $G_c \approx 2\,V(x)^*\ \sigma_{ys}$ from [12], where $2\,V(x)$ stands for the maximum crack opening. In the case of the sample No2 (see Fig. 2a), the maximum crack opening COD_{cr} corresponds approximately to $CTOD$ and ΔL_{cr}. Taking $2\,V(x) = COD_{cr} = 0.6\,\mathrm{mm}$ and $\sigma_{ys} = 5.63\,\mathrm{MPa}$ (as suggested above) we obtain the estimate $G_c = 3378\,\mathrm{J/m}$ and the corresponding values $Kc(ps) = 28.95\,\mathrm{MPa\,m^{1/2}}$, $Kc(pd) = 29.54\,\mathrm{MPa\,m^{1/2}}$ which agrees well with K_{cr} presented in Table 2 (utilizing F_I by Harris [20]). Here the abbreviation (ps) means plane stress and (pd) plane strain (deformation).

In the case of the samples No1 and No3 loaded with the bending grippers the situation is different (see Fig. 2b). Here the maximum crack opening at the edge of the crack (COD) differs from the maximum crack tip opening displacements $CTOD$ measured from the on-line microscope records. We evaluated COD_{cr} from the camera records at the time corresponding to P_{cr} and after that calculated $Gc = COD_{cr}{}^*\ \sigma_{ys}$:

$$COD_{cr}(\mathrm{No1}) = 4.51\,\mathrm{mm}, Gc(\mathrm{No1}) = 25391\,\mathrm{J/m^2},\ Kc(ps) = 79.38,$$
$$Kc(pd) = 81.00\,\mathrm{MPa\,m^{1/2}},$$
$$COD_{cr}(\mathrm{No3}) = 2.33\,\mathrm{mm},\ Gc(\mathrm{No3}) = 13135\,\mathrm{J/m^2},\ Kc(ps) = 57.09,$$
$$Kc(pd) = 58.26\,\mathrm{MPa\,m^{1/2}}.$$

This independent estimate of the fracture toughness K_c for the specimen No1 complies well with the critical value K_{cr} from Table 2. It is not so in the case of the sample No3 because of its terrible shape and thus we exclude No3 from further considerations. (It served rather as a test specimen for the new bending grippers).

The ductile fracture for this crack orientation was accompanied by an extensive crack blunting in all the samples under increasing loading, which is illustrated in Fig. 5 where the details at the crack front from the on-line microscope are shown for the individual specimens under the critical loading P_{cr}. The inclination angle ($\theta \approx 55°$) of the slip bands indicates that the ⟨1 1 1⟩{1 1 2} slip systems have been activated at the front of the ($\bar{1}$ 1 0) crack. The behavior of the specimens behind the maximum P_{cr} is discussed below. Note that while dislocation emission on the inclined slip systems ⟨1 1 1⟩{1 1 2} causes crack blunting, the emission on oblique slip systems (e.g. on ⟨1 1 1⟩{1 1 0}) creates jog in the crack front which may cause crack deflection. This probably concerns the specimen No1 in Fig. 5.

Topography of the specimen No2 in Fig. 6 shows that no significant changes at the sample surface LW in the perpendicular z-direction [1 1 0] are monitored at the crack front (see the lower part in Fig. 6a,b) since the Burgers vector of the active slip systems ⟨1 1 1⟩{1 1 2} lies in the observation plane (1 1 0) – see Fig. 3. Significant changes are visible in Fig. 6c in the vertical direction, where the plastic deformation of the sample width W reaches of about 240 μm, while along the free surface in horizontal direction the z-coordinate varies slightly in the range by about 4 μm. This is caused by dominant activity of the inclined slip systems ⟨1 1 1⟩{1 1 2} which is clarified in the next Section "MD results".

As to T-stress, it can reduce or increase the critical shear stress for slip processes on the inclined slip planes. It can be easy understood via a continuum model by Rice [34], where the critical shear stress τ_c in a slip system inclined with respect to the crack plane under an angle θ is reduced via a simple interchange $\tau_c \to \tau_c + T \sin\theta \cos\theta$. It may be seen that negative T-stress will make the dislocation generation at the crack front more easy, while positive T-stress will increase the stress barrier for dislocation generation which makes it more difficult. It is documented in Fig. 7 where the experimental dependencies P vs $CTOD$ are presented for the specimens No2 with $T < 0$ and No1, No3 with $T > 0$ according to [21,19] – see Table 2. The quantity $CTOD$ reflects crack blunting caused by dislocation emission or motion of pre-existing dislocations on the inclined slip systems ⟨1 1 1⟩{1 1 2} at the crack front. Fig. 7 shows that higher external loading P is needed for the samples No1, No3 with positive T-stress to reach the same $CTOD$ (i.e. crack blunting) in comparison with the sample Vz2 with $T < 0$. This complies with the prediction by Rice [34] mentioned above. The sign of the T-stress in our anisotropic crystals is treated below on the atomistic level.

MD results

The static stress field in front of an atomically sharp crack in the elastic phase of loading can be described sufficiently well by the two parametric LFM including K-factor and T-stress [16]. In an anisotropic continuum at distance r from the crack tip along the axis of crack propagation (angle $\theta = 0$), we may write

$$\sigma_{xx} = -\frac{\mathrm{Re}(\mu_1\mu_2)\mathrm{K_I}}{\sqrt{2\pi \mathrm{r}}} + \mathrm{T}, \quad \sigma_{yy} = \frac{\mathrm{K_I}}{\sqrt{2\pi \mathrm{r}}}, \tag{1}$$

where $\mathrm{Re}(\mu_1\mu_2)$ is an anisotropic factor depending on the crack orientation. Under plane strain conditions prevailing in the middle of our crystal, $-\mathrm{Re}(\mu_1\mu_2) = +0.8857$ [16] for the crack orientation ($\bar{1}$ 1 0) [1 1 0]. In the isotropic case, it is $-\mathrm{Re}(\mu_1\mu_2) = +1$. The relation between K_I and T in an extended anisotropic crystal loaded under uniaxial tension mode I can be written as $T = \mathrm{Re}(\mu_1\mu_2)\ K_I/(\pi\ a)^{1/2}$ which follows from [16]. If a finite crystal with an edge crack is considered, then the boundary correction factors have to be included. This is treated bellow.

Prescribed end displacements (MD model for the specimen No2)

The treatment by Fett [21] for isotropic continuum under the

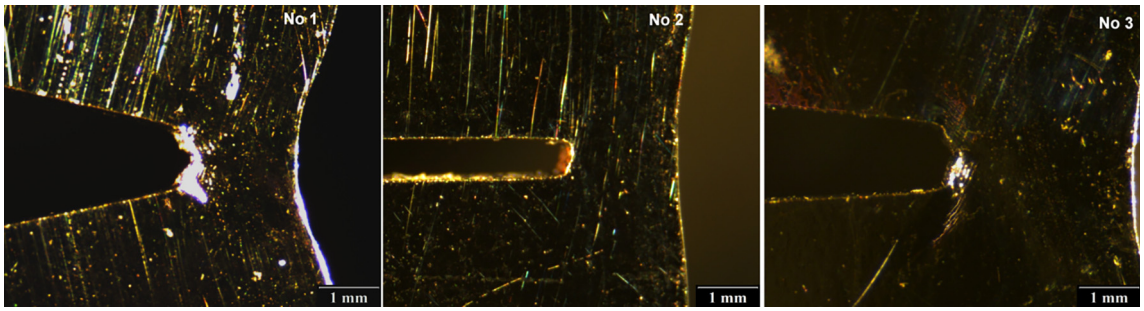

Fig. 5. Crack opening at the maximum of the total force P(t) for the individual specimens (visualized from the left to the right): No1; No2; No3.

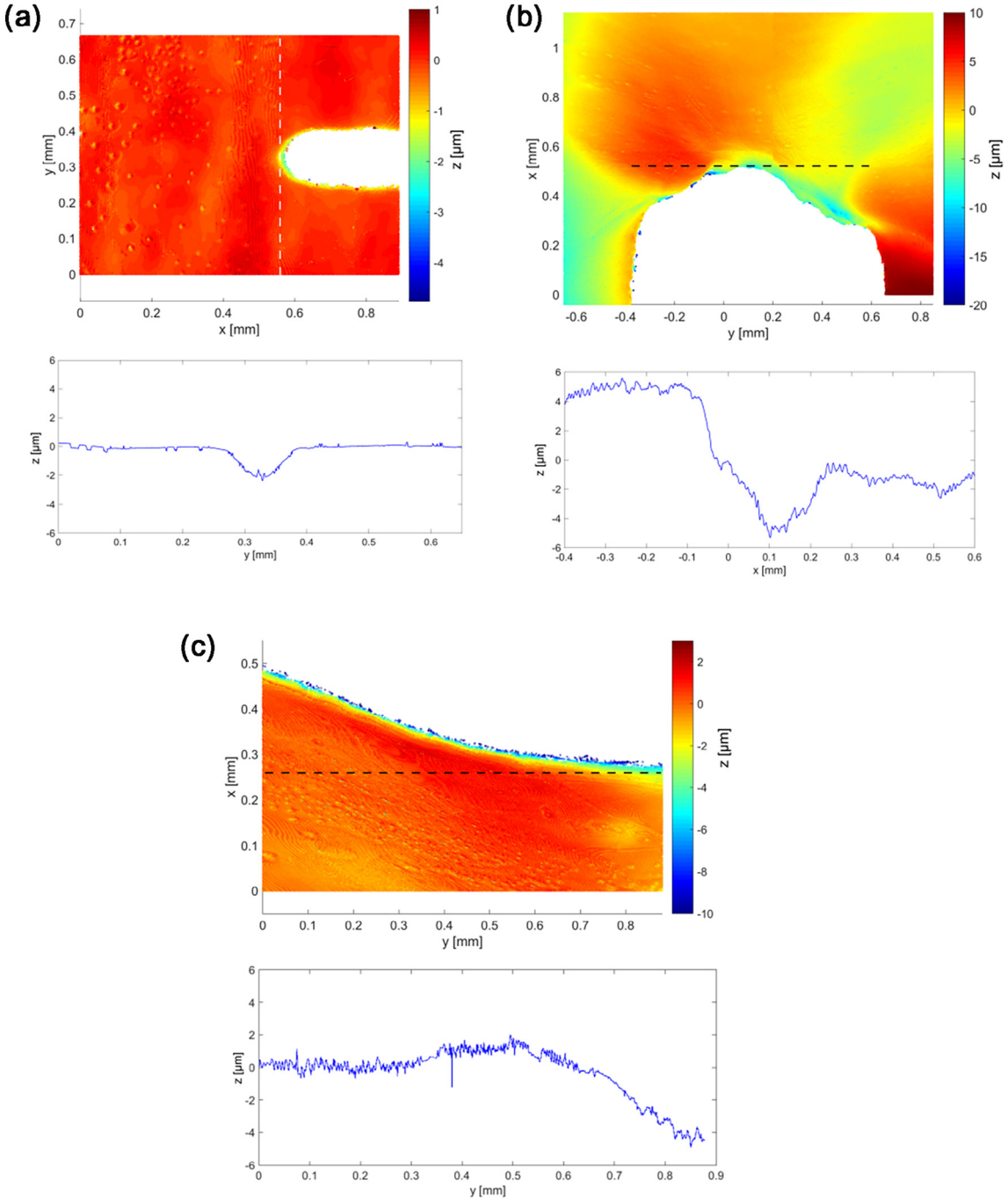

Fig. 6. Topography on the *LW* surface (1 1 0) of the specimen No2 before and after fracture test via the white light interferometer: a/ initial state before loading at the crack front; b/ final state at the crack front; c/ final state at the edge perpendicular to *W*-direction [0 0 1]. The dashed line denotes where the *z*-coordinate in the lower part of the figure is measured.

constant boundary conditions need to be modified for our anisotropic case. We may replace the isotropic elastic constants occurring in the solution via relations $E = 1/A22 = 2.237 \times 10^{11}\,\mathrm{N/m^2}$ and Poisson ratio ν with an average value $\nu \approx 0.3$ mentioned above. We extrapolated the data for $H/W = 0.25, 0.5, 1$ given in [21] to our value $H/W = 1.4$. We have gained $F_I \cong 0.80$ and $T/\sigma_o \cong -0.78 = f_I$ (in Table 2) relevant for our MD simulations with the edge crack $a/W = 0.8$ under the constant displacements conditions.

Static stress calculations on the atomistic level presented below have been performed at initial temperature of 0 K in agreement with continuum models where no thermal activation is considered.

In the treatment by Harris [20] the characteristic stress is given by the measured external force P according to the relation $\sigma = P/WB$ and by the shape function $F_I = 2.24$ for $a/W = 0.8$ (see Table 2). (Note that the T-stress was not treated in [20].) In MD simulations with the prescribed end displacements V_A the external tension force P acting at the bottom and the top of the crystal in Fig. 1 should be equal to resulting interatomic force $RF = \Sigma R_n(li)$ in one half of the crystal loaded with the prescribed end displacements. Here $R_n(li)$ denotes the normal component of the resolved force at one individual atom *li*, acting in the normal direction $n = [\bar{1}\ 1\ 0]$ (see Fig. 1). Time development of *RF* during a relatively slow loading rate 14.7 Å/20 000 h is shown in Fig. 8a. The horizontal line near the time step 0 is caused by the flight time of the loading waves needed to travel from the upper sample border to x-axis

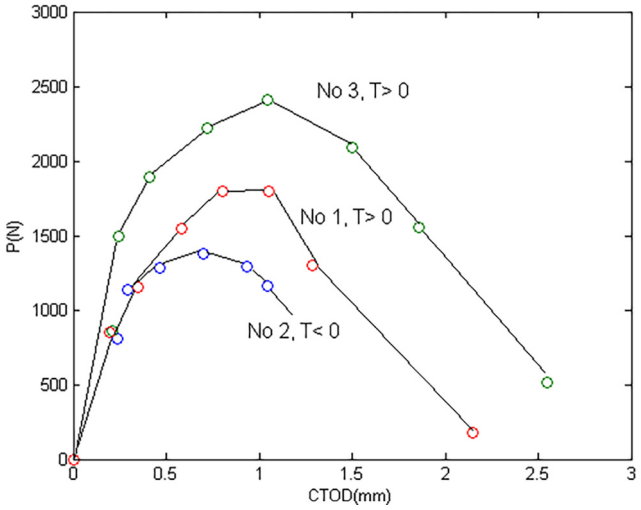

Fig. 7. The dependence total force *P* vs. *CTOD* for the specimens with the different border conditions: No2 – constant displacements with negative *T*-stress, VE = 1 mm/min; No1 – applied stress enabling bending with positive *T*-stress, VE = 1 mm/min; No3 – applied stress enabling bending with positive *T*-stress, VE = 0.2 mm/min.

(for the fastest C_L waves in the normal [$\bar{1}$ 1 0] direction it takes about 710 h). In the linear phase of loading, no change in the number of the interactions *LINT* was detected until the time step 10 750 and the kinetic energy in the system was very low. The first maximum at time step ~11 100 indicates dislocation generation, accompanied with an increase in the kinetic energy and in number of interactions *LINT* in the system. Dislocation emission to further distances from the crack tip is monitored [38] at time step 11 600 leading to decrease of *RF* in Fig. 8a.

To compare the solutions by Fett [21] and Harris [20] in MD model we decided to obtain the static solution under a higher applied displacement $V_A = 7.35$ Å (which corresponds to time step 10 000 in Fig. 8a, close to the nonlinear region of loading). The static solution was obtained utilizing after the time step 10 000 h a viscous damping term in Newtonian equations of motion corresponding to critical attenuation for the basic mode of sample vibrations $\lambda = L$. The results are shown in Fig. 8b. The equilibrium static value of the resulting force is $P = RF = 0.2595 \times 10^{-6}$ N. The stress components in front of the crack in the middle of the crystal (at $B/2$) are shown in Fig. 8c. Here the distance from the crack tip on x-axis is denoted by means of the dimensionless parameter r/ao where ao is the lattice parameter. Similar to [17], the stress component Sx and Sy are corrected by the relatively small initial stress arising after the surface relaxation. Note that the third stress component Sz in MD is positive ($Sz > 0$) which means that plane strain conditions prevails [17] in the middle (at $B/2$) of the nanosized crystal. The *T*-stress in MD is determined from the relation $T_{MD} = Sx - 0.8857\ Sy$ following from the anisotropic LFM equations given above. The anisotropic LFM prediction is denoted in Fig. 8c by the lines, using $F_I = 2.24$ and $\sigma = P/WB = 1.356$ GPa by Harris [20] which gives $K_I = F_I\ \sigma\ (\pi\ a)^{1/2} = 0.855$ MPa m$^{1/2}$. For *T*-stress, an average value $T_{MD} = -2.72$ GPa is used, following from MD results in the interval $r/ao \in < 1, 10 >$. As may be seen in Fig. 8c the *T*-stress from MD with the constant displacement condition is negative (unlike the positive *T*-stress under constant stress boundary conditions presented in Fig. 8 in [17]). This T_{MD} complies fairly well with continuum predictions $T = -2.878$ GPa by Fett [21] utilizing σ_o and f_I defined above.

However, the elastic estimates for the stress $\sigma_o = E\ V_A/H = 3.690$ GPa and for the resulting force $P = \sigma_0\ WB = 0.71 \times 10^{-6}$ N are significantly larger in comparison with the treatment by Harris and by MD, similarly as the work $W = P\ V_A$ done by the resulting force *P* acting at the bottom and the top of crystal. By Fett it is $W_F = 5.200 \times 10^{-16}$ J and by Harris and MD it is $W_H = 1.907 \times 10^{-16}$ J. The last value by Harris agrees well with an independent atomistic value for the static potential (strain) energy $\Delta EPOT = 1.861 \times 10^{-16}$ J monitored in MD under prescribed end displacements $V_A = 7.35$ Å at the borders. (As mentioned in Section "MD simulations", the potential and kinetic energy in the MD atomistic system are monitored in each time step.)

In nonlinear region of loading, the presented results show that a combination of LFM solutions by Harris [20] for *K*-factor and by Fett [21] for *T*-stress is acceptable in the case of constant displacement

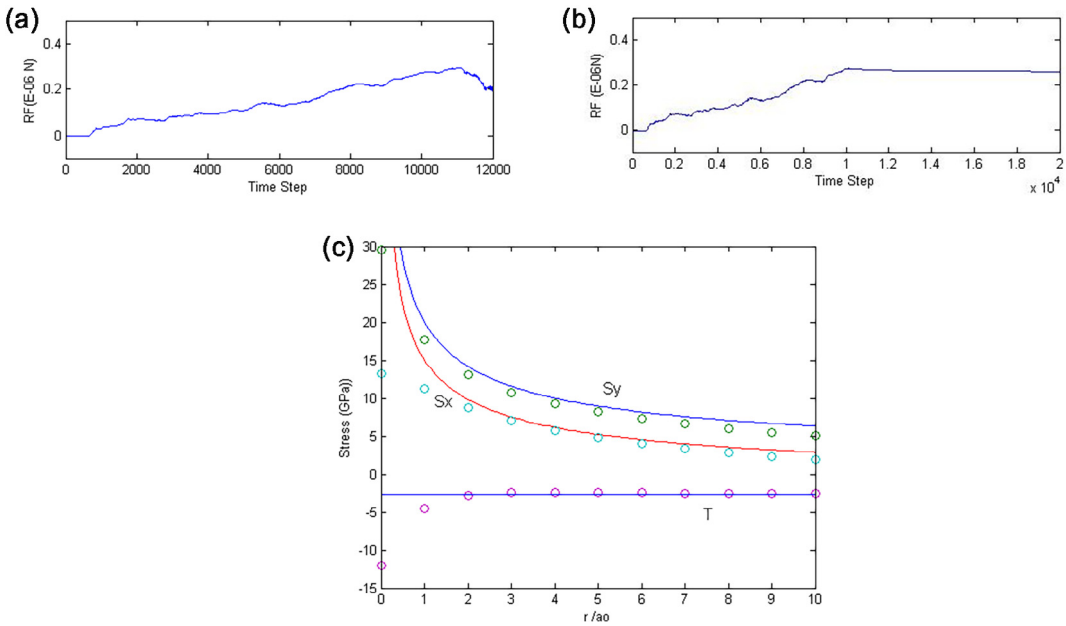

Fig. 8. MD results at 0 K for the constant displacement boundary conditions (model for No2): a/ time development of the resulting force *RF* acting in the normal direction in one half of the crystal under linear loading $\Delta V_A/\Delta t = 14.7$ Å/20 000 h ($\Delta K_A/\Delta t = 0.01\ K_G$/ps); b/ static solution for *RF* corresponding to prescribed end displacements $V_A = 7.35$ Å; c/ static elastic stress components at the crack $a/W = 0.8$ under the prescribed end displacements $V_A = 7.35$ Å. The lines (—) denote LEFM prediction with K_I by Harris [20] and with an average constant *T*-stress following from MD. Circles (o) denote atomic stress from MD and ao is the lattice parameter in bcc iron.

boundary conditions, as it was done in evaluation procedure of the experiment with the specimen No2.

In linear phase of loading the dynamic value of *RF(t)* at time step 10 000 in Fig. 8a is somewhat higher in comparison with the static value and consequently also the applied stress intensity: $RF(t) = 0.2715 \times 10^{-6}$ N, $\sigma(t) = 1.416$ GPa, $F_I = 2.24$ by Harris [20], $K_A(t) = 0.893$ MPa m$^{1/2} \approx 1\, K_G$ with the used potential for bcc iron (see Section "MD simulations"). It means that in elastic region the loading rate can be characterized by means of $\Delta K_A/\Delta t = 0.01\, K_G$/ps (since 100 h = 1 ps). This notation is often used in crack simulations as it enables a comparison of different MD results and also to determine the instantaneous applied stress intensity via a relation $K_A(t) = \Delta t^*(0.01\, K_G/\text{ps})$, where $\Delta t = t - 268$ h, $t = n\,h$ and n means a time integration step. The maximum of *RF*-curve in Fig. 8a (near the time step 11 100) represents the critical force $RF = 0.293 \times 10^{-6}$ N for dislocation generation in the atomistic 3D model. The critical level of the applied stress intensity at this point corresponds to $K_A(tg) = 0.963$ MPa m$^{1/2}$ (according to Harris treatment [20]) which exceeds the *K*-factor needed for dislocation generation $K_{disl} = 0.892$ MPa m$^{1/2}$ by continuum model [16] and so, dislocation emission of complete dislocations in 3D is monitored at time step 11 600 in MD simulations with initial temperature of 0 K, which decreases the strain energy in the system [38] and also the resulting force *RF* in Fig. 8a. It is similar to *P-t* diagram in fracture tests with the specimen No2.

Figs. 9 and 10 comes from MD simulations at 300 K and they are related to fracture tests of the specimen No2 at room temperature. The atomistic sample in MD was heated initially at 300 K during 268 time steps and after the time step 268 h the sample was loaded gradually via the prescribed end displacements $V_A(t)$ increasing linearly with time *t*. Here we present the results for the same loading rate $\Delta V_A(t)/\Delta t = 14.7$ Å/20 000 h as above for 0 K. While at low temperature (close to 0 K) a simultaneous pair emission of the curved dislocations was monitored in [38] on the upper and lower slip systems ⟨1 1 1⟩{1 1 2} above and below the crack plane, at temperature of 300 K the emission was not simultaneous due to a random character of thermal atomic vibrations that can support the process. The first emission at 300 K was detected on the upper slip system ⟨1 1 1⟩ {1 1 2} at time step 11,700 (see Fig. 9a) under the applied end displacements $V_A(t) = 8.403$ Å which corresponds to $K_A(t) = (11\,700\text{ h} - 268\text{ h})^*0.01\, K_G/\text{ps} = 1.14\, K_G$. This is lower in comparison with 0 K where the first emission was detected at time step 11,600 at $V_A(t) = 8.526$ Å and $K_A(t) = 1.16\, K_G$. It can be explained by thermal activation of the process, similar to continuum model presented in [14].

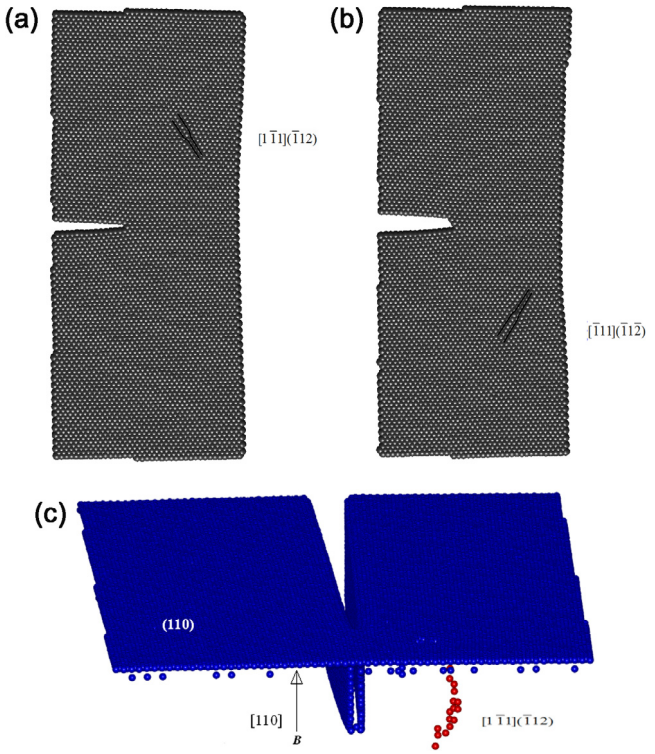

Fig. 9. MD results at temperature of 300 K (model for No2) – detail at the crack front from the dislocation emission on the ⟨1 1 1⟩{1 1 2} slip systems under loading rate 0.01 K_G/ps: a/ the first emission in the upper part of the plane (1 1 0) at time step 11 700, i.e. at the applied stress intensity $K_A(t) = (11\,700\text{ h} - 268\text{ h})^*0.01\, K_G/\text{ps} = 1.14\, K_G$; b/ the delayed second emission at time step 15,000 in the lower part of the plane (1 1 0); c/ 3D visualization of the first dislocation emission by means of the coordination numbers *KNT*: the detail shows the emitted dislocation via red atoms with *KNT* = 16–17 and a part of the sample surface (LW) with the inclined crack faces via blue atoms with *KNT* = 10. (For interpretation of the references to color in this figure legend, the reader is referred to the web version of this article.)

The second emission at 300 K is delayed in MD by 33 ps. It occurred at time step 15 000 in the lower symmetric slip system ⟨1 1 1⟩{1 1 2} as shown in Fig. 9b. This figure also shows that the asymmetric dislocation emission leads to ledge formation in the crack front which makes the subsequent emission more easy – see e.g. [39]. Ledge formation in the crack front after the asymmetric dislocation emission may explain the oblique crack blunting monitored in the case of the specimen No2 – see Figs. 5b and 6. 3D visualization of the first dislocation emission from the crack front at 300 K is shown in Fig. 9c by means of the local coordination numbers *KNT* of individual atoms. The surface atoms with *KNT* = 10 are shown via blue color (including crack faces) while the interstitial atoms in the dislocation core with *KNT* = 16–17 are shown via red color. Note that the *KNT* numbers are valid for the used short-ranged potential and they may differ for other interatomic models with a longer range of interactions.

Fig. 10a shows the final crack shape and the surface steps on the right free surface at the end of MD simulations. The figure illustrates how the dislocation emission in the inclined slip systems ⟨1 1 1⟩{1 1 2} contribute to crack opening and crack growth. When dislocations arrive to the right *LB* free surface (0 0 1) they create surface steps visible also in Fig. 9. The surface steps contribute to lateral plastic contraction of the sample width (*W*), but it does not concern the sample thickness (*B*) since the Burgers vector lies in the *LW* plane. Such behavior was monitored in fracture test with the sample No2.

The quantity that describes well the dislocation emission ⟨1 1 1⟩ {1 1 2} at temperature of 300 K is the relative shear displacement U10/b at the crack tip. Here, U means the displacement of one slip plane in the direction of the Burges vector *b*, U0 is related to the slip plane where the crack tip (bounded) atom lies in the position $r = 0$ (see Fig. 8), U1 is related to the slip plane where the nearest left neighboring (free) atom lies in the position $r = -1ao$ on the free crack faces and U10 = U1 − U0. Time development of U10/b at the crack tip in the middle of the crystal No2 is shown in Fig. 10b. The first dislocation emission is complete when U10/b reaches the value 1, which is already near by the time step 11 500, while graphically it shown at the step 11700 in Fig. 9a. When the second emission occurs in the lower slip system (Fig. 9b, time step 15 000), the relative shear displacement U10/b corresponds to a value ~2 in Fig. 10b, … etc. The detail from the first emission is shown in Fig. 10c. Here, the relative shear displacements U10 determines the local shear strain $U10/h_{112}$ arising during the first emission between the neighboring {1 1 2} planes with interplanar distance h_{112}. Corresponding time development of the shear stress τ_{tip} at the crack tip on the slip system ⟨1 1 1⟩{1 1 2} in the middle of the crystal (at *B*/2) from MD simulations at 300 K is shown in Fig. 10d. This value is calculated from the atomic stress components Sij on the x-axis at $r = 0$ (see Fig. 8c) as $\tau_{tip} = \sqrt{2}\,(Sy - Sx)/3$, where for the angle $\theta = 0$ on the x-axis the shear stress components $Sxy = 0$. (Precise relations for the shear stress in slip system ⟨1 1 1⟩{1 1 2} are given below). The crack

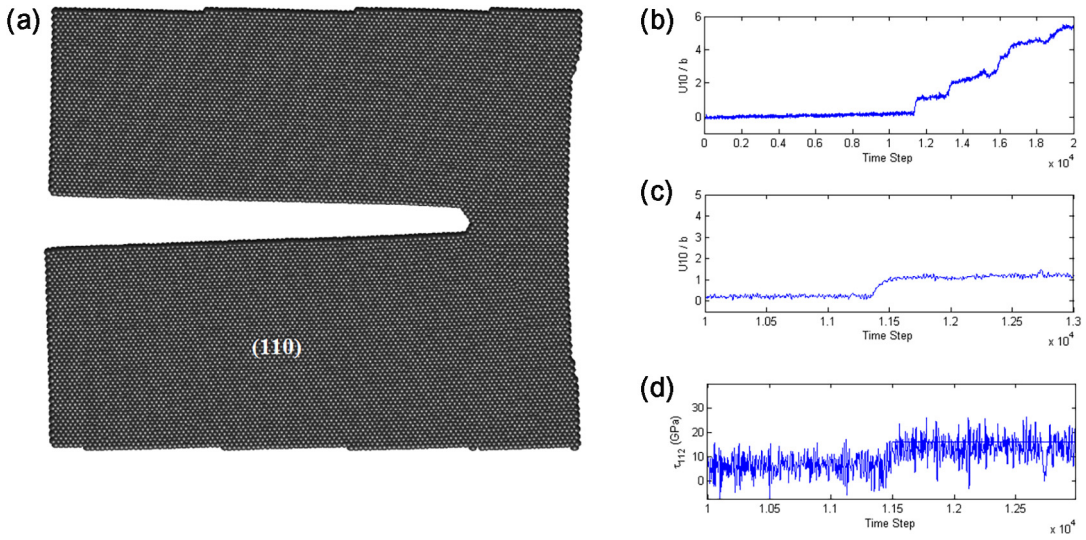

Fig. 10. MD model for No2 at 300 K. a/ complete edge crack at later time step 20 000 ($K_A(t) = 1.973\,K_G$) after multiple dislocation emissions, visible via the surface steps on the right free surface; b/ time development of the relative shear displacements U10/b at the crack tip in the middle of the crystal (B/2) during the multiple dislocation emission ⟨1 1 1⟩{1 1 2}; c/ a detail from the first emission; d/ corresponding time development of the shear stress τ_{112} at the crack tip during the first emission.

tip values Sij on the x-axis are valid in the interval $< 0,\ +ao/2 >$, which for τ_{tip} corresponds to an interval $< 0,\ +b >$ in the slip system ⟨1 1 1⟩{1 1 2}.

Due to random thermal atomic motion in MD at 300 K, the quantities in Fig. 10b-d oscillate. Oscillations in the relative shear displacements U10/b are smaller since they depend just on the resulting forces acting at the crack tip atoms, not on the stress. As mentioned in Section "MD simulations", MD simulations need not the stress, they utilize only the displacements and interatomic forces acting at the individual atoms. The complementary, additional stress calculations are performed just for comparison with continuum predictions. In MD simulations with initial temperature of 0 K, the interplanar stress at the crack front has a smooth, monotonic course as in Figs. 8c and 11 or e.g. in [17]. At elevated temperature of 300 K, the random thermal atomic motion causes random changes in local number of interactions at an atom and as a consequence, the atomic stress oscillate in time and dislocation emission differ in comparison with the temperature close to 0 K. Nevertheless, even the oscillating shear stress in Fig. 10d reflects well the first emission ⟨1 1 1⟩ {1 1 2} near by the time step 11 500, where it moves from the one lower average level to the higher average level corresponding roughly to the critical shear stress $\tau_c = 16.3$ GPa [40] needed for the dislocation emission on the ⟨1 1 1⟩{1 1 2}slip systems with the used potential [35]. The critical shear stress is denoted in Fig. 10d by the line. It represents an interior stress barrier (lattice resistance) for dislocation generation, as follows from the block like shear (BLS) simulations in perfect bcc iron crystals [40]. (Note that a normal relaxation between the {1 1 2} slip planes (observed in MD crack simulations [16]) decreases the stress barrier and consequently the critical value K_{disl}, as presented in [16]).

The atomic stress in Fig. 10d represents the part of virial stress [41] coming from the potential energy in the system and depending just on interatomic forces and atomic positions. The study [41] demonstrates that the interatomic force term is a valid stress measure and can be identified with Cauchy stress in continuum under external loading. The second term (thermal pressure) coming from the average thermal kinetic energy in the system at temperature T = 300 K can be approximated [42] by the average stress components $^{T}Sxx = {}^{T}Syy = {}^{T}Szz = k_B$ T/Vo, where Vo is the volume per one atom. This term is associated with thermal expansion in the system.

The critical shear stress in the Frenkel sin model (utilized by Rice in [13]) corresponds to the critical relative slip displacement $\Delta u = b/4$ and it is given by the relation $\tau_F = \mu b/2\pi h$, where μ is the shear modulus for a considered slip system with an interplanar distance h between the slip planes. The shear modulus and the interplanar distance in the case of the slip system ⟨1 1 1⟩{1 1 2} in pure bcc iron correspond to $\mu = (C_{11} - C_{12} + C_{44})/3 = 71.4$ GPa and $h = ao/\sqrt{6}$ which leads to a large critical value of the shear stress $\tau_{F1} = 24.1$ GPa. As follows from block like shear simulations in the perfect bcc iron crystals [40] with our nonlinear atomistic model [35], the critical shear stress is lower ($\tau_c = 16.3$ GPa), but the critical slip displacement is practically the same, i.e. $\Delta u \cong b/4$. It means that the local critical shear strain for the slip system ⟨1 1 1⟩{1 1 2} is $\Delta u/h = 0.53$, independently on the model. However, mechanical stability of the bcc lattice requires to include at least the interactions between the first and the second neighboring atoms in the lattice [44]. It means that the range of the interaction between the {1 1 2} planes includes in the bcc lattice at least the first and the second neighboring planes {1 1 2}, which is the case of the potential [35] in use. Thus, the critical shear strain can be eventually defined as (b/4)/2h = 0.265 from the continuum point of view. This corresponds to $\tau_{F2} = 12.05$ GPa. Elastic estimate of the critical shear stress $\tau_{el} = \mu^{*}0.265 = 18.9$ GPa is akin to an average Frenkel value $\tau_F = 18.07$ GPa, lying closer to the BLS value of 16.3 GPa following from our atomistic model.

To illustrate the stress state by *LFM* during the first emission in MD, the situation in Fig. 9a for the upper inclined slip system [1 $\bar{1}$ 1]($\bar{1}$ 1 2) will be analyzed.

After transformation of the stress tensor from the original coordinate system $x_1 = [0\,0\,1]$, $x_2 = [\bar{1}\,1\,0]$, $x_3 = [1\,1\,0]$ (relevant for Eq. (1)) to a new Cartesian system '$x_1 = [1\,\bar{1}\,1]$ – direction of the Burgers vector b_1, '$x_2 = [\bar{1}\,1\,2]$ – normal direction to the slip plane and '$x_3 = x_3 = [1\,1\,0]$ – direction of the crack front, we obtain the shear stress acting in the inclined slip system as:

$$\tau_{b1} = \sigma_{\theta r} = \frac{\sqrt{2}}{3}(\sigma_{yy} - \sigma_{xx}) - \frac{\sigma_{xy}}{3} \quad \text{for } \theta = 55°,\ [1\,\bar{1}\,1](\bar{1}\,1\,2),$$
$$\text{or } \tau_{b1} = {}^{0}\sigma_{\theta r} - \frac{\sqrt{2}}{3}T. \tag{2}$$

Here $^{0}\sigma_{\theta r} = {}^{0}\sigma_{\theta r}$ (K_I, μ_1, μ_2, r, θ) is the part of the shear stress without T, depending just on the stress intensity factor K_I at the crack front, further on the distance r from the crack tip, on the inclination angle θ and the complex variables μ_1, μ_2 for given crack orientation in anisotropic continuum. As well the individual stress components σ_{yy},

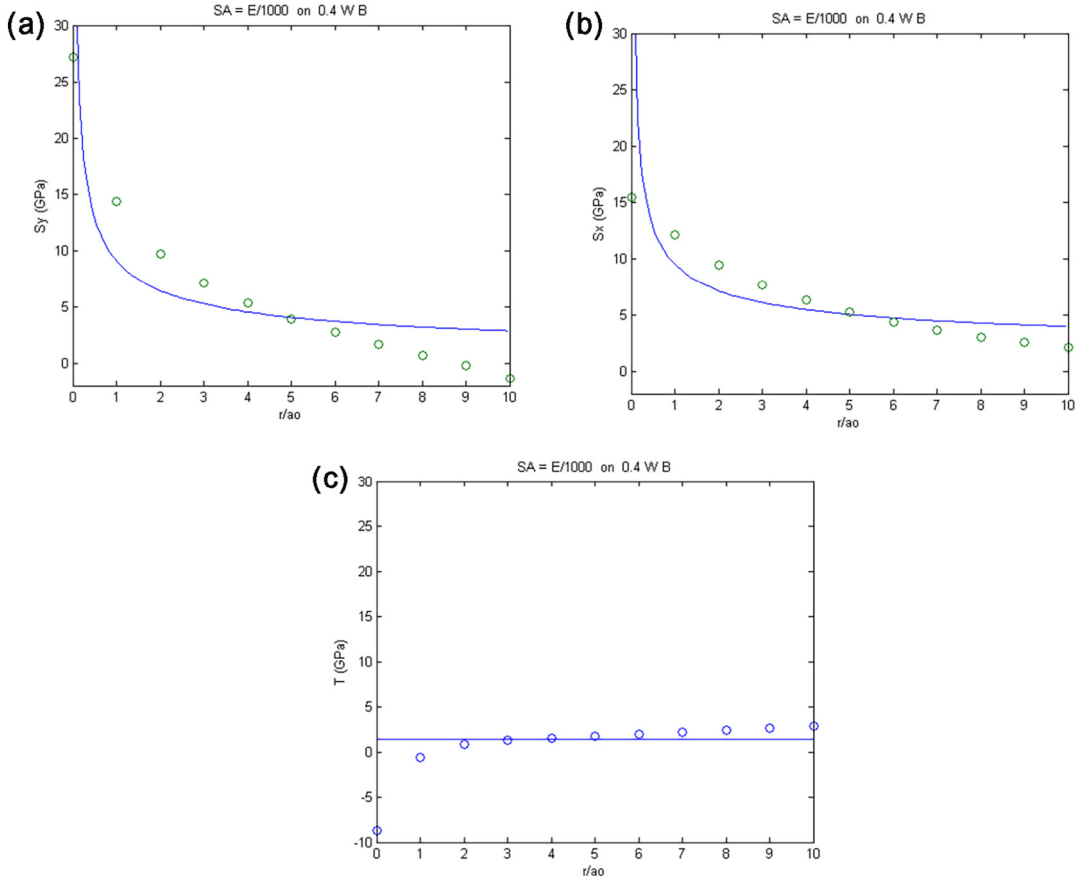

Fig. 11. MD model for No1 at 0 K. Static elastic stress at the crack $a/W = 0.8$ under small applied stress σ_A = E/1000 = 0.22 GPa along the distance $d = 0.4\,W$ at the borders. Lines (—) denote *LEFM* prediction with average values $K_{MD} = 0.387$ MPa m$^{1/2}$ and $T_{MD} = 1.44$ GPa determined from MD results. Circles (o) denote atomic stress from MD and ao is the lattice parameter in bcc iron: a/ stress component Sy; b/ stress component Sx; c/ *T*-stress.

σ_{xx} and σ_{xy} depends on *C*, μ_1, μ_2, *r*, θ. For our crack orientation it is treated in detail in [43] utilizing the elastic constants for bcc iron from [35]. For plane strain conditions it leads to ${}^0\sigma_{\theta r} = 0.362\ K_I/(2\pi r)^{1/2}$, close to isotropic case where the coefficient is 0.363. For plane stress conditions, the coefficient is slightly larger due to different values μ_1, μ_2. The relation above shows that the negative *T*-stress for the used constant displacement conditions will increase the shear stress in the slip system, [1 $\bar{1}$ 1]($\bar{1}$ 1 2) which support dislocation emission in this slip system. (This is valid both for atomistic and experimental samples, but the level of the *T*-contribution will be different in the two cases as discussed below.) If we suppose that the stress intensity K_I at the crack front reached (during the dynamic loading) the level of the material parameter $K_{disl} = 0.892$ MPa m$^{1/2}$ predicted for bcc iron in [16], then the *LFM* shear stress ${}^0\sigma_{\theta r}$ at the nearest distances $r = b/4$, $r = b/2$ and $r = b$ from the crack tip corresponds to ${}^0\sigma_{\theta r}$ $(b) = 8.18$ GPa, ${}^0\sigma_{\theta r}$ $(b/2) = 11.56$ GPa and ${}^0\sigma_{\theta r}(b/4) = 16.35$ GPa. Here $b = a_o\sqrt{3}/2$ means the magnitude of the Burgers vector in the bcc lattice. The atomistic results in Fig. 8c correspond to biaxiality ratio $\beta_{MD} = -0.9$ that can be utilized to evaluate the *T*-stress corresponding to $K_I = K_{disl}$ from the relation $\beta = -0.9 = (\pi a)^{1/2}\ T/K_{disl}$ in the atomistic sample No2. For $a = 88a_o$ in MD, the *T*-contribution to the shear stress $-\sqrt{2}\ T/3 = +1.34$ GPa which leads to $\tau_{b1}(b) = 9.52$ GPa, τ_{b1} $(b/2) = 12.90$ GPa and $\tau_{b1}(b/4) = 17.69$ GPa. The last value exceeds the stress barrier $\tau_c = 16.3$ GPa for dislocation formation in the inclined slip systems ⟨1 1 1⟩{1 1 2} following from the potential in use and so, dislocation emission ⟨1 1 1⟩{1 1 2} is theoretically possible both from the atomistic and continuum point of view.

Note that the distance $b/4$ represents the critical shear displacement in the Frenkel sin model utilized in [13], and approximately as well in atomistic models, where the shear stress reaches the maximum – the stress barrier for dislocation generation (see e.g. Fig. 7a in [40]). At the distance $b/2$ the models reach the maximum of the potential energy (γ_{us} in [13] or Fig. 5a in [40]) needed for dislocation formation. The distance *b* in bcc corresponds to the distance between the first neighboring atoms.

The simplified quasi-static *LFM* analysis above shows: i/ the magnitude of the *T*-stress contribution in the atomistic samples is significant due to the short crack length; ii/ if the *T*-stress is included into *LFM* description, the shear stress in the nearest vicinity of the crack front is sufficiently high to overcome the stress barrier for dislocation emission ⟨1 1 1⟩{1 1 2} in the atomistic model No2 with the prescribed end displacements and negative *T*-stress.

In finite atomistic samples under dynamic gradual loading, the level of the applied stress intensity $K_A(t)$ coming from the loaded borders differs from the instantaneous value of $K_I(t)$ at the crack front. The difference is given approximately by the flight time $\Delta t = (L/2)/V_L$ needed for the longitudinal (L) waves to transfer information from the loaded border to the crack front. In our case it corresponds approximately to about 838 time integration steps *h*. (Here, the same Young modulus $E = 223.7$ GPa as above has been used to estimate the velocity of the longitudinal loading waves V_L.) The level $K_A(t) = K_{disl}$ is reached at the loaded borders at time 10 113 h, while on the x-axis at the crack front it will be later at (10 113 + 838) h, i.e. roughly at time step ~11 000. Independent atomistic results in Fig. 10c show that the gradual process of dislocation generation starts roughly at this time step. More precise determination of $K_I(t)$ at the crack front is possible in MD simulations with initial temperature of 0 K via linear extrapolation procedure from the normal stress component Sy at the crack front

according to Freund definition $K_I = lim_{r\to 0}\,(Sy(r)*(2\pi r)^{1/2})$. It was done e.g. in [16], but not here due to the oscillations of the atomic stress at elevated temperature of 300 K.

We should also note that the relation $\tau_{b1} = {}^0\sigma_{\theta r} - \sqrt{2}\ T/3$ is equivalent with Rice prediction [34] for the inclined slip systems at the crack tip. If one assumes that dislocation emission is possible at $\tau_{b1} = \tau_c$ then ${}^0\sigma_{\theta r} = \tau_c + T\sin\theta\cos\theta$, because $\sin\theta\cos\theta = \sqrt{2}/3$ in the case of the inclined slip systems ⟨1 1 1⟩{1 1 2} in the bcc lattice. The right site of the equation $\tau_c + T\sin\theta\cos\theta$ is the new corrected stress barrier by Rice in [34] that must be overcome by the classical *LFM* shear stress ${}^0\sigma_{\theta r}$ free of the *T*-contribution.

Partially applied stress at the borders (MD model for the specimen No1)

Testing of the specimen No1 was modeled in MD by means of a partially loaded sample shown in Fig. 1b along the distance $d = 0.4$ W. Fig. 11 shows the static elastic stress components Sy, Sx and T-stress in elastic region of loading under $\sigma_A = E/1000 = 0.22$ GPa. MD results are shown via circles (o). We evaluated an average stress intensity factor $K_{MD} = 0.387$ MPa m$^{1/2}$ from the Sy-component (Fig. 11a) in the interval of positive values r/ao ∈ ⟨1, 8⟩ in front of the crack. Similar to Fig. 8, the individual values of the *T*-stress are determined from the relation $T_{MD} = Sx - 0.8857\ Sy$ which yields the average value $T_{MD} = +1.44$ GPa in the interval r/ao ∈ ⟨1, 8⟩. It leads to biaxiality ratio $\beta_{MD} = T_{MD}\,(\pi\ 88\ ao)^{1/2}/K_{MD} = 1.047$. The values K_{MD} and T_{MD} are used for the theoretical *LFM* description in anisotropic continuum by the relations (1). In Fig. 11a, b, c one may see that *LFM* lines describes satisfactory well the independent stress calculations on the atomistic level. According to Table 2, the expected values of the stress intensity and of the biaxiality ratio for $\sigma_A = 0.22$ GPa are: $K_I = F_I\,\sigma_A\,(\pi\ 88\ ao)^{1/2} = 0.348$ MPa m$^{1/2}$ and $\beta = 0.85$ by the compendium [19]. These values by isotropic continuum predictions do not differ significantly from the independent anisotropic MD values and so we may state that evaluation of the experiments by Table 2 is eligible (satisfactory).

The simulations at temperature of 300 K for No1 have been performed in a similar way as in the previous run modeling No2. The atomistic sample (modeling No1) was heated without any loading up to the time step 268. After that the atomistic sample was loaded gradually (linearly in time) from zero up to 2 σ_G during 20 000 h where σ_G is the Griffith level of loading. It corresponds to loading rate $\Delta K_A/\Delta t = 0.01\ K_G$/ps, as in the case No2. Partial loading at the borders (see Fig. 1b) corresponded to $d = 0.4$ W (the model for No1) with $F_I = 5.65$ by Table 2, so that $\sigma_G = 0.57$ GPa as follows from the relation $K_I = K_G$.

In these MD simulations, a mixed brittle-ductile character of crack initiation was monitored – see Fig. 12a. Beside bond breakage at the crack, one may see in Fig. 12a as well a generation of the blunting

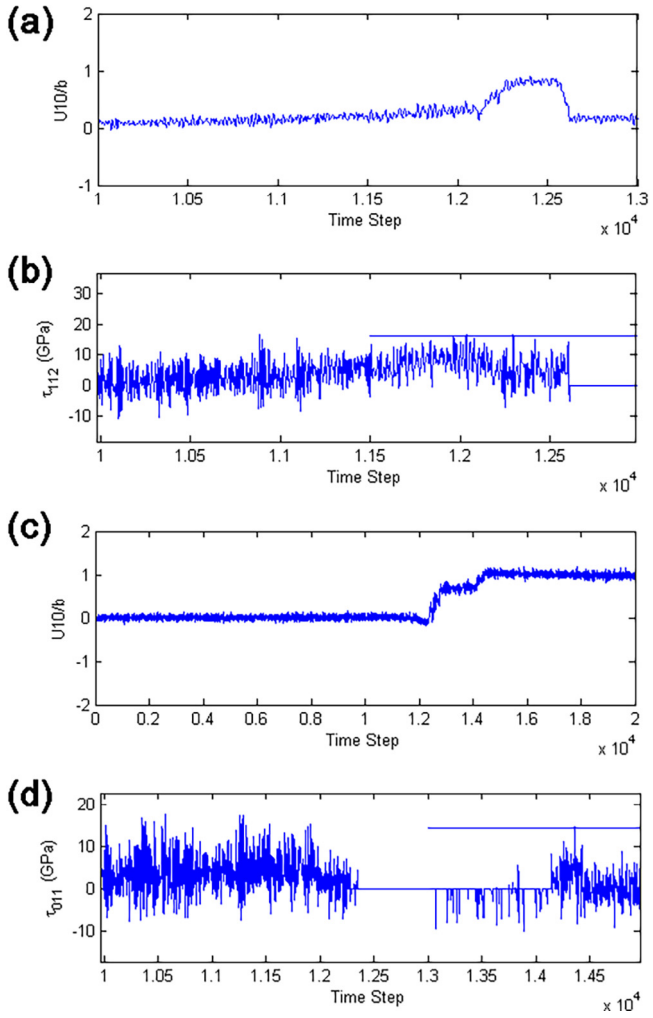

Fig. 13. Activity of the individual slip systems in MD model for No1 at 300 K: a/ incomplete dislocation emission [1 $\bar{1}$ 1]($\bar{1}$ 1 2) in the middle of the crystal (*B*/2) by means of the relative shear displacements U10/*b* at the crack tip; b/ corresponding time development of the shear stress τ_{112} at the crack tip during the dislocation generation; c/ oblique dislocation emission [1 1 $\bar{1}$](0 1 1) from the second surface layer (1 1 0) at the lower crack face by means of U10/*b;* d/ corresponding shear stress τ_{011} at the lower crack tip.

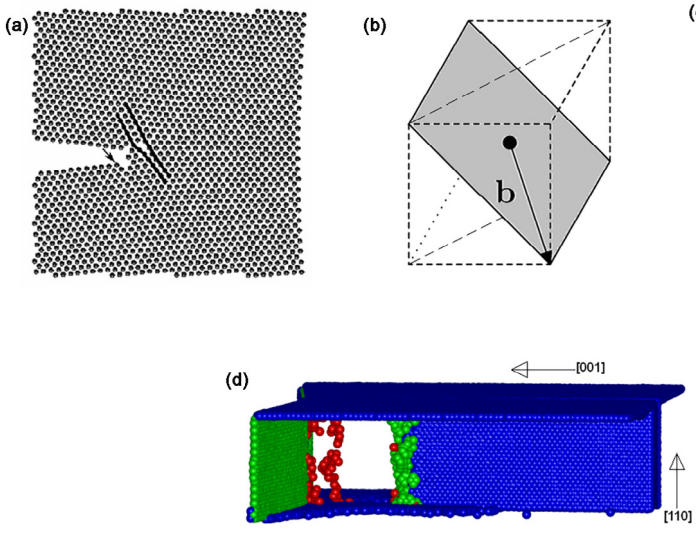

Fig. 12. MD model for No1 at 300 K: a/ crack initiation at time step 13 000 ($K_A(t) = 1.273\ K_G$) in the second surface layer (1 1 0) accompanied by dislocation generation in the ⟨1 1 1⟩(1 1 2) slip system above the crack and, in the lower part, by dislocation generation on oblique slip system ⟨1 1 1⟩{0 1 1}, denoted by the arrow; b/ scheme of the oblique system with a (0 1 1) slip plane and Burgers vector $b = ao/2$ [1 1 $\bar{1}$], where our observation plane (1 1 0) is indicated by the dashed line; c/ slip patterns arising in the observation plane (1 1 0) after the oblique slip in the perfect bcc lattice; d/ 3D visualization of the oblique emission in MD at time step 13 800: view toward crack faces ($\bar{1}$ 1 0) shows a dislocation loop (red atoms) near the free surface (green atoms) and the crack front (blue atoms) generating vacancies (green atoms). (For interpretation of the references to color in this figure legend, the reader is referred to the web version of this article.)

dislocation ⟨1 1 1⟩ {1 1 2} above the crack tip and generation of the oblique dislocations ⟨1 1 1⟩ {0 1 1} at the lower crack face shown via the arrow.

As to the upper inclined slip system [1 $\bar{1}$ 1]($\bar{1}$ 1 2), the shear stress is described by the relations (2) as in the case of the atomistic model No2, i.e. $\tau_{b1} = {}^0\sigma_{\theta r} - \sqrt{2}\ T/3$, but the *T*-stress is positive in the atomistic model No1 (unlike the model No2). The configuration in Fig. 12a represents just generation, not the emission of the complete dislocation ⟨1 1 1⟩{1 1 2} to larger distances from the crack tip as in Fig. 9. This is documented by means of the relative shear displacement and the shear stress at the crack tip in Fig. 13a,b from the middle of the crystal No1. The figures show that U10/b does not reach the value 1 and the average value of the shear stress τ_{112} at the crack tip during the generation process lies below the critical value of 16.3 GPa needed for dislocation emission (denoted by the upper line). Instead of, the shear stress decreases to zero, since the crack tip atom finds itself on the free crack face after an elementary crack advance. The shear stress at the crack tip has been calculated from the atomic stress components Sij in the same way as in the case of the model No2, i.e. $\tau_{112} = \sqrt{2}\ (Sy - Sx)/3$, where the component Sx intrinsically includes the T-stress. This complies with LFM treatment. The component ${}^0\sigma_{\theta r}$ is the same as in MD model No2, i.e. ${}^0\sigma_{\theta r}\ (b/4) = 16.35$ GPa for $K_I = K_{disl}$, but the contribution from the T-stress is different. Taking into account the biaxiality ratio β according to Fig. 11c as $\beta_{MD} = +1.047$, we obtain from the relation $\beta_{MD} = T\ (\pi a)^{1/2}/K_{disl}$ a value $T = +3.32$ GPa. It causes by *LFM* a decrease of the shear stress at the crack tip to a level $\tau_{b1}(b/4) = {}^0\sigma_{\theta r} - \sqrt{2}\ T/3 = 14.78$ GPa that is lower than the critical shear stress $\tau_c = 16.3$ GPa needed for the complete dislocation emission ⟨1 1 1⟩{1 1 2} with the used potential from [35]. It is clear that in atomistic model No1, the positive *T*-stress makes the emission of the blunting dislocations more difficult.

Beside generation of the blunting dislocation, one may see in Fig. 12a below the crack as well a small crack deflection (at the arrow) that can arise after dislocation emission on the oblique slip systems ⟨1 1 1⟩{0 1 1} illustrated by the scheme in Fig. 12b,c. Here the shadow plane with Burgers vector $b = a_0/2$ [1 1 $\bar{1}$] shows the slip plane (0 1 1), while the dashed lines indicate our observation plane (1 1 0). The plane (0 1 1) intersects our crack front [1 1 0] in the oblique direction under the angle 45°. Fig. 12c shows the slip patterns arising in the observation plane (1 1 0) after the oblique slip in the perfect bcc lattice. The oblique slip leads to separation of the {1 1 2} slip planes which is denoted in Fig. 12c by the double arrow. It may contribute to decohesion along the slip planes {1 1 2} and lead to crack deflections, as observed in MD and as well in fracture test with the specimen No1.

If we introduce at the crack tip a new coordinate system $x_1' = [1\ 1\ \bar{1}]$ (*b*-direction), $x_2' = [0\ 1\ 1]$ (*n*-direction) and $x_3' = [2\ \bar{1}\ 1]$ (the perpendicular direction) instead of the original system $x = x_1 = [0\ 0\ 1]$, $y = x_2 = [\bar{1}\ 1\ 0]$ and $z = x_3 = [1\ 1\ 0]$, then by transformation of the stress tensor in anisotropic continuum, the shear stress acting at the crack tip in the direction *b* (see Fig. 12b) is given by

$$\tau_b = \frac{1}{\sqrt{6}}\left(\frac{\sigma_{xy}}{\sqrt{2}} + \sigma_{xx} - \sigma_{zz}\right),\ \sigma_{ij} = \sigma_{ij}(\mu_1, \mu_2, r, \theta),\ \theta = -55°,$$
$$\tau_b = {}^0\tau_b + \frac{T}{\sqrt{6}} \qquad (3)$$

on [1 1 $\bar{1}$](0 1 1).

Here θ means the angle between the original x-axis and the line where the slip plane (0 1 1) penetrates the observation plane (1 1 0). Unlike the inclined system ⟨1 1 1⟩{1 1 2} treated above, in the case of the oblique system [1 1 $\bar{1}$](0 1 1) τ_b differs from $\sigma_{\theta r}$ since the Burgers vector $b = a_0/2$ [1 1 $\bar{1}$] is oriented out from our observation plane (1 1 0) which is clear (obvious) from Fig. 12b. There is also apparent from the relations (3) that generation of the oblique dislocations [1 1 $\bar{1}$](0 1 1) will be favored for positive *T* and for $\sigma_{zz} \sim 0$ near by the free surface (1 1 0) perpendicular to the crack front. This is documented via Fig. 12a and further by means of Fig. 13c and Fig. 13d presenting time development of the relative shear displacements and of the shear stress at the lower crack tip in the second surface layer. The stress barrier for generation of the dislocations ⟨1 1 1⟩{0 1 1} following from BLS simulations with the used potential in the perfect bcc iron lattice is $\tau_c = 14.5$ GPa [45], which is marked in Fig. 13d by the upper line. Fig. 13c shows that a fast generation of the dislocation starts nearby time step 12 000, but below the level 1 the process stops due to sudden decrease of the shear stress at the crack tip (Fig. 13d). This is because some interatomic bonds at the crack tip are temporarily broken, the coordination number decreases to *KNT* = 10 which means that the crack tip atom already lies on the free crack face. The program for atomic stress calculation signalizes such situation via the zero stress components. The broken bonds can be renewed (namely due to the random thermal atomic motion), the interplanar shear stress is renewed as well (see Fig. 13d) and the emission process continue until the level 1 is reached, i.e. the complete dislocation emission from the free surface is achieved. The complete emission was not monitored in the middle of the crystal where plane strain conditions prevail. It complies with anisotropic *LFM*, as explained below.

The expressions for ${}^0\tau_b$ in anisotropic *LFM* are different [43] for plane strain ($\sigma_{zz} \neq 0$) and for plane stress ($\sigma_{zz} = 0$). It can be shown that for

$$\text{plane strain } {}^0\tau_b = 0.117K_I/\sqrt{2\pi r}, \quad \text{plane stress } {}^0\tau_b = 0.214K_I/\sqrt{2\pi r}, \qquad (4)$$

which means that the shear stress in the ⟨1 1 1⟩ {0 1 1} slip system near the free surfaces (1 1 0) is larger almost by a factor 2 in comparison with the bulk crystal. It favors dislocation generation from the corners were the crack penetrate the free surface as observed in MD, not from the bulk crystal.

The competition between the dislocation emission and bond breakage in front of the crack tip causes a slow ductile-brittle crack growth in MD model No1. The applied stress intensity needed for dislocation generation in the atomistic model No1 is higher in comparison with MD model No2 due to the positive *T*-stress. The configuration in Fig. 12a corresponds to the unstable dislocation position *b*/2 discussed in [13,16]. After a subsequent crack advance, the unstable dislocation may disappear on the free crack faces creating the surface steps.

The critical slip displacement for generation of the dislocations ⟨1 1 1⟩{0 1 1} both by Frenkel sin model and with potential in use corresponds well to b/4 (see Fig. 11 in [45]) The interplanar distance $h = d_{011} = a_0/\sqrt{2}$ includes both the interactions between the first and the second neighbors in the bcc lattice and so, the critical shear strain is (b/4)/h = 0.306 and the critical shear stress by Frenkel $\tau_F = \mu b/2\pi h = 13.9$ GPa. It is in a reasonable agreement with the critical shear stress $\tau_c = 14.5$ GPa following from [45] with the potential in use. (For Frenkel estimate, the same shear modulus $\mu = 71.4$ GPa was utilized as in the case of the {1 1 2} slip planes, since propagation of the shear waves in the ⟨1 1 1⟩ direction does not depend on the plane of polarization [25].)

As follows from the scheme in Fig. 12b, dislocation emission from the oblique slip system [1 1 $\bar{1}$](0 1 1) does not contribute to crack opening and blunting, since the projection of the Burgers vector $b = a_0/2$ [1 1 $\bar{1}$] to y-axis oriented in the direction [$\bar{1}$ 1 0] is zero. The non-zero components of the Burgers vector *b* lie in the [0 0 1] and [1 1 0] directions. Instead of blunting, this oblique emission makes jogs in the crack front and in our observation plane (1 1 0).

Due to activity of the oblique slip system ⟨1 1 1⟩{0 1 1}, the crack growth in model No1 is rougher in comparison with model No2 which is in qualitative agreement with experimental results in Fig. 5. Later, transient generation of a dislocation loop is monitored in MD near the free surface which is viewed in Fig. 12d. Here, the green wall represents the second surface layer at the *LB* surface that is occupied by atoms with coordination number *KNT* = 13. Note that *KNT* = 14 in the perfect bcc iron lattice modeled by the short ranged potential in use and so,

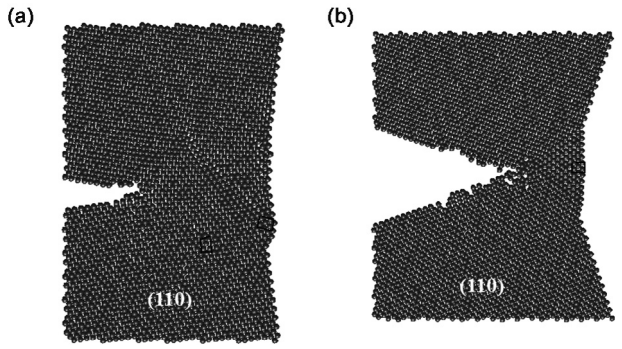

Fig. 14. MD model for No1 at 300 K: a/ generation of twins from the free sample surface shown by the line patterns in the observation plane (1 1 0) (time step 15 000, $K_A(t) = 1.473\,K_G$); b/ the inclined twinned area from the free surface toward the crack front, time step 20 000 before the end of MD simulations ($K_A(t) = 1.973\,K_G$), observation plane (1 1 0).

a group of 14 green atoms represents a vacancy in the bcc lattice.

Disappearing of the dislocation loop at the right free surface *LB* create surface steps that represents new stress concentrators and serve as a nucleus for twin generation at the free right surface *LB* – see Fig. 13. Slip traces on LB surface planes (0 0 1) indicate that the loop was generated on oblique slip systems ⟨1 1 1⟩ {0 1 1}.

Final plastic failure of the atomistic sample is caused via twinning from the free surface toward the crack front – see Fig. 14. The direction corresponds to easy twinning direction with relatively low stress barrier (τ_{twin} = 9.3 GPa) in comparison with dislocation formation (τ_{disl} = 16.3 GPa) for the interatomic potential in use. Such inclined plastic zone was observed as well in experiments with the bending grippers – see Fig. 15 (or video from fracture test No1).

Stress analysis and slip processes in Fe(2 wt%Si) single crystals

As above, we will consider only the slip processes on the inclined ⟨1 1 1⟩{1 1 2} and oblique ⟨1 1 1⟩{0 1 1} slip systems, since the third possible slip system {1 1 1}⟨1 2 3⟩ is not favored due to a low Schmid factor 0.15 and so, it was not observed in the presented crack simulations in pure bcc iron.

To estimate the stress barrier for generation of the blunting dislocation on the inclined slip systems ⟨1 1 1⟩ {1 1 2} and for generation of the dislocations on the oblique slip systems ⟨1 1 1⟩{0 1 1} we will utilize the elastic constants of the tested Fe(2 wt%Si) single crystals evaluated in the Section "Ultrasonic measurements" and further, the Frenkel sin model, leading to reasonable agreement with our atomistic

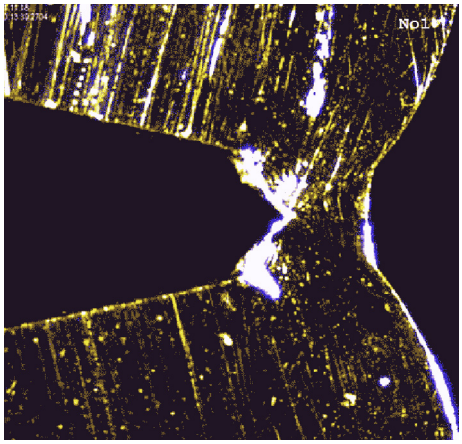

Fig. 15. Fracture test with the specimen No1, the sharp crack before final fracture with inclined (twinned) area from the free surface of the specimen.

model for pure bcc iron – see Section "MD results". The shear modulus in the ⟨1 1 1⟩ direction corresponds to $\mu_{FeSi} = (C_{11} - C_{12} + C_{44})/3 = 69$ GPa, the lattice parameter is ao = 2.864 Å, the interplanar distances $h_{112} = ao/\sqrt{6}$ and $h_{011} = ao\,\sqrt{2}/2$, Burgers vector $b = ao\sqrt{3}/2$, and the stress barrier by the Frenkel model is given by $\tau_F = (\mu/2\pi)^*(b/h)$. The value b/h and the critical shear strain $(b/4)/h$ are given by the geometry of the bcc lattice and $\mu/2\pi$ = 10.98 GPa, so that the following data are obtained for the individual slip systems:

$<111>\{011\}$: $b/h = \sqrt{3}/\sqrt{2}$, $(b/4)/h = \sqrt{3}/4\sqrt{2}$, τ_F = 13.45 GPa;

$<111>\{112\}$: $b/h = 3/\sqrt{2}$, $(b/4)/h = 3/4\sqrt{2}$, ${}^1\tau_F$ = 23.30 GPa;

τ_F = 17.47 GPa − *average*; $(b/4)/2\ h = 3/8\sqrt{2}$, ${}^2\tau_F$ = 11.65 GPa;

To assess the activity of the individual slip systems in the experimental specimens No1 and No2 we will describe the stress state at the crack via the two parametric *LFM* relations presented above, which is relevant for the macroscopic samples where the fight time correction of the loading waves is negligible during the applied gradual loading and $K_A\ (t) \approx K_I$.

Inclined slip systems ⟨1 1 1⟩ {1 1 2}

The relation (2) in the form $\tau_{b1} = {}^0\sigma_{\theta r} - \sqrt{2}T/3$ can be rewritten by means of the biaxiality ratio $\beta = (\pi a)^{1/2}\,T/K_I$ as $\tau_{b1} = 0.362\,K_I/(2\pi r)^{1/2} - (\sqrt{2}/3)\,\beta\,K_I/(\pi a)^{1/2}$ which by Table 2 leads to

$$\tau_{b1} = 0.362\,K_I/(2\pi r)^{1/2} - (\sqrt{2}/3)\,0.85\,K_I/(\pi a)^{1/2} \quad \text{for No 1 with } \beta = +0.85,$$

$$\tau_{b1} = 0.362K_I/(2\pi r)^{1/2} + (\sqrt{2}/3)\ 0.98\,K_I/(\pi a)^{1/2} \quad \text{for No2 with } \beta = -0.98.$$

At the critical distance r = $b/4$ = 1.24 Å, from the crack tip, the second term coming from the T-stress is negligible due to the macroscopic crack length a from Table 1 (unlike the atomistic samples, it is smaller by 4 orders). The critical value of $K_I = K_{disl}$ needed for generation of the blunting dislocations can be estimated from the relation $\tau_F = {}^0\sigma_{\theta r}$ which gives the critical value K_F = 0. 95 MPa $m^{1/2}$, both for the FeSi crystals No1 and No2. This means that the starting line for crack blunting in the experimental specimens No1 and No2 is the same by *LFM* treatment (if we suppose the initial crack tip zone free of pre-existing dislocations). The critical value K_F for emission of the dislocations ⟨1 1 1⟩{1 1 2} is smaller than the experimental estimate K_G = 1.09–1.13 MPa $m^{1/2}$ for cleavage in our Fe (2 wt%Si) crystals (see Section "Experimental results and continuum predictions") and thus, the emission of the blunting dislocations is favored instead of cleavage, in agreement with the Rice-Beltz continuum predictions [13,16]. Since the emission leads to crack blunting and to decrease of the stress intensity at the crack front (see e.g. [38]), an increased level of external loading is required for the next emission, and during this process, the magnitude of the second T-term will increase gradually as well. The crack length a in specimens No1 and No2 is practically the same. The relations above shows that the positive T-stress in the specimen No1 with $\beta = +0.85$ will decrease the shear stress in the ⟨1 1 1⟩{1 1 2} slip systems at the crack front, while the negative T in the specimen No 2 with $\beta = -0.98$ will increase the shear stress. With increasing level of external loading and consequently increasing value of K_I, this difference will be more and more significant, so that the crack induced generation of the blunting dislocations in the specimen No1 should be more difficult in comparison with the specimen No2, which complies with experimental results in Fig. 7

Oblique slip systems ⟨1 1 1⟩{0 1 1}

The relation (3) in the form $\tau_b = {}^0\tau_b + T/\sqrt{6}$ can be rewritten by means of the biaxiality ratio $\beta = (\pi a)^{1/2}\,T/K_I$ as $\tau_b = 0.214\,K_I/(2\pi r)^{1/2} + (1/\sqrt{6})\,\beta\,K_I/(\pi a)^{1/2}$, valid for plane stress at the free surface, which complies with MD and experimental observations, presented e.g. in Fig. 12a or Fig. 5. Utilizing β from Table 2 we obtain

$\tau_b = 0.214\,K_I/(2\pi r)^{1/2} + (1/\sqrt{6})\,0.85\,K_I/(\pi a)^{1/2}$ for No 1 with $\beta = +0.85$,

$\tau_b = 0.214\,K_I/(2\pi r)^{1/2} - (1/\sqrt{6})\,K_I/(\pi a)^{1/2}$ for No 2 with $\beta = -0.98$.

Due to the macroscopic crack length a presented in Table 1, the second T-term is again negligible in the case of the first emission, and the critical value of the stress intensity can be estimated from the relation ${}^0\tau_b = \tau_F$ at the position $r = b/4$ as above. This leads to a relatively high value of the critical stress intensity $K_F = 1.24\ \mathrm{MPa\,m^{1/2}}$ for the first dislocation emission on the oblique slip planes ⟨1 1 1⟩ {0 1 1} in the FeSi crystals at the corners where the crack front penetrates the free surfaces (1 1 0). The value is higher than $K_F = 0.96\ \mathrm{MPa\,m^{1/2}}$ for the emission of the blunting dislocations ⟨1 1 1⟩{1 1 2}. It means that in the initial phase of the external loading, the activity of the slip systems ⟨1 1 1⟩{1 1 2} is expected, leading to crack blunting in the experiments. This was really observed via the on-line microscopy during the fracture tests on the specimen No2 and as well during the fracture test with the specimen No1. According to the *LFM* equations above, with increasing level of K_I (from external loading), the increasing T-contribution at the crack front in the specimen No1 will support the emission in the oblique ⟨1 1 1⟩{0 1 1} slip systems, while in the specimen No2 it will be vice versa. It complies with experimental observations presented in Fig. 5.

Common feature in the atomistic and experimental results is a similar relation $K_{disl} < K_G$ in the case of the blunting dislocations ⟨1 1 1⟩ {1 1 2)} and further, the higher applied stress intensity needed for emission of the oblique dislocations ⟨1 1 1⟩{0 1 1} in comparison with the dislocations ⟨1 1 1⟩{1 1 2}.

Recently different criteria for the ductile-brittle behavior at the crack tip have been tested in [46] by means of the molecular static, applied to cracked nickel single crystals. Motivation of the study was a finding that the unstable stacking fault energy γ_{us} in the Rice model [13] depends on the stress state at the crack tip. We should note that this effect has been reflected in [16] by means of normal relaxation between the slip planes at the crack tip, as already mentioned above.

The significant difference between the experimental values of the fracture toughness presented in Table 2 and the low values of $K_A(t)$ needed for the ductile crack growth in MD simulations can be explained simply by the fact that significant part of the energy from external loading is spent on a motion of pre-existing dislocations, hindered by pre-existing obstacles like Si-atoms and other impurities and defects. Peierls-Nabarro stress needed for motion of pre-existing dislocations is $\tau_{PN} \sim 3{*}10^{-3}\,\mu$ for the edge dislocations ⟨1 1 1⟩{1 1 2} in bcc crystals [47]. In our case $\mu = (C_{11} - C_{12} + C_{66})/3 = 0.69 \times 10^{11}\ \mathrm{N/m^2}$ (see Section "Ultrasonic measurements") and $\tau_{PN} = 0.207$ GPa which is lower by two orders in comparison with the shear stress $\tau_c = 16.3$ GPa needed for dislocation generation in bcc iron. The pre-existing dislocations occurring at the crack front can also contribute to crack blunting. No such pre-existing defects exists in atomistic samples before loading, only the studied pre-existing crack. Nevertheless, MD results in Figs. 8–14 are in qualitative agreement with experimental results, including the experimental (Fig. 2) and atomistic shape (Fig. 16) of the tested samples No1 and No2.

Note that a nice review on other aspects of the T-effect on crack behavior is published in [48].

Summary

Experimental results of the fracture tests in mode I performed on single crystals of the bcc dilute Fe-2.1wt.%Si alloy at room temperature show that mechanical response of a long edge crack ($\bar{1}$ 1 0)[1 1 0] loaded in mode I is influenced by the sign of T-stress. This complies with 3D atomistic simulations via MD technique performed at temperature of 300 K on the atomistic samples of bcc iron with similar geometry and type of loading in mode I. Ultrasonic measurements of the elastic constants revealed that they differ only slightly from those in pure bcc iron. Thus, the mechanical response of the crack to external loading should be very similar in the bcc iron and Fe-2.1 wt%Si crystals.

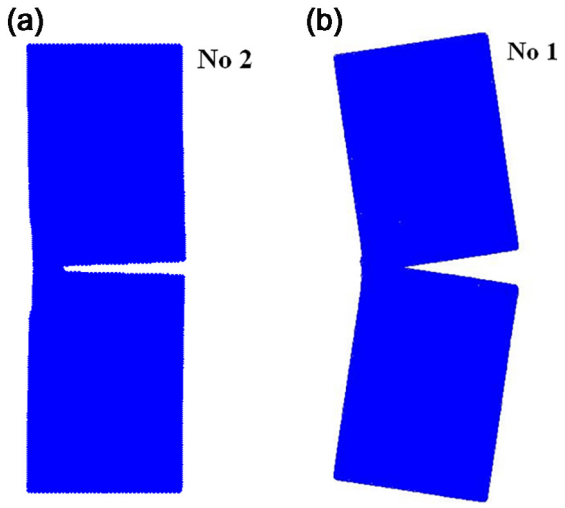

Fig. 16. Final total shape of the atomistic samples at the end of MD simulations: a/ model No2; b/ model No1. (a back projection (1 1 0) comparable with the experimental Fig. 2a and Fig. 2b.)

Under border condition with prescribed end displacements (specimen No2) the T-stress is negative both by continuum predictions and by stress calculations on the atomistic level. The initial crack is blunted to a large extent under the lowest critical force observed in fracture tests and after that the crack slowly, gradually extends into the bulk crystal. The largest Schmid factor, the angle of the slip bands at the crack front of about ≈55° indicate that the slip processes occur predominantly on the inclined ⟨1 1 1⟩{1 1 2} systems. Topography of the experimental specimen No2 via light white interferometry complies with the finding. MD simulations at temperature of 300 K with equivalent border conditions confirm that the crack itself contributes to its own blunting via emission of the dislocations from the crack front on the inclined slip systems ⟨1 1 1⟩{1 1 2}. The subsequent slow crack growth is realized via the blunting mechanism. In comparison with MD results for 0 K, lower applied stress intensity $K_A(t)$ is needed for dislocation emission at 300 K due to thermal activation. The presented atomistic results also show that in nonlinear region of loading a combination of LFM solutions by Harris [20] for K-factor and by Fett [21] for T-stress is acceptable for the constant displacement boundary conditions.

Under border condition enabling bending in mode I (partially loaded specimens No1 and No3 via prescribed stress at the borders) the T-stress is positive, again both by continuum treatment and by stress calculations on the atomistic level in elastic region of loading. Due to the border conditions enabling bending, the crack opening at the edge of the crack (*COD*) was significantly larger from the very beginning of loading in comparison with the specimen No2. However, to reach the same degree of crack blunting at the crack front (measured via *CTOD* by the on line optical microscope) much larger level of the external force $P(t)$ was needed in the fracture tests on the specimens No1 and No3 (positive T) in comparison with the specimen No2 (negative T). It means that higher applied stress intensity $K_A(t)$ is needed for activity of the slip systems contributing to crack blunting. This is in qualitative agreement with equivalent MD simulations at 300 K where just nucleation of the blunting dislocations and no complete dislocation emission on the inclined slip system ⟨1 1 1⟩{1 1 2} was monitored at the crack front due to the positive T-stress. The crack growth in MD was of a mixed brittle-ductile character. Before the final fracture, necking of the remaining cross section via twinning (from the free surface toward the crack front) was monitored in MD which can explain the sharp crack profile and the inclined plastic zone (started from the free right surface) in the experiment with No1 before the final fracture.

The experimental results presented here are in qualitative agreement with the predictions obtained from continuum and atomistic modeling. Post-fracture scanning or transmission electron microscopy cannot distinguish an influence of the pre-existing and crack-induced defects on the brittle-ductile behavior. MD simulations offer a useful complementary tool in this field, since they can bring information about the defects produced by the crack itself and about the influence of these defects on crack stability.

Acknowledgements

The work was supported by Institute Research Program RVO:61388998 and by the projects of the Czech Science Foundation under grants GACR 17-12925S and P108/12/G043. The work of J. Štefan was supported by the European Regional Development Fund under Grant No. CZ.02.1.01/0.0/0.0/15_003/0000493 (Centre of Excellence for Nonlinear Dynamic Behavior of Advanced Materials in Engineering). The work of J. Čapek and P. Lejček was also supported by the European Structural and Investment Funds and the Czech Ministry of Education, Youth and Sports under Operational Program Research, Development and Education (Project No. SOLID21 – CZ.02.1.01/0.0/0.0/16_019/0000760). The authors thank Ms. Gabriela Urbanová for precise preparation of Fe-Si single crystals and Petr Hora for graphical programs in Matlab used for 3D visualization of the dislocations.

Appendix A. Supplementary data

Supplementary data to this article can be found online at https://doi.org/10.1016/j.rinp.2019.102450.

References

[1] Biggs WD, Pratt PL. The deformation and fracture of alpha-iron at low temperatures. Acta Metall 1958;6:694–703. https://doi.org/10.1016/0001-6160(58) 90060-9.
[2] (a) Hull D. Effect of grain size and temperature on slip, twinning and fracture in 3% silicon iron. Acta Metall 1961;9:191–204. https://doi.org/10.1016/0001-6160(61)90069-4;
(b) Hull D. Nucleation of cracks by the intersection of twins in α-iron. Phil Mag 1958;3:1468–9. https://doi.org/10.1080/14786435808233336.
[3] (a) Zielinski W, Lii MJ, Gerberich WW. Crack tip dislocation emission arrangements for equilibrium-I. In situ TEM observations of Fe-2wt%Si. Acta Metall Mater 1992;40:2861–71. https://doi.org/10.1016/0956-7151(92)90451-J;
(b) Marsh PG, Zielinski W, Huang H, Gerberich WW. Crack-tip dislocation emission arrangements for equilibrium – III. Application to large applied stress intensities. Acta Metall Mater 1992;40:2883–94. https://doi.org/10.1016/0956-7151(92)90453-L.
[4] Landa M, Machová A, Převorovský Z, Červ J, Adámek J. *Crack growth in single crystals of α-iron (3wt.%Si)*. Czech J Phys 1998;48:1589–606. https://doi.org/10.1023/A:102287492.
[5] Sorbello F, et al. A consideration of cleavage crack propagation in Fe2Si steel. In: Advances in fracture and damage mechanics (Eds. Lee HS, Yoon IS, Aliabadi MH) Vol. 385–387; 2008; p. 1.Book Series: Key Engineering Materials, https://doi.org/10.4028/www.scientific.net/KEM.385-387.1.
[6] Sorbello F, Flewitt PEJ, Smith G, Crocker AG. The role of deformation twins in brittle crack propagation in iron-silicon steel. Acta Mater 2009;57:2646–56. https://doi.org/10.1016/j.actamat.2009.02.011.
[7] Mine Y, Moriya T, Ando S, Takashima K, Tonda H. Effect of crystallographic orientation on fatigue crack growth of an Fe-3 mass%Si single crystal. J Jpn Inst Met 1998;62:150–8. https://doi.org/10.2320/jinstmet1952.62.2_150.
[8] Prahl J, Machová A, Landa M, Haušild P, Karlík M, Spielmanová A, et al. Fracture of Fe-3wt%Si single crystals. Mater Sci Eng A 2007;462:178–82. https://doi.org/10.1016/j.msea.2006.02.456.
[9] Spielmanová A, Landa M, Machová A, Haušild P, Lejček P. Influence of crack orientation on the brittle ductile behavior in Fe-3wt%Si single crystals. Mater Charact 2007;38:892–900http://doi:10.1016/j.matchar.2006.09.001.
[10] Prahl J, Machová A, Spielmannová A, Karlík M, Landa M, Haušild P, et al. Ductile-brittle behavior at the (110)[001] crack in bcc iron crystals loaded in modeI. Eng Fract Mech 2010;77:184–92. https://doi.org/10.1016/j.engfracmech.2009.02.011.
[11] Landa M, Machová A, Uhnáková A, Pokluda J, Lejček P. Crack growth in Fe-2.7wt% Si crystals under cyclic loading and 3D atomistic results in bcc iron. Int J Fatigue 2016;87:63–70. https://doi.org/10.1016/j.ijfatigue.2015.12.012.
[12] Hertzberg RW. Deformation and fracture mechanics of engineering materials. New York: John Wiley & Sons; 1983.
[13] Rice JR. Dislocation nucleation from a crack tip: an analysis based on the Peierls concept. J Mech Phys Solids 1992;40:239–71. https://doi.org/10.1016/S0022-5096(05)80012-2.
[14] Rice JR, Beltz GE. The activation energy for dislocation nucleation at a crack. J Mech Phys Solids 1994;42:333–60. https://doi.org/10.1016/0022-5096(94)90013-2.
[15] Beltz GE, Fischer LL. *Effect of T-stress on edge dislocation formation at a crack tip under mode I loading*. In: Chuang TJ, Rudnicki JW, editors. Multiscale deformation and fracture in materials and structures. Boston: Kluwer Academic Publishers; 2001. p. 237–42. ISBN 0-7923-6718-9.
[16] Beltz GE, Machová A. Reconciliation of continuum and atomistic models for the ductile versus brittle response of iron. Modelling Simul Mater Sci Eng 2007;15:65–83. https://doi.org/10.1088/0965-0393/15/2/005.
[17] Machová A, Uhnáková A, Hora P. Growth of 3D edge cracks in mode I and T-stress on the atomistic level. Comput Mater Sci 2017;138:315–22. https://doi.org/10.1016/j.commatsci.2017.06.045.
[18] Tada H, Paris P, Irwin G. *Stress analysis of crack handbook*. Hellertown, PA: Del Research Co; 1973. ISBN 978-1-86058-304-9.
[19] Sherry AH, France CC, Goldthorpe MR. Compendium of T-stress solutions for two and three dimensional cracked geometries. Fatique Fract Eng Mater Sruct 1993;18:141–55. https://doi.org/10.1111/j.1460-2695.1995.tb00148.x.
[20] Harris DO. *Stress intensity factors for hollow circumferentially notched round bars*. J Bas Eng, Trans ASME, Series D 1967;B9:49–54. WOS:A19679105200009, ISSN: 0021-9223.
[21] Stress Fett T. Intensity factors, T-stresses, weight functions. Universitatsverlag Karlsruhe; 2008. ISSN: 1436-3488, ISBN: 978-3-86644-235-1.
[22] Bitzek E, Kermode JR, Gumbsch P. Atomistic aspects of fracture. Int J Fract 2015;191:13–30. https://doi.org/10.1007/s1070.
[23] Zhang Y, Jiang S, Zhu X, Zhao Y. Mechanism of crack propagation in nanoscale single crystal, bicrystal, and tricrystal nikels based on molecular dynamic simulation. Results Phys 2017;7:1722–33. https://doi.org/10.1016/j.rinp.2017.04.039.
[24] Lejček P, Kopeček J. Growth of metallic crystals by floating zone technique with optical heating. Mater Sci Forum 2007;567–568:277–80. https://doi.org/10.4028/www.scientific.net/MSF.567-568.277.
[25] Hearmon RFS. Introduction to applied anisotropic elasticity. Oxford: Clarendon Press; 1961.
[26] Machová A, Kadečková S. Elastic constants of iron silicon alloy single crystals. Czech J Phys B 1977;27:555–63. https://doi.org/10.1007/BF01587133.
[27] Rayne JA, Chandrasekhar BS. *Elastic constants of iron from 4.2 to 300 K*. Phys Rev 1961;122:1714–6. https://doi.org/10.1103/PhysRev.122.1714.
[28] Saengdeejing A, Chen Y, Suzuki K, Miura H, Mohri T. *First principle study on the dilute Si in bcc Fe: electronic and elastic properties up to 12.5 at % Si*. Comput Mater Sci 2013;70:100–6. https://doi.org/10.1016/j.commatsci.2012.12.028.
[29] (a) Miedema AR. Surface energies of solid metals. Z Mettalkunde 1978;69:287–92. WOS:A1978FC39900001, ISSN: 0044-3093;
(b) Tyson WR. Surface energies of metals. Can Metall Q 1975;14:307–14. https://doi.org/10.1179/000844375795049997;
(c) Tyson WR, Ayres RA, Stein DF. Anisotropy of cleavage in bcc transition metals. Acta Metall 1973;21:621–7. https://doi.org/10.1016/0001-6160(73)90071-0.
[30] Gilman JJ. Direct measurements of the surface energies of crystals. J Appl Phys 1960;31:2208–18. https://doi.org/10.1063/1.1735524.
[31] Machová A. Fracture micromechanics in α-iron and other metals. BISITS Ferrous Metallurgy, Series B, BISI 27586, p. 1–15. Institute of Metals, London (translated from Czech, Strojirenstvi 38 (1988) 615–620.
[32] Shastry V, Farkas D. Molecular statics simulations of fracture in α-iron. Model Simul Mater Sci Eng 1996;4:473–92. https://doi.org/10.1088/0965-0393/4/5/004.
[33] Marchand N, Parks DM, Pelloux RM. K_I – solutions for single edge notch specimens under fixed end displacements. Int J Fract 1986;31:53–6. https://doi.org/10.1007/BF00033929.
[34] Rice JR. Limitations to the small scale yielding approximation for crack tip plasticity. J Mech Phys Solids 1974;22:17–26. https://doi.org/10.1016/0022-5096(74)90010-6.
[35] Ackland GJ, Bacon DJ, Calder AF, Harry T. Computer simulation of point defect properties in dilute Fe-Cu alloy using a many-body interatomic potential. Phil Mag A 1997;75:713–32. https://doi.org/10.1080/01418619708207198.
[36] Machová A. Stress calculations on the atomistic level. Modell Simul Mater Sci Eng 2001;9:327–37. https://doi.org/10.1088/0965-0393/9/4/306.
[37] Gintalas TM, Ainsworth RA, Scenini F. *T-stress solutions for through-wall circumferential cracks in straight pipes under bending*. Int J Press Vessels Pip 2017;152:27–37. https://doi.org/10.1016/j.ijpvp.2017.04.004.
[38] Hora P, Machová A, Cerv J, Uhnáková A. *Kinetics of dislocation emission: from the crack toward the free surface*. Kovove Mater Metall Mater 2019;57:1–19. https://doi.org/10.4149/km.2019.1.75.
[39] Xu G. *Dislocation nucleation from crack tips and brittle to ductile transition in cleavage fracture*. New York: Elsevier; 2004. p. 81–145.
[40] Machová A, Beltz GE, Chang M. Atomistic simulation of stacking fault formation in bcc iron. Modell Simul Mater Sci Eng 1999;7:949–74. https://doi.org/10.1088/0965-0393/7/6/304.
[41] Zhou M. A new look at the atomic level virial stression continuum-molecular system equivalence. Proc R Soc Lond A 2003;459:2347–92. https://doi.org/10.1098/rspa.2003.1127.
[42] Machová A. Residual stress in Fe-Cu alloys at 0 and 600K. Comput Mater Sci 2002;24:535–43. https://doi.org/10.1016/S0927-0256(02)00235-5.
[43] Spielmannová A, Machová A. *Crack induced stress and generation of twins and dislocations in BCC iron*. 17th European conference on fracture 2008: multilevel approach to fracture of materials, components and structures. 2008.
[44] Born M, Huang K. Dynamical theory of crystal lattices. Oxford: Clarendon; 1954.
[45] Pelikán V, Hora P, Machová A, Spielmanová A. Brittle-Ductile behavior in 3D iron crystals. Czech J Phys 2005;55:1245–60. https://doi.org/10.1007/s10582-005-

0132-9.
[46] Singh R, Mahajan DK. Role of stress triaxiality on ductile versus brittle fracture in pre-cracked FCC single crystas: an atomistic study. Modell Simul Mater Sci Eng 2019;27. https://doi.org/10.1088/1361-651X/ab1cb1.
[47] Vitek, V. Crystal lattice defects, 5, (1974) p. 1–34, WOS:A1974T426300001, ISSN: 0011-2305.
[48] Gupta M, Alderstein RC, Benedictus R. A review of T-stress and its effects in fracture mechanics. Eng Fract Mech 2015;134:218–41. https://doi.org/10.1016/j.engfracmech.2014.10.013.